Characterisation of Multiple-Injection Diesel Sprays at Elevated Pressures and Temperatures

Kourosh Karimi

A thesis submitted in partial fulfilment of the requirements of the
University of Brighton for the degree of
Doctor of Philosophy

May 2007

School of Engineering, University of Brighton
in collaboration with
Ricardo UK

COPYRIGHT

Attention is drawn to the fact that copyright of this thesis rests with its author. This copy of the thesis has been supplied on condition that anyone who consults it is understood to recognise that its copyright rests with the author and that no quotation from the thesis and no information derived from it may be published without the prior written consent of the author.

This thesis may be made available for consultation within the University Library and may be photocopied or lent to other libraries for the purposes of consultation.

ABSTRACT

This thesis describes work undertaken at the University of Brighton on a rapid compression machine based on a two-stroke diesel engine (Proteus) with an optical head to allow observation of the fuel spray. A long-tube, rate of injection rig was used to measure the injection rate of the fuel injection system. Quantification of cyclic variation and rate of injection were carried out for single and multiple-injection strategy. For multiple-injections, it was found that the injected mass of the first of the split was approximately 19% less than that of the single injection strategy for the same injection duration. The second split reduction was less than 4% in comparison to the single injection strategy.

The transient response of the fuel injection equipment was characterised and compared with steady-state behaviour.

The characteristics of the Proteus rig in terms of trapped air mass and transient in-cylinder temperature were investigated and quantified.

The effect of in-cylinder temperature, density and pressure, as well as injection pressure on the characteristics of spray formation, for single and multi-hole nozzles were investigated using high speed video cameras. Cycle-to-cycle and hole-to-hole variations for multi-hole nozzles were investigated and attributed to uneven fuel pressure distribution round the needle seat, and subsequent cavitation phenomena.

Simultaneous Planar Laser Induced Fluorescence (*PLIF*) and *Mie* scattering techniques were used to investigate spray formation and vapour propagation for multi-hole nozzles for single and multiple-injection strategy. The multiple injection work focused on the effect of dwell period between each injection. Two different modes of flow were identified. These are described as 'wake impingement' and 'cavity mode wake effect', resulting in increased tip velocity of the second split spray. The increase in tip velocity depended on dwell period and distance downstream of the nozzle exit. The maximum increase was calculated at 17 *m/s*. A spray pattern growth for the second of the split injections, the 'exceed type' was identified, resulting from an increase in tip penetration due to air entrainment of the first split and propagation into the cooler vapour phase from the first split.

The effect of liquid core length near the nozzle exit was investigated using modified empirical correlations and the evolution of the discharge coefficient obtained from

rate of injection measurements. The results showed increased injection pressure and increased in-cylinder gas pressure reduce both break-up length and break-up time. Penetration was modelled using conservation of mass and momentum of the injected fuel mass. The input to the numerical model was the measured transient rate of injection. The model traced the centre-of-mass of the spray and was validated against PLIF data for centre-of-mass. Overall, the same value of modelling parameters gave good agreement for single and split injection strategy.

DECLARATION

I hereby certify that this report is my own work except where otherwise indicated. I have identified my source of information, and in particular have put in quotation marks any passages that have been quoted word for word and identified their origins.

Signed: Date:

ACKNOWLEDGMENTS

CONTENTS

LIST OF TABLES

LIST OF FIGURES

NOMENCLATURE

Latin symbols

a ---*Velocity of Sound [m/s]*

A_d ---*Droplet Area [m^2]*

A_{delay} ----------------------------------*Internal Cross sectional Area of the Rate Tube Delay Line [m^2]*

$A_{P.Lp/2}$ ------------------*Projected Area of Upstream Half of the Spray Penetration Length [m^2]*

A_{ul} ---*Lower Electron State Fluoresce*

C --*Constant*

CC --*Cubic Capacity*

$C_{blasius}$ ---*Blasius Scaling Constant*

C_d --*Coefficient of Discharge*

C_D ---*Coefficient of Drag*

C_{Drop} ---*Coefficient of Drag for an Isolated Droplet*

C_{Lp} ---*Penetration Length Correlation Constant*

C_t --*Time Constant*

d_d --*Droplet Diameter [m]*

d_{32} --*Sauter Mean Diameter [m]*

D_e ---*Equivalent Nozzle Diameter [m]*

D_{in} --*Nozzle Orifice Entrance Diameter (inlet) [m]*

D_n ---*Nozzle Orifice Diameter [m]*

D_o --*Sac Chamber Diameter of Nozzle [m]*

I_i --*Incident Light Intensity*

k ---*Coefficient for Mass Blowby [kg $K^{1/2}$/s Pa]*

L_{cm} ------------------------------------*The Distance from the Nozzle Exit to the Centre-of-Mass [m]*

L_{crit} --*Critical Penetration Length [m]*

L_{def} ---*Deformable Length of the Spray [m]*

L_n ---*Nozzle Length [m]*

L_p --*Penetration Length [m]*

L_b ---*Breakup Length [m]*

L_d ---*Deformation Length [m]*

L_s --*Effective Spray Length [m]*

m -- *Mass [kg]*

m_d ---Droplet Mass [kg]

$\dot{m}$ ---Mass Flow Rate [kg/s]

n---Refractive Index of the Particle to Medium

n_p--Polytropic Coefficient

n_{rel}--Ratio of the Refractive Index of Diesel Fuel to Air

Oh---Ohnesorge Number

P---Pressure [Pa]

P_{inj}---Injection Pressure [Pa]

P_g--In-cylinder Gas Pressure [Pa]

Q_{st}--Injected Volume per Stoke [m^3/st]

Q_{elec}--Inelastic Collision

Q_{pre}---Pre-Breaking Up

$Q_{rot,vib}$---Rotational and Vibrational Energy Transfer

R---Specific Gas Constant [kJ/kg K]

Re--Reynolds Number

$Re_{initial}$--------------Reynolds Number Based on the Value of the Rod Diameter and Velocity

r_r---Radius of Nozzle (round) [m]

S--Signal

S_{Lif}---LIF Signal

$S_{C,Mie}$---Scattering Function

S_{Mie}---Mie Signal

t---Time [s]

t_b--Breakup Time [s]

T--Temperature [K]

T_g---Gas Temperature [K]

u_b--Breakup Velocity [m/s]

u_{cm}--Velocity of the Centre-of-Mass of the spray [m/s]

u_d---Droplet Velocity [m/s]

u_{inj}---Injection Velocity [m/s]

u_p--Penetration Velocity [m/s]

u_r--Relative Velocity [m/s]

U--Flow Velocity [m/s]

V--Volume [m^3]

We--Weber Number

Greek symbols

θ ---Spray Cone Angle [deg]

ρ --Density [kg/m³]

σ ---Surface Tension [N/m]

μ ---Dynamic Viscosity [Pa]

ν --Kinematic Viscosity [m²/s]

γ ---Adiabatic Coefficient

λ --Wavelength of the Laser Beam [nm]

ΔP ---Pressure Differences [Pa]

Δt ---Difference in Time [s]

ω ---Breakup Lengths Proportionality Constant

Subscripts

g ---Ambient Gas

l ---Liquid

t_r --Throat

ro --Reservoir

Acronyms

ATDC --After Top Dead Centre

BDC ---Bottom Dead Centre

BTDC --Before Top Dead Centre

CA --Crank Angle

CCD ---Charge Coupled Device

CFD ---Computational Fluid Dynamics

CMOS --Complementary Metal-Oxide Semiconductor

CN --Cavitation Number

CO ---Carbon Monoxide

CoM ---Centre-of-Mass

CRS --Common Rail System

DI--Direct Injection

EGR--Exhaust Gas Recirculation

EOI---End of Injection

FIE--Fuel Injection Equipment

GDI--Gasoline Direct Injection

GLR---Gas Liquid Ratio by Mass

HC--Hydrocarbon

HSV--High Speed Video

ICP--In-Cylinder Pressure

LDA--Laser Doppler Anemometry

LIF---Laser Induced Fluorescence

LSD--Laser Sheet Dropsizing

Mie--Mie Scattering

NO_X---Nitrogen Oxide

PCI--Printed Circuit Interface

PIV--Particle Image Velocimetry

PDA--Phase Doppler Anemometry

PDPA---Phase Doppler Particle Anemometry

PLIF--Planar-Laser Induced Fluorescence

PMAS---Particle Motion Analyser

PTV---Particle Tracking Velocimetry

rpm--Revolution Per Minute

RoI--Rate of Injection

SFC---Specific Fuel Consumption

SMD--Sauter Mean Diameter

SO_2--Sulphur Dioxides

TDC---Top Dead Centre

TTL---Transistor Transistor Logic

UoB--University of Brighton

UV--Ultra Violet

VCO---Valve covered orifice

1.   *INTRODUCTION*

1.1   GENERAL STATEMENT OF THE PROBLEM AND OBJECTIVES

A major concern with the increasing popularity of diesel-powered vehicles is the resultant increased level of pollution. Diesel engines are a source of two major pollutants; nitrogen oxides (NO_X) and particulate matter, which both have an undesirable effect on public health and the environment (Pierpont et al., 1995). They are also a source of carbon dioxide, one of the most important green house gases.

Nitrogen oxides contribute towards acid rain and ground-level ozone, whilst particulate emissions constitute a major health hazard.

This is a growing problem as more stringent legislation on emissions is introduced. To comply with such legislation, more effective and environmentally-friendly combustion systems need to be designed and manufactured. There are several ways of tackling this problem. Some engine designers favour exhaust gas after-treatment, whilst others prefer the introduction of more sophisticated fuel-injection systems. In some cases, both technologies are applied side by side. However, the most beneficial way of reducing emissions is at source, and to develop fuel-injection systems capable of meeting the requirements over the complete range of engine operating conditions. Diesel fuel-injection equipment is known to lend itself to the control and quality of the emerging spray. Engine load conditions have a direct influence on the combustion process, which is dependent upon the quantity, the quality and the timing of the fuel spray emerging from the injector nozzle.

Subsequently, the characteristics of the fuel spray are reliant upon many parameters such as injection pressure and in-cylinder conditions, as well as the characteristics of the fuel-injection equipment (*FIE*) such as nozzle size, nozzle geometry and the rate of injection. Different combinations of these variables can provide the correct combustion environment for reduced emissions. The extent to which this can be accomplished depends, for a diesel engine in particular, on the degree of control achieved over the combustion process, which in turn is a function of fuel properties, chamber design and injection and spray characteristics. The degree of air and fuel mixing is a key issue for an effective combustion. To accomplish such a task, careful

matching of various injection parameters/equipment and combustion chambers is needed.

The manner in which diesel fuel is introduced into the combustion chamber is determined by the fuel-injection equipment (*FIE*). The rate of injection (*RoI)* can be used as a feedback in design and development of the *FIE*, as an input for different types of models in addition to identifying the influence of the *RoI* on air/ fuel mixing and consequently pollutant formation (Baniasad, 1994).

To assess the influence of the *RoI* on spray formation, an injection rate device was utilised as part of this research programme.

For an effective and efficient combustion, the fuel delivery per cycle needs to be repeatable as well as metered for a given load condition. Historically, the rate at which fuel is injected and its resultant effect on noise, emission and performance has been studied since the early days of diesel engines. Fig 1-1 highlights these effects (Dolenc, 1990).
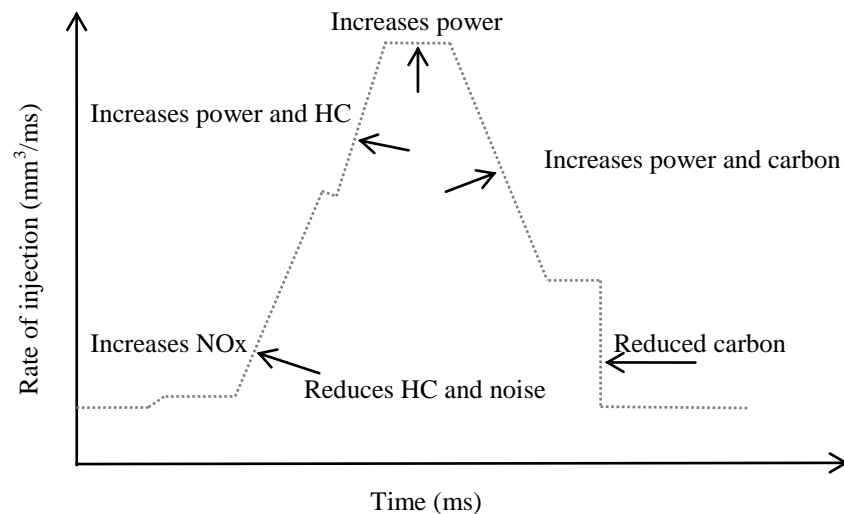
Fig 1-1. Influence of injection rate on engine power, noise, and emissions (adapted from Dolenc, 1990)

As shown in Fig 1-1, the rate of injection can contribute towards emissions and noise levels even towards the end of injection where fuel dribble is a source of unburnt Hydrocarbons (HC).

To reduce the aforementioned noise and pollutant formations, development has led to the introduction of an injection system capable of metering and delivering the required mass of fuel at a given rate for a given cycle and load condition (multiple or split injection strategy). In some cases, stable and consistent fuel delivery as low as 1 mm^3 per injection has been achieved (Birch, 2004). Further reductions in emissions are thought to be realised when split injection strategies are coupled with high injection pressures (Pierpont et al., 1995; Nehmer & Reitz, 1994; Tow et al., 1994).

However, the overall combustion process is acknowledged to be strongly dependent upon the microscopic and the macroscopic spray structure. The spray formation during the primary and secondary break-up phases must be considered. This is in order to improve both the understanding and the operational benefits achieved when multiple injection strategies are applied.

In general, diesel fuel sprays can be characterised as unsteady two phase turbulent flows. Eddies with various temporal and spatial distributions are present within the flow, mainly created by the interaction between the spray and the surrounding gas. Owing to turbulence effects, the initial characteristics of the jet can rapidly disappear within the steady-state period of the injection.

However, unlike the conventional single injection strategy, two additional parameters must be accounted for when considering the spray characteristics with multiple injection strategies. These are:

- The dwell period between the first and consecutive injection

- The quantity of fuel injected for each injection within a cycle.

The resultant effects could be as follows:

- Interaction between the first and consecutive spray depending on the dwell period

- Enhanced air entrainment into the fuel spray due to increased vortex structure

- Greater homogeneity between liquid fuel and air, as well as vapour fuel and air

- Due to the evolution of the second spray into the first, the internal structure of the first split can be analysed by observing the behaviour of the second spray.

It could be concluded that when applying a multiple injection strategy in comparison to a conventional single injection strategy, the spray behaviour significantly alters. It is therefore necessary to improve the understanding of such new strategies both quantitatively and qualitatively. This is with reference to variables such as injection parameters (injection pressure, response period, injected mass and dwell periods) and in-cylinder conditions. The experimental programme under the current work included the following steps:

- Rate of injection meter, for injector characterisation

- A high-speed video (*HSV*) imaging technique (using side-lighting), to record complete injection cycles

- Simultaneous Planar-Laser Induced Fluorescence (*PLIF*) and *Mie* scattering technique, to investigate planar images of the liquid and vapour phase for a variety of split injection strategies.

Based on the above, the main objective of this research programme is to provide an in-depth understanding of the characteristics of diesel fuel sprays from multi-hole nozzles. This concerns both single and split injection strategies and their relation to the characteristics of the fuel injection equipment (*FIE*) for two different types of injector. In addition to the experimental studies underlined in this research programme, modelling work based upon conservation of momentum theory (for spray penetration) and the derivation of empirical correlations to evaluate the transient behaviour of the break-up length and time were developed.

1.2 THESIS LAY-OUT

Chapter 2 is a review of the literature providing general characteristics of the diesel fuel spray formation obtained by various techniques. Chapter 3 focuses on characterisation of the Fuel-Injection Equipment (*FIE*) and the Rate of Injection (*RoI*). The fourth chapter gives a description of the optical Rapid Compression Machine (*RCM*), and characterises the optical Proteus spray rig for use in the current experimental studies. The last three chapters describe the work undertaken to study conventional diesel spray formation (single injection strategy), split injection characterisation and modelling. These subjects are analysed in Chapters 5, 6 and 7 respectively. Finally, the conclusions drawn and recommendations for further work is summarised in Chapter 8. Additional information with regard to various chapters are

presented in the Appendices A, B, C, D and E, corresponding to Chapters 3, 4, 5, 6 and 7 respectively.

2. REVIEW OF SPRAY CHARACTERISATION AND TECHNIQUES

2.1 INTRODUCTION

The utilisation of liquid fuel sprays in order to increase the fuel surface area and thus increase vaporisation and combustion rate is exercised by a number of applications such as boilers, oil-fired furnaces, gas turbines and diesel engines. For instance, breaking up a 3 *mm* droplet into 30 *μm* drops results in a surface area 10,000 times greater. This makes spray combustion not only a strong motivation in the above applications, but also in the conventional spark ignition engines where carburation had a dominant role.

In diesel engines, the characteristics of the fuel spray affect the combustion efficiency and pollutant formation. The combustion emissions must satisfy governmentally-imposed emission standards for selected compounds in the products, such as carbon monoxide (CO), hydrocarbons (HC), nitrogen oxides (NO_X) and sulphur dioxide.

To appreciate the combustion processes, one must look at the overall picture. This must commence at the injector nozzle, and the injection of liquid fuel into combustion chamber. The injected liquid fuel undergoes atomisation which causes the liquid to break up into a number of droplets with various sizes and velocities. Depending on various parameters (such as the in-cylinder conditions, injection pressure, droplet size and velocity, viscosity and surface tension), some of the drops may continue to break up even further, and some may recombine when they collide. With the evaporation of some droplets, the vapour fuel mixes with air. Given enough time, the entire amount of diesel fuel will be converted into combustion products.

Carbon particles produced during rich combustion may either continue to oxidise to produce gaseous products, or may rigidly join together to form microscopic air-borne material in the exhaust.

Given the need to reduce emissions and fuel consumption, an in-depth understanding of in-cylinder fluid dynamics and combustion processes is essential.

Until recently, the trend has been to increase the injection pressure in order to reduce particulate emissions. However, due to increased parasitic losses, material strength

and increased fuel system cost, there are limitations on the maximum practical injection pressures (Pierpont et al., 1995). Raising the injection pressure, also is generally known to increase NO_X emissions. Although NO_X production can be slowed down by retarding the injection timing (which has the effect of decreasing peak in-cylinder pressure and temperature), the fuel consumption increases and engine efficiency is compromised.

In recent years, advances in diesel fuel system technology (multiple injection strategy) and combined high injection pressures have allowed simultaneous reductions in particulate and NO_X emissions (Montgomery & Reitz 1996, Nehmer & Reitz 1994, Lee & Reitz 2003, Pierpont et al., 1995, Shundoh et al., 1992, Takeda & Niimura 1995, Tow et al., 1994). Although some of the after-effects are well known (in terms of emissions), many characteristics of a multiple injection strategy, such as the evolution of the liquid/vapour spray interaction and fuel dispersion between each consecutive injection, are poorly understood.

In this chapter, the characteristics of conventional diesel fuel spray formation and relevant experimental techniques will be reviewed. The review presented will include two main sections. The first section (section 2.2) is focused on spray atomisation, including three subsections on break-up length, spray cone angle and penetration length respectively (section 2.2.1, 2.2.2, and 2.2.3).

The second section (section 2.3) will describe some relevant techniques applied to in-cylinder diagnostics.

Finally, the main conclusions of this chapter are summarised in section 2.4.

2.2   ATOMISATION AND SPRAY BREAK-UP

Fuel injected into the combustion chamber is subjected to internal as well as external forces, leading to disintegration of numerous drops of different sizes, shapes (thin jets or liquid sheets) and concentrations within the spray. The thin jets or liquid sheets that are present have the highest surface energy due to disintegration, and are more subjected to aerodynamic forces and instabilities due to surface tension.

The instabilities of liquid fuel give way to different atomisation processes. Arcoumanis et al. (1997) reported three different types of mechanisms for break-up; aerodynamically-induced atomisation, jet turbulence-induced atomisation and cavitation-induced atomisation.

Aerodynamically-induced atomisation takes the form of waves developing on the liquid jet surface, primarily caused by the relative motion between the injected fuel and the ambient gas.

Jet turbulence-induced atomisation is a phenomenon that takes place within the injector nozzle hole, where fully turbulent flow leads to radial velocity components in the jet that disrupt the surface film followed by general disintegration of the jet itself.

It has been reported that, even if injected into a vacuumed chamber, the jet, through turbulence induced-atomisation process, will disintegrate due to turbulence within the nozzle.

Cavitation-induced atomisation is due to the sudden growth and collapse of the vapour bubbles at the nozzle exit (Arcoumanis et al., 2000 & 2001, Afzal et al., 1999, Badock et al., 1999, Chaves et al., 1995, Schmidt et al., 1999, Schmidt & Corradini, 2001, Soteriou et al., 1995). The formation and growth of these vapour bubbles take place within the liquid at low-pressure regions of the injector, starting at the vena contracta, where the liquid has been accelerated to high velocities.

One way in which the atomisation process, and hence the behaviour of a jet from a simple injector orifice, can be characterised, is by the following dimensionless numbers (Lefebvre, 1989).

$$\mathrm{Re} \ = \frac{\rho_l \ u_d \ D_n}{\mu_l}, \tag{2.1}$$

$$We = \frac{\rho_g\, u_d^{\,2}\, D_n}{\sigma_l}, \tag{2.2}$$

$$Oh = \frac{\mu_l}{\sqrt{\rho_l \sigma_l\, D_n}}. \tag{2.3}$$

Where Reynolds number (*Re*) is the ratio of inertia forces and viscous forces acting on the fluid, thus, ρ_l is the liquid density, u_d is the droplet velocity, D_n is the nozzle diameter and μ_l is the dynamic viscosity of the liquid. The Weber number (*We*) is defined as the ratio of inertia forces to tension forces, thus, ρ_g is the gas density and σ_l is the liquid surface tension. The Ohnesorge number (*Oh*) is the ratio of internal viscosity forces to an interfacial surface tension force.

2.2.1 Break-up Length

Once injection commences, not all the fluid out of the nozzle breaks up instantly. There are some unbroken portions as well as an intact core. The length of the intact core is referred to as break-up length L_b, and is in the vicinity of the nozzle exit as shown in Fig 2-1.

This core has few cavitating bubbles, if any, and the break-up length is dependent on many parameters (such as the injection velocity, surface tension, viscosity and aerodynamic forces). Therefore, the break-up length can be categorised as the boundary between liquid sheets and ligaments, into an atomised regime of droplets.
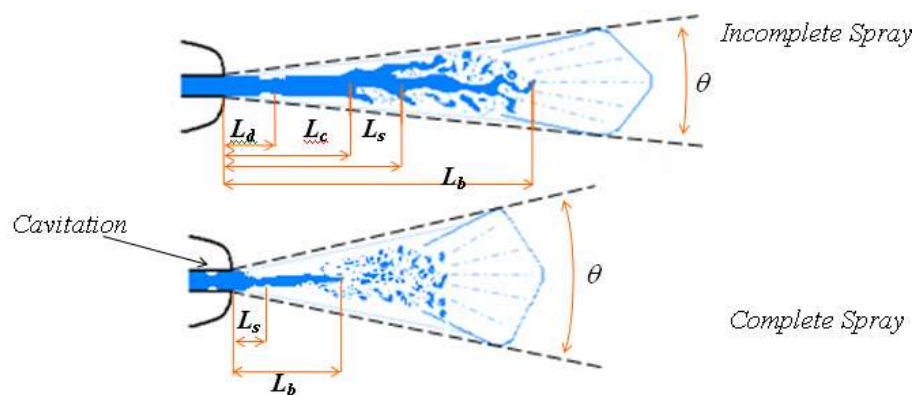
Fig 2-1. Schematic of the break-up length in complete and incomplete spray region (modified from Hiroyasu & Arai, 1990)

Hiroyasu (1998 & 2000) and Hiroyasu & Arai (1990) reported that an increase in ambient gas pressure from 0.1 to 3 *MPa* resulted in the reduction of the break-up length by approximately 35 *mm*. Also, the authors found that an increase in injection velocity from 20 to 60 *m/s* resulted in a increase in the break-up length (Fig 2-2). However, a further increase of the injection velocity led to a decrease in break-up length, until any further increase in the velocity gave almost a constant value for break-up length as shown in Fig 2-2.
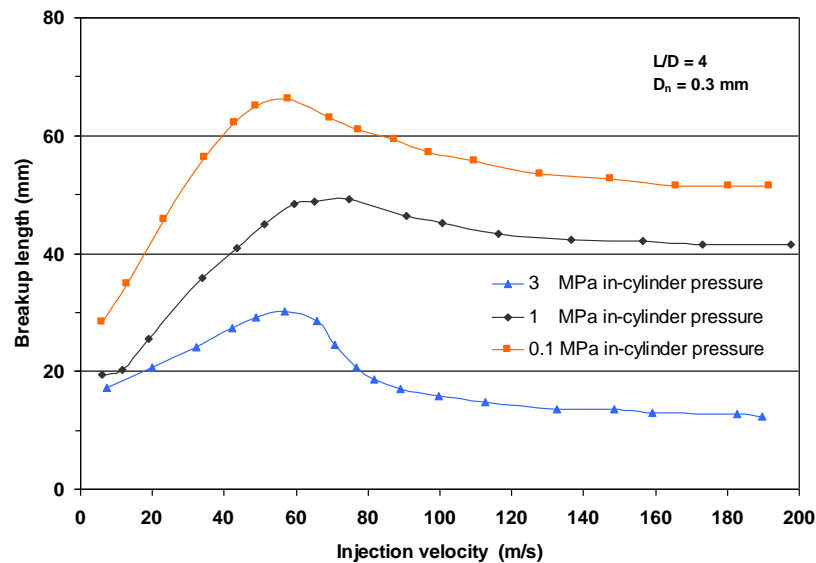
Fig 2-2. Break-up length against injection velocity for different in-cylinder pressures (adapted from Hiroyasu, 1998)

The authors also showed a non-linear dependency of break-up length on the injection velocity (Fig 2-2). The break-up length was reported to vary inversely with the ambient gas pressure (Hiroyasu, 1998).

Hiroyasu (1998) categorised the break-up length and relative atomisation in the complete and incomplete sprays region (Fig 2-1). In the incomplete atomised region, Hiroyasu explained, the jet undergoes a relatively slow disintegration process. Hence, transformation from liquid core to drops has to develop along the liquid jet. Only at some distance from the nozzle exit are fine droplets formed. The complete atomised region, however, was attributed to the increase of the injection velocity, and, thus, the disintegration of liquid core to a finer spray, appearing almost at the nozzle exit (Hiroyasu & Arai, 1990).

Yule & Filipovic (1991) subdivided the break-up zone into three areas (Fig 2-1), and described that one or all of these three zones existed according to the time after commencement of injection.

The first is the intact liquid core length at relatively low injection velocity (within the incomplete spray region), as reported by other researchers. The core length is assumed to stretch to a distance L_c from the nozzle exit. In the second zone, from L_c to L_b, further detachment of ligaments, sheets and larger droplets continue to subdivide into finer droplets. This is regarded as the end of break-up zone and the commencement of atomised spray (final zone). The distances L_d and L_s from the nozzle exit correspond to the effective origin of deformation and the effective origin of the spray cone respectively.

In the complete atomised spray region, Hiroyasu & Arai (1990) suggested that the deformation process of the core vanishes, owing to the disintegration processes reported by Arcoumanis et al. (1997) - that is, aerodynamically-induced atomisation, jet turbulence-induced atomisation and cavitation-induced atomisation.

The break-up length or the disintegration of drops has been reported to vary between 10 and 40 *mm,* according to Lee & Park (2002). These authors conducted an experiment using spray particle motion analyser (*PMAS*) and phase Doppler particle analyser (*PDPA*) in conjunction with a common rail diesel fuel injection system.

With injection pressures ranging from 60 to 80 *MPa*, the fuel was injected into atmospheric pressure at room temperature through an injector nozzle hole diameter of 0.3 *mm*. From their observation, they concluded that mean droplet size and axial mean velocity are constantly disrupted at a region 40 *mm* downstream of the nozzle exit.

Shimizu et al. (1984) measured the break-up length by means of an electrical resistance between the nozzle and a fine wire net located within the spray path downstream of the injector nozzle. The authors found that the break-up length decreased with an increase in the injection pressure. Moreover, a further decrease in the break-up length was observed as the nozzle exit hole was decreased. The authors' findings also suggest that the nozzle geometry such as entrance shape and nozzle length have a direct influence on the break-up length, in addition to the reported atomisation processes (Arcoumanis et al., 1997; Chaves et al., 1995; Laoonual et al., 2001). This phenomenon was experimentally confirmed by Hiroyasu (1998), showing

the dependence of break-up length on the nozzle hole diameter (as well as the injection velocity) (Fig 2-3).
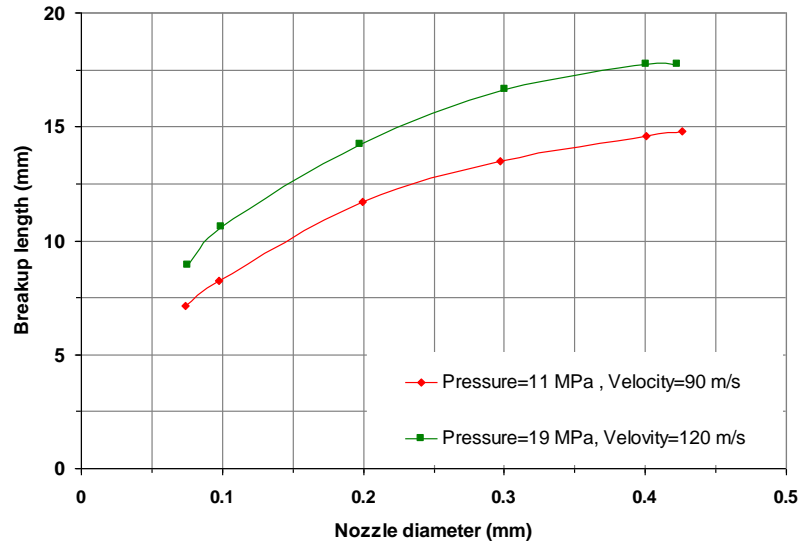
Fig 2-3. The effect of nozzle diameter on the break-up length (adapted from Hiroyasu, 1998)

Due to the experimental difficulties involved in obtaining reliable data, in particular for a wide range of conditions, a correlation was presented for the break-up length by Hiroyasu (1998), valid for any complete spray region.

$$L_b = \left(\frac{(1 + 0.4)\, r_r}{D_n} \right) \left(\frac{P_g}{\rho_l\, u_{inj}^2} \right)^{0.05} \left(\frac{L_n}{D_n} \right)^{0.13} \left(\frac{\rho_l}{\rho_g} \right)^{0.5} 7\, D_n \, . \tag{2.4}$$

Where L_b is the break-up length, r_r is the nozzle radius for a round inlet hole, P_g is the gas pressure, u_{inj} is the injection velocity and L_n is the nozzle length.

As a result of experiments at elevated pressures, Yule & Filipovic (1991) also presented a correlation for the break-up length and the break-up time for diesel fuel sprays. Utilising an indirect technique (curve fitting), and computation of the overall void fraction (from their images) in the spray as a function of time, they correlated the break-up time (t_b) and break-up length from measured spray tip penetration data. Thus, the break-up length and break-up time is given as:

$$L_b = D_n (2.8 \times 10^4)\, We_b^{-0.46} \, , \tag{2.5}$$

$$t_b = \frac{(8.9 \times 10^5)\,(We_b^{\;-0.46}\;Re_b^{\;-0.3})\,D_n}{u_{inj}},$$ (2.6)

where t_b is the break-up time. The Weber and Reynolds numbers for break-up are defined as:

$$We_b = \frac{\rho_g\,u_b^2\,D_n}{\sigma_l},$$ (2.7)

$$Re_b = \frac{u_b\,D_e\,\rho_l}{\mu_l},$$ (2.8)

$$u_{inj} = u_b\;31.7\;Re_b^{\;-0.3}.$$ (2.9)

Where u_b is the break-up velocity and the equivalent nozzle diameter is defined as:

$$D_e = D_n\,\sqrt{\frac{\rho_l}{\rho_g}}.$$ (2.10)

Eq. (2.9) is only applicable for $Re_b \leq 10^5$.

The authors conclude that the relative lengths of the intact core and continuous liquid path zone are respectively approximately 20% and 35% of the full break-up zone.

Browne et al. (1986) conducted an experiment into the effect of fuel properties on the spray break-up length for three different fuels (sunflower oil, ethanol, and diesel). A 1.6 litre single cylinder, pre-chambered diesel engine was utilised, in conjunction with shadowgraphy technique and diffused rear-illumination photographs for visualisation. With an ambient air temperature of 373 K, each fuel in turn was injected into the combustion chamber via an orifice 0.25 mm in diameter. Fig 2-4 shows the break-up rate for the three different fuels. The injection pressures in the author's experiments are not known.
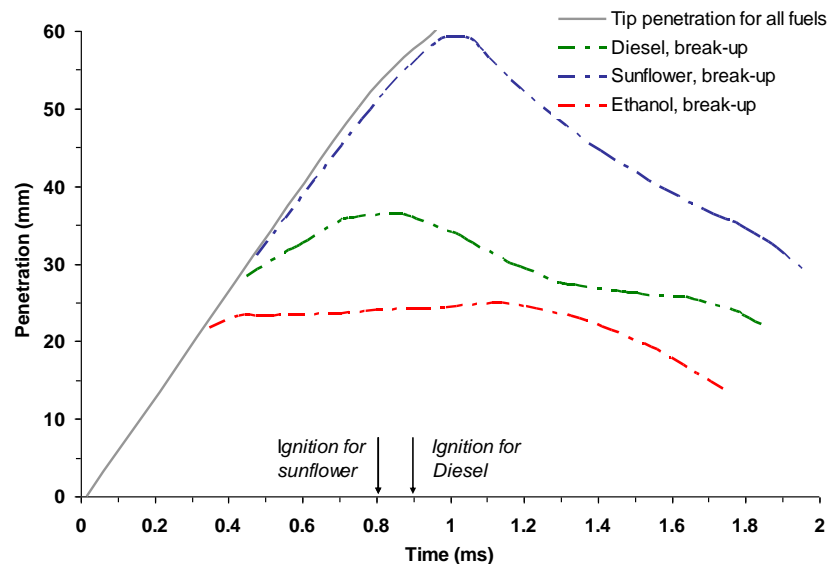
Fig 2-4. Comparison of break-up length for three different fuels (adapted from Browne et al., 1986)

Results for the three fuels at 373 *K* intake air temperature are shown in Fig 2-4. Whilst there are similarities for the tip penetration, the dependency of the break-up length on fuel properties is shown. For diesel fuel, the author reports a maximum break-up length of 35 *mm*. However, after auto ignition, the break-up length is shown to shorten for diesel as well as sunflower oil due to higher local temperatures. For ethanol, the maximum break-up length recorded was at 23 *mm* (with no auto ignition for ethanol). This was reported as being due to the differences in the vapour pressure of the fuels.

2.2.2   Spray Cone Angle

The spray cone angle θ is the angle that is formed by the outer boundary of the spray cone, taken from the injector nozzle exit hole, to some location on the spray axis. This location can be defined in various ways, depending on the macroscopic or the microscopic cone structure to be examined (Bae & Kang, 2000). Fig 2-1 shows the macroscopic dispersion angle defined by Hiroyasu & Arai (1990).

Hiroyasu & Arai (1990) demonstrated the effect of injection pressure and kinematic viscosity of the fuel on the spray cone angle. With an increase in the injection velocity, the authors reported that the spray cone angle increased until a maximum value was reached, and, thereafter, a constant value in the complete atomised spray region was persisting (Fig 2-5).

14

An empirical equation by Hiroyasu & Arai, (1990) for the spray cone in the complete atomised spray region is given as:

$$\theta = 83.5 \left(\frac{L_n}{D_n} \right)^{-0.22} \left(\frac{D_n}{D_o} \right)^{0.15} \left(\frac{\rho_g}{\rho_l} \right)^{0.26} .$$ (2.11)

Where D_o is the sac chamber diameter of the nozzle.
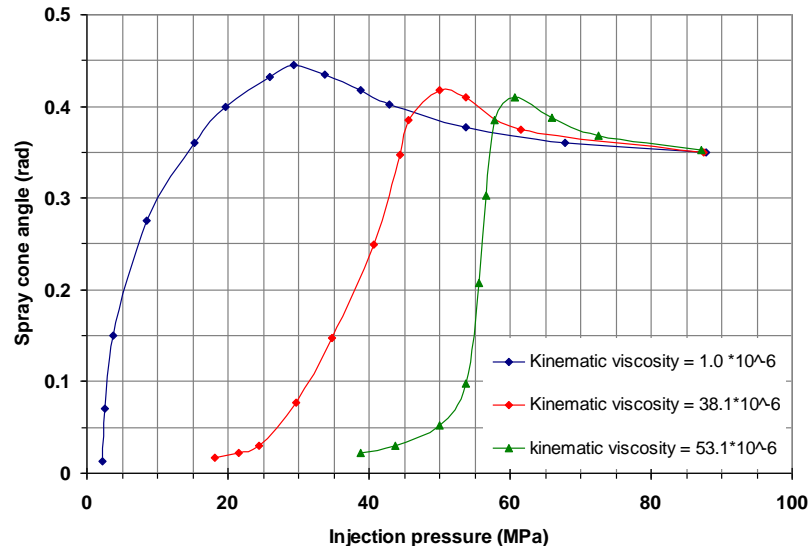
Fig 2-5. The effect of injection pressure on spray cone angle (adapted from Hiroyasu & Arai, 1990)

Naber & Siebers (1996) have taken the definition of spray cone angle one step further. The authors suggested that the spray dispersion angle and penetration are a coupled process, and thus the definition used for the dispersion angle depends on the penetration length. Hence, the spray dispersion angle θ by Naber & Siebers (1996) is given by the following relationship:

$$\theta = \tan^{-1} \left(\frac{A_{p,L_p/2}}{\left(L_p/2 \right)^2} \right) .$$ (2.12)

Where $A_{p.Lp/2}$ is the projected area of the upstream half of the spray in an image, and L_p is the penetration length.

Sovani et al. (2000) experimented with an effervescent diesel injector. With injection pressure between 12.6 and 36.5 *MPa*, the working fluid was injected into a vessel

15

with pressures ranging from 0.27 to 5.5 *MPa*. The authors used a mixture of water and metal cutting coolant to avoid an explosion and thus simulate benz oil, which is similar in physical property to diesel fuel. Injecting the two-phase mixture (nitrogen being one of the two mixtures) via an orifice 0.3 *mm* in diameter and 0.8 *mm* in length, the ratio of atomised gas to liquid ratio by mass (*GLR*) varied from 0.8% to 13.6%. The authors concluded that the spray cone half angle *θ/2* lies between 5.8^o and 11.5^o over the entire range of parameters in their study. However, an increase in the ambient pressure was observed to increase the spray cone angle.

A correlation for the spray cone angle applicable to effervescent diesel injectors based on experimental data was presented by Sovani et al. (2000) as follows:

$$\theta = 2\left(7 + 0.15\ GLR + 0.039\ P_{inj} + 0.0451\ P_g^4 - 0.6211\ P_g^3 + 2.7551\ P_g^2 - 3.62\ P_g\right). \qquad (2.13)$$

Other parameters that have an effect on the spray cone angle are the length and diameter of the nozzle orifice. These effects have been reported by several authors such as Laoonual et al. (2001), Chaves et al. (1995) and Schmidt et al. (1999), concluding an increase in the L_n/D_n ratio gave a decrease in the spray cone angle. Furthermore, Hiroyasu (1998) reported the effect of kinematic viscosity on the spray cone angle. The author observed that a decrease in the kinematic viscosity was followed by an increase in the spray cone angle.

Schugger & Renz (2003) conducted an experiment investigating the effect of nozzle hole geometry on the spray cone angle for different injection pressures (with multi-hole nozzles). Two different nozzle hole geometries were used. The first had a sharp inlet edge with a hole diameter of 150 *μm* and a separation angle of 162°. The second nozzle had a hydro-eroded inlet edge and a conical spray hole shape with a inlet hole diameter of 151 *μm*. The exit hole diameter was 137 *μm*, resulting in a *k*-factor of 1.4 and a spray separation angle of 160° (*k*-factor = $(D_{in}-D_n)/10$). Both nozzles provided the same mass flux at 10 *MPa*. The authors used a *CCD* camera and a laser light sheet for illumination.

The authors concluded that the spray hole geometry plays an important role on the spray cone angle. This was observed even at few nozzle hole diameters downstream of the nozzle exit, during fully established flow conditions (namely complete

atomised spray region). The rounded edge in combination with the conical shaped spray hole was also found to lead to a lower perturbation levels in the primary break-up zone, resulting in a reduced near nozzle spray break-up length and spray cone angle.

2.2.3   Penetration Length

Penetration length can be defined in two ways - the distance of droplet ensemble (cluster) that proceeds the farthest length downstream of the nozzle exit, or the furthest spray distance from the nozzle that is unbroken. The penetration phenomenon is most important in characterisation of spray formation within a combustion chamber. Information on spray tip penetration or length is crucial in the design process of an internal combustion engine. The penetration length must be neither too long nor too short for efficient in-cylinder combustion. If too long, impingement could occur. This will result in wetting of the combustion chamber wall and/or piston crown. Consequently, formation of soot and wastage of fuel will be enhanced. If the length is too short, mixing efficiency and good combustion can be compromised.

Based on a diesel spray atomisation model, Huh et al. (1998) studied the effects of spray tip penetration for various ambient gas pressures. The authors compared their computed results to some experimental data, for an ambient gas pressure ranging from 0.5 *MPa* to 4.5 *MPa* (Fig 2-6).
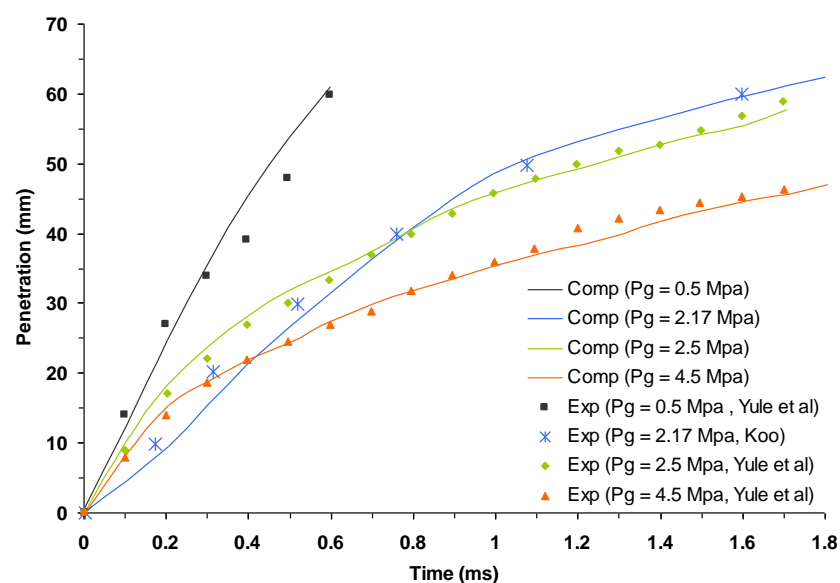
Fig 2-6. Tip penetration as a function of time (adapted from Huh et al., 1998)

17

Fig 2-6 shows that an increase in the in-cylinder gas pressure results in a decrease in the penetration length. However, although there is good agreement between the experimental and the modelling results, the model seems to over-predict the tip penetration length during the later stage of injection for low in-cylinder pressure condition. Similar studies by Reitz & Diwakar (1987) have also shown that their model over-predicts the spray tip penetration length during the later stages of injection.

A spray penetration formula derived from experimental data based on steady gas flow jet mixing was correlated by Dent (1971). For a hot bomb or an engine environment the penetration distance is given by:

$$L_p = 3.1 \left[\left(\frac{\Delta P}{\rho_g} \right)^{1/2} \times t \times D_n \right]^{1/2} \left(\frac{294}{T_g} \right)^{1/4} . \qquad (2.14)$$

Where ΔP is the difference between the injection pressure and the ambient gas pressure, t is the injection time and T_g is the gas temperature.

For a cold bomb, the expression $(294/T_g)^{1/4} = 1$. This expression is a correction factor that takes into account the temperature of the in-cylinder gas at the nozzle exit.

The above expression was compared with experimental data by Dent (1971). In general, the report shows good agreement between his correlation (Eq. (2.14)) and the experimental data. However, experimentally determined penetration distances for injection time ≤ 0.5 *ms* were generally found to be much smaller than those predicted by Eq. (2.14). In other words, Eq. (2.14) over-predicts the penetration length during the early stage of injection.

An experiment, with the aid of photographic visualisation into the effect of ambient conditions and the injection pressures on the spray tip penetration was conducted by Hiroyasu & Arai (1990). A constant volume bomb filled with nitrogen was heated to temperatures of 295, 423, and 593 *K*. For a constant injection duration, the authors report a linear relationship between penetration and time, with two distinct slopes for the calculated results (Fig 2-7).
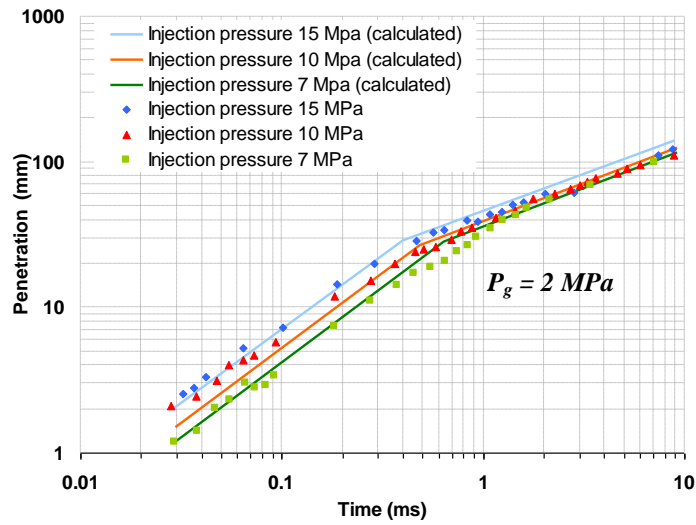
Fig 2-7. Log of penetration against log of injection pressure (adapted from Hiroyasu & Arai, 1990)
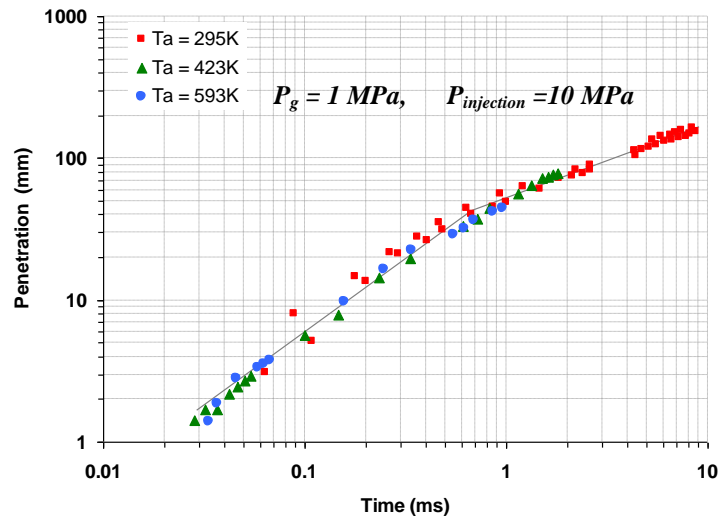
Fig 2-8. Log of penetration against log of injection pressure, for varied ambient gas temperatures (adapted from Hiroyasu & Arai, 1990)

The authors reported that an increase in the injection pressure yields an increase in the tip penetration. Moreover, an increase in the injection pressure reduced the duration that the penetration length was proportional to $t^{1.0}$ (the intersection of the solid lines for the calculated results). They concluded that the effect of ambient temperature on tip penetration was insignificant (Fig 2-8). Similar studies by Kennaird et al. (2002) propose a noticeable effect on the penetration length with a change in the ambient temperature. This can be attributed to the evaporation of the fuel droplets on the tip periphery of the spray outline.

The final conclusion by Hiroyasu & Arai (1990) was that the spray tip penetration appears to be proportional to time in the early stage of injection (incomplete atomised

19

region), and for the later stage of injection, tip penetration is proportional to the square root of time. As a result, the initial stage of the spray evolves with a steady tip penetration velocity equal to the injection velocity. During the complete atomised stage, the jet is considered to disintegrate to form a spray with a tip penetration length proportional to $t^{1/2}$.

Hiroyasu & Arai (1990) expressed this phenomenon with the following expressions:

When $0 < t < t_b$

$$L_p = 0.39 \left(\frac{2 \, \Delta P}{\rho_1} \right)^{1/2} t \ , \qquad\qquad (2.15)$$

and when $t > t_b$

$$L_p = 2.95 \left(\frac{\Delta P}{\rho_g} \right)^{1/4} (D_n \, t)^{1/2} \ , \qquad\qquad (2.16)$$

$$t_b = 28.65 \left(\frac{\rho_1 \, D_n}{(\rho_g \, \Delta P)^{1/2}} \right) . \qquad\qquad (2.17)$$

Furthermore, Hiroyasu & Arai (1990) reported that an increase in tip penetration results from an increase in the nozzle hole diameter. Also, a decrease in the tip penetration length, and an increase in the spray cone angle, was attributed to an increase in the ambient gas pressure (density). The authors concluded that an increase in the ambient gas temperature resulted in a noticeable decrease in the spray cone angle (due to the evaporation of the droplets on the spray periphery).

Referring to the dependency of penetration length on time, Yule & Filipovic (1991) have pointed out that there is indeed a transition from an approximately $t^{1.0}$ to a $t^{1/2}$. However, spray penetration data are usually found to have gradual transition without the clear break point that the two-equation approach of Arai et al. (1984) implies (Fig 2-7 and 2-8, also Eq. (2.15) and (2.16)). Hence, Yule & Filipovic (1991) have suggested a correlation for the spray tip penetration length based on gradual transition from the nozzle to some distance downstream of the spray. Thus, the penetration length is given as:

$$L_p = 3.8 \left(\frac{\Delta P}{\rho_g} \right)^{1/4} (D_n \, t)^{1/2} \tanh \left[\left(\frac{t}{t_b} \right)^{3/5} \right].$$
(2.18)

For the above correlation, t_b is given as an adjustable constant. Therefore, for any given experimental spray data, obtaining a best fit between the above correlation and experimental data provides a value for t_b (Yule & Filipovic, 1991).

As mentioned earlier, an examination into the effect of in-cylinder gas density on liquid and vapour penetration was investigated by Kennaird et al. (2002). With in-cylinder gas densities varying between 14 kg/m^3 and 49 kg/m^3, the injection pressures were varied between 60 MPa and 160 MPa. With a nozzle hole diameter of 0.2 mm, diesel fuel was dispensed at 30 mm^3 per cycle. Fig 2-9 shows the tip penetration for several values of in-cylinder density.
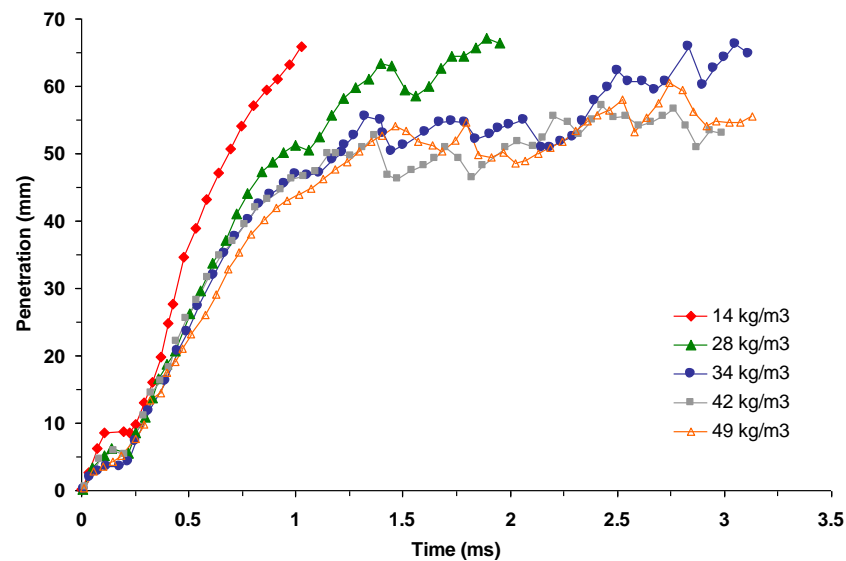
Fig 2-9. Influence of in-cylinder gas density on spray penetration (adapted from Kennaird et al., 2002)

The authors observed the dependency of the vapour penetration upon both the injection pressure and the in-cylinder densities. An increase in the injection pressure and a decrease in the in-cylinder gas density resulted in a greater vapour penetration.

An experiment into the effect of ambient gas density and vaporisation on the spray penetration was also conducted by Naber & Siebers (1996). With a nozzle hole diameter of 0.257 mm, the pressure difference across the nozzle orifice was 137 MPa.

Diesel fuel was injected into a nitrogen atmosphere, with a temperature of 451 *K*. The range of density was, 3.6 *kg/m³* to 124 *kg/m³* for non-vaporising condition. The authors compared their results to the penetration correlation of Hiroyasu & Arai (1990). From the analysis of the results, the authors concluded that for low gas densities, predictions based on the correlation of Hiroyasu & Arai (1990) consistently under-predicted the penetration length, whilst over-predicting at higher ambient densities (Fig 2-10 and Fig 2-11).
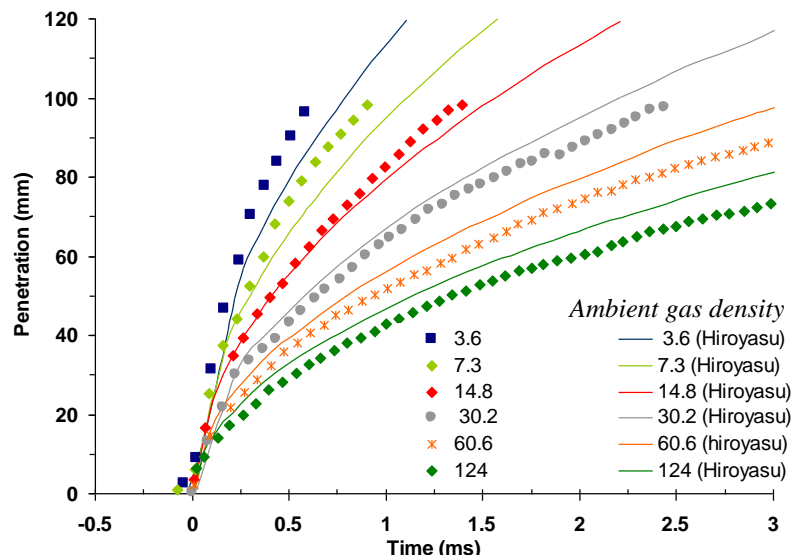
Fig 2-10. Spray penetration versus time for non-vaporising spray (adapted from Naber & Siebers, 1996)

For the same range of ambient densities and injection pressure for vaporising conditions, the results are plotted against non-vaporising conditions as shown in Fig 2-11. The comparison shows that vaporisation reduces or slows down penetration, with the effect being most noticeable at low-density conditions. The authors also conclude that this reduction is as much as 20% at low-density conditions. Also, for higher densities and longer penetration distances, the effect of vaporisation becomes smaller.
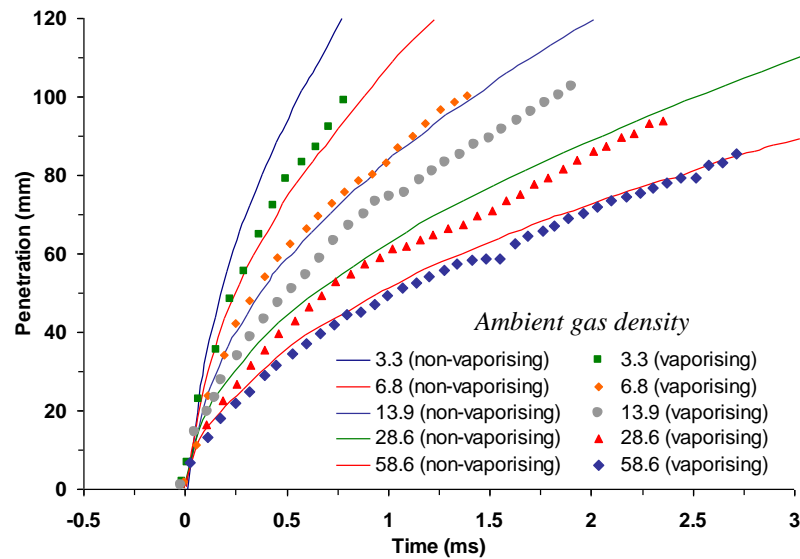
Fig 2-11. Spray penetration versus time for non-vaporising and vaporizing spray; non-vaporising ambient temp is defined as 451K; vaporising ambient temp is defined as 1000K (adapted from Naber & Siebers, 1996)

Naber & Siebers (1996) also point out that the practice of using spray penetration data from non-vaporising sprays to represent vaporising sprays is only reasonable at highest density conditions.

2.3   TECHNIQUES FOR IN-CYLINDER DIAGNOSTICS

In the last decades, an increase in the number of different techniques applied to address mixture preparation and in-cylinder mixture distribution have been developed. The techniques for spray characterisation fall into three broad categories - mechanical, electrical/electronic and optical methods (Lefebvre, 1989).

A mechanical technique consists of capturing the spray droplets in a cell or a solid surface. The droplets are then observed or photographed via a microscope. The downsides to this method are the acquisition of sufficient data to characterise the total spray and the time involved collecting sufficient data.

Electrical or electronic techniques utilise the detection and analysis of electronic pulses produced by the drops for calculating the size distributions. This technique is often referred to as hot-wiring or charged-wiring, and it operates on the principle that when a droplet impinges on an electrically-charged wire it removes a certain amount of charge, dependent on its size (Lefebvre, 1989). Hence, by conversion of the charge transfer into measurable voltage pulse, the droplet sizes are established. Nevertheless,

this technique is intrusive and can only be applied if the droplet velocities are relatively low (in the order of 10 *m/s* or less), and for large drops, shattering will occur on impact on the wire (Lefebvre, 1989).

The optical technique can be broadly divided into two sub-categories - direct imaging and non-imaging techniques. These are the most frequently applied techniques due to their non-intrusive nature.

The trend to use direct imaging in diesel combustion diagnostics has tended to focus on observation of the spray/flame structure, auto ignition sites, the spray geometry such as spray cone angle, cluster break-up, wall impingement and penetration length. Non-imaging optical techniques, however, are usually focused on spatial and temporal drop size distribution, velocities and number densities in general.

A review of optical diagnostics principles, both for direct imaging and non-imaging techniques, is presented in the subsequent sections, starting with the *Mie* scattering technique.

2.3.1   Principles of Mie Light Scattering

The *Mie* scattering theory is applicable to homogeneous, dielectric, spherical particles of arbitrary size illuminated by plane waves (Begg, 2003). The formulation of light describes scattering in all modes such as reflection, refraction, diffraction and absorption. The theory states that the intensity of the scattered light which reaches an observer is a function of the incident light intensity and scattering function (Begg, 2003).

For an unpolarised incident light source through a particle, the particle will scatter light that consists of polarised light in the plane of observation, parallel polarisation and perpendicular polarisation (Begg, 2003). The plane of observation is the plane formed by the incident light source transmitting. A schematic of scattering theory is illustrated for an incident laser beam linearly polarised in Fig 2-12.

As shown in Fig 2-13, a particle at point *P* scatters light as it passes through the laser beam along the x-axis. A camera or an observer in space, for example at point *CO*, receives light at an angle θ, in the *z-PCO* plane, as well as receiving light at an angle of φ, from the *xz* polarisation plane.
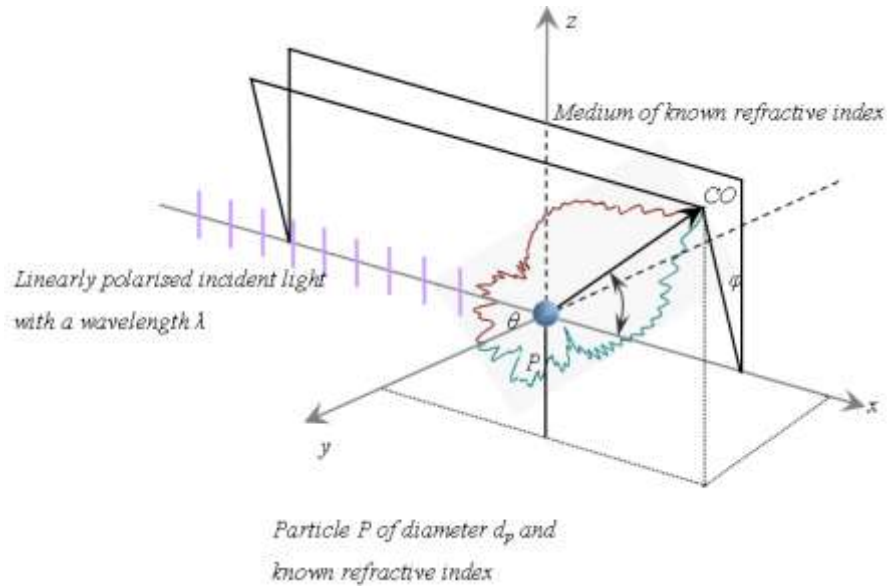
Fig 2-12. Principle of light scattering from a homogenous spherical droplet (adapted from Begg, 2003)

The intensity of the scattered light which reaches an observer or a camera at point *CO* is a function of the incident light intensity, I_i and scattering function, $S_{C, Mie.}$

2.3.2 Non-imaging Diagnostics

As with imaging techniques, laser anemometry is a non-intrusive optical technique that can be applied for investigation of velocity of liquid and gas flows in an IC engine. This technique has been used for measurements in many engineering applications, from subsonic to supersonic high-speed flows. This popularity is due to high spatial and temporal resolution of laser anemometry techniques. In addition, this technique requires little or no calibration, and for most practical purposes it can be considered being unaffected by some physical condition such as temperature and pressure.

Non-imaging technique such as *LDA*/*PDA* is based upon the determination of the Doppler shift of laser light scattered from a moving particles in a fluid flow or gas. The particles either occur naturally or are artificially seeded. The way in which the Doppler shift is defined is by changes in the frequency of wave motion due to the relative motion of the source and/or receiver. The basic principles are outlined in the next section.

2.3.2.1 Principle of the PDA

Phase Doppler anemometry (*PDA*) is an extension of laser Doppler anemometry (*LDA*), which can detect scattered light from a single particle and simultaneously measure its diameter and instantaneous velocity. *PDA* also has the ability to provide temporal and spatial characteristics of the spray at a relatively large distance from the spray source or nozzle.

The principle of *PDA* technique is that of introducing a single laser beam passing through a suitable beam splitter (Bragg cell) in order to produce two coherent beams of equal intensity. The beams are crossed at some focal distance to form a small volume (Probe volume) of high intensity light (Fig 2-13).
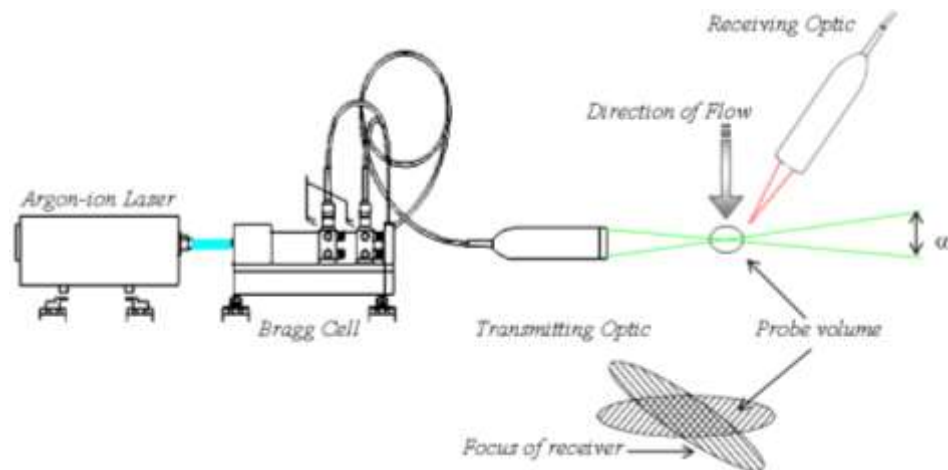
Fig 2-13. Schematics diagram of the Laser Doppler Anemometry Technique (Dantec, 2000)

The interference of the light beams in the probe volume creates a set of equally spaced bright and dark bands due to the phase difference of the interfering light waves. These bands produced by the interfering light waves are called fringes. When a particle travels through the probe volume, the amount of light it receives from the fringes fluctuates. The particle scatters the light in all directions. The scattered light is then collected in the forward scattered direction by the receiving optic. It can also be collected in the backscattered light if there are no limitations on the optical access. However, backscattered light usually results in a reduction of the signal to noise ratio, and thus a more powerful laser has to be employed. Nevertheless, once the scattered light is collected by the receiving optics, providing the fringe spacing in the probe volume is known, the local droplet velocity and droplet size can be determined by analysing the Doppler shift of the scattered light (Dantec, 2000; Begg, 2003; Lacoste, 2004).

2.3.3 Direct Imaging

In the simplest terms, direct imaging consists of taking photographs at high-speed or by utilisation of a charge-coupled device camera (*CCD*) to capture images of the spray or spray particle. The illumination is often carried out with the aid of a mercury vapour lamp, electrical spark, flashlight or laser pulses to create a high intensity light source of short duration. The schematic of such set-up is shown in Fig 2-14. The duration depends on the light source in use. For example, flashlight source has duration of 1 *μs,* while lasers have pulse duration in the order of nanoseconds. This technique requires analysis of the captured images. For highly dense sprays, the droplet images may become very closely packed, or even overlap. High magnification at the image stage may alleviate this problem. However, this is considered as the limitation of the technique.

Direct imaging can also be used to obtain information on droplet velocity. For velocity measurement, the approach is based on the following idea. If two light pulses are generated in a rapid succession, a double image is obtained of a single droplet on the photographic plate, from which the velocity of the drop can be determined by measuring the distance travelled by the drop and dividing it by the time interval between the two pulses (Lefebvre, 1989). Furthermore, directional movement of drops can be directly determined from the captured image as an angle of flight with respect to the central axis of the spray. This method provides instantaneous measurements of individual drops, and from a series of measurements time-average and space-average quantities can be obtained. In general, this method could offer simultaneous measurement of both drop size and velocity when a high magnification double-pulse laser imaging is applied.
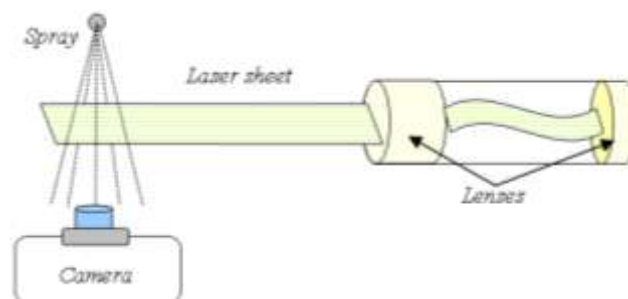
Fig 2-14. Schematic diagram of direct imaging

2.3.3.1 Holography

Holography has many similarities with photography. The principle of this method involves illumination of the moving droplets in a measuring volume with a coherent beam of light in the form of very short pulses. Since the duration of the laser beam is very short, the drops contained in the measuring volume appear frozen. The resulting hologram provides a three-dimensional image of the spray on a holographic plate. The advantage of this method is, in principle, that it requires no calibration. The main disadvantage of this technique is its limited application to dense sprays, due to its reliance on conservation of phase difference in the light scattered from the droplets. Furthermore, it is a relatively complicated technique to set up, requiring intricate manipulation of the light source. All the same, it has the potential to measure droplets as small as 15 μm (Lefebvre, 1989).

Anezaki et al. (2002) conducted several experiments utilising laser holography technique to capture the spray droplets in a 3D format in a gasoline direct injector (*GDI)*. Simulating engine conditions at 1,200 *rpm*, the in-cylinder pressure was 0.21 *MPa*. With an injection pressure of 13 *MPa*, the combustion chamber was heated to a temperature of 523 *K* 65 *K*. With two measurement locations 30 *mm* downstream of the nozzle exit, and then 12 *mm* radial, the holography experiments were compared and validated against *PDA* data (Fig 2-15 and 2-16). Recording of holographic images was conducted at 1*ms* after the start of injection. Comparative measurements between the two techniques for both measuring points are shown in Fig 2-15 and 2-16.
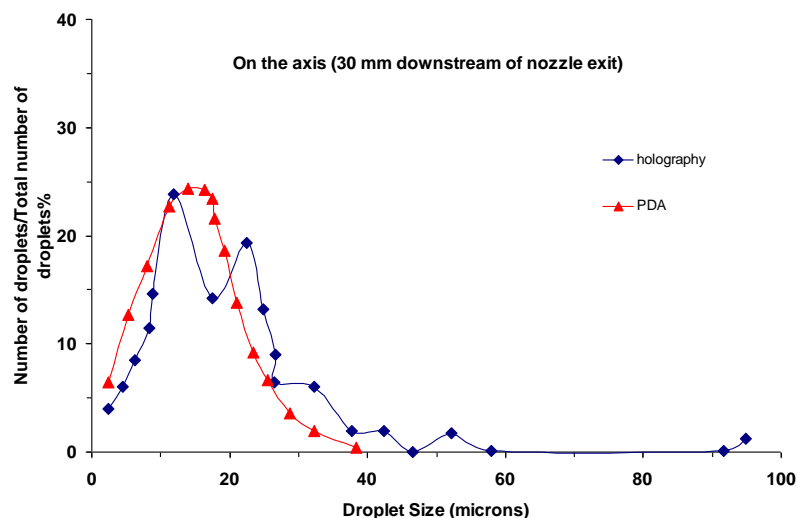
Fig 2-15. Droplet number against drop size at 30 mm downstream of the nozzle exit (adapted from Anezaki et al., 2002
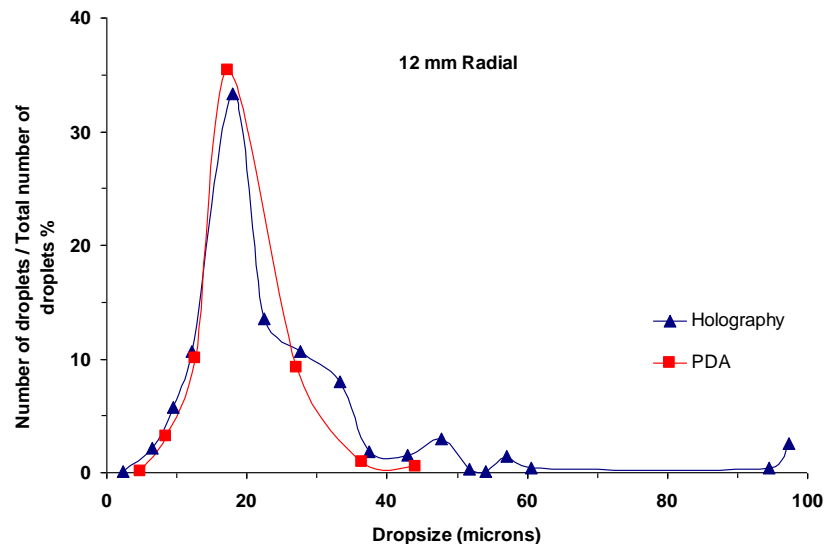
Fig 2-16. Same as Fig 2-15, with the exception of 12 mm radial; 30 mm downstream of the nozzle exit, on the spray axis (adapted from Anezaki et al., 2002)

Although a good overall agreement was observed, Anezaki et al. (2002) explained that with the *PDA* technique the numbers of samples required against holography were 2 to 5 times greater. Moreover, where *PDA* failed to detect drop sizes larger than 40 μm, the holographic technique did not. For drop sizes larger than 40 μm, *PDA* assumes they are either non-spherical or ghost droplets (Lacoste 2004), thus treating such drops as noise. In theory, diesel injectors produce droplets much smaller than 40 μm. However, the conditions associated with diesel spray environment, are much denser than those found in a Gasoline Direct Injection (*GDI*). It can be concluded, therefore, that holography is a powerful tool that can be adopted for visualisation of spray characteristics.

2.3.3.2 Laser Sheet Dropsizing (*LSD*)

The technique Laser Sheet Dropsizing (*LSD*) has been developed to produce instantaneous two-dimensional images of spray Sauter Mean Diameter (*SMD*) by combining the laser sheet diagnostic techniques of *Mie* scatter and Laser Induced Fluorescence (*LIF*).

LSD combines elastic and inelastic light scattered from a laser sheet (Le Gal et al., 1999). This means that when a particle within the spray is illuminated by a laser sheet, a portion of the incident light energy is absorbed by the excited molecules (inelastic

scattering), and thus radiates as fluorescence signal. The remaining portion of incident light is elastically scattered.

The scattered light in the near forward direction has an angular distribution width, inversely proportional to the particle diameter. Fig 2-17 illustrates the different light scattering regimes in *LSD*.

Laser Light Sheet $S_{scattered}$; d_d^{n}

$\longrightarrow$ *Laser Mie Scattering n = 2*

$\longrightarrow$ *LIF: Low absorption n = 3*

$\longrightarrow$ *LIF: High absorption 2 < n < 3*
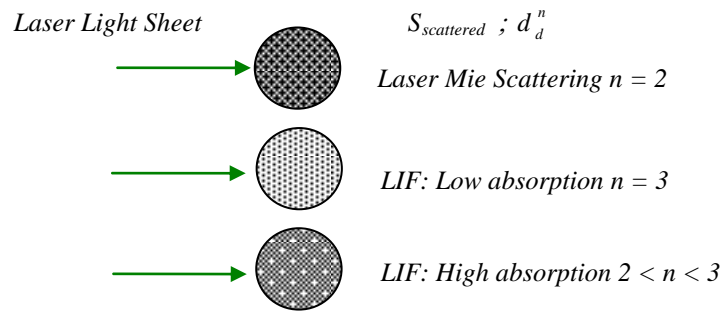
Fig 2-17. Different light scattering regimes for a spherical droplet (adapted from Le Gal et al., 1999)

In general, fluorophores can occur naturally in the fluid spray. In some cases more are added in a controlled amount to produce the correct signal response.

For liquid systems, the florescence signal is red-shifted with respect to the laser wavelength and a spectral filter is used to discriminate it from the *Mie* scattered light.

For spherical absorbing droplets of diameter greater than 1 *μm*, the *Mie* signal can be expressed as:

$$S_{Mie} = C_{Mie}\ d_d^{2}, \tag{2.19}$$

where *C* is an experimental calibration constant, which depends on the imaging system used. The expression for *LIF* is given by:

$$S_{LIF} = C_{LIF}\ d_d^{3} \tag{2.20}$$

The signal *S* for each pixel will represent the total intensity for all the droplets imaged within the measurement volume (pixel). To extract droplet sizes, the number of droplets must be known. However, the *LIF* signal gives the liquid volume fraction distribution.

The *LSD* signal is obtained by dividing *LIF* signals by the *Mie* scattering signal shown in Eq. (2.21) and Eq. (2.22) (Le Gal et al., 1999).

$$\frac{S_{LIF}}{S_{Mie}} = \frac{C_{LIF} \sum_i d_d^3}{C_{Mie} \sum_i d_d^2} \tag{2.21}$$

This expression is proportional to the Sauter Mean Diameter (SMD), therefore:

$$SMD = D_{32} = \frac{S_{LIF}}{S_{Mie}} = \frac{C_{LIF} \sum_i d_d^3}{C_{Mie} \sum_i d_d^2} \tag{2.22}$$

The above equations do not hold for the immediate vicinity of the nozzle exit, since the signals are not well defined due to the presence of ligaments.

Although *LSD* has the advantage of characterising dense spray, the downside to this technique is the requirement of known drop sizes in order to calibrate the drop size dependences of the scattered signals. This calibration is usually carried out with the aid of techniques such as *PDA*, or from a prior knowledge such as images of mono-disperse sprays of a known drop size. Also, the use of *LSD* is limited to measuring *SMD* only.

Validation of *LSD* technique was conducted by Le Gal et al. (1999). The author utilised *PDA* to compare his results compiled by *LSD* technique. With a correct dye concentration, 3,000 single shot images were obtained for both *Mie* and *LIF*, using a Delavan pressure-swirl atomiser 30 *mm* from the nozzle exit.

Representing *SMD* of 3,000 sampled droplets with the aide of *PDA*, the authors noted that *LSD* technique allowed more qualitative data sets to be acquired much more rapidly than the *PDA* technique. They conclude that although the agreement between *PDA* and *LSD* measurements was encouraging, *LSD* fails to measure drop sizes less than 10 *μm*.

2.3.2.3 Schlieren Technique

Schlieren technique allows visualisation of slight changes in the direction of the light with the change of density in the medium. A simplified outline of the arrangement is shown in Fig 2-18.

A source sends out a beam of light through Schlieren apparatus to a film. Half of the field is cut off by a knife-edged screen K_1, which is imaged by a lens, L_1, to a position, K_1^1, in the same plane as a matching screen K_2. The knife-edges of the image and the screen coincide exactly. A test position T, is sharply focused on the film. Thus the light flow past K_1 to K_2 is cut off from the film if the space at T is completely uniform. Any non-uniformity caused by a wave front in the air at T, causes a scattered light beam to evade the screen, K_2 (path a), and reach the film.
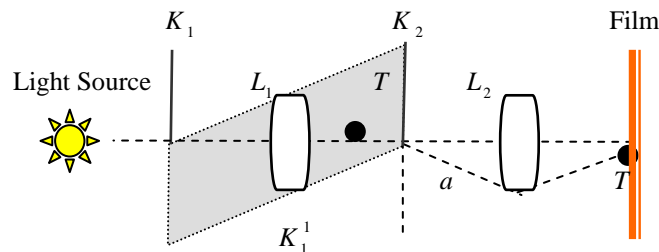
Fig 2-18. Schematic of Schlieren optics

Vapour dispersion measurements were taken by Crua (2002) using Schlieren video imaging technique. With the aid of a sodium lamp for illumination, an iris diaphragm was placed in front of the lamp to eliminate any off target beam and hence produce a point source of light. The author observed the presence of fuel vapour alongside the liquid fuel during the early stage of injection for hot air intake. With the increase of the penetration length, the author observed an increase in the width of vapour cloud, suggesting this phenomenon was attributed to increased vapour concentration and local turbulent mixing.

The influence of in-cylinder density on vapour penetration was also observed by Crua (2002) by the Schlieren method. It was found that vapour penetration increased linearly with time for all in-cylinder densities in the author's experiment. Furthermore, the influence of injection pressure was observed to have a significant effect on the rate of vapour penetration.

2.3.3.4 Laser Induced Fluorescence (*LIF*)

Laser Induced Fluorescence (*LIF*) is based on excitation of the molecules in a flow field with a monochromatic source of light (usually Nd: YAG lasers or XeC1 excimer

laser). The emission of the fluorescence signal can be considered as a result of several stage processes that occur within certain molecules as illustrated in Fig 2-19. These stages are generally known as the excitation stage, the lifetime stage and the emission stage (Seitzman & Hanson, 1993).

As shown in Fig 2-19, at the excitation stage, molecules in their ground level (stage 1) are stimulated to a higher electron level (stage 2) by monochromatic light source energy ($B_{12}I_v$) such as a laser beam. The molecules then either return to their ground level ($B_{21}I_v$), or they can be excited to a higher molecular state, including ionisation by absorption of further photons from the laser energy ($B_{2i}I_v$). However, some molecules at the same electronic level can lose their energy through inelastic collision (Q_{elec}) with other molecules producing rotational and vibrational energy transfer ($Q_{rot,vib}$), as well as electronic energy transfer, where often it is referred to as quenching. The transfer of internal energy causes molecular instability and a change at an atomic level, resulting in pre-breaking up (Q_{pre}) of molecules from the system.

After the elapse of a few nanoseconds, the molecules within the system at higher electronic state and nearby state populated through the collision process return to lower electron states and fluoresce (A_{ul}), producing the *LIF* signal.
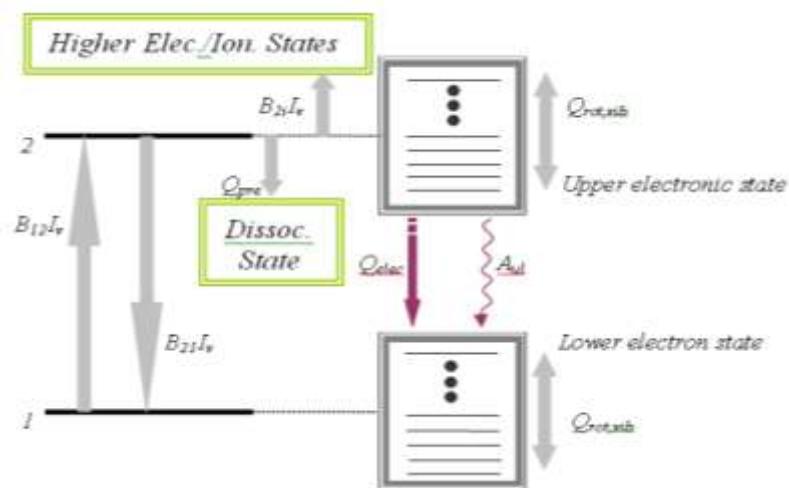
Fig 2-19. Schematics of the energy transfer process in LIF technique (adapted from Seitzman & Hanson, 1993)

It must be noted that transfer of electronic energy and inelastic collision with other molecules, referred to as quenching, is strongly influenced by the local temperature, pressure and species concentration. This means that quantitative in-cylinder measurements are fraught with difficulties because the exact influence of quenching

on the output signal is difficult to assess (Crua, 2002). No satisfactory models have been processed to address the collision losses on a quantitative level so far. It has been suggested that no possible direct correction of the results for the intensity losses due to quenching can be made.

Although some techniques have successfully reduced the influence of quenching (Seitzman & Hanson, 1993), none is thought to be applicable to realistic in-cylinder environment for species concentration measurements (Crua, 2002).

The lifetime of fluorescence is given between 10^{-5} and 10^{-10} seconds at a wavelength either equal to the excitation wavelength (resonance fluorescence) or longer than the excitation wavelength (fluorescence) as shown in Fig 2-20.

Resonance fluorescence is a term referred to as the radiation emitted by an atom or a molecule of the same wavelength as the longest one capable of exciting its fluorescence.
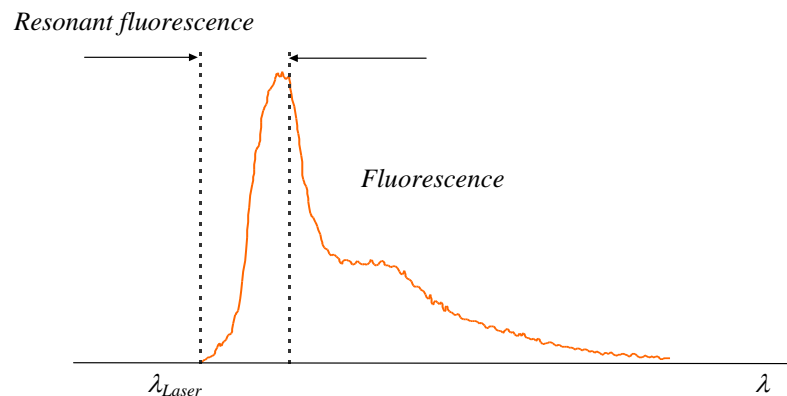
Fig 2-20. Simplified energy profile of the fluorescence signal (adapted from Crua, 2002)

LIF can be applied to in-cylinder flow measurements in a number of forms. In natural fluorescence, the fluorescence signal is totally dependent on the fluorescing compounds naturally available in standard fuels, such as pump diesel. This exercise can give misleading results due to the different characteristics of the fuel from batch to batch, and thus it is of limited use and it is only suitable for qualitative studies.

For trace fluorescence, where suitable dopants are used, it allows qualitative and quantitative measurements if careful calibrations are carried out. The downside of using dopant is the changes in the properties of the fuel that can be generated. The

change of fuel properties on the reference fuel can have a significant effect on the representation of the measurement.

2.4   CONCLUSIONS OF CHAPTER 2

Many different techniques for spray diagnostics have been developed, each with its own advantages and constraints. It is clear that no single measurement method is totally satisfactory. Direct imaging allows the spray to be seen. For droplet sizing, however, the difficulty comes when determining the size of the viewing volume to be assigned to given drop sizes (Lefebvre, 1989). Mechanical techniques are simple and inexpensive, but intrusive. However, the difficulty with such techniques is the extraction and collection of representative data. Furthermore, mechanical techniques set limitations on droplet velocities due to the break-up of the drops on impact with the collection instrument.

PDA, as well as being non-intrusive, shows considerable promise over other techniques for obtaining simultaneous drop size and velocity measurements in dense diesel sprays. However, the drawback of this technique is its failure to address the fuel vapour dispersion, propagation and concentration within the combustion chamber.

To address the above concern in the current study, the chosen experimental method is direct imaging.

Initially, high-speed video imaging will be utilised to capture the liquid portion of the emerging spray, and for simultaneous liquid and vapour phase, Planar-Laser Induced Fluorescence (*PLIF*) and *Mie* scattering technique will be applied.

In general, most of the reviews in the current study show the steady-state behaviour of the spray formation. Moreover, overall, the steady-state durations have been increased beyond conditions found in a realistic diesel engine environment. Also, with the introduction of multiple injection strategies and multi-hole nozzles, the steady-state period of injection duration is significantly reduced if not completely eliminated.

It is the aim of the current study to follow realistic and representative conditions in Direct Injection diesel combustion.

Tab 2.1 shows a summary of the main findings and the applied techniques in the current literature review.

Author	Technique Used	Results
Afzal et al., 1999	Photographic visualisation of magnified transparent injector nozzles, for the onset and further development of cavitation.	Simultaneous matching of Reynolds and cavitation numbers. Two different types of cavitation were identified: conventional hole cavitation and vortex or string-type cavitation.
Arai et al., 1984	Electrical resistance method, to determine the break-up length of a high speed jet in a pressurised vessel.	The injected liquid does not break up instantly after injection. Break-up length increases with increased nozzle diameter.
Arcoumanis et al., 1997	Development of a diesel spray model based on Lagrangian-Eulerian approach, and validation of which against experimental data obtained.	Comparison between the computational and experimental results made for temporal and spatial distribution of the droplet SMD, droplet velocity, tip penetration and number of droplets.
Badock et al., 1999	Observation of cavitation, using laser light sheet technique, *CCD* camera, and shadowgraphy.	Under diesel pressure conditions, an intact liquid core is observed.
Browne et al., 1986	Shadowgraphy, diffused rear illumination and high magnification direct rear illumination optics.	Liquid core stabilisation at a maximum value prior to auto ignition for diesel, toluene and ethanol sprays. Fast evaporation of individual droplets in dispersed phase, and low evaporation at the centre of the spray.
Chaves et al., 1995	Visualisation of transparent nozzle hole, to study cavitation with a *CCD* camera.	Supercavitation and turbulence within the nozzle will cause finite disturbances of the jet, initiating atomisation at the nozzle exit.
Chou & Faeth (1998)	Shadowgraphy and holography to measure the structure, size and velocity of the drops produced by the secondary break-up and the parent drops.	The parent drop experiences large acceleration due to development of large cross-sectional area and drag coefficient caused by drop deformation and bag formation.
Dent 1971	Review of data on spray penetration for cold and hot air intake bombs, simulating engine conditions.	Spray tip penetration correlation for gas jet experiments.
Dai & Faeth 2000	Shadowgraphy and holography to observe the mechanism and outcome of break-up	With increased We number the multimode break-up regime begins at the end of bag break-up regime and at the start of shear break-up regime. Drop deformation and drag properties prior to the onset of break-up appear to be relatively universal for *We* 13-150. Liquid volume fraction associated with the bag, ring, plume and core drops have been found for *We* of 18-80 and the sizes of ring, plume and core drops have been found for the same range of conditions.
Fox & Stark, 1998	Experimental determination of the discharge coefficient for a sharp-edged short-tube nozzle orifice, with the aid of pressurised reservoir for control of flow rate in the system. (working fluid: water)	Recommendation that for a sharp inlet edged nozzle the length to diameter ratio *L/d* should be in excess of 14 if flow instabilities are to be avoided. Also, if high C_d is required, then *L/d* ratio of 6 or less should be used.
Hiroyasu & Arai 1990	Electrical resistance to measure break-up length in a constant volume chamber. Visualisation with the aid of photographic technique and light interception for spray penetration and cone angle.	Increase of ambient pressure results in a decrease of the break-up length. Longer break-up length is a result of increased *L/d* ratio. Increase of ambient pressure results in decrease of penetration length and larger cone angle.
Huh et al., 1998	Atomisation is a combined process of turbulent effects and subsequent break-up by wave growth.	Good agreement between atomisation model and experimental measurement on spray angle, tip penetration, spray shape, drop size distribution.

Kennaird et al., 2002	Schlieren and high speed video camera technique used on high pressure spray rig to examine high injection pressures from a common-rail injection system.	Dependence of vapour penetration on injection pressure and ambient density. Faster liquid penetration at higher injection pressures.
Koo & Martin 1990	*PDA* and short-exposure still photography to obtain measurements of droplet sizes and velocities for a transient diesel spray in a quiescent chamber at an atmospheric temperature and pressure.	Calculated and measured average velocities are consistent when discharge coefficient for the nozzle and rate of fuel injection are taken into account. Symmetry of the spray with high velocities near the injector tip and radial dependence of velocities consistent from observed photographs. Range of droplet diameters from nozzle hole diameter to micron size. Existence of surface waves on the liquid exiting from the nozzle is revealed when photographs are examined.
Laoonual et al., 2001	Investigation of transient fluid flow within the nozzle holes (four different entry conditions) using a high-speed motion imaging system.	No hydraulic flip using a counter-bore nozzle with an *L/d* ratio of 10, but continuation of supercavitation until end of injection. Less abrupt inlet nozzles generate thin layers of cavitation near the nozzle wall with imperfect hydraulic flip.
Le Gal et al., 1999	Laser sheet Dropsizing (a combined *Mie* scattering and *LIF* technique) and *PDA* to calibrate droplet streams.	The ability of laser sheet Dropsizing technique to produce data as good as *PDA* (for large values of SMD).
Lee & Park 2002	Experimental and numerical study investigating macroscopic spray structure and characteristics of common rail high pressure injectors at various injection pressures using *PDA* and *KIVA-3* code with *KH-RT* hybrid model.	Predicted and experimental results showed good agreement due to variation of injection pressure. Disintegration into smaller droplets on the periphery of the spray downstream of the nozzle due to relative velocities between the spray and ambient gas. Occurrence of *KH* break-up near the nozzle, but *RT* doses not occur near the nozzle and distributes more widely than *KH*.
Lee et al., 2002	High-speed video camera images of light diesel fuel spray and combustion, analysed by their penetration and evaporation characteristics.	Promotion of atomisation and evaporation due to lower boiling point and density. Weaker flame luminosity of light diesel.
Mohammadi et al., 1998	Nano-spark back light photography and particle tracking Velocimetry (*PTV*) used when diesel sprayed in to high pressure nitrogen gas. Two dimensional size and velocity measurements of droplets based on photography. Droplet gas interaction when ambient gas was seeded using *PTV*.	Disintegration of diesel spray at a very early stage of injection ($t=50\mu m$). Thus large numbers of droplets are produced. The relative velocity of droplets and ambient gas is high at early stage of injection. However, it decreases rapidly. Up to middle of the injection duration, the relative velocity of droplets and ambient gas around the spray tip is much higher than the nozzle exit region.
Naber & Siebers 1996	Schlieren and high speed photography to study vaporising and non-vaporising spray in a constant volume chamber at high injection pressures using a common rail system.	Increase of cone angle with an increase of ambient gas pressure. A reduction in penetration length with an increase in ambient gas pressure. Development of a correlation for penetration in a non vaporising regime.
Nurick 1976	An investigation of cavitation in different nozzle orifices using a Heise gauge to measure the upstream pressure in the entrance region to the orifice, and a manometer to measure the orifice cavity pressure.	Sharp-edged orifices are more prone to cavitation, thus leading to hydraulic flip or reattachment, depending on the flow condition and *L/d* ratio. Critical flow conditions producing cavitation can be calculated by using a relatively simple correlation in terms of cavitation number *CN* and C_d. Critical cavitation number is dependent on the orifice entrance sharpness.

Schmidt & Corradini 2001	A review of internal nozzle flow of a diesel injector.	Cavitation in axisymmetric nozzle reduces mass flow and creates a contraction in the centre of the nozzle. Cavitation is connected to turbulence. In real-scale nozzles, cavitation may cause large cyclic disturbances in the exiting jet.
Shimizu et al., 1984	With the aid of an electrical resistance between a nozzle and a fine wire screen detector, or hot wiring, break-up length using number of different nozzles in a high-pressure gas chamber was measured.	Increase of injection velocity results in an increase of break-up length in a turbulent flow region. Effect of *L/d* on break-up length is greater at atmospheric ambient pressure. As ambient pressure increases, break-up length decreases. Increase of ambient pressure also results in an increase in cone angle.
Soteriou et al., 1995	Visualisation of cavitation phenomena with the aid of photography and video camera, using Large-scale injector nozzles.	Geometry induced cavitation occurs in standard nozzles and produces an opaque foam and chokes the nozzle. This type of cavitation causes atomisation in the spray. When the nozzle is choked, the entire cross section of the nozzle could be filled with cavitation bubbles.
Sovani et al., 2000	High speed video camera visualisation of effervescent injector in a high pressure gas chamber.	Effervescent diesel injector (*EDI*) cone angle are compared with conventional diesel injector cone angles. Cone angle is nonlinearly dependent on ambient pressure. This is thought to happen due to the two-phase flow emerging out of the injector, initially choking, then un-choking as the ambient pressure increases.
Strakey et al., 1998	*PDA* and a flow splitter to measure volume flux, drop sizes and velocity in a dense spray.	The use of flow splitter was found to give minimal adverse effect on the flow-field. Also a reduction in multiple particle occurrences within the probe volume and a reduction in background light due to multiple scattering was achieved. In addition, a reduction in particles in the beam path was observed.
Tsue et al., 1992	Visualisation of isothermal and evaporating diesel fuel spray including near nozzle tip region using exciplex-based planar fluorescence technique.	Existence of liquid core in the very near nozzle tip region. Break-up at a location millimetre downstream of the nozzle tip due to growth of the surface wave. A rapid decrease in the core length when ambient pressure increases up to 1 *MPa*, and then it becomes constant. Internal structure of non-evaporating spray is the same as evaporating conditions, except that cone angle of evaporating spray is smaller.
Yule et al., 1998	Effect of fuel properties on atomisation and spray structure using *PDA*.	No sizeable difference in droplet diameter was seen either for different fuel densities, viscosity or volatility.
Yule & Filipovic 1991	Computation of the overall void fraction of the spray as a function of time. Curve fitting for a new penetration rate correlation that is applicable to complete and incomplete atomised region.	Three interrelated Equations are derived for break-up time, break-up length, and characteristic velocity in the break-up zone. The equations are in good agreements with published experimental data.

Tab 2-1. Literature review and summary of main findings

3. CHARACTERISATION AND ANALYSIS OF THE FUEL INJECTION EQUIPMENT

3.1 INTRODUCTION

In recent years, more stringent emission standards have led to the development of very high pressure fuel-injection equipment (*FIE*) as a means of improving combustion processes in diesel engines (Bower & Foster 1991).

The importance of an adequate *FIE* in diesel engines is paramount for controlling the rate of injection, the quantity and the timing of the fuel introduced into the combustion chamber over the entire operational range. Whilst at idle or low-load conditions it is difficult to keep the engine speed stable, at high speeds and high loads due to the high pressures and high injection rates involved, cavitation erosion and parasitic losses are common with fuel injectors and fuel pumps. Accordingly, this could seriously degrade engine performance due to cyclic variations (Suzuki et al., 1982).

Historically, the control and measurement of the injection rate has been one of the most important objectives in the design process of the diesel engine. This is mainly attributed to the way in which the rate of injection influences the fuel spray formation, atomisation, droplets size and velocity distribution. The shape of the injection rate curve is also thought to determine pollutant formations, such as unburnt hydrocarbons, particulate matter and NOx emissions (Baniasad, 1994).

Within the combustion chamber, the composition of injected fuel with air mixture determines the combustion processes, which are controlled to a large degree by the injection characteristics (Bosch, 1966).

The injection rate curve is the main characteristic of an injector. The area under the injection rate curve represents the total quantity of the fuel discharged within a given shot for a given cycle. Whilst it is relatively simple to design injection systems that would give an accurate and uniform delivery of fuel per cycle, an apt shaping of the injection rate curve over an entire operational range for an engine is a much more complicated task (Bosch, 1966). Generally, the shape of the injection rate curve is known as the rate shape, and it has been shown to significantly influence the spray

characteristics, engine knock and emissions output (Baniasad, 1994; Dolenc, 1990; Bower & Foster, 1991). With this in mind, accurate measurements of the injection rate are essential for establishing the characteristics of the *FIE*. This should also facilitate the identification of the abnormal characteristics of the fuel delivery regime.

3.1.1   Fuel Delivery System

The function of the fuel injection system is to introduce accurately a given quantity of fuel into the cylinder of an engine, at a predetermined rate and crank angle position over an entire operational range. For improved accuracy and control, a high pressure second-generation common rail fuel injection system (*CRS*) was used to generate the high pressures required to maintain pressures ranging from 60 to 160 *MPa* (Fig 3-1) in this study.

The fuel pump was driven externally via an electric motor running at 1,400 *rpm* to maintain the required high pressure levels in the fuel rail, and ensure a stable line pressure with minimum fluctuation. The common rail and delivery pipe were both instrumented with a Kistler pressure transducer 4067. The delivery pipe was kept short to represent a modern fuelling system. Independent control of the injection pressure and duration, number of injections within a cycle, period between each injection (dwell period) for multiple injection events, and the number of injection skip cycles were achieved by a custom-built controller unit. These parameters were uploaded via a personal computer which gave time accuracy and greater parameter control. The control unit also provided an output trigger point to facilitate synchronisation of other instruments such as laser equipments, flash gun and *CCD* cameras during injection period. The custom-built controller was driven via a personal computer as shown in Fig 3-1.
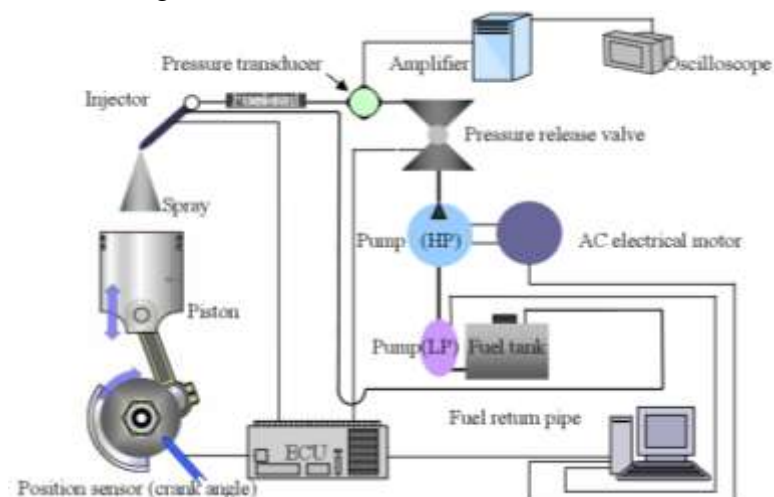
Fig 3-1. Schematics diagram of common rail fuel delivery system

3.1.2   Fuel Injectors

Two different designs of fuel injectors were used (by Bosch & Delphi). Both were of modern electro-magnetic actuated common rail type. The Bosch injector was equipped with a needle lift sensor to obtain exact needle position during injection, whilst the Delphi injector could not accommodate a needle lift trace sensor due to its size and complexity. The Bosch injector also allowed the nozzle to be replaced for the testing of different nozzle configurations (number of holes and diameter).

With the Delphi injector, the replacement of the nozzles was not possible, as this would have changed the manufacturer's torque setting, and consequently the working response. With the Delphi injector, three identical injectors were available to the current study in case of failure to one of the injectors.

The difference between the two makes of injectors will be highlighted in the forthcoming sections.

3.1.3   Nozzle Library

There are three basic types of injector nozzles as shown in Fig 3-2 - micro-sac, mini-sac and valve covered orifice (*VCO*) nozzles. Each type has its own advantages and disadvantages.

With *VCO* nozzles, the volume has been reduced to such an extent that the spray holes branch off near the needle seat. Therefore, the opening and closing of the nozzle hole(s) is carried out by the needle itself.

Micro-sac volume   *Mini-sac volume*   *Valve covered orifice (VCO)*
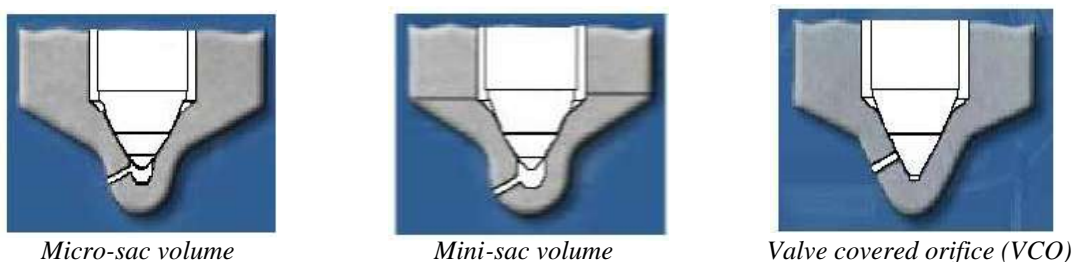
Fig 3-2. Basic types of single-hole injector nozzles (Bosch 2003)

For the *VCO* configuration there is almost no residual fuel to vaporise. In addition, control of injection timing and quantities are much improved with *VCO* configuration, since no time is required to fill the sac volume. The major drawback is the unequal pressure distribution of fuel through individual nozzle holes when multi-hole nozzles are utilised. This is due to random oscillations of the needle in the transverse direction

during needle lift and fall. This eccentricity of the needle transforms the axial symmetry of the flow around the needle and can result in asymmetry of the spray from each individual hole. This important phenomenon will be described in more detail later.

Mini-sac nozzles are not sensitive to needle concentricity, since equal fuel pressure distribution is governed by the sac volume below the needle tip. However, a small amount of fuel remains in the sac volume following the end of injection. At some point, this fuel dribbles out into the combustion chamber and increases hydrocarbon emissions. This residual volume of fuel must be kept to a minimum if hydrocarbon emissions are to be reduced.

The micro-sac nozzle has inherited the advantages of the mini-sac nozzle, with the addition of a smaller sac volume that results in a reduction of residual fuel in the sac, and, consequently, a reduction in hydrocarbon emissions.

The injector type and nozzle configurations used in the current study are summarised in Table 3-1.

Make	Type	Diameter (mm)	L/D_n	Number of holes	Injection Strategy	
					Spray Characterisation	Rate Measurements
Bosch	*VCO single guided*	*0.2*	*5*	*1, 3, and 5*	*Single*	*Single (for 1 & 3-hole nozzle)*
Bosch	*VCO double guided*	*0.2*	*5*	*1*	*Single*	
Delphi	*VCO*	*Measured at 0.135*	*Measured at 8*	*7*	*Single & Split Strategy*	*Single & Split Strategy*

Tab 3-1. Characteristics of the test nozzles, and injection strategy

For the Delphi injector, information on the nozzle configuration was not available. Consequently, the nozzle diameter and the corresponding length were accurately measured using an electron microscope, as shown in Fig 3-3
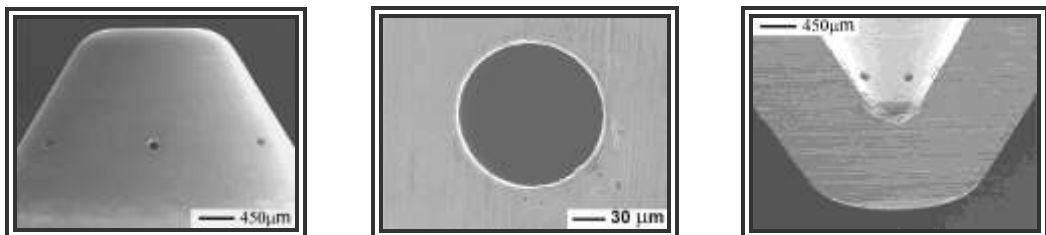
Fig 3-3. Electron microscope images showing the Delphi injector nozzle hole diameter (obtained by the author)

Overall, the majority of the experiments in the current study were carried out using the 3-hole Bosch, and the 7-hole Delphi injector.

3.2 EVALUATION OF THE FUEL DELIVERY SYSTEM, SELECTION AND CHARACTERISATION

3.2.1 Evaluation Method

In the current study, a long-tube rate of injection method was utilised in order to characterise two different types of second-generation common-rail fuel injector (Bosch & Delphi). This was carried out with reference to a single injection strategy for both types of injector, and split injection strategy for the Delphi injector only. It is thought that for the Delphi injector, this type of solenoid actuator can achieve up to five injections per cycle, allowing high flexibility for combustion optimisation, and providing a level of economy and performance that is usually available with the piezo type system (Birch, 2004). Furthermore, this new type of solenoid injector is understood to support Euro IV and V compliance without the expense of the piezo technology. In the current study, however, only of two injections per cycle were investigated.

Comprehensive studies and comparison of various rate measurement techniques for diesel fuel have been presented by many researchers (Arcoumanis et al., 1992; Baniasad, 1994); and Bower & Foster, 1991).

The operating concept of the long-tube rate gauge method can be described as follows. Liquid fuel is injected into a long tube (delay line of 10 meters) containing the same working fluid under pressure. This in turn creates a pressure wave which travels along the tube at sonic speed in the fluid. The concept of measuring the rate of injection is based on the pressure-velocity equation applicable for a single pressure wave in an in-stationary flow, and derived from the hydraulic pulse theory (Eq. (3.1)) under the assumption of one-dimensional flow (Arcoumanis & Baniasad, 1993).

$$P = a \, \rho_l \, U \, , \tag{3.1}$$

where P is the pressure , a is the velocity of sound, U is the flow velocity, and ρ_l is the liquid fuel density. The theory of pressure waves in liquids states that, at any instant in time, the magnitude of the pressure wave is directly proportional to the flow

velocity at a given cross-section in the tube. Given a tube of uniform cross-sectional area, the flow velocity, and hence the pressure wave, are proportional to the rate of injection (Arcoumanis et al., 1992, Arcoumanis & Baniasad, 1993).

A pair of strain gauges located near the injector nozzle outlet (in the rate meter) measures variation in the pressure waves, and a second pair is used for temperature compensation (Fig 3-4). The strain gauges are connected to a bridge amplifier and the output signals are then recorded on a storage oscilloscope at a suitable sampling rate. By combining the continuity equation (Eq. (3.2)) with Eq. (3.1), the governing equation to define the quantity of fuel injected is Eq. (3.3) (Bosch 1996). To calculate the fuel quantity per stroke Eq. (3.3) is integrated giving Eq. (3.4).

$$Q = A_{delay} \; U \; , \tag{3.2}$$

$$\frac{dQ}{dt} = \frac{A_{delay} \quad P}{a \; \rho} \; , \tag{3.3}$$

$$Q_{St} = \int_{t_1}^{t_2} \frac{dQ}{dt} \quad dt \quad = \frac{A_{delay}}{a \; \rho} \int_{t_1}^{t_2} P \quad dt \; . \tag{3.4}$$

Where A_{delay} is the internal cross-sectional area of the delay line, dQ/dt is the fuel quantity per unit time, Q_{St} is the injected volume per stroke, and t_1 & t_2 are the time at beginning and the end of injection respectively.
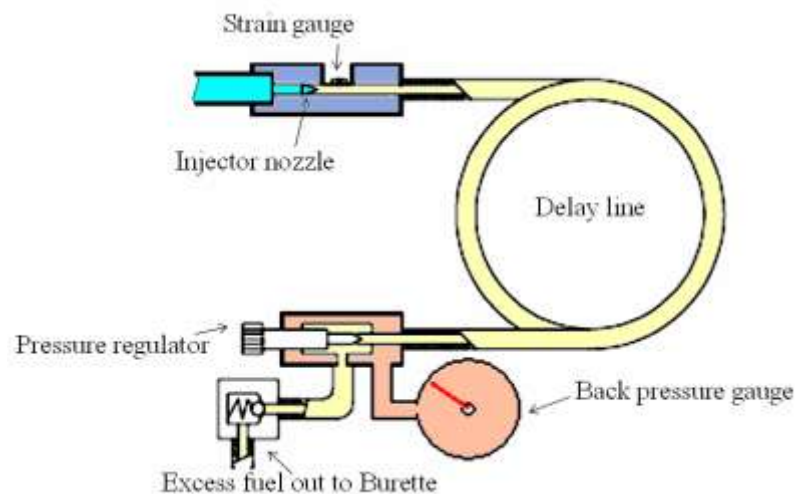
Fig 3-4. Schematic diagram of a rate tube

To allow simulation of the in-cylinder pressure at the time of injection, the pressure within the delay line was adjusted via the pressure regulator (Fig 3-4).

As mentioned previously, two different makes of injector were available to the current study, Delphi & Bosch. With each make of injector mounted on the fuel calibration test-bed in turn, and by adjusting the injection duration for a given rail pressure (60, 100, 140, and 160 MPa), the desired volume (5, 10, 15, 20, 30, 40, and 50 mm^3 for the Delphi injector, and 30, 50 mm^3 for the Bosch injector) was measured and recorded for an average of 100 cycles each (Fig 3-5).
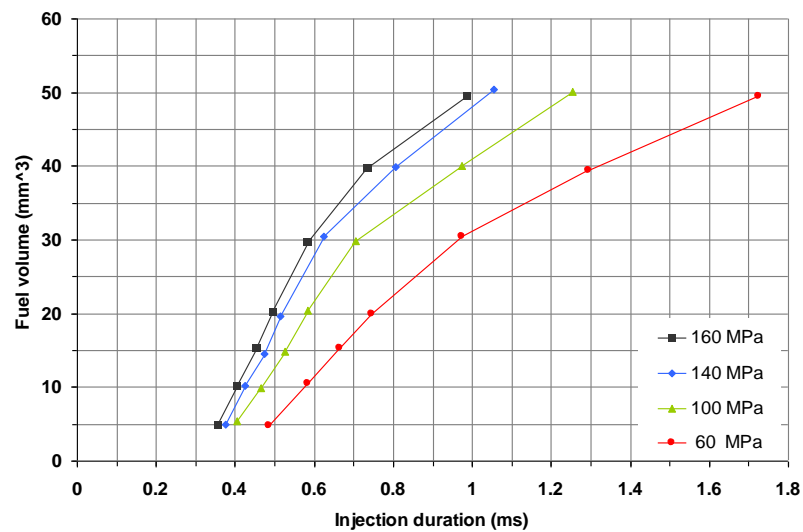
Fig 3-5. Comparison of the injected volumes at different injection pressures; injector No2, Delphi

With the fuel volumes established, the injectors were then mounted on the long-tube rate gauge. With the oscilloscope capable of averaging over a specified number of cycles, an average of one hundred cycles as well as individual cases were recorded for the rate of injection, the rail pressure, the injector current and the *TTL* output signals on a LeCroy LT224 storage oscilloscope at a suitable sampling rate. For the Bosch injector, needle trace lift signals were also recorded.

Once the data was collected, it was then exported to an Excel worksheet, and the area under the rate curve was integrated.
For each injector, the calibration factor (ratio of fuel volume and the area under the curves) was calculated and the transient rate of injection in *kg/s* was established.
With the calibration constant known (for each different make of injector), it was then applied to the split injection strategy for the Delphi injector.

3.2.2 Injector Selection and Characterisation

As explained in section 3.1.2, three Delphi injectors were available to the current study in case of failure of one of the injectors. To ascertain that the injectors were identical, each injector was evaluated independently with the rate tube.

With the Delphi injectors numbered, injector No2 was selected as the reference injector and mounted on the fuel calibration test-bed, as explained in section 3.2.1.

The minimum amount of fuel that could have been injected and measured with the Delphi injector was 5 mm^3. Attempts to ascertain sustainable and smaller amounts of fuel delivery failed, particularly at 160 MPa injection pressure, due to a minimum time limit (0.2 ms) needed for the needle to rise and fall. This indicates the dependence of needle ascent velocity on injection pressure. Accordingly, this phenomenon will be described in more detail in the forthcoming sections. Fig 3-6 shows the rate of injection, the TTL signal and current trace for three Delphi injectors.
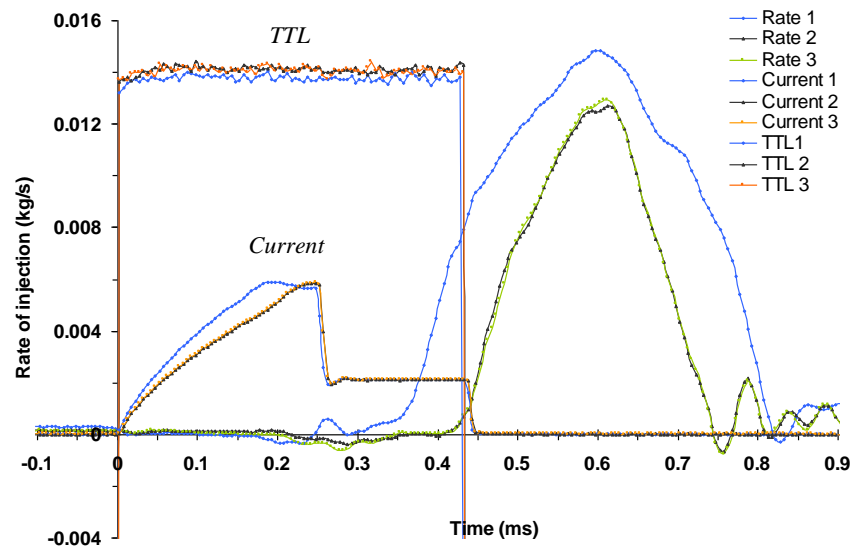
Fig 3-6. Comparison of injected rate, current, and TTL signal from the 3 Delphi 7-hole VCO injectors at 60 MPa injection pressure, and 0.4125 ms triggered injection duration

As can be seen from Fig 3-6, whilst the TTL and the current trace durations are identical for all three injectors, injector No 1 can be seen to respond slightly faster to reach peak current than injectors Nos 2 and 3 by 0.05 ms. The resultant effect being not only a shorter injection delay, but also a displaced area almost twice as large when compared with injectors Nos 2 and No 3. This behaviour was consistent for all injection pressures, indicating possible differences in the inductance and/or the magnetic permeability of the solenoid core material of the injectors.

46

To test this hypothesis, the injection duration for injector No 2 (and No 3) was increased by 0.05 *ms* and compared with injector No 1 as shown in Fig 3-7.
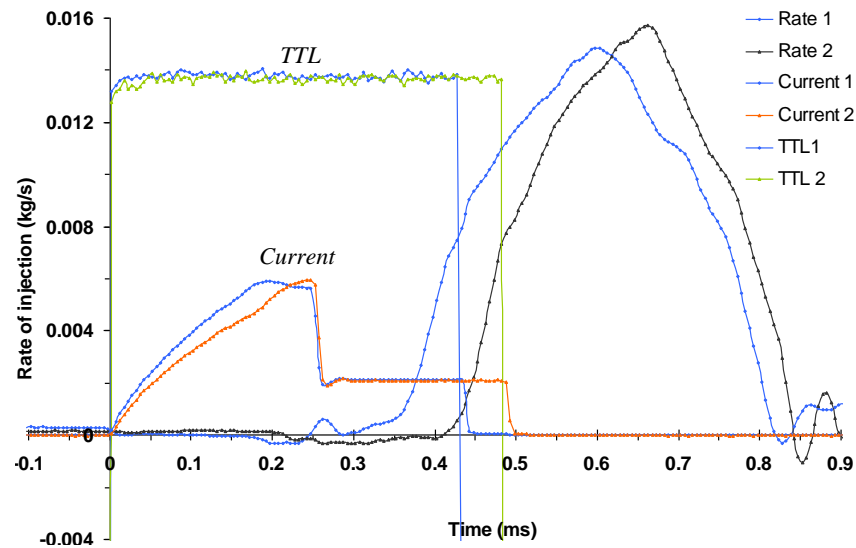
Fig 3-7. Comparison of injector No 1 and No 2; 60 MPa injection pressure; 0.41 ms target injection duration for injector No1, and 0.46 ms target injection duration for No 2

As can be seen from Fig 3-7, the opening delays between the two injectors are the same as before, whereas the integrated areas under both curves are identical giving the same mass of fuel injected. For longer injection durations operating at the same injection pressures, the differences in the area under the rate curves appear negligible. This is due to the insignificant differences in time, when the total injection duration is compared with the differences between the injector current rise time to reach peak current (Fig 3-8).
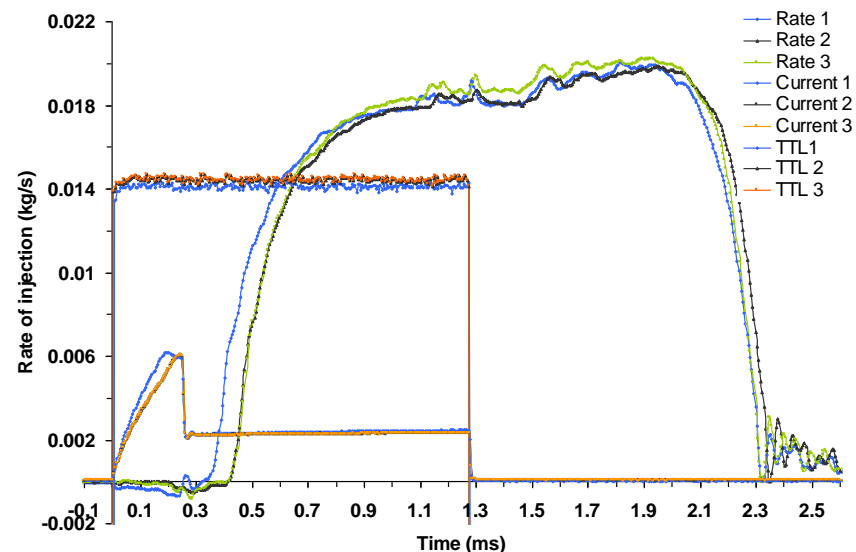
Fig 3-8. Comparison of injected rate, current, and TTL from a batch of 7-hole VCO Delphi injectors; 60 MPa injection pressure; 1.275 ms target injection duration

47

Further experiments into variation in the rate of injection with single and split injection strategies were carried out using Delphi injector No 2.

As before, with injector No 2 mounted on the long-tube (Lucas rate) gauge, the chosen dwell periods (separation time between each pulse for split injection) varied in the range of 0.325 *ms* to 1.025 *ms*, with increments of 0.1 *ms*, and from 1.025 *ms* to 2.525 *ms* with increments of 0.5 *ms*. The injected volume was kept in the range of 5 to 20 *mm³* with increments of 5 *mm³*, whilst the rail pressures varied as before (60, 100, 140, and 160 *MPa*).

Fig 3-9 and Fig 3-10 represent the rate of injection, current, and the *TTL* signal for the split injection strategy, with the addition of a single injection event superimposed on the same figure twice for comparative reasons (once for the first split and once for the second split strategy).
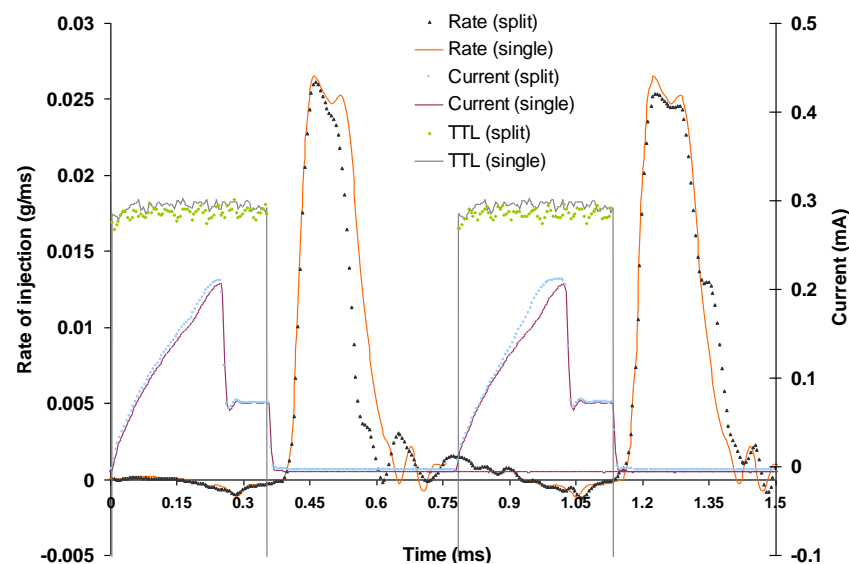
Fig 3-9. Differences in the rate of injection between single (solid lines) and split injection strategy (doted lines). The data for the single injection event has been superimposed on the above figure twice, with an offset to match the second of the split strategy; 160 MPa injection pressure; 0.355 ms target injection duration corresponding to 5 mm³ fuelling; 0.425 ms dwell period

Intuitively, one would expect similarity between the first of the split and the single injection strategy. However, from Fig 3-9, whilst the *TTL* and the current signal durations for each of the two strategies are the same, the mass injected is approximately 19% less for the first split when compared to single injection strategy; the second split mass portion is approximately 4% less than the single injection strategy.

Although the upper needle bounce is thought to contribute to this effect (detailed description will be given in forthcoming section), the prime difference is attributed to the "actual" period of injection duration between the first and the second split, even though the command injection duration is identical for both splits, as can be seen from the current and the *TTL* signals in Fig 3-9.

This inconsistency was mainly valid for high injection pressures, short dwell periods, and very low fuelling under consideration (5 mm^3). As the injection pressure was decreased and the dwell period and the fuelling increased, an improved agreement between the two split rates was observed in addition to correlations between the single and split injection strategy (Fig 3-10). Additional injection rate profiles can be found in Appendix A.
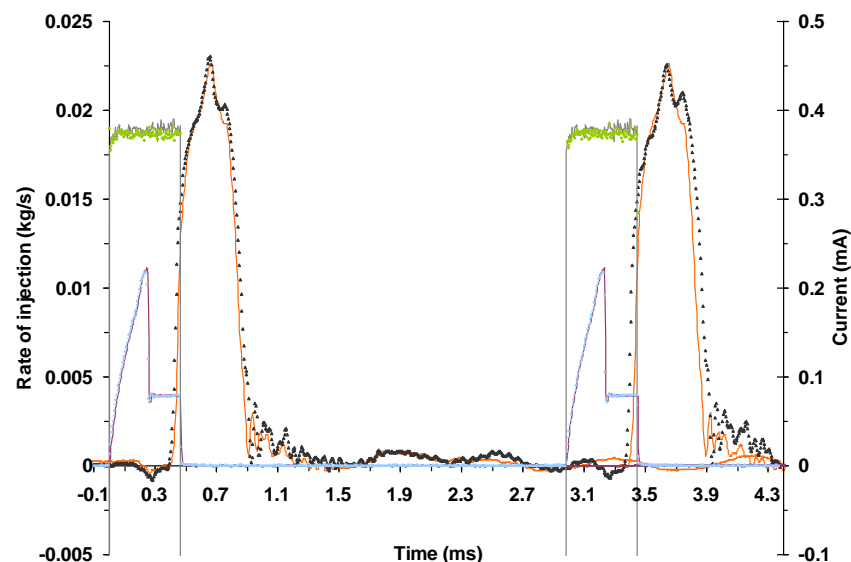
Fig 3-10. Differences in the rate of injection between single (solid lines) and split injection strategy (doted lines). The data for the single injection event has been superimposed on the above figure twice, with an offset to match the second of the split strategy. 100 MPa injection pressure; 0.465 ms target injection duration corresponding to 10 mm^3 fuelling; 2.5 ms dwell period

3.2.3 Injection Rate Analysis, for Single and Split Injection Strategies

To appreciate the sequence of events responsible for irregularities and variations that may occur during cycle-to-cycle, as well as shot-to-shot for split injection strategies, it is often necessary to examine individual cycles.

With the current experimental setup, the rail pressures are at a nominal set point prior to the start of injection. Once the injector is triggered, the needle starts to open. During the needle ascent, the rail pressure starts to decrease due to needle upward

motion, resulting in finite volume of fuel to be added to the system volume, and, accordingly, a reduction in the injection pressure. Once the needle has reached its maximum lift, the pressure regulator attempts to maintain the required pressure levels. Generally, the injection rate signal could start slightly after the opening of the needle lift for two prime reasons (Arcoumanis et al., 1992; Arcoumanis & Baniasad, 1993); first, particularly in the case of mini-sac or micro-sac, the time taken for the pressure to build up and occupy the sac volume, in addition to the acceleration time of fuel needed through the nozzle; secondly, due to the position of the pressure transducer. The former can be neglected in the current study, since valve covered orifice (*VCO*) nozzles are being used. The latter is significant, due to the pressure transducer being approximately 200 *mm* away from the nozzle exit (for the Delphi injector). From the data collected, the lag periods between the two signal positions were found to be approximately 0.1 *ms* for the Delphi injector and approximately 0.17 *ms* for the Bosch injector.

As indicated above, once the needle starts to open, the rail pressure starts to reduce. Fig 3-11 shows the initial rail pressure decay occurring between the start of needle lift and the maximum needle lift, exhibiting high levels of correlation to all needle lift characteristics throughout the experiment.

At the end of injection duration, although due to a rapid needle closure low rates of injection are almost eliminated, needle bounce could still occur. The bounce period is estimated at circa 0.05 *ms* for the Delphi injector and circa 0.14 *ms* for the Bosch injector from the injection rate data.
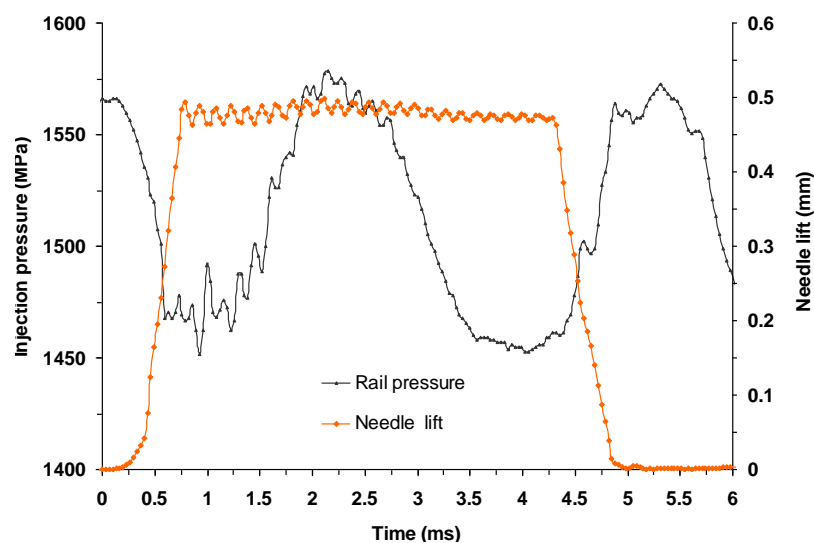
Fig 3-11. Correlation between start of needle lift, and rail pressure drop; Bosch single-hole single guided nozzle; 50 mm³ fuelling

Fig 3-12 and Fig 3-13 show the cycle-to-cycle variation in the rate of injection and the rail pressure over 15 consecutive injections, including the mean and the standard deviation of the signals for the first and the second of a split injection strategy over the steady-state injection period.

Intuitively, one would expect a precise correlation between the maxima of the injection rate signal and the injection pressure. In the current experiments, however, although no precise correlation between the two maxima was observed, better agreement for the second of the splits compared with the first split was found (Fig 3-12 and Fig 3-13). This was attributed to the effect of upper needle bounce on the maximum rate of injection, and variations in the maximum needle lift and injection pressure (Arcoumanis et al., 1992, Arcoumanis & Baniasad 1993).

For pressure, on the first split, Max (mean = 134.7 MPa, Stdev = 1.295)
For rate, on the first split, Max (mean = 0.01877 kg/s, Stdev = 0.0042)
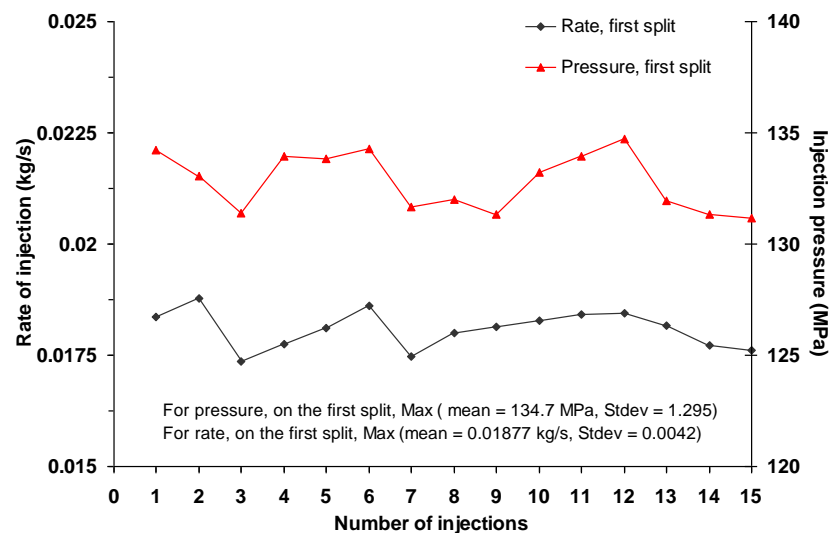
Fig 3-12. Comparison of the cycle-to-cycle variation in the rate of injection and the rail pressure for the first of the split injection strategy; the number of injections refers to 15 individual cycles; Delphi injector; 10 mm^3 fuelling

For pressure, on the second split, Max (mean = 137.13 MPa, Stdev = 1.75)
For rate, on the second split, Max (mean = 0.0209 kg/s, Stdev = 0.0061)
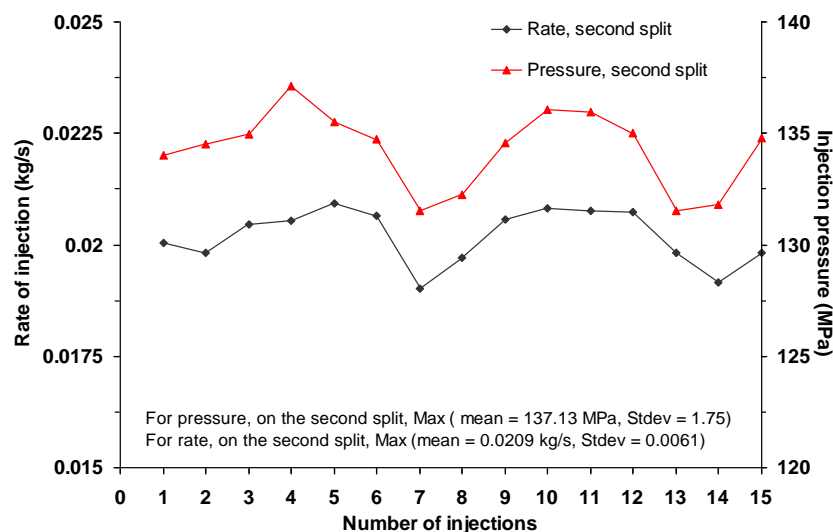
Fig 3-13. Same as Fig 3-12, with the exeption of the second shot of the split injection strategy

3.2.4 Needle Lift Analysis

In the previous section, it was explained that the time taken for the needle to rise and fall is governed by needle ascent velocity, which is primarily a function of rail pressure, with respect to common rail injectors. With distributor pump injectors, however, the fuel quantity and the pump speed also influence the needle ascent velocity (Arcoumanis & Baniasad, 1993). In the current experiment, the high pressure fuel pump was operating at a constant speed of 1400 *rpm*.

Although needle lift traces are not available for the Delphi injector (for reasons given in section 3.1.2), an analysis of the needle ascent and descent velocities can be performed based on the injection rate shapes, where Arcoumanis et al. (1992) have shown a high level of correlation between the two traces. For the Bosch common rail injector, however, there are needle lift traces available.

Fig 3-14 and Fig 3-15 show the dependence of injection pressure on needle ascent and descent velocity, and the independence of needle ascent and descent velocity with respect to fuel quantity for an average of 100 cycles.
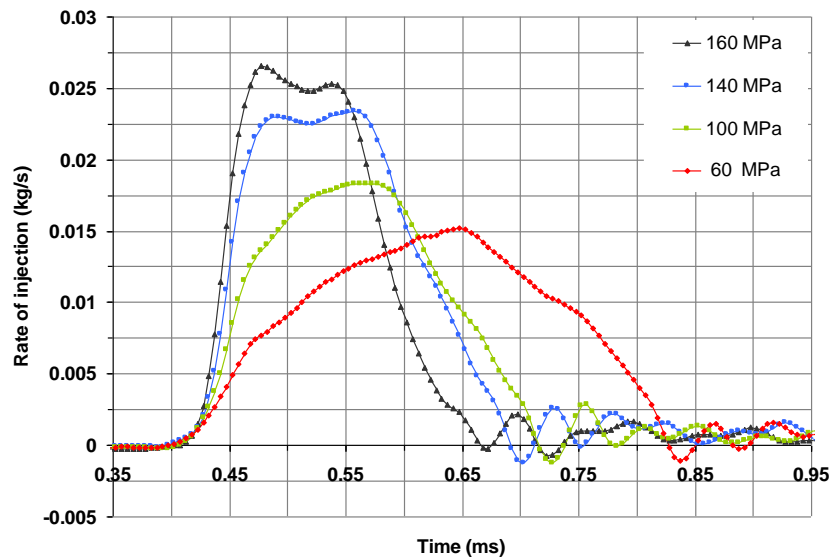
Fig 3-14. The dependence of the needle ascent and descent velocity on injection pressure; fuel delivery 5 mm³; Delphi injector
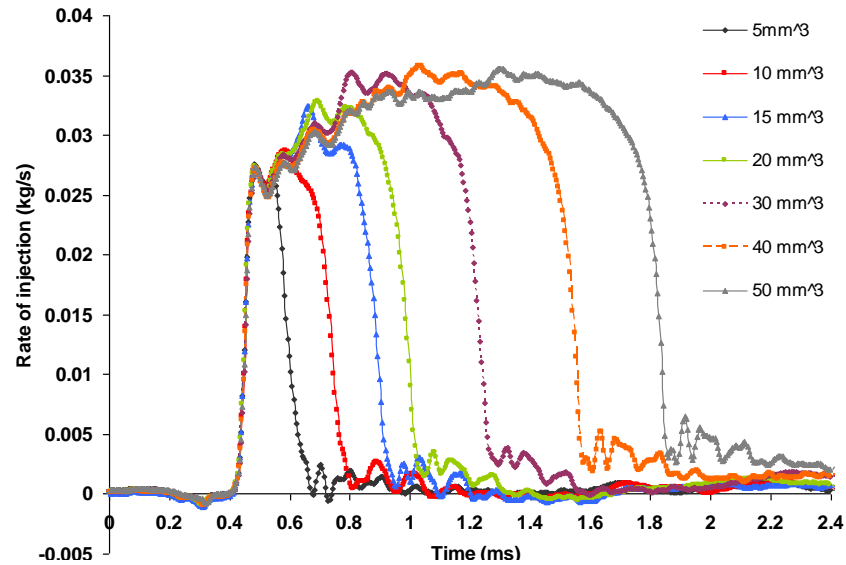
Fig 3-15. The independence of needle ascent and decent velocity with respect to the fuel quantity injected at 160 MPa injection pressure; Delphi injector

From Fig 3-14, it can be deduced that the injection pressure determines the needle opening and closing period and not the fuel quantity (Fig 3-15). Therefore, the minimum fuel quantity that can be injected becomes a function of rail pressure.

This is because, although the needle opening pressure is constant for a given injector (according to the needle spring stiffness), the rate at which the pressure rises between the needle opening pressure and the maximum injection pressure determines the needle ascent velocity, and hence time.

This phenomenon can be observed from Fig 3-16, where the differences between the needle lift signal and the rate of injection for two rail pressures are presented.
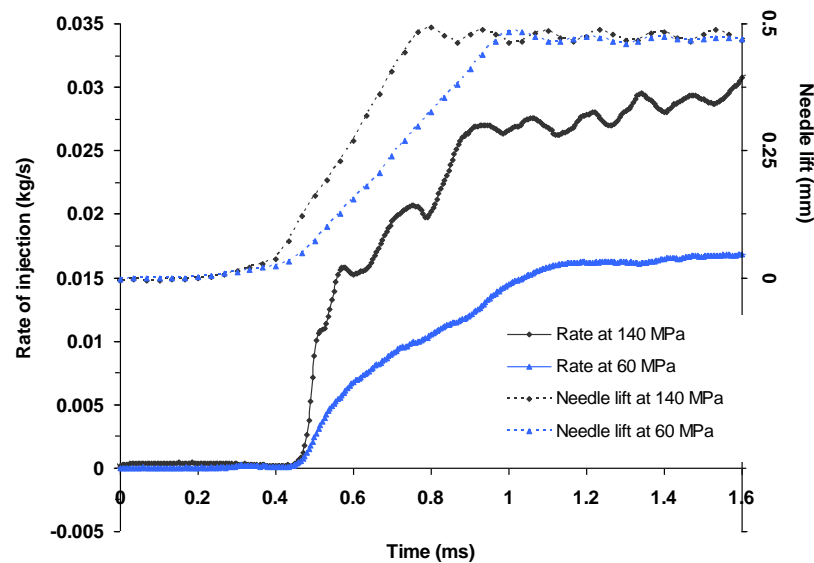
Fig 3-16. Rate of injection and needle lift trace for two rail pressures; Bosch single guided 3-hole nozzle; the data for 60 MPa rail pressure has been offset for comparative reasons

53

Fig 3-16 shows the high level of correlation between the rail pressure and the corresponding needle ascent velocity and the rate of injection. The needle ascent velocity was estimated at 2.7 *m/s* at 60 *MPa*, and 3.95 *m/s* at 140 *MPa* rail pressure from the needle trace data.

The upper needle bounce and the corresponding rate of injection fluctuations for the 3-hole Bosch injector can also be observed from Fig 3-17. As can be seen, there is good agreement between the two traces, even though there is a slight shift in phase which is attributed to the lag period between the two signals. Nevertheless, the frequency of the upper needle bounce and the corresponding upper injection rate fluctuations closely agree at 7.2 *kHz* and 7.4 *kHz* respectively. The standard deviation is 0.1 *kHz* averaged over eight cycles.

The effect of needle bounce prohibits a steady flow through the nozzle exit, causing approximately sinusoidal flow perturbation (Chaves et al., 2000), and corresponding fluctuations in the rate of injection. This can result in a highly heterogeneous spray structure and a reduction in the average mass flow rate through the nozzle exit.
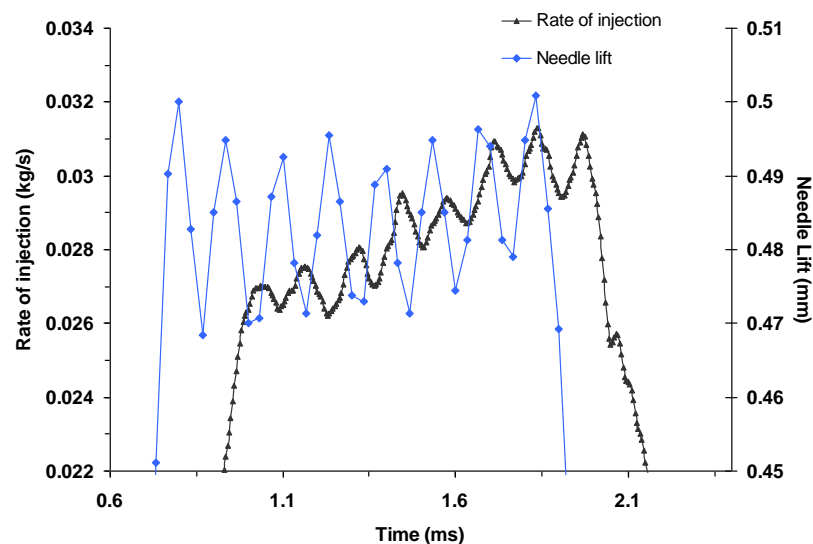
Fig 3-17. Upper needle bounce and corresponding flow fluctuations observed in the rate of injection signal; Bosch 3-hole single guides VCO nozzle; 50 mm³ fuelling at 140 MPa injection pressure

For the Delphi injector, assuming a good correlation between the upper needle bounce signal and the upper portion of injection rate signal, it can be deduced accordingly from Fig 3-15 that the magnitude of the bounce decays as time progresses. The

resulting effect is a steadier flow through the nozzle exit and an increased rate of injection.

Given that the magnitude of the upper needle bounce decreases with increased injection duration, a degree of inconsistency for the rate of injection between the two splits for a split injection strategy (in the current experiment) could also be attributed to the magnitude of the upper needle bounce during the actual injection duration (Fig 3-9 & 3-15). In other words, the longer the needle remains open from rest position, the lower the magnitude of needle bounce, and hence this results in an increased rate of injection.

Information on the lower needle bounce could not be deduced from the needle lift traces (Fig 3-11). Nevertheless it can be seen from Fig 3-18 that at the end of injection needle oscillation transversely or vertically prohibits a sharp end to fuel delivery. Although the quantity of fuel delivered during this period is small, this is an undesirable fuel quantity, under the influence of much-reduced injection pressure. This phenomenon was confirmed by high speed video photographs (*HSV*) detailed in Chapter 5.
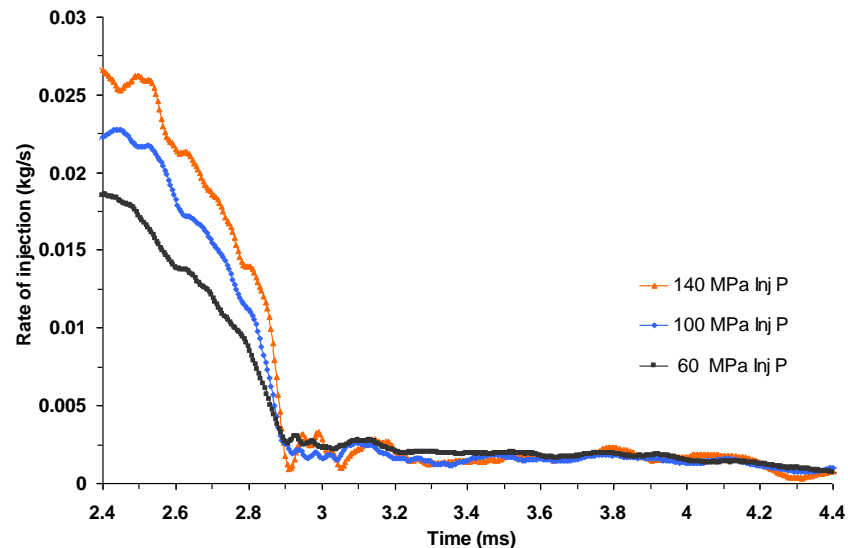
Fig 3-18. Undesirable fuel delivery at the end of injection; the above data has been offset for comparative reasons; 3-hole Bosch injector VCO single guided nozzle; 30 mm³ injected volume

3.3   CONCLUSIONS OF CHAPTER 3

The results presented in this chapter underline the importance of injector characterisation via techniques such as rate of injection measurement, needle lift trace signals, current clamp signals, and *TTL* signals prior to spray characterisation. The analysis of the results has given rise to the following conclusions.

- Due to a minimum time limit of 0.2 *ms* (at 160 *MPa* injection pressure) for the needle to rise and fall for the Delphi injector, sustainable volumes injected below 5 mm^3 could not be reproduced.

- Comparison between the three Delphi injectors revealed that the response time between injector No 1 and No 2 & 3 varied by as much as 0.05 *ms*.

The resultant effect was variation in the fuel quantity. This phenomenon was attributed to the possible differences in the inductance and/or the magnetic permeability of the solenoid core material of the injectors. For long injection durations, the insignificance of 0.05 *ms* showed negligible volume flow differences, between injector No 1 and Nos 2 & 3.

For the split injection strategy, it was found that the rate of injection is approximately 19% less for the first shot of the split, in comparison to single injection strategy; the second split was found to be approximately 4% less than the single injection strategy. The differences were primarily due to the actual injection duration, even though, the command injection duration was identical. Nevertheless, a part of the discrepancy is thought to be the result of upper needle bounce. For decreased injection pressure and increased dwell periods, improved correlation between the two split rates was observed, as well as correlation between the single and split injection strategy.

- Cycle-to-cycle variation, mean and the standard deviation of the injection rate signals and the rail pressure signals over 15 consecutive injections were examined for the first and the second of the split injection strategy. Although no precise correlations between the two maxima of the signals were observed, improved correlation was evident for the second of the split injection strategy.

- The dependence of needle ascent and descent velocity on injection pressure was examined from the injection rate profiles. It was concluded from the analysis of the data that, although the needle opening pressure is constant for a given injector, the rate at which the pressure rises between the needle opening pressure and the maximum injection pressure determines the needle ascent velocity, and hence the ascent time.

- Since the injection pressure determines the needle opening and closing period beyond the needle opening and closing pressure, the minimum fuel delivery becomes a function of the rail pressure.

- Good agreement between frequency of the upper needle lift trace signal and the corresponding rate of injection signal were observed. The frequency of the upper needle bounce signal and the corresponding upper injection rate fluctuations were estimated at 7.2 *kHz* and 7.4 *kHz*, with a standard deviation of 0.1 *kHz*.

- At the end of injection duration, traces of undesirable fuel quantity were evident from the injection rate signals. During this period, the fuel is believed to be delivered at an injection pressure less than or equal to the needle spring compression pressure (20 *MPa*).

4. EXPERIMENTAL CONSIDERATION OF THE OPTICAL TEST RIG

4.1 THE PROTEUS RAPID COMPRESSION MACHINE

A high pressure and temperature rapid compression machine (*RCM*) was installed at University of Brighton in 1999. This compression machine was based on the Ricardo Proteus engine to enable realistic combustion conditions for spray analysis of up to 10 *MPa* in-cylinder pressure (*ICP*). In addition to representative in-cylinder pressures, the intake air temperature was adjustable up to 423 *K*. The Proteus rig is a single cylinder two-stroke rapid compression machine, with a specially designed head for optical access as shown in Fig 4-1.
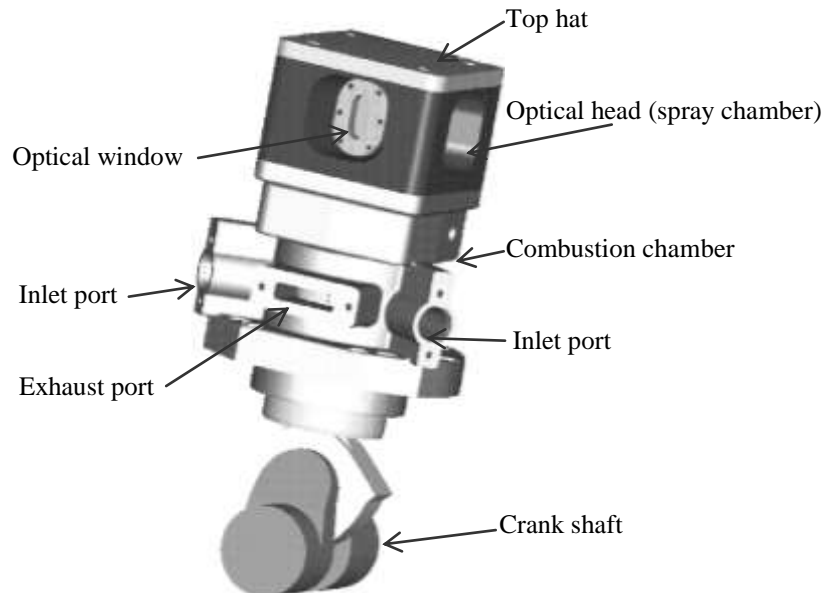
Fig 4-1. CAD drawing of the rapid compression machine, Proteus

The optical head (spray chamber) and the combustion chamber were designed using Ricardo *VECTIS CFD* code. The design aimed to acquire near quiescent condition in the spray chamber at a maximum predicted air velocity of $1ms^{-1}$. This was in order to avoid disturbances by the air motion on the spray development, and to achieve maximum loop scavenging efficiency in the combustion chamber. The Proteus rig was coupled to a DC dynamometer via reduction belts. With an operating speed of 3,000 *rpm* at the dynamometer, the reduction was 6:1, corresponding to an engine operating speed of 500 *rpm*.

With an external water pump and water heater, the engine was brought to its normal operational temperature of 353 *K*. The engine oil was also heated to a temperature around 353 *K* within the oil sump, and driven via an external oil pump to the engine oil galleries.

In order to minimise heat losses by heat transfer from the in-cylinder gas to the surrounding walls, the heated oil and water were pumped prior to running the engine. Fitted to the engine, three slow response thermocouples were used to monitor the coolant temperature, the oil temperature, and the air intake temperature at plenum. Fitted to the crankshaft was an encoder with a resolution of 3,600 pulses per revolution (corresponding to 10 resolutions per crank angle), in order to provide *TDC* pulse marking.

Two Kistler pressure transducers were fitted to the engine combustion chamber. The first was a water-cooled Kistler 6061 transducer fitted to the optical head to monitor the in-cylinder gauge pressure. The working pressure and the temperature range of Kistler 6061 were 0 to 25 *MPa* and 223 to 623 *K* respectively. The second pressure transducer was a Kistler 4045-A10, fitted just above one of the inlet ports in the combustion chamber, in order to monitor the absolute boost pressure. The working pressure and temperature range of Kistler 4045-A10 were 0 to 1 *MPa* and 273 and 413 *K* respectively.

Instrumented with two slow response Druck pressure transducers, the exhaust and plenum pressures were also monitored. The working gauge pressure and operating temperature range of both pressure transducers were 0 to 1.5 *MPa* and 273 to 323 *K* respectively.

The Proteus rig has a stroke of 150 *mm*, a bore of 135 *mm* and a displacement of 2200 *cc*.

4.1.1   Optical Head and Windows

Optical access into the spray chamber was provided by four removable windows (Fig 4-1). The spray chamber within the optical head was cylindrical and had dimensions of 25 *mm* in radius, and 80 *mm* in height. This allowed sufficient space for the spray to develop without any wall impingement.

In a combustion environment, windows fitted to a combustion chamber will absorb part of the emission spectrum. In addition, window fouling can occur during the

compression or injection process. This could subsequently affect measurements, and, therefore, a suitable material must be selected. The material used in the current study was sapphire. This material is a synthetic hexagonal crystal structure formed from aluminium oxide ($Al_2 O_3$). Sapphire exhibits the high mechanical strength, chemical resistance and thermal stability that are needed in a high temperature combustion environment. With a melting point of 2303 *K*, sapphire has an excellent optical transmission in both ultra violet (*UV*) and infra-red. A typical transmission profile for sapphire specimen 10 *mm* in thickness is shown in Fig 4-2.
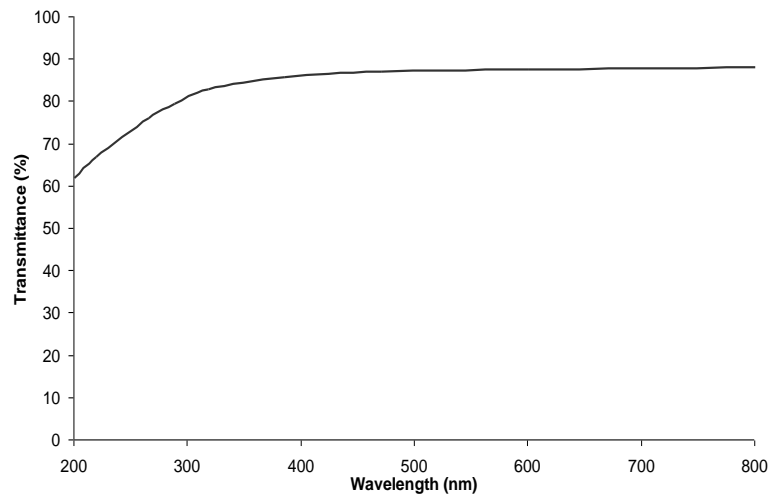
Fig 4-2. Transmittance of a sapphire window

The removable optical windows had an optical access 25 *mm* in width and 55 *mm* in height (Fig 4-3). The outer edges of the windows were fitted with O rings to eliminate any leakage. The sapphire glasses were secured in the window holders with a special silicon-based resin. The windows were secured in the wall of the Proteus head with annealed copper gaskets. The gaskets also secured the sapphire windows against the head casting. This configuration allowed quick overhaul and cleaning to take place.

Sapphire window

Window holder
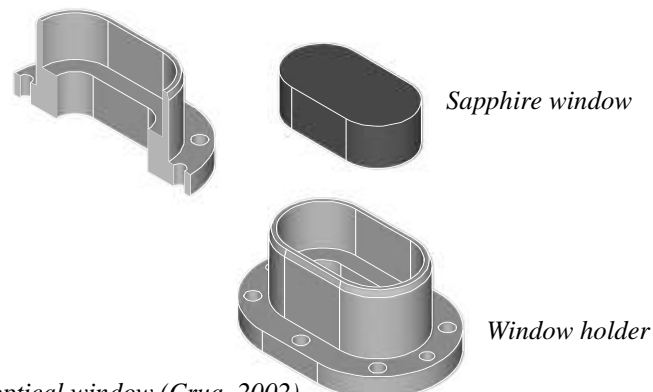
Fig 4-3. CAD drawings of the optical window (Crua, 2002)

4.2   EVALUATION OF THE OPTICAL PROTEUS RIG

4.2.1   Introduction

The study of the compression process of a reciprocating internal combustion engine, operating without combustion, is a useful tool in determining different parameters associated with the engine configuration or its operating condition. Once parameters such as trapped air mass, effective polytropic coefficient and compression ratio are established, the performance of the rig can be evaluated in terms of conditions such as evolution of heat transfer, the heat transfer coefficient, in-cylinder gas temperature variations, surface wall temperatures and gas density during a cycle. It is common practice in engine diagnostics to test the engine in a motored condition with air as the only constituent in the combustion chamber.

The objective of this chapter is to characterise the Proteus rig in terms of in-cylinder gas temperature as a consequence of trapped air mass. In the following section, an alternative approach for calculation of the in-cylinder mass, after gas blow-by has been presented. Although mass losses could proceed via any crevices, gas blow-by past the piston rings has some detrimental effects on the engine and its performance. On a physical level, blow-by contains acid water (Hawas & Muneer, 1981), polluting the lubrication oil within the crankcase. Also, blow-by increases the lubricant temperature, resulting in lower oil viscosity; hence additional ring wear and blow-by. On a performance level, it reduces the trapped air mass, and, as a consequence, increases fuel consumption, increases the gas temperature, decreasing performance, and increases combustion knock and NOx emissions. However, in this study consideration is only given to mass blow-by as indicated.

4.2.2   The Evaluation of Trapped Air Mass and Blow-by

The volumetric capacity of the Proteus rig had been determined by calculating the swept volume and the clearance volume, using specified engine data.

For the compression stroke, it was necessary to take the start of compression from the moment the inlet and exhaust ports were covered by the top compression ring at 243° crank angle. For the cases considered in this study, the range of in-cylinder pressures varied from 2 to 8 *MPa,* with increments of 1 *MPa*, both for cold (293 *K*) and hot (373 *K*) air intake.

The in-cylinder pressure signals were recorded via a piezoelectric pressure transducer with the aid of an oscilloscope at a suitable sampling rate.

Initially, by using the combustion chamber as a fixed volume (locked crankshaft), the chamber was filled with nitrogen at room temperature with a pressure of 1 *MPa*, at a known crank angle, corresponding to a known chamber volume. The decay in pressure with time was then measured in order to establish the rate of the trapped mass lost due to blow-by (Fig 4-4).

The transducer used for the pressure decay analysis was a piezoelectric 4045-A10 Kistler, measuring absolute pressures up to 1 *MPa*, and operating between temperatures of 273 and 413 *K*, with a thermal sensitivity shift of $\leq \pm 1\%$.
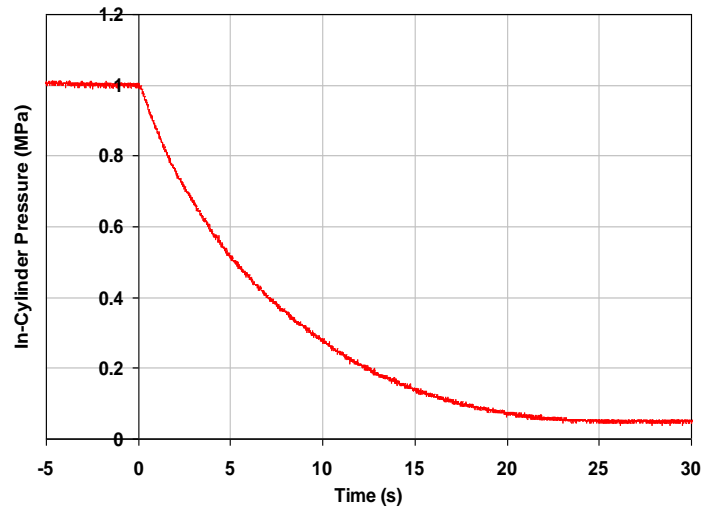
Fig 4-4. Experimental pressure decay against time in a closed loop system (Proteus)

Assuming that the decay in pressure against time is exponential (Fig 4-4) the following expression can be written.

$$p = j\,e^{bt}.$$
(4.1)

Where p is the pressure, j and b are constants, and t is the time taken for the pressure to decay. By taking the time derivative of Eq. (4.1) it can be written as,

$$\frac{dp}{dt} = j\,b\,e^{bt}.$$
(4.2)

The following expression is given by the gas law.

$$p = \left(\frac{R}{V}\right) mT \ .$$
(4.3)

Differentiating Eq. (4.3) gives,

$$\frac{dp}{dt} = \left(\frac{R}{V}\right)\frac{dmT}{dt} = \left(\frac{R}{V}\right)\left(\frac{mdT}{dt} + \frac{Tdm}{dt}\right).$$
(4.4)

Under the current experimental set-up (where the combustion chamber is static) the gas temperature (T) is constant. Thus $dT/dt = 0$, and by rearranging and substituting Eq. (4.2) into Eq. (4.4) the mass flow rate becomes,

$$\overset{\bullet}{m} = \frac{dm}{dt} = \left(\frac{V}{RT}\right)\frac{dp}{dt} = \left(\frac{V}{RT}\right)j\,b\,e^{bt} \ .$$
(4.5)

Due to the pressure ratios between the crankcase and the in-cylinder pressures being much less than 0.5, the system is assumed to be choked. Therefore, by using Laval's nozzle theorem, the maximum mass flow rate past the piston rings occurs when the Mach number is unity, assuming adiabatic condition. Hence, the maximum flow rate can be written as,

$$\overset{\bullet}{m} = \rho_{t_r}\, A_{t_r}\, a \ .$$
(4.6)

Where a, A_{tr}, ρ_{tr} are the value of velocity of sound, cross-sectional area and the density at the throat respectively. Also,

$$a = \sqrt{\gamma RT_{t_r}} \ .$$
(4.7)

By substituting Eq. (4.7) into Eq. (4.6), the mass flow rate can be written as,.

$$\overset{\bullet}{m} = \rho_{t_r}\, A_{t_r}\, \sqrt{\gamma\, RT_{t_r}} \ .$$
(4.8)

The maximum flow rate can also be expressed in terms of the reservoir conditions, ρ_{ro}, P_{ro} and T_{ro}, where

$$\rho_{t_r} = \rho_{ro}\left[\frac{2}{(\gamma + 1)}\right]^{\frac{1}{(\gamma - 1)}},$$
(4.9)

and

$$T_{t_r} = T_{ro} \left[\frac{2}{(\gamma + 1)} \right], \tag{4.10}$$

giving

$$\dot{m} = \rho_{ro} \left(\frac{2}{\gamma + 1} \right)^{\frac{1}{(\gamma - 1)}} A_{t_r} \sqrt{ \left(\frac{2 \gamma R T_{ro}}{\gamma - 1} \right) }. \tag{4.11}$$

By substituting for the density (ρ), since $\rho_{ro} = P_{ro} / RT_{ro}$, the expression for mass flow rate becomes:

$$\dot{m} = A_{t_r} \frac{p_{ro}}{\sqrt{T_{ro}}} \sqrt{ \left[\frac{\gamma}{R} \left(\frac{2}{\gamma + 1} \right)^{(\gamma + 1)/(\gamma - 1)} \right] }. \tag{4.12}$$

Introducing a blow-by coefficient (k) into Eq. (4.12),

$$k = A_{t_r} \sqrt{ \left[\frac{\gamma}{R} \left(\frac{2}{\gamma + 1} \right)^{(\gamma + 1)/(\gamma - 1)} \right] }, \tag{4.13}$$

and hence, Eq. (4.12) can be rewritten as,

$$\dot{m} = k \frac{p_{ro}}{\sqrt{T_{ro}}}. \tag{4.14}$$

From the mass flow rate data collected using Eq. (4.5) under isothermal conditions the results are then applied to Eq. (4.14).

By plotting Eq. (4.14), a best fit trendline gives a value for the slope (k) as shown in Fig 4-5.
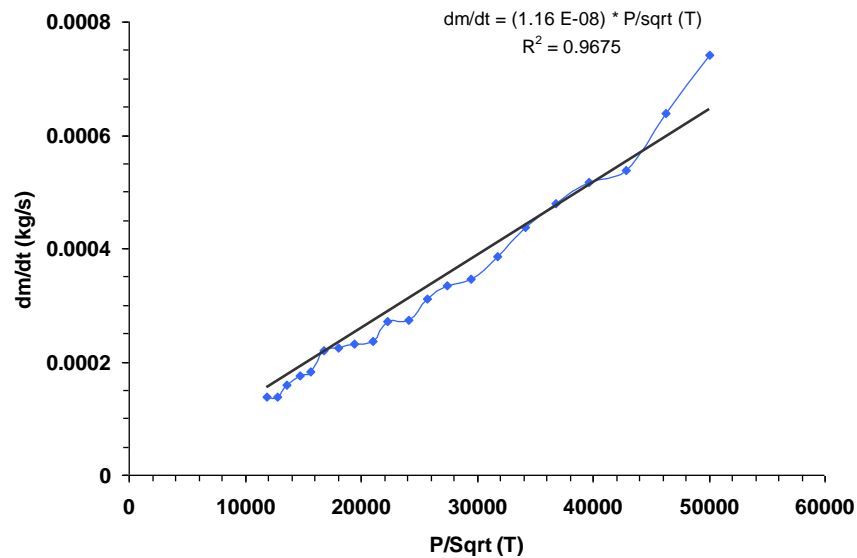
Fig 4-5. The gradient representing the blow-by coefficient k

For the second stage of the experiment, Proteus was motored at 500 *rpm*. The in-cylinder pressures and volume increments were monitored and measured as a function of crank angle. The engine was fired for several minutes between each test for hot air-intake study. This ensured the working temperature of the rig had been reached. For motored conditions, the in-cylinder and the inlet manifold pressures were obtained using piezoelectric Kistler pressure transducers 4045-A10 and 6061 respectively. The operating temperature range of the water-cooled Kistler 6061 is between 223 and 623 *K*, and has a working pressure range between 0 and 25 *MPa,* with a sensitivity shift of $\leq \pm 0.5\%$ between 323 and 623 *K*.

Since the 6061 pressure transducer operated at gauge pressure, absolute pressure levels were established in further treatment of the pressure signals.

With in-cylinder pressure signals and the volume increments taken at each crank angle, the polytropic coefficient (n_p) and the constant (*d*) using the relationships below were established (Fig 4-6). This was for a range of in-cylinder pressures (2 to 8 *MPa*).
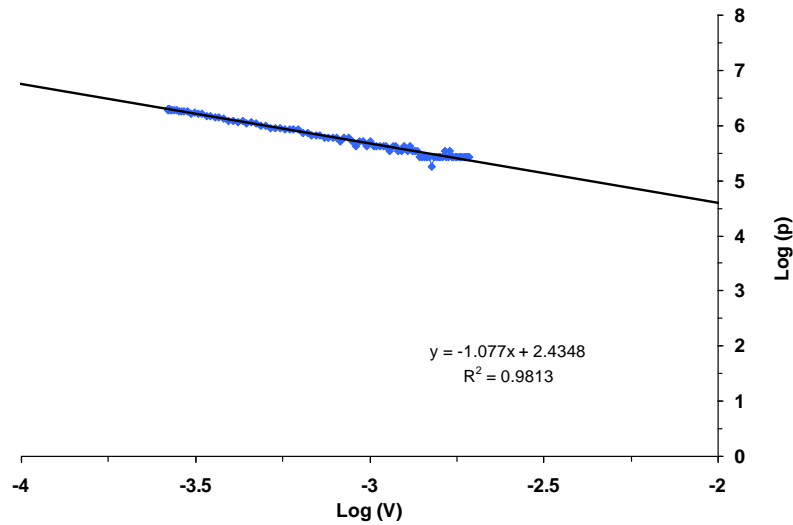
Fig 4-6. Log of pressure against log of volume; 2 MPa in-cylinder pressure (at TDC); cold air intake (295 K at BDC)

$$pV^{n_p} = d \qquad (4.15)$$

$$p = dV^{-n_p} \qquad (4.16)$$

$$\log(p) = \log(d) - n_p \log(V) \qquad (4.17)$$

$$Y = A_O + A_1 X \qquad (4.18)$$

$$d = 10^{A_O} \qquad (4.19)$$

$$n_p = -A_1 \qquad (4.20)$$

Once polytropic coefficient (n_p) and constant (d) were realised, a smoothest pressure curve data was computed. This was to eliminate possible noise from the system. Fig 4-7 shows the computed and the measured pressure curves, where the fluctuations in the measured signal has been eliminated. The test conditions and the experimental pressure data can be found in Appendix B.
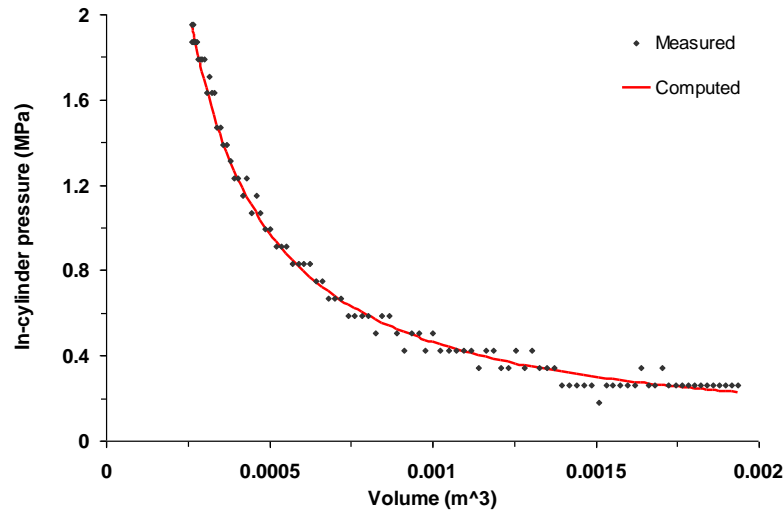
Fig 4-7. PV diagram for measured and computed pressure data; 2 MPa in-cylinder pressure; cold air intake (295 K at BDC)

With the computed pressure data, Eq. (4.3) and Eq. (4.14), together with the value for the blow-by coefficient k obtained from the first stage of the experiment, a series of mass, temperature and mass flow rate data were compiled using iterative computation (for the motored condition). Tab 4-1 shows the estimated mass lost due to blow-by.

Pressure (*MPa*)	% of mass lost (±0.01)	
	Cold intake (Circa *295° K*)	Hot intake (Circa *375° K*)
2	0.37%	0.43%
3	0.38%	0.46%
4	0.4%	0.46%
6	0.4%	0.46%
8	0.4%	0.47%

Tab 4-1. Percentage of mass lost due to blow-by at different in-cylinder pressures for Proteus rig

As can be seen from Tab 4-1, although the percentage of mass-loss due to blow-by during the compression stroke is negligible, it is greater for the hot air intake than for the cold air intake. On the other hand, from Fig 4-8, it appears that losses are greater for the cold air intake. However, Fig 4-9 shows that the initial trapped air mass in the

chamber is greater for the cold air intake than for the hot air intake, due to the differences in the density of the charge. Therefore, the inconsistency that may appear from Fig 4-8 is the result of starting level of the trapped air mass. Nevertheless, as can be seen from Tab 4-1, the percentage of mass loss due to blow-by increases with increased in-cylinder pressure levels and intake air temperature. A possible cause of increased blow-by due to air intake temperature can be attributed to the absence of an oil film of considerable thickness during the hot air intake (as opposed to cold air intake).
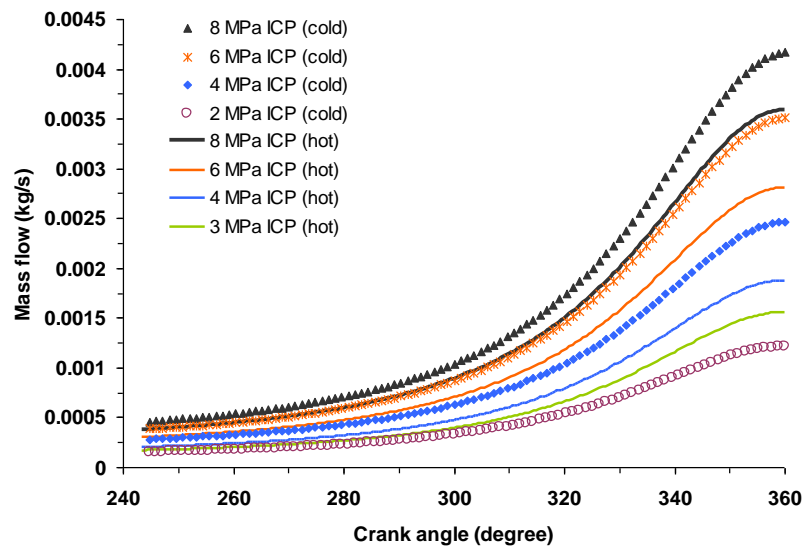
Fig 4-8. Instantaneous in-cylinder mass blow-by for hot and cold air intake, with air as the only constituent
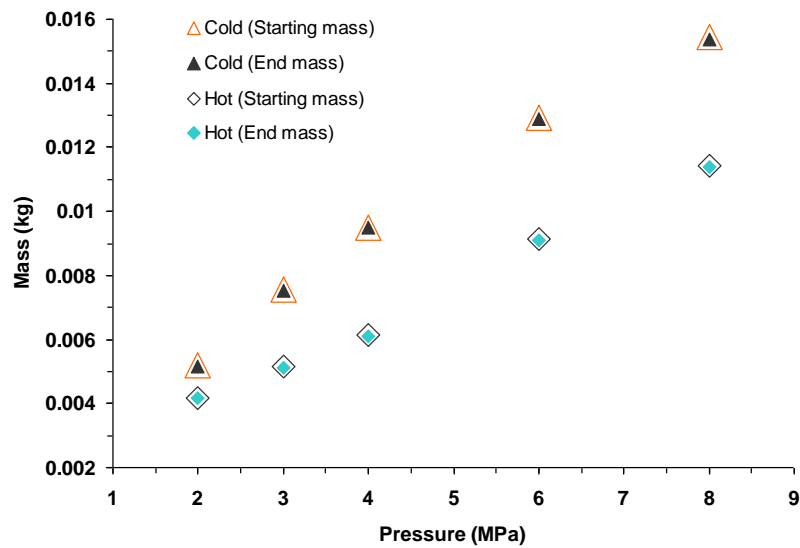
Fig 4-9. Trapped air mass at the start and the end of compression stroke

Another function of interest is the polytropic coefficient which is the characteristic indicator of any thermodynamic transformation in a closed loop system.

Fig 4-10 shows the relationship between the compression ratio and the polytropic coefficient for various in-cylinder pressures and temperatures. It can be seen (from Fig 4-10) that an increase in the boost pressure and the intake air temperature results in an increase in the polytropic coefficient. In the current study, the compression ratio is defined as the pressure ratio at *BDC* and *TDC*. It can also be expected that an increase in the water jacket temperature, and hence the in-cylinder wall temperature, would result in an increase in the polytropic coefficient due to reduction in transfer of heat. In general, the stability of the Proteus rig appears to have increased for the hot air intake (neglecting the 2 *MPa* in-cylinder pressure case). This has a direct influence on the temperature of the trapped air mass (Fig 4-11), and hence the heat transfer.
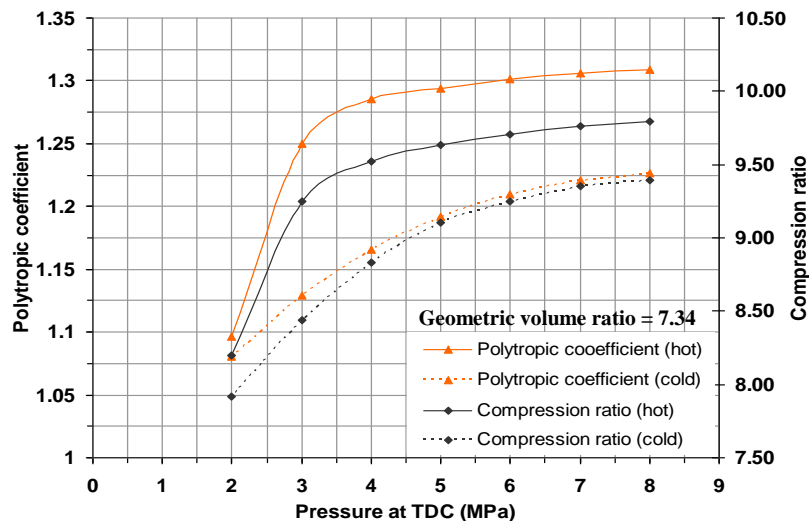
Fig 4-10. Comparison of the polytropic coefficient and the compression ratio at various in-cylinder pressures (at TDC), generated by the computed pressure data
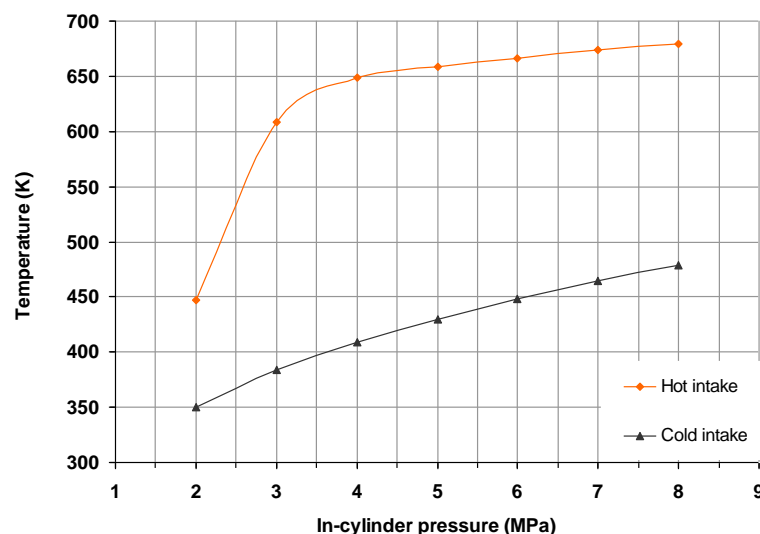
Fig 4-11. In-cylinder temperature against in-cylinder pressure (at TDC), for hot and cold air intake

4.2.3 Possible Associated Errors

Despite the information that could be obtained from the instantaneous polytropic coefficient, trapped air mass and the compression ratio, their determination could be subjected to errors. A summary of errors for motored condition is given in Tab 4-2.

Possible cause of error	Error magnitude	Assessment method
Engine speed fluctuation (motored)	*± 1 %*	*Measured*
Decreased engine speed due to increased in-cylinder pressure between 6 and 10 MPa	*< 0.5 %*	*Measured*
Effect of temperature on pressure transducer referencing level.	*≤ ± 0.5 %* *(between 323 and 623 K)*	*Pressure transducer data*

Tab 4-2. Summary of errors at motored condition

The most common experimental errors, however, are thought to occur due to calibration of the clearance volume, pegging of the intake boost pressure to the in-cylinder pressure (Brunt & Platts, 1999; Lapuerta et al., 2000 & 2003), and synchronisation of the pressure signals to the volume signals. Errors generated by wrong pressure level referencing and pressure transducer calibration are also significant. For the pressure transducer, the absolute level of the output signal may vary slightly as a function of temperature. To improve accuracy, the zero line must be adjusted with the engine near its working temperature, but not running (in case of combustion analysis).

4.3 CONCLUSIONS OF CHAPTER 4

The results presented in the current chapter underline the characteristics of the Proteus rig and the importance of quantifying the in-cylinder trapped air mass, as well as the polytropic coefficient. These results directly influence other variables, such as the in-cylinder gas temperature and density, heat transfer and, thus, the in-cylinder wall temperature calculations. The analysis of the aforementioned results has given rise to the following conclusions.

The trapped air mass after blow-by has been investigated and quantified. This was carried out with reference to a newly-introduced blow-by coefficient and the analysis of the experimental data. The blow-by coefficient k (1.16×10^{-7}) is considered approximately constant in the current experiment.

It was found in general that an increase in the intake air temperature increased blow-by slightly. This was attributed to the reduction of oil film thickness during the hot air intake (as opposed to cold air intake). For the current rig, the results have shown that trapped air-mass losses are small, and, hence, blow-by can be neglected.

For the cases considered in the current experiment, it was shown that the polytropic coefficient and the compression ratio increased as the in-cylinder pressure and temperature increased. Therefore, it can be assumed that the polytropic coefficient reduces as the heat transfer increases.

From the results obtained, it was concluded that the application of an average value for the compression ratio or the polytropic coefficient would not be appropriate. This would generate an incorrect estimation of the in-cylinder gas temperature, and, hence, the gas density for the current rig.

5. DIESEL SPRAY CHARACTERISATION, CONVENTIONAL STRATEGY

5.1 INTRODUCTION

A detailed knowledge of spray penetration and formation is widely understood to be fundamental in improving air-fuel mixing and, hence, combustion processes.

A reliable prediction of spray tip penetration and spray dispersion angle is also crucial in the design process of an internal combustion engine. It could lead to a better understanding of the parameters used to judge fuel spray performance. For example, the penetration length must be neither too long nor too short in a combustion chamber. If it is too long, impingement could occur, leading to wetting of the cylinder walls and/or piston crown. This would consequently lead to formation of soot and wastage of fuel. If the spray penetration is too short, this can result in reduction of mixing efficiency, and, hence, good combustion has been compromised.

The dependency of fuel spray formation on parameters such as the in-cylinder gas density, pressure and temperature, as well as the injection pressure has been investigated by many researchers (Crua, 2002; Hiroyasu & Arai, 1990; Kennaird et al., 2002; Karimi et al., 2006; Naber & Siebers, 1996).

Bae & Kang (2000) also investigated the influence of nozzle hole geometry on penetration rate and fuel droplet distribution within the cylinder volume. The penetration rate was found to be slightly higher for the *VCO* type nozzle than for the sac-volume type nozzle at low in-cylinder pressure conditions. Bergstrand & Denbratt (2001) have concluded the benefit of having small orifice diameter at low load conditions, particularly in terms of CO levels and soot emissions. This was attributed to more efficient fuel mixing due to smaller droplet size, thus giving rise to a shorter ignition delay.

The nozzle geometry is also known to affect the cavitation phenomenon and subsequent spray performance. An investigation by Chaves et al. (1995), Soteriou et al. (1995), Arcoumanis et al. (2000, 2001), Schmidt et al. (1999), Afzal et al. (1999), has revealed two different types of cavitation occurring within *VCO* type and sac-volume type nozzles; that is conventional hole cavitation and vortex or string type

cavitation forming inside the sac volume and inducing hole-to-hole variation even in axisymmetric nozzle hole configurations (Bae & Kang, 2000). The sudden growth and collapse of these vapour cavities is believed to cause the distortion of the flow pattern associated with the extreme pressure gradients that can damage the inside surface of the injector nozzle holes by pitting. With the flow discharge being effected as a result, the spray flow pattern could contribute to cycle-to-cycle variation. The discharge coefficient of the flow indicates the efficiency of an injector orifice, with regard to the degree of head loss sustained by the flow through the nozzle exit (Fox & Stark, 1998). With this in mind, the dependency of the fuel spray behaviour on nozzle geometry is all the more obvious.

With the popularity of increasing the nozzle hole numbers, and reducing the nozzle hole diameter in order to reduce CO levels and soot emissions (Bergstrand & Denbratt, 2001), a more in-depth understanding of the flow pattern is required.

It should be noted that, with the increase of nozzle hole numbers, the steady-state duration of the injection period is considerably reduced.

The current work describes the experiments undertaken to quantify liquid diesel fuel and vapour fuel distribution in the Proteus optical chamber. The Proteus rig is equipped with a modern diesel common rail fuel injection system as described in Chapter 3. The experiments were conducted at a realistic high pressure and temperature engine environment. In addition to the high pressure and temperature experiments, atmospheric experiments were also performed as a bench mark for the spray and injector characterisation. Two types of fuel injector (Bosch & Delphi) were used as listed in Tab 3-1.

Characteristics of diesel fuel spray such as liquid core length, penetration rate, spray dispersion angle and droplet break-up can often be assessed by direct imaging with the aid of a camera (Hattori et al., 2002, Heimgartner & Leipertz, 2000, Huh et al., 1991, Karimi, 1989, Kennaird et al., 2002). There are a number of direct imaging strategies that can be applied. High-speed visualisation is one of the adopted techniques in the current study, along with simultaneous Planer Laser Induced Fluorescence (*PLIF*) and *Mie* scattering techniques, which will be described in Chapter 6.

5.2   EXPERIMENTAL APPARATUS AND PROCEDURE

5.2.1   High-Speed Image Acquisition System and Setup

A Photron Ultima APX Fastcam high-speed camera was used in this series of experiments. The camera featured a 10-bit monochromatic Complementary Metal-Oxide Semiconductor sensor (*CMOS*) and a maximum electronic shutter exposure of 4 μs, with a recording rate adjustable from 60 to 2,000 frames per second at maximum resolution (1024 $\times$ 1024), and 4,000 to 120,000 frames per second at progressively reduced resolution. Compromise between acquisition rate and resolution was obtained with a frame rate of 20,000, 30,000, and 40,000 frames per second, with a corresponding maximum resolution of 128 $\times$ 256, 256 $\times$ 128, and 512 $\times$ 64 respectively. With frame exposure set to 4 μs for the Photron camera, over-exposure protection ensured optimum image quality for every pixel, regardless of illumination levels within the recorded images. To ensure maximum intensity of the recorded images, the gamma correction factor was set to 1.0.

A Phantom V 7.1 high-speed camera was also used in this series of experiments. The camera featured an 8-bit monochromatic *CMOS* sensor, and a maximum electronic shutter exposure of 2 μs, with a recording rate adjustable up to 4,800 frames per second at maximum resolution (800 $\times$ 600), and 4,800 to 150,000 frames per second at progressively reduced resolution. Compromise between acquisition rate and resolution was obtained with a frame rate of 34,300 frames per second, with a corresponding maximum resolution of 128 $\times$ 320. For the Phantom camera, the frame exposure was set to 2 μs. In order to maximise intensity of the recorded images, the gamma correction factor was set to 1.0. To ensure the best possible image recording, a black reference level (background grey levels reference) was performed prior to capturing and recording of the images. This black reference was set automatically by the camera at a level of 40 (out of 256 levels of grey for an 8-bit camera).

For illumination, two 125 *W* halogen flood lights fitted with a diffuser were arranged as shown in Fig 5-1.
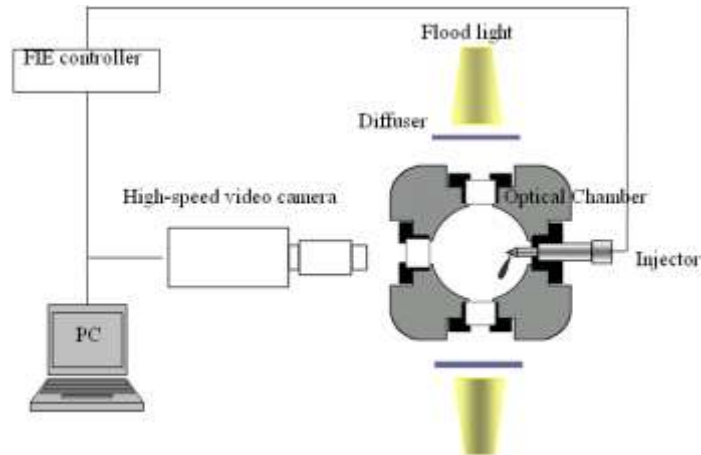
Fig 5-1. Schematic diagram of the experimental set-up for side-light spray photography

This set-up gave the best performance for a homogeneous illumination of the spray background (as oppose to backlighting).

The camera's trigger was synchronised with the transistor transistor logic (*TTL*) output signal of the *FIE* controller. The captured images were then downloaded to a computer directly connected to the high-speed cameras. The fuel line pressure and camera trigger signal, the in-cylinder pressures, the intake boost pressure, exhaust pressure and the injection current were recorded with the *AVL* Indiset system.

The processing of the video images for measurement of the spray penetration was performed by purpose-developed software (Crua 2002). Suitable pixel thresholding was carried out in order to pick out the tip of continuous spray outline, furthest from the nozzle on the spray axis (± 1 pixel) from the background. Fig 5-2 shows a typical image before and after thresholding.

The threshold level was subjectively chosen by selecting one image from the batch of images generated by a test run, and varying the threshold level to obtain optimum results. This threshold value became suitable for all images in that batch since the quality and the illumination of the spray images remained constant. Due to the inclination of the nozzle holes, the central axis of the spray trajectory was towards the camera, and not perpendicular to the focal lens (Fig 5-1). A trigonometric correction factor was implemented in order to establish the actual penetration length.
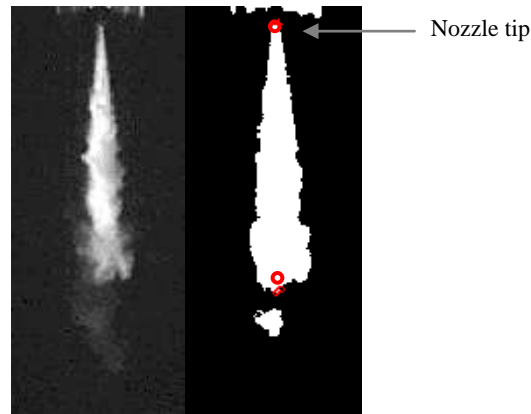
Nozzle tip

Fig 5-2. Images showing maximum tip penetration before cluster detachment; the right hand side is a binary image, and the red dots indicate the position of the nozzle tip and the unbroken liquid tip; acquired with the Phantom camera

A number of repeatability tests for all test conditions were conducted in order to assess variability in penetration. The variation in penetration was found to be $\pm 4.6\%$ for a typical set of tests at the same condition.

The resolution chosen with the Phantom camera (128×320), gave a pixel size of 0.15×0.15 mm per pixel. This gave an uncertainty value of ± 0.075 *mm*. With a variation of $\pm 10\%$ for the threshold level chosen, the change in measured penetration length was 2% (Fig 5-3).
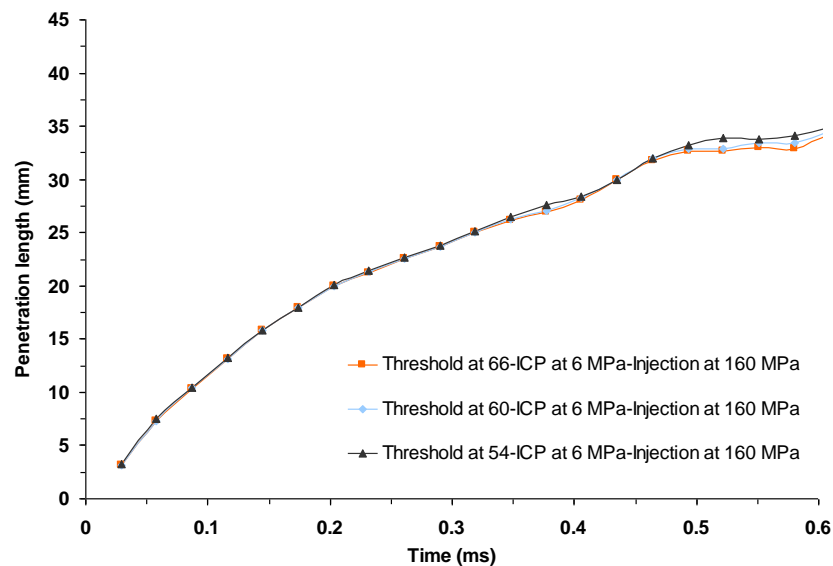
Fig 5-3. Graphical representation of threshold level at $\pm 10\%$ (chosen level of grey at 60 out of 256)

5.2.2   Laplacian Edge Detection

Edge detection technique is commonly used in order to filter out the unwanted image information, whilst preserving the important structural properties. A number of edge detection options were available within the Phantom camera's processing software.

The Laplacian edge detection was chosen in this mode of study as it gave the best results. The principles of edge detection operating automatically on features extracted from target images are described below.

Prior to applying Laplacian edge detection method, the images are blurred by a Gaussian filter. This has the tendency to smooth out the ripples (the high frequency noise) in a signal.

Fig 5-4 shows the edge represented by the jump in intensity of the original signal.

By analysing the gradient of the signal (which in one-dimension is the first derivative with respect to time), the derivative shows a maximum peak intensity located at the centre of the edge of the original signal (Fig 5-4). Thus, by comparing the gradient value to the threshold value, an edge is detected (a pixel location is said to be an edge location if the value of the gradient exceeds some threshold).
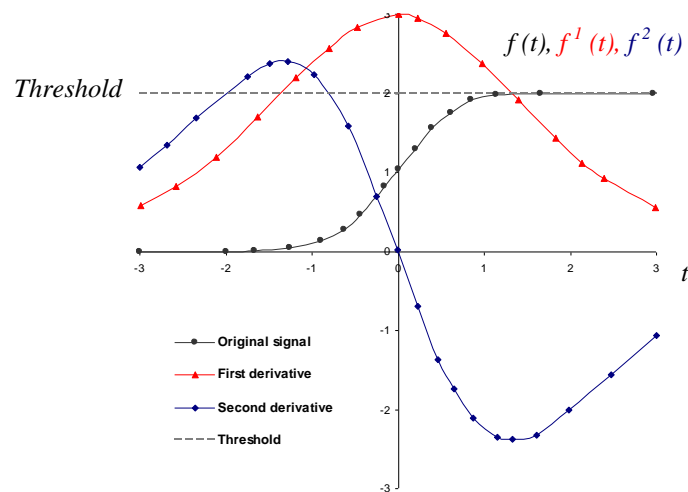
Fig 5-4. The first and the second derivative of the signal with respect to time, compared to the threshold taken from the original signal

At the same time, when the first derivative is at maximum, the second derivative is at zero (Fig 5-4). Therefore, instead of looking for the maximum in the first derivative of the image with the gradient method, the Laplacian method searches for zero crossings in the second derivative of the signal to find the edges. However, there could be many false edges (zero crossings) due to the ripples in an image (even after applying the Gaussian filter). The false edges are thus removed by adding a step to the algorithm,

and estimating the local variance of the test image. Hence, if the variance is low when compared with the threshold, then the ripples have caused the zero crossings, and if it exceeds the threshold, an edge is declared. A comprehensive description of the Laplacian edge detection can be found from Drexel University information website.

5.3   EXPERIMENTAL RESULTS

5.3.1   Hole-to-Hole Variations

Experimental studies of hole-to-hole variation were performed with the set-up described in section 5.2.1.

Tab 5-1 shows the characteristics of the injectors and nozzles used in the current study for spray characterisation. With injection pressures of 60, 100, 140, and 160 *MPa*, the in-cylinder pressure varied from 2, 4, and 6 *MPa*.

Make	Type	Nozzle hole diameter (*mm*)	Length / diameter L/D_n	Nº of holes	Fuelling mm^3	Spray characterisation	Injection pressure (*MPa*)
Bosch	*VCO single guided*	*0.2*	*5*	*1, 3, and 5*	*30 and 50*	*Single, 3 and 5-hole nozzle*	*60, 100, 140, 160*
Bosch	*VCO double guided*	*0.2*	*5*	*1*	*30 and 50*		*60, 100, 140, 160*
Delphi	*VCO*	*Measured at 0.135*	*Measured at 8*	*7*	*20*	*7-hole nozzle*	*60, 100, 140, 160*

Tab 5-1. Characteristics of the test nozzles, and the test matrix for a single injection strategy in the current chapter

Fig 5-5 shows images taken for a 3-hole Bosch injector nozzle, and indicates the existence of hole-to-hole variation, as well as variations during three different cycles. This phenomenon can be observed by the difference in the penetration lengths and the spray cone angles, as Bae & Kang (2000) observed from their experiments.

From the same images, it appears that during the third cycle little difference in the spray cone angle between each individual nozzle hole exists, whilst the penetration length is slightly longer with hole No 3. This irregularity suggests a transverse movement of the injector needle, and a variation in the magnitude of the needle oscillation.

| Cycle 1 | Cycle 2 | Cycle 3 |
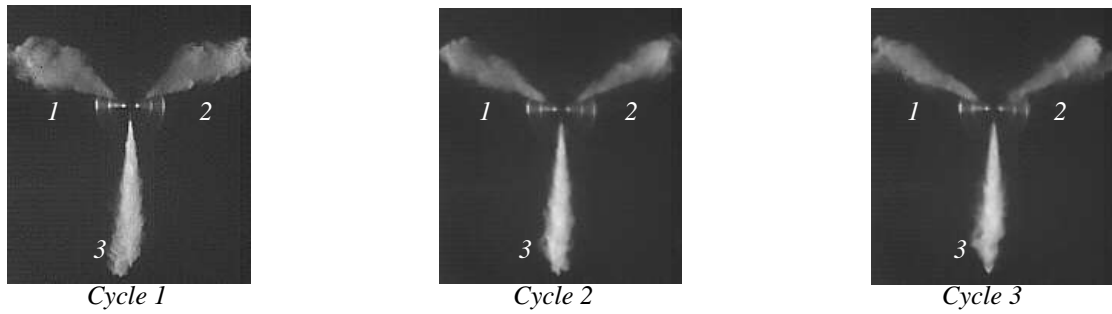
Fig 5-5. Hole-to-hole and cycle-to-cycle variation from a 3-hole VCO single guided nozzle; 20 kg m^{-3} in-cylinder density; 2 MPa in-cylinder pressure; cold air intake (350 K at TDC); 60 MPa injection pressure; 50 mm^3 fuelling; the images are captured 0.17 ms after first sight of fuel, acquired with the Phantom camera

For the 5-hole Bosch injector nozzle shown in Fig 5-6, the hole-to-hole variation in spray penetration and particularly the spray cone angle was also evident during the initial (a), and the end of injection stage (b). This phenomenon occurred regardless of the injection or the in-cylinder pressure.

Although needle oscillation is attributed to the needle stability, it is the pressure distribution round the needle that causes the needle transverse movement.

0.10 ms after SOI   *1.17 ms after SOI*

(a)   (b)
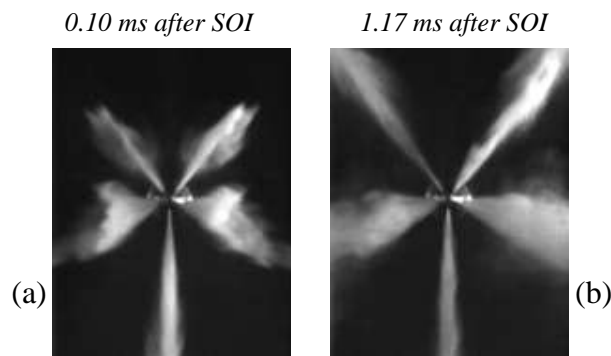
Fig 5-6. Hole-to-hole variation from a 5-hole Bosch single guided VCO nozzle, with an injection pressure of 140 MPa, injecting into atmospheric conditions at 50 mm^3 fuelling; acquired with the APX camera

Considering imperfection or under-sizing of one of the nozzle holes (for a multi-hole nozzle), the pressure distribution round the needle can become unbalanced on vertical movement of the nozzle needle. The peak pressure will then occur on the side that the imperfect or under-size nozzle hole is situated (Fig 5-7). This will move the needle transversely towards the opposite side, temporarily blocking the opposing nozzle holes, whilst allowing the fuel to escape through the imperfect or the smaller size nozzle hole with relative ease initially.
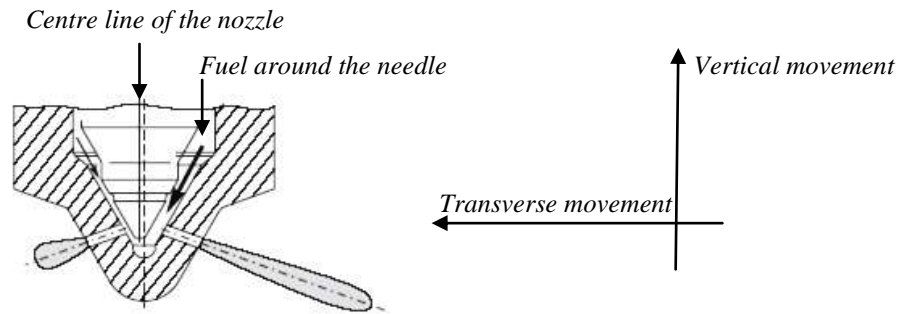
Fig 5-7. Transverse movement of the needle caused by differences in the pressure distribution for a multi-hole VCO nozzle (modified from Bae et al., 2002)

With the vertical movement of the needle at a later stage, the pressure distribution becomes more stable. Once the needle uncovers all the holes, the penetration and the spray cone angle of each nozzle hole become more uniform compared with the initial stage of injection (Fig 5-8, and Fig 5-6).
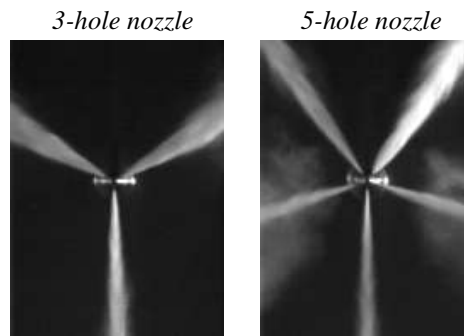
Fig 5-8. A 3 and a 5-hole nozzle, with an injection pressure of 60 MPa; 50 mm³ fuelling; acquired with the APX camera

With the increase of nozzle hole numbers, the pressure distribution around the needle becomes more balanced, even though the vertical and transversal oscillations of the needle could still persist. The stability of pressure distribution round the needle, and, hence, reduced hole-to-hole variation was more evident for the 7-hole Delphi injector as shown in Fig 5-9.
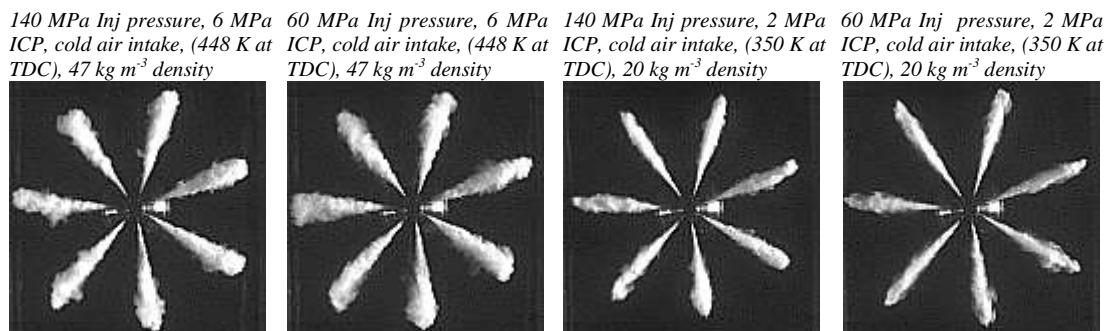
Fig 5-9. Comparison of the hole-to-hole variation for the Delphi injector; the images are captured at 0.131 ms after first sight of fuel; acquired with the Phantom camera

5.3.2 Injection Delay, Hesitation and Fuel Dribble

Fig 5-10 shows a variation of time delay between the injection signal and the first sight of fuel for the single-hole, the 3-hole, and the 5-hole Bosch single guided *VCO* nozzles. The time delay was recorded with the setup described in section 5.2.1.

The magnitude of the delay was found to be dependent on the injection pressures for the Bosch injector (Abdelghaffar et al., 2006). For the 7-hole Delphi injector, no such dependency was observed. Both types of fuel injector showed no dependency on the in-cylinder pressure (Fig 5-11). It is, therefore, acceptable to neglect the influence of in-cylinder pressure (for the range of pressures examined in the current experiment) when considering the injection delay.
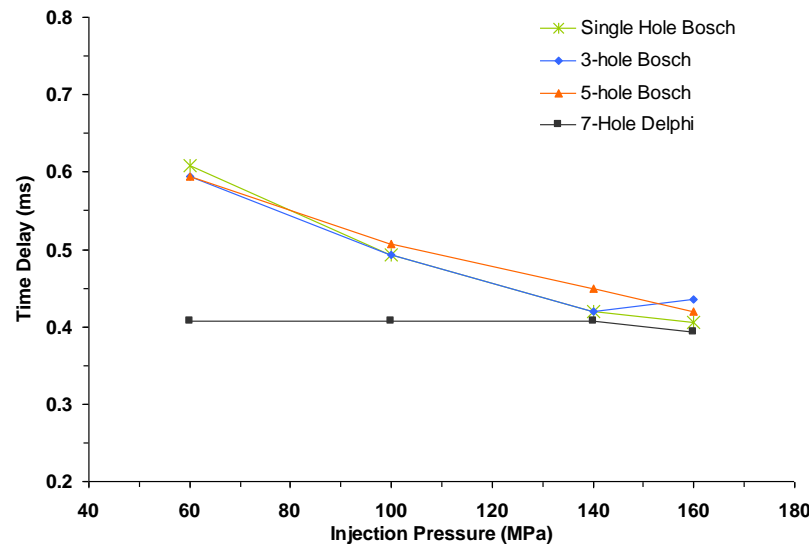
Fig 5-10. Graphical representation of the injection time delay versus injection pressure; 47 kg m^{-3} in-cylinder density; 6 MPa in-cylinder pressure at TDC

As can be seen from Figs 5-10 and 5-11, the Delphi injector exhibits little or no change in injection delay, regardless of the in-cylinder or the injection pressure. This would suggest that different types of injectors have different response times and a varied level of dependency on the injection pressure that causes the time delay.
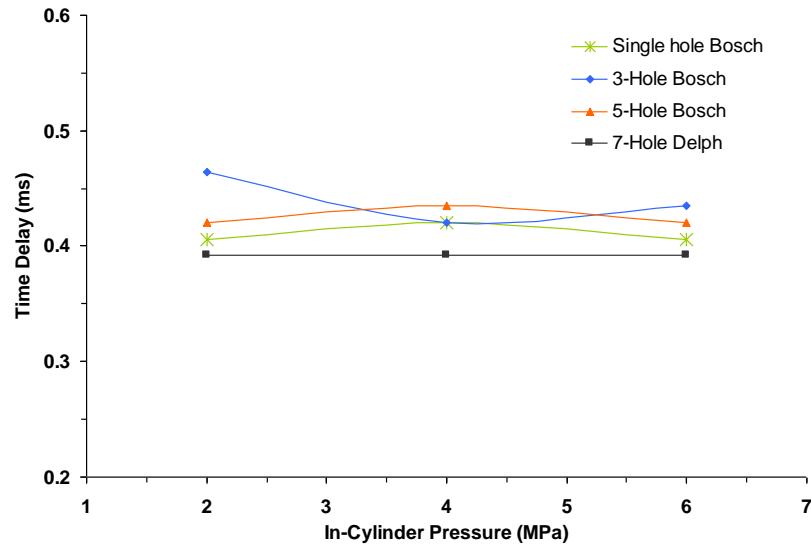
Fig 5-11. Time delay versus in-cylinder pressures; 160 MPa injection pressure

For assessing the injector hesitation, reference is made to Fig 5-12 and the rate of injection profile shown in Fig 5-13. At circa 0.15 *ms* after the first visibility of the liquid spray from the single guided *VCO* single-hole nozzle, the flow seems to be interrupted. This interruption appears to be caused by the injector needle closure long before the end of injection duration. At circa 0.075 *ms* after the initial interruption (0.225 *ms*), the flow through the nozzle continues without any further delay. This behaviour was also observed with the double-guided *VCO* single-hole nozzle to a lesser extent. The hesitation behaviour for the single-hole nozzle is attributed to the transverse movement of the needle. With the multi-hole nozzles tested, no hesitation was observed (Fig 5-12).
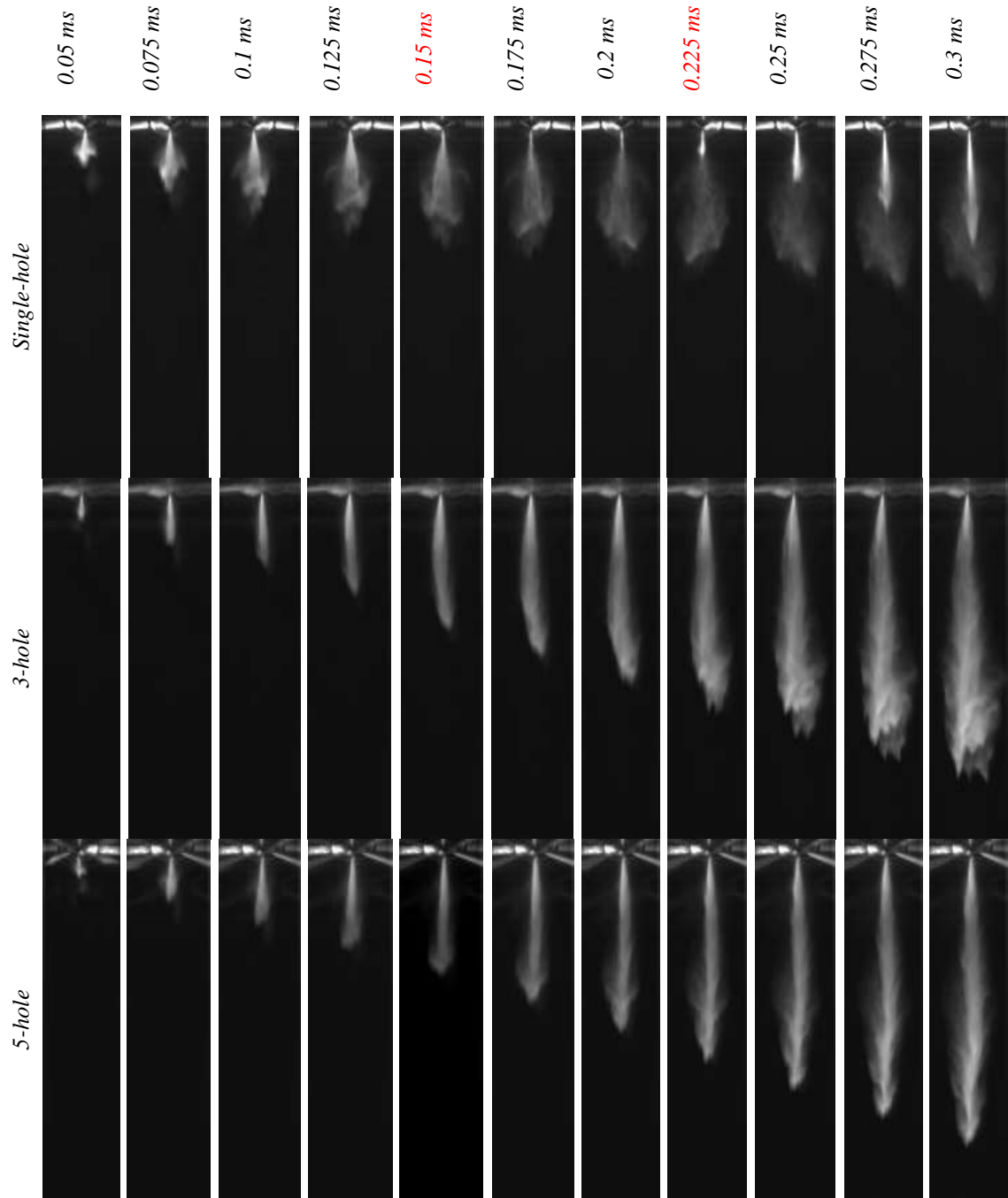
Fig 5-12. Comparison between single-hole, 3-hole, and 5-hole single guided VCO 0.2 mm nozzle; injection pressure 140 MPa; fuelling 30 mm³; times are in milliseconds after first sight of fuel; acquired with the APX camera
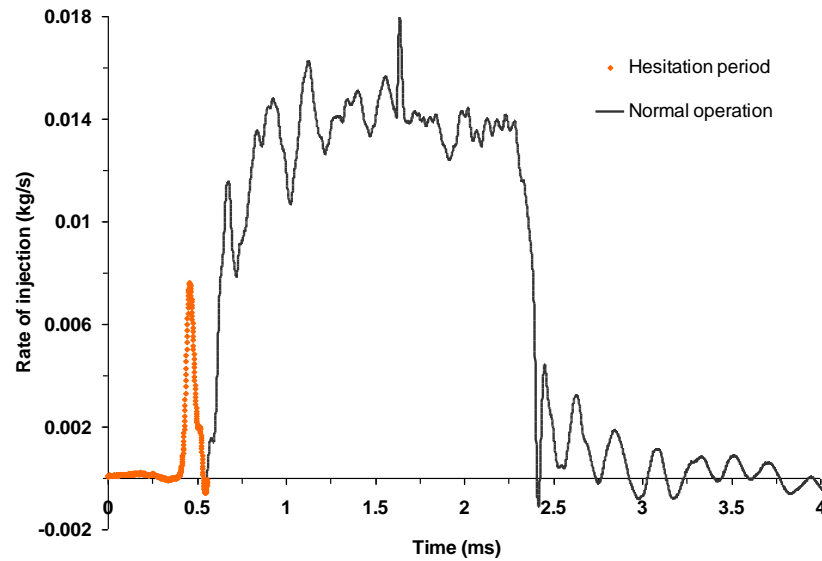
Fig 5-13. Rate of injection profile showing the hesitation period for the single-hole Bosch injector, VCO single guided nozzle; 160 MPa injection pressure, 30mm^3 fuelling

As explained in section 3.2.4, at the end of injection period under the influence of the spring compression force, an undesirable fuel quantity is injected. The quantity of fuel delivered during this period is governed by the stability and the pressure distribution around the needle. For the single-hole nozzle tested in the current experiment, needle oscillation at the end of injection appears more significant than for the multi-hole nozzles (5-13). For the single and double guided single-hole *VCO* nozzles, the undesirable fuel delivery at the end of injection duration was observed as ligaments and spherical droplets, apparently the same size as the nozzle hole orifice (Fig 5-14). Slight improvement with the double guided nozzle was observed, as shown in Fig 5-14. This phenomenon occurred for the range of injection pressures in the current experiment.
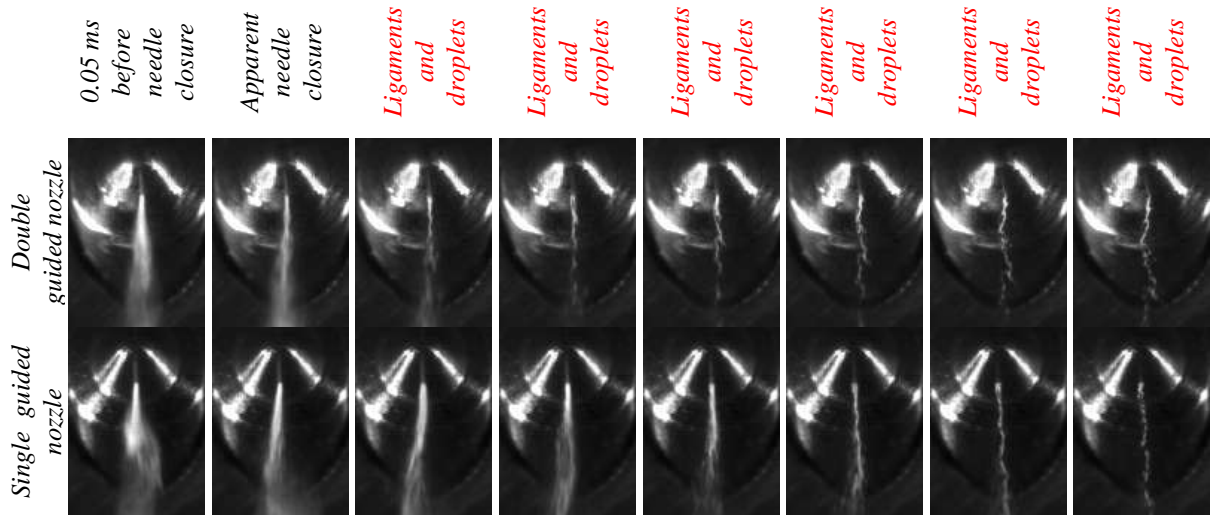
Fig 5-14. Comparison between a single and a double guided VCO single-hole Bosch nozzle; injection pressure 140 MPa; acquired with the APX camera

For the 3-hole nozzle tested as shown in Fig 5-15, undesirable fuel quantity was also evident at the end of injection duration. This phenomenon is also confirmed with the rate of injection profiles shown in Chapter 3 and Fig 5-16.
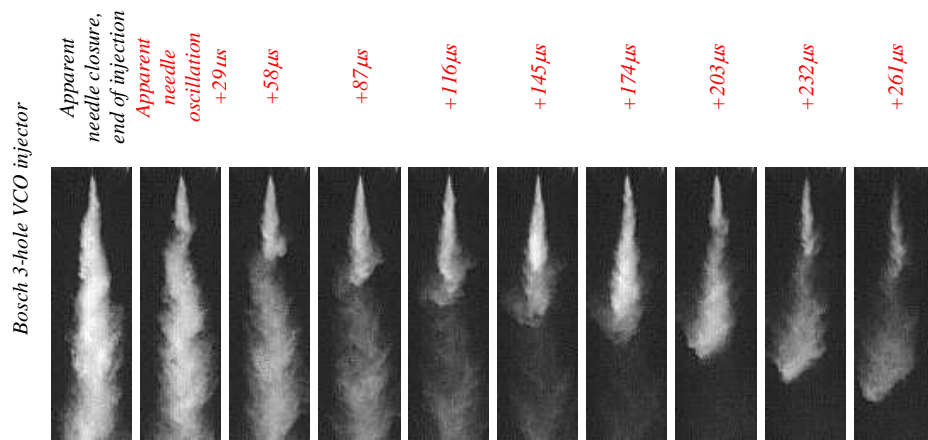
Fig 5-15. Undesirable fuel delivery at the end of injection duration; 140 MPa injection pressure; 20 kg/m³ in-cylinder density; 2 MPa in-cylinder pressure; cold air intake (corresponding to 350 K at TDC); 30 mm³ fuelling; 3-hole single guided VCO Bosch injector
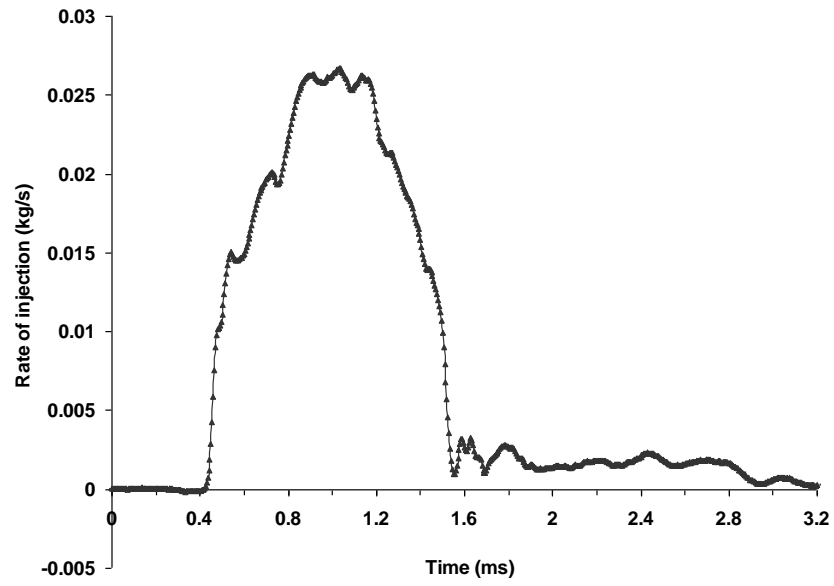
Fig 5-16. Rate of injection profile for the 3-hole Bosch injector, VCO single guided nozzle; 140 MPa injection pressure; 30 mm³ fuelling

5.3.3 The Spray Structure

The structure of diesel fuel spray has been observed with the set-up described in section 5.2.1 (high-speed Phantom video camera). Tests were carried out for three different *ICP* at *TDC* (2, 4, and 6 *MPa*), four different injection pressures (60, 100, 140, and 160 *MPa)*, two air intake temperatures (293 and 373 *K*, cold and hot intakes) and two fuelling rates (30 and 50 mm^3 per stroke).

The experiments were conducted for both types of injector described in Tab 5-1, with the exception of the single-hole double-guided Bosch *VCO* nozzle (for the penetration and spray cone angle experiments). Each test was repeated a number of times in order to ascertain repeatability for liquid spray penetration and the spray cone angle.

The aim of the current study was to examine the tip of unbroken portion of the spray outline furthest from the nozzle exit.

On the basis of the data obtained (Fig 5-17), there exists a highly dense portion where the spatial distribution of the liquid fuel is uniform relatively close to the nozzle exit. Further downstream of the nozzle, the high density portion begins to break up and the surface-wave appears to takes place on the outer edge of the spray structure (Fig 5-17). This appeared as a repeatable fish-bone shaped structure on the spray image, and was evident for all the nozzles tested (Fig 5-18). For the low in-cylinder pressure and temperature environment, this was more evident, due to reduced absorption of light through the dense air.

Fish-bone structures due to surface-wave have been reported by a number of authors (Tsue et al., 1992; Koo & Martin, 1990; Yule & Salters, 1995). These surface waves are repeatable, and with an increase of the axial distance from the nozzle exit, the neighbouring stripes (fish-bones) increased with an increase in the downstream distance.
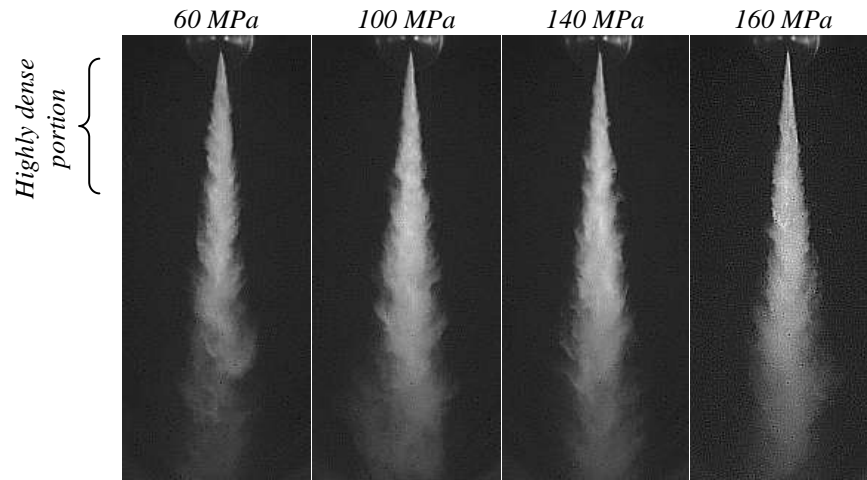
Fig 5-17. Fish-bone shaped structure of the Diesel spray from a 3-hole VCO single guided Bosch nozzle; 20 kg m^{-3} in-cylinder density; 2 MPa in-cylinder pressure (at TDC); cold air intake (350 K at TDC); images acquired with the Phantom camera

An exact array of the images shown in Fig 5-17 is processed using the Laplacian edge detection option of the Phantom camera, as described in Section 5.2.2 (Fig 5-18). As can be seen from Fig 5-18, the stripes are clearly highlighted. The images show that, close to the nozzle exit, the stripes are closely packed. With the increase of the axial distance downstream of the nozzle exit, the distance between stripes also increases.

Close examination of the images has revealed the injection pressure or the *ICP* has little effect on the distance between the stripes or the existence of what appears as initial liquid core. Furthermore, inspection of image from frame-to-frame (as well as cycle-to-cycle) has revealed the randomness in distance between two strips, for any combination of injection with the in-cylinder pressure in the current experiment.
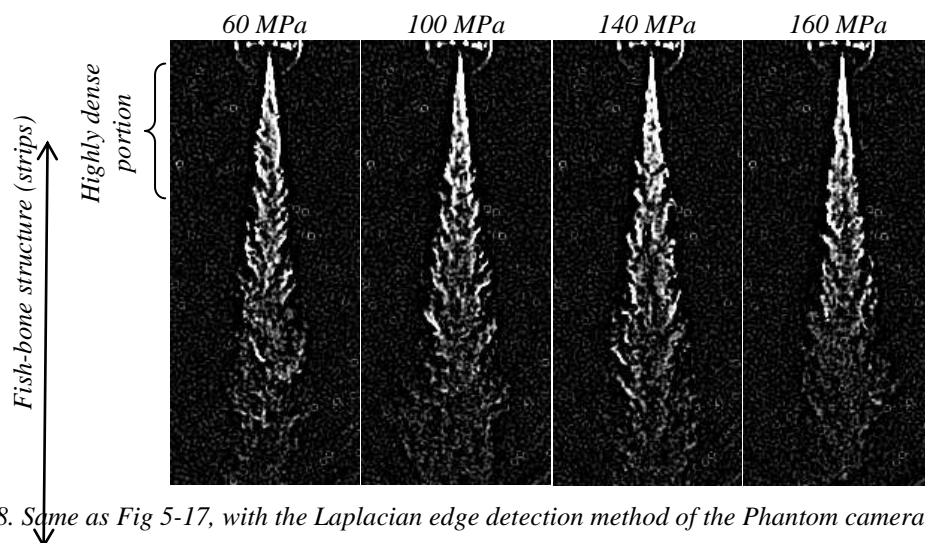
Fig 5-18. Same as Fig 5-17, with the Laplacian edge detection method of the Phantom camera applied

Chaves et al. (2000) conducted an experiment investigating possible patterns in perturbation of the spray jet (such as Fig 5-18). This was achieved with the aid of a purpose-developed experimental rig to vary independently the exit flow velocity, the frequency and the amplitude of the velocity modulations. With the modulation frequency driven via a sine wave generator, the author observed the disintegration of harmonically-excited liquid jet. This could be recognised in the current study as the result of resonance effect on the liquid fuel (within the nozzle), when excited by a number of sinusoidal components at various frequencies, each having a certain amplitude and phase (such as high and low pressure fuel pumps, fuel pressure regulator and the injector solenoid).

Fig 5-19 and Fig 5-20 show a series of images taken at 0.41 *ms* after first sight of fuel. As expected, an increase in penetration length resulted from an increase in injection pressure, as well as a decrease in the in-cylinder pressure. This observation is consistent with previous studies by Arai et al. (1984), Hiroyasu (2000), Kennaird et al. (2002), Naber & Siebers (1996), and Reitz & Diwakar (1987).
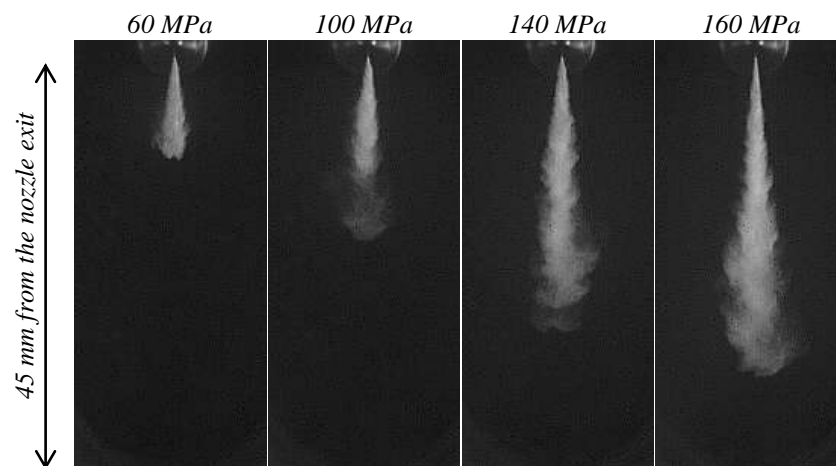
Fig 5-19. Spray images taken at 0.41 ms after first sight of fuel; 20 kg m^{-3} in-cylinder density; 2 MPa in-cylinder pressure (at TDC); temperature 350 K (at TDC); 30 mm^3 fuelling; images acquired with the Phantom camera; using a 3-hole Bosch injector nozzle
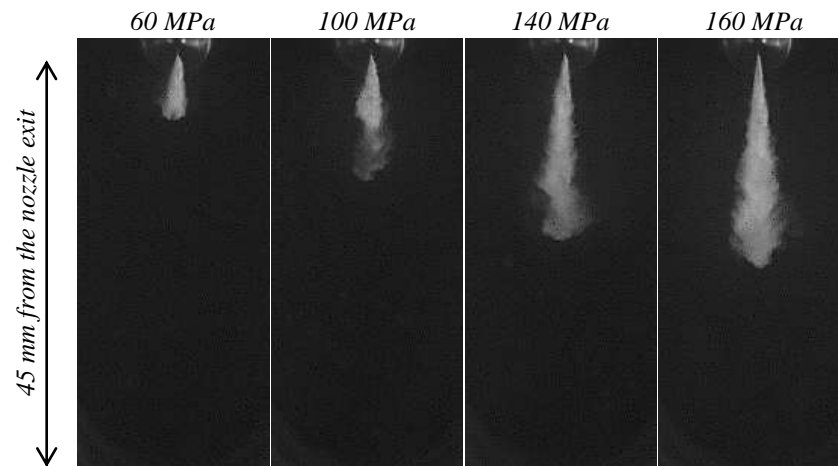
Fig 5-20. Spray images taken at 0.41 ms after first sight of fuel; 47 kg m^{-3} in-cylinder density; 6 MPa in-cylinder pressure; temperature 448 K (at TDC); 30 mm^3 fuelling; images acquired with the Phantom camera; using a 3-hole Bosch injector nozzle

As can be seen from the above images, the interaction between the stagnant gas field and the leading edge of the spray during the initial stage of injection has the effect of compressing clusters of droplets together as the spray jet penetrates. Further downstream of the nozzle exit, the exchange of momentum between the droplets and the local gas field induces dense air along the edges of the spray periphery. The resultant effect is small clusters of droplets stripping back or detaching from the bulk of the spray. At the leading edge (the tip of the spray), however, when the spray is fully developed, larger clusters of droplets are starting to detach as the air entrainment increases, whilst the momentum of droplets decreases (Fig 5-21).

The level of stripping and detachment of droplets was observed to be dependent on the magnitude of the injection and the in-cylinder pressures. This was attributed to increased liquid surface area at higher injection pressures (smaller droplets), and increased gas viscosity due to increased gas density at high in-cylinder pressures. For elevated in-cylinder pressures, this can also be viewed as the result of higher tangential stresses acting on the moving spray which leads to stripping and detachment of clusters of droplets as well as individual (larger) droplets breaking up.
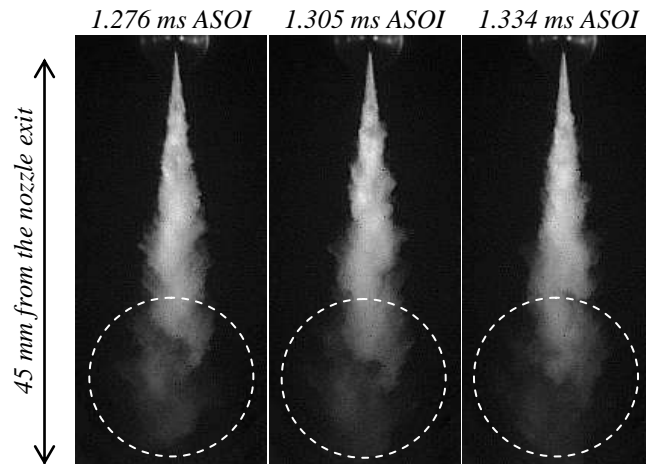
Fig 5-21. High-speed video sequence in steps of 29 μs showing clusters of droplet starting to detach along the leading edge of the spray; 160 MPa injection pressure; 20 kg/m^3 in-cylinder density; 2 MPa in-cylinder pressure; cold air intake (350 K at TDC); acquired with the Phantom camera; using a 3-hole Bosch injector nozzle

5.3.4   The Effect of Multi-Hole Nozzle

Fig 5-22 graphically represents the liquid spray penetration for a 7-hole Delphi injector, and a 5-hole, a 3-hole and a single-hole, single-guided *VCO* Bosch injector nozzle (additional profiles can be found in Appendix C). The data for the multi-hole nozzles have been offset by 0.17 *ms*, in order to allow a direct comparison with the single-hole injector. This is the result of the initial hesitation described (in section 5.3.2) for the single-hole nozzle.

For the Bosch injectors tested in this study, the number of holes within a nozzle was found to have a slight effect on the rate of penetration for a given mass of injected fuel (Fig 5-22 and 5-23). This effect was attributed to the drop in rail pressure across the nozzle holes, once the injector needle had reached full lift.

For the 7-hole Delphi injector as shown in Fig 5-22, the penetration length is significantly reduced when compared to the single-hole, 3-hole and 5-hole Bosch injector nozzles. This was attributed to smaller nozzle hole diameter reducing drop sizes, and, hence, increased rate of atomisation and air entrainment.

It is therefore considered inappropriate to directly compare the two sets of data for the Bosch and the Delphi injector, due to the difference in nozzle hole geometry and injected mass (Tab 5-1). However, the overall trends in the spray penetration length

and the dispersion angle should be common for both types of injector (additional spray penetration profiles for the Delphi injector are presented in Appendix C).
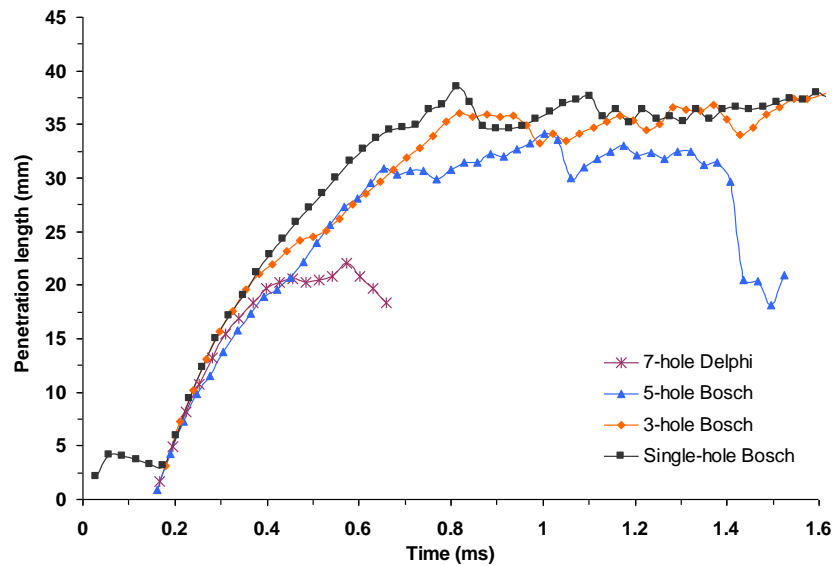
Fig 5-22. Spray penetration from a 0.2 mm VCO single guided Bosch nozzle, and a 7-hole Delphi nozzle; 160 MPa injection pressure; 47 kg/m^3 in-cylinder density; 6 MPa in-cylinder pressure; cold air intake (448 K at TDC); 50 mm^3 fuelling

Fig 5-23 shows the rail pressure drop recorded by an *AVL* Indiset high-speed data acquisition system for the cases presented in Fig 5-22. As can be seen, the drop in rail pressure is clearly more dominant for the 5-hole and the 3-hole nozzle than for the single-hole nozzle. This indicates that an increase in the number of nozzle holes (for a given orifice size) could lead to a decrease in the rail pressure. Subsequently, this tendency could reduce the penetration rate.

Fig 5-23 shows the rail pressure at 60 *MPa* and the 160 *MPa*. It can be seen that the magnitude of drop in rail pressure is dependent on the injection pressure and on the number of holes within the nozzle. It can also be expected that the nozzle hole size has the same influence, with larger holes causing more pressure drop.
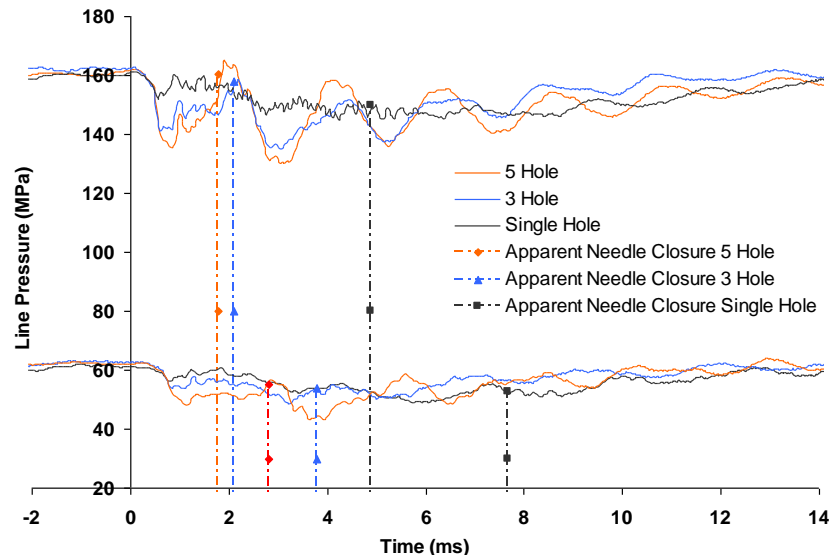
Fig 5-23. Rail pressure traces recorded by an AVL Indiset high speed data acquisition system at 60 and 160 MPa injection pressure; 47 kg m^{-3} in-cylinder density; 6 MPa in-cylinder pressure; 50 mm^3 fuelling; broken lines indicate apparent needle closure

5.3.5 The Effect of Injection Pressure

As expected, the fuel rail pressure was found to have a significant effect on the rate of penetration. Fig 5-24 shows the influence of higher injection pressures producing more developed sprays within shorter injection durations (additional profiles can be found in Appendix C). In addition, higher injection pressure has the tendency to improve the vaporisation processes, since the surface area of the liquid spray has increased, due to smaller droplet sizes (Lacoste, 2004).

Shortly after the fuel spray has fully developed, the liquid penetration profiles fluctuate around a slowly increasing average. These fluctuations are thought to be the result of air entrainment breaking away clusters of droplets around the periphery of the spray, with the maximum effect on the leading edge of the spray tip (Fig 5-21).

Studies by Browne et al. (1986), Hiroyasu et al. (1989), Hiroyasu & Arai (1990), Shimizu et al. (1984) have also shown similar trends for the spray profile. However, due to the differences in the experimental set-up, a comprehensive comparison with the current study is inconclusive.
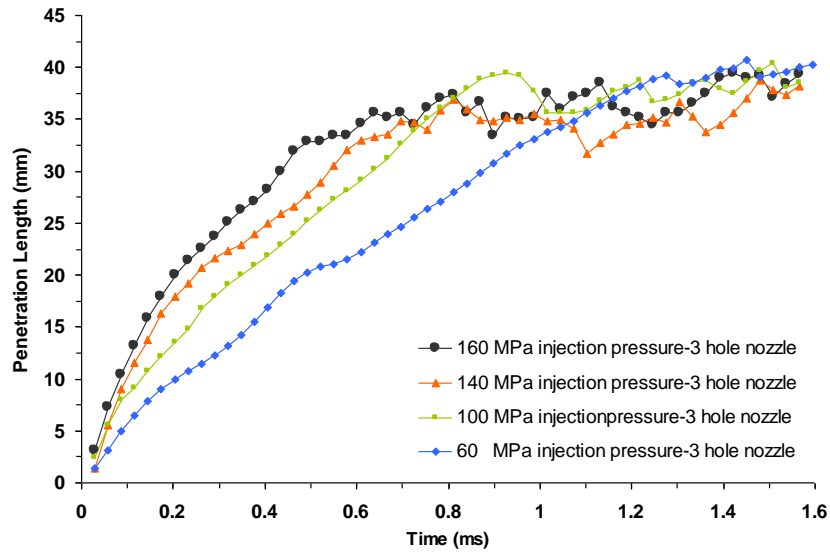
Fig 5-24. The effect of injection pressure on spray penetration for a 3-hole single guided VCO nozzle; 47 kg m^{-3} in-cylinder density; 6 MPa in-cylinder pressure; 50 mm^3 fuelling; cold air intake (448 K at TDC)

Cluster shedding was observed for all the test conditions using the nozzle configurations shown in Tab 5-1. For the same injection pressure, the location of cluster shedding is observed to be almost the same distance downstream of the nozzle exit for the nozzles under consideration (Fig 5-25). When comparing the spray penetration from the single-hole nozzle with that of the 5-hole nozzle, it can be seen that the spray from a single-hole penetrates at a slightly higher velocity (Fig 5-22). The same tendency can be observed when comparing the spray from the 3-hole nozzle and the 5-hole nozzle as shown in Fig 5-25. This can be attributed to the previously described dependency of rail pressure drop on the number of nozzle holes.
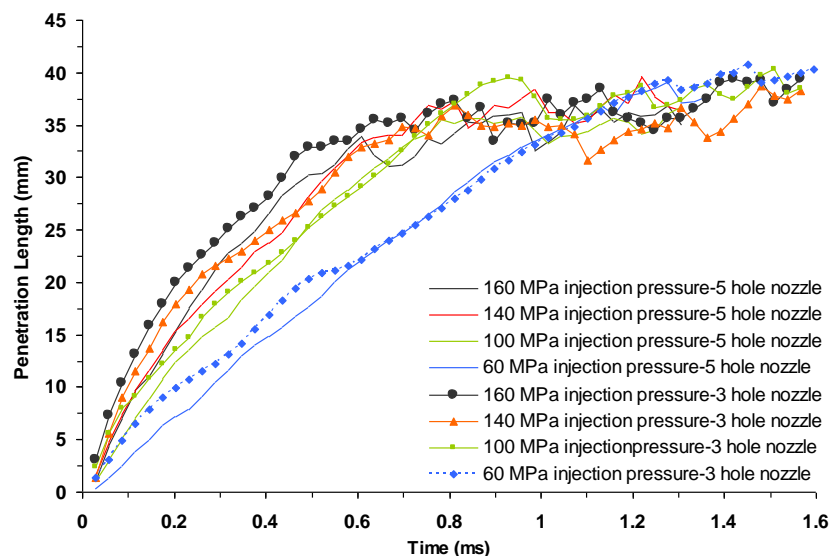
Fig 5-25. The effect of injection pressure on spray penetration for a 3 and a 5-hole single guided VCO nozzle; 47 kg m^{-3} in-cylinder density; 6 MPa in-cylinder pressure; cold air intake (448 K at TDC)

Fig 5-26 shows the (full) spray cone angle at different injection pressures into an ambient in-cylinder gas density of 47 *kg m^-3*. The definition of the dispersion cone angle in the current study is taken as the angle formed by the outer boundary of the spray to half the location of the penetration length (Naber & Siebers, 1996).

After an initial and final wide spray cone, the dispersion angle progressively reduces to a stable value at circa 20 °. For 60 *MPa* injection pressure, however, the initial progressive reduction upto the first 1 *ms* after first sight of fuel gives a wider spray cone dispersion angle than at higher injection pressures. This could be attributed to the initial low penetration velocity at 60 *MPa* injection pressure into a highly dense environment. Similar studies by Crua (2002) using the same type of injector has shown a full dispersion cone angle of 11 °, with no particular difference for the 60 *MPa* injection pressure. The differences between the current result and that obtained by Crua (2002) are attributed to the experimental set-up, in particular the level of lighting and luminosity of the spray. Nevertheless, the overall trend and conclusions are in agreement with Crua (2002), with no obvious connection between the injection pressure and the spray full cone angle being observed.
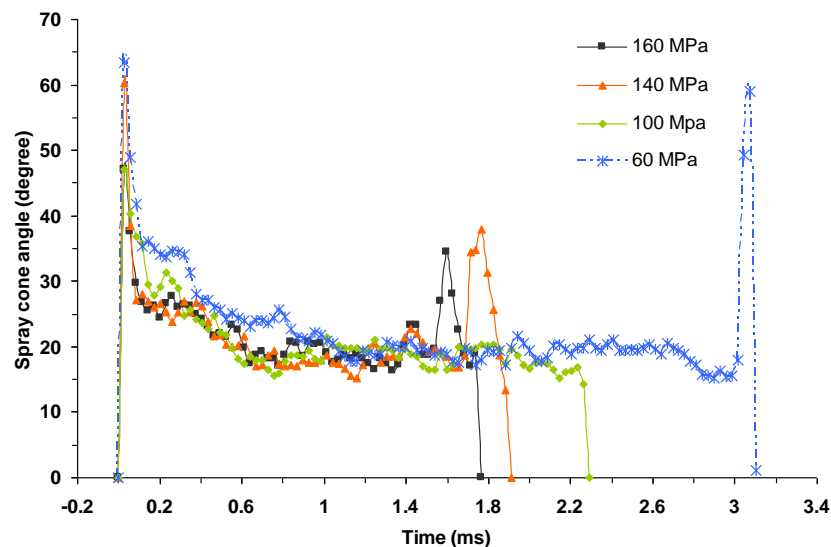
Fig 5-26. Evolution of the spray full cone angle at different injection pressures for a 3-hole single guided VCO nozzle; 47 kg m^-3 in-cylinder density; 6 MPa in-cylinder pressure; 50 mm^3 fuelling; cold air intake (448 K at TDC)

5.3.6   The Effect of In-Cylinder Gas Pressure at Cold Air Intake

Neglecting evaporation for cold air intake (350 *K* at 2 *MPa*, 410 *K* at 4 *MPa*, and 448 *K* at 6 *MPa*), a decrease in the spray penetration rate was observed as the ambient gas pressure was increased. The rate of spray penetration appeared to follow two diverse

phases; an almost linear phase lasting between 0.6 *ms* and 1.2 *ms* after first sight of fuel, particularly at low in-cylinder gas density and low injection pressure, and a rapid transition to a steadier penetration length fluctuating around a slowly increasing average (cluster shedding). Fig 5-27 and Fig 5-28 show the influence of in-cylinder gas density for two injection pressures. The same trend was observed for the complete range of injection pressures in the current study (additional profiles can be found in Appendix C). The penetration rate was observed to be directly dependent on the ambient gas density as well as the injection pressure. The same dependency has been observed by many authors (Crua, 2002; Hiroyasu & Arai, 1990; Huh et al., 1998; Kennaird et al., 2002; Naber & Siebers, 1996; Yule & Filipovic, 1991).
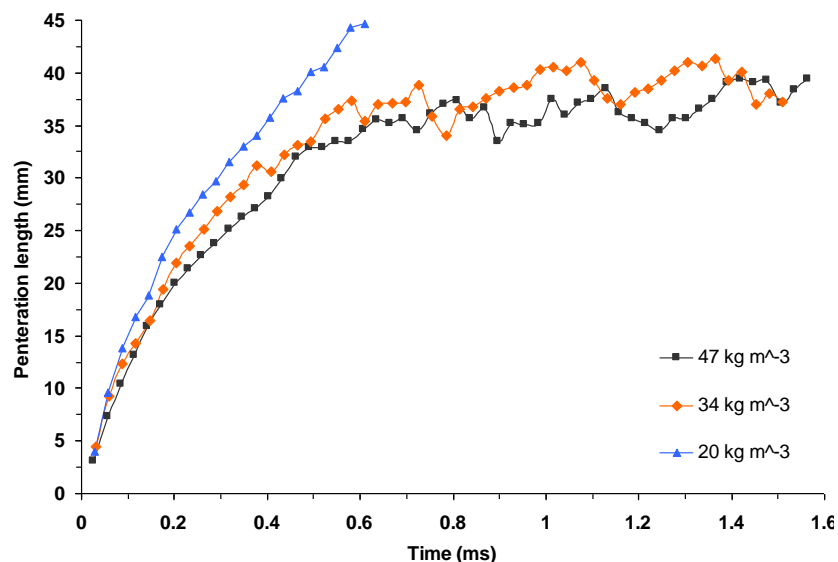
Fig 5-27. The effect of ambient gas density on liquid spray penetration for cold air intake; 160 MPa injection pressure; 3-hole single guided VCO nozzle; 50 mm³ fuelling
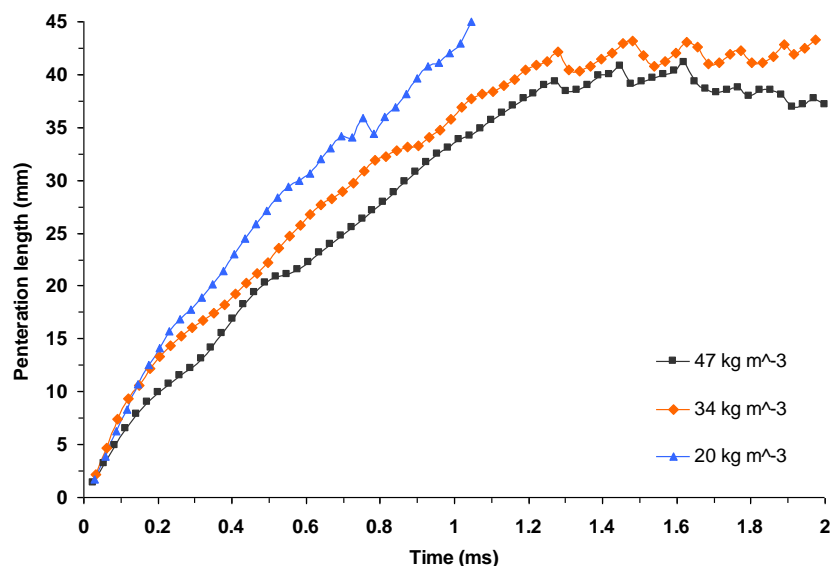
Fig 5-28. The effect of ambient gas density on liquid spray penetration for cold air intake; 60 MPa injection pressure; 3-hole single guided VCO nozzle; 50 mm³ fuelling

The effect of gas density on the evolution of the spray full cone angle is shown in Fig 5-29. After the initial wide spray cone angle as observed in the previous section, the spray dispersion progressively reduced to a narrow full cone angle. The maximum reduction in the spray cone angle, however, was more evident for the low density charge. The mean spray full cone angle was found to reduce from circa 20 $^{\circ}$ to 16 $^{\circ}$ for an in-cylinder density of 47 *kg m*$^{-3}$ and 20 *kg m*$^{-3}$ respectively.
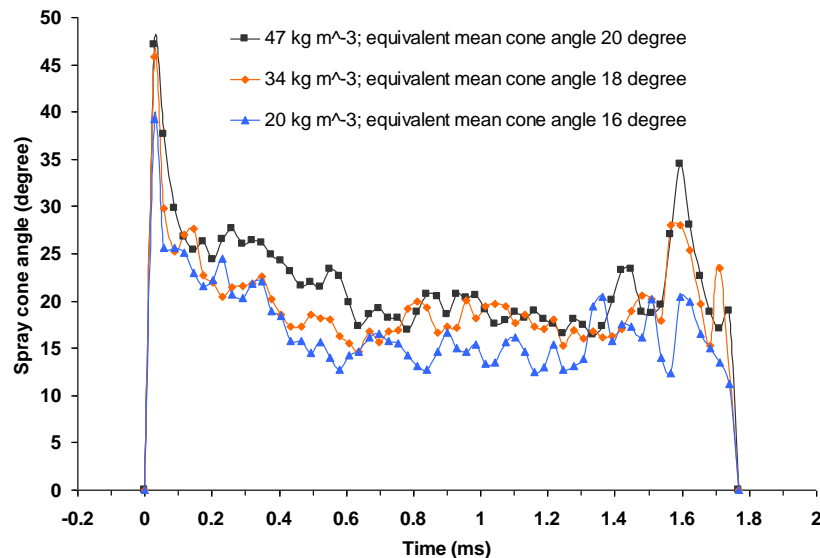
Fig 5-29. Evolution of the spray full cone angle at different in-cylinder gas density; 160 MPa injection pressure; 3-hole single guided VCO nozzle; 50 mm^3 fuelling; cold air intake, corresponding to 448 K at 6 MPa, 410 K at 4 MPa, and 350 K at 2 MPa in-cylinder pressure (at TDC) respectively

5.3.7   The Effect of In-Cylinder Gas Pressure at Hot Air Intake

With the increase of in-cylinder gas pressure and in-cylinder intake gas temperature, a reduction in the penetration length was observed from the data. This was attributed to enhanced droplet evaporation around the periphery of the penetrating spray (Fig 5-30). Nevertheless, the two distinct phases that were observed with the cold gas intake were also observed for elevated ambient gas temperature (Abdelghaffar et al., 2006). That is, an almost linear phase followed by a rapid transition to a steadier penetration length fluctuates around a slowly increasing average as shown in Fig 5-31 and Fig 5-32 (additional profiles can be found in Appendix C).

For the initial stage of injection (the first 0.2 *ms* after first sight of fuel), the rate of penetration is not observed to be greatly influenced by the gas temperature, but rather the in-cylinder gas density. This is due to the existence of highly dense droplet concentration, as well as an intact core length within the vicinity of the nozzle exit. Further downstream of the nozzle (at circa 20 *mm*), the penetration rate decreases

96

rapidly. This is attributed to a rapid evaporation of clusters/spray tip at elevated gas temperatures, although a decrease in the in-cylinder gas density (due to increased in-cylinder gas temperature) increases the rate of penetration. In addition, cluster shedding at the leading edge of the spray is attributed to loss of momentum, and the thermal interaction between the droplets (within a given cluster) and the surrounding air is thought to be greatly enhanced (at elevated temperatures). Fig 5-30 and Fig 5-33 highlight the influence of ambient gas temperature and the reduction in penetration length (0.25 *ms* after first sight of liquid fuel), from a maximum of 39 *mm* (at 448 *K* at *TDC*) to 28 *mm* (at 667 *K* at *TDC*).

Cold air intake, ρ_g = 47 Kg m^{-3}   *Hot air intake, ρ_g = 31 Kg m^{-3}*
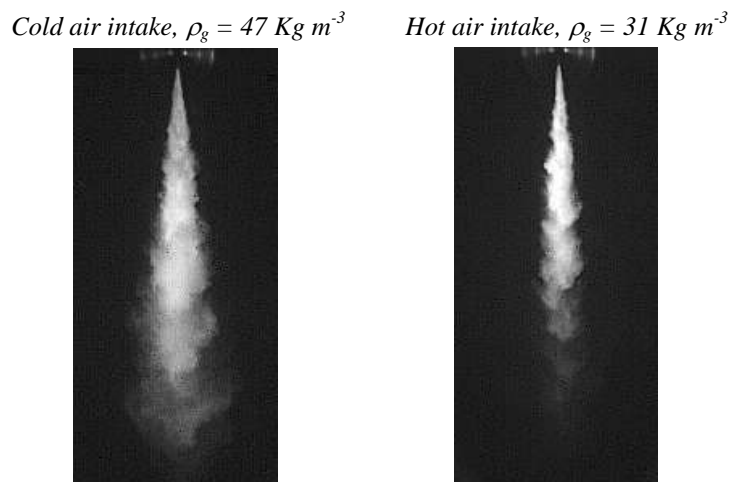
Fig 5-30. Comparison between non-evaporating and evaporating spray at 0.6 ms after first sight of fuel; 160 MPa injection pressure; 6 MPa in-cylinder pressure; 50 mm^3 fuelling; single guided 3-hole VCO nozzle; acquired with the Phantom camera
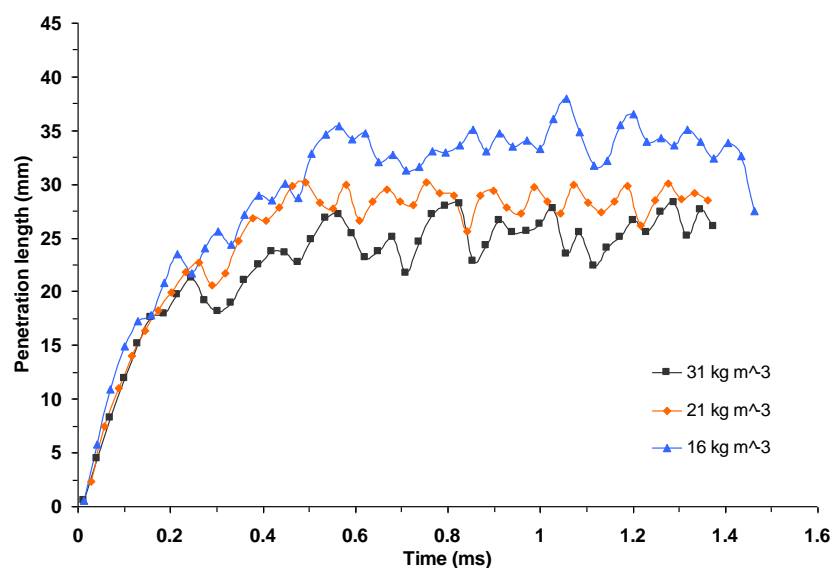
Fig 5-31. The effect of in-cylinder gas density on liquid spray penetration for hot air intake (corresponding to 667 K at 6 MPa, 649 K at 4 MPa, and 448 K at 2 MPa in-cylinder pressure at TDC respectively); 160 MPa injection pressure; single guided 3-hole VCO nozzle; 50 mm^3 fuelling
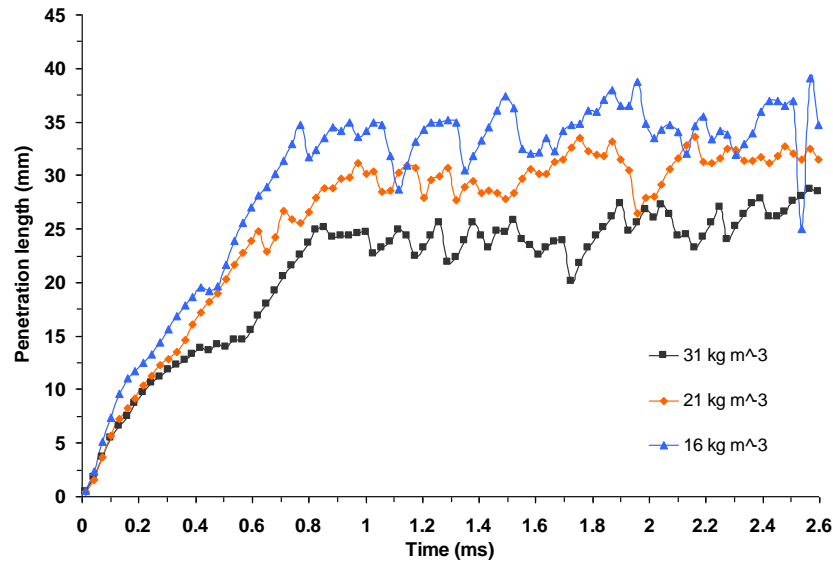
Fig 5-32. The effect of in-cylinder gas density on liquid spray penetration for hot air intake (corresponding to 667 K at 6 MPa, 649 K at 4 MPa, and 448 K at 2 MPa in-cylinder pressure at TDC respectively); 60 MPa injection pressure; single guided 3-hole VCO nozzle; 50 mm³ fuelling
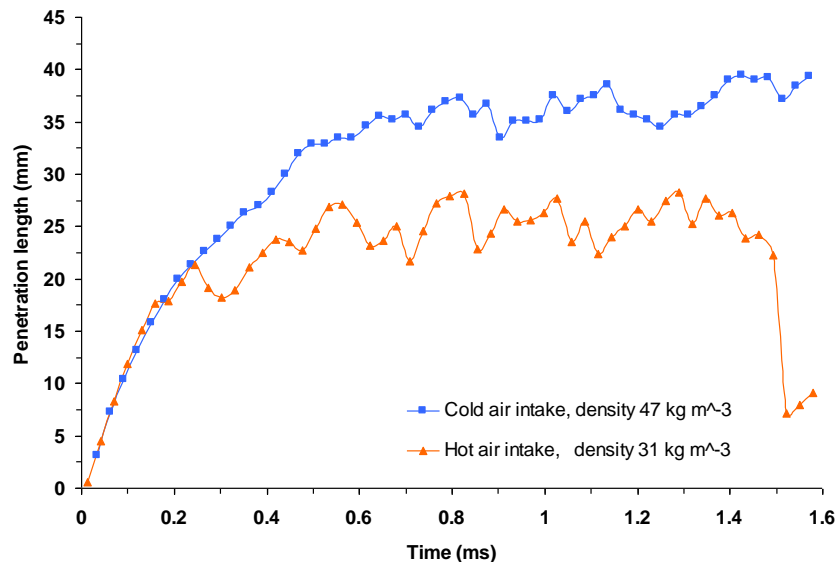
Fig 5-33. The effect of in-cylinder gas temperature on liquid spray penetration length; 6 MPa in-cylinder pressure (at TDC); 160 MPa injection pressure; single guided 3-hole VCO nozzle; 50 mm³ fuelling

As can be seen from Fig 5-33, at circa 0.25 *ms* after first sight of liquid fuel the second phase of spray penetration commences for the hot air intake. Liquid penetration becomes largely influenced by shedding and the evaporation of the droplet clusters. However, the ambient density has a considerable effect on the maximum penetration length compared with its cold counterpart (Fig 5-31 and Fig 5-32). Furthermore, the initial stage of penetration for the hot air intake appears to have a steeper, more linear penetration profile, particularly at higher injection pressures. This is attributed to a reduced in-cylinder gas density.

98

Fig 5-34 and Fig 5-35 represent the liquid spray full cone angle for the hot air intake. The overall trend is similar to that described for the cold air intake, but a slightly narrower mean full dispersion cone angle for the hot air intake is observed. This angle is estimated at 18° for an in-cylinder gas density of 31 *kg/m^3* (Fig 5-34).
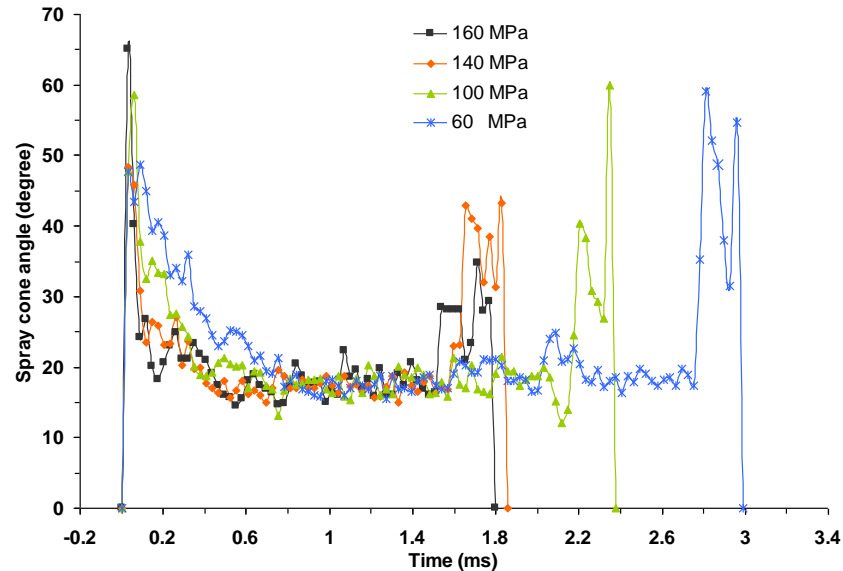
Fig 5-34. The evolution of the spray full cone angle at different injection pressures for a 3-hole single guided VCO nozzle; 31 kg/m^3 in-cylinder density; 6 MPa in-cylinder pressure; 50 mm^3 fuelling; hot air intake (667 K at TDC)

Fig 5-35 shows the influence of in-cylinder gas density on the spray cone angle for hot air intake. As can be seen, a reduction in the mean spray cone angle is observed from 18° to 15° when the in-cylinder gas density is decreased from 31 kg/m^3 to 16 kg/m^3 respectively.
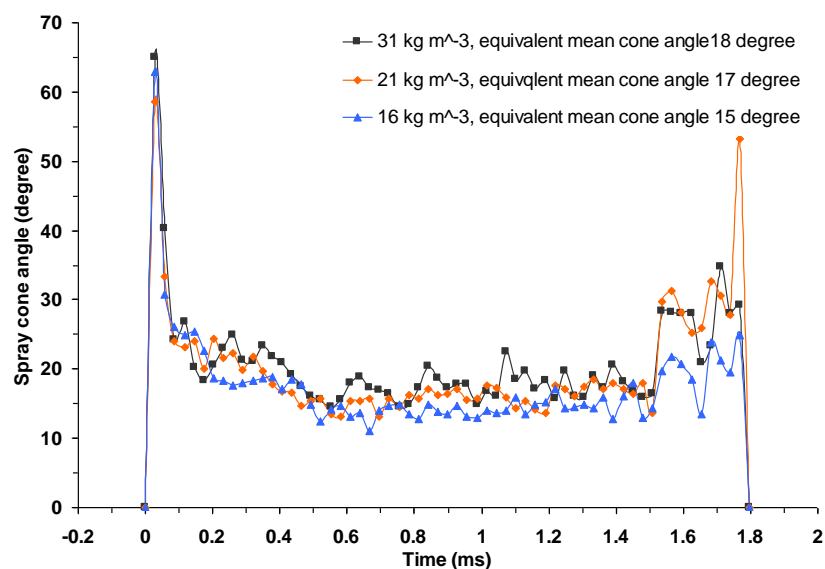
Fig 5-35. The evolution of the spray full cone angle for different in-cylinder gas density; 160 MPa injection pressure; 3-hole single guided VCO nozzle; 50 mm^3 fuelling; hot air intake (corresponding to 667 K at 6 MPa, 649 K at 4 MPa, and 448 K at 2 MPa in-cylinder pressure at TDC respectively)

5.4   CONCLUSIONS OF CHAPTER 5

From the experimental data obtained with the set-up described in section 5.2.1, a number of parameters influencing the formation and break-up of diesel fuel spray have been identified. These parameters are the injection pressure, the in-cylinder gas temperature, density and pressure. The analysis has been performed for a number of nozzle configurations. The following will outline the main conclusions drawn from this investigation.

For multi-hole nozzles, hole-to-hole variations occur as a result of unbalanced pressure distribution around the injector needle. This causes transverse movement of the needle, and, hence, temporarily obscures some nozzle holes during the initial stage of needle lift and the final stage of needle descent.

The hole-to-hole variations were clearly evident from the images of the spray cone angle and the penetration length for each individual hole during the initial stage of injection. This phenomenon occurred regardless of the injection pressure or the in-cylinder pressure. For the 7-hole Delphi injector considered, a significant reduction in hole-to-hole variation was observed when compared with the Bosch injector nozzles. This was attributed to improved uniformity of fuel pressure distribution around the needle.

The injection delays for the single-hole and the multi-hole nozzles were investigated. It was found that the Bosch injector exhibits a delay dependency on the injection pressure. For the Delphi injector in the current experiment, a constant delay of 0.40 *ms* was observed, with no dependency on the injection pressure.

The hesitation period during the initial stage of injection for the single-hole nozzle was attributed to the transverse movement of the needle (as discussed above). However, after the initial hesitation, the subsequent spray penetration was unaffected (if the magnitude of the rail pressure drop for the single-hole nozzle in comparison to the multi-hole counterpart is neglected).

The undesirable fuel at the end of the injection duration was found to be the result of unbalanced pressure distribution around the injector needle and subsequent needle oscillation. For the single-hole nozzle, unbalanced fuel pressure distribution appears

more significant for the single guided *VCO* nozzle, than the double guided counterpart. This quantity of fuel at the end of injection was observed as ligaments and spherical droplets, apparently the same size as the nozzle orifice diameter. This phenomenon occurred for the range of injection pressures in the current experiment. A sharp end to fuel delivery was also not evident for the 3-hole Bosch injector nozzle. This was attributed to transverse and/or vertical oscillation of the injector needle.

The number of holes within a nozzle, and subsequently the exit flow area, was found to have an effect on the rate of penetration. Although this may require more investigation, in the current study this was attributed to the initial drop in the rail pressure for the Bosch injectors and improved atomisation and air entrainment for the Delphi injector (due to small nozzle hole sizes). It is, therefore, recommended that caution should be taken when validating a multi-hole nozzle on the basis of a single-hole nozzle (for the same nozzle hole diameter, but different number of holes).

From the images obtained experimentally, a relatively uniform spatial distribution of the liquid fuel close to the nozzle exit is identified. This phenomenon appears to be independent of the injection or the in-cylinder pressure.

Increased detachment of large clusters of droplets around the periphery of the leading edge and stripping back, smaller clusters of droplets on the edge of the spray cone were attributed to the air entrainment. The magnitude of air entrainment is the result of momentum exchange between fuel droplets and the surrounding gas (particularly in a quiescent environment). The detachment and stripping of the droplet clusters were found to be directly dependent on injection and in-cylinder pressures.

The penetrating spray tips for all the nozzles tested were dependent on the in-cylinder and the injection pressure.

The spray cone angle was found to be independent of the injection pressure, but dependent on the in-cylinder gas density and in-cylinder gas temperature. This is attributed to increased rate of cluster shedding on the spray cone periphery and evaporation. The reduction in full spray cone angle (at cold air intake) was found to reduce from circa 20° to 16° for an in-cylinder density of 47 kg/m^3 and 20 kg/m^3

respectively. At hot air intake, the mean spray full cone angle was estimated at 18° for an in-cylinder gas density of 31 kg/m^3 and 15° at 16 kg/m^3 in-cylinder gas density.

The effect of increased gas temperature was seen to clearly increase vaporisation and reduce tip penetration. For the early stage of injection, however, a slightly linear penetration profile was observed for the hot air intake, particularly for the 160 MPa injection pressure.

6. EXPERIMENTAL STUDY OF MULTIPLE INJECTION SPRAYS

6.1 BACKGROUND

The common rail system (*CRS*) has recently increased in popularity for diesel engines due to enhanced pressures generated by the fuel injection pumps and the control capability of the injectors. Moreover, since the control capability of the injector has become independent of the fuel pump system, the degree of flexibility has also increased, enabling precise control of injection timing, duration and frequency of injection within a cycle over an entire operational range. This enables a reduction in emissions such as NOx and particulate emissions, combustion noise and injection delay periods.

For example, the formation of NO_x is dependent on combustion temperature, local oxygen concentration, time spent at high temperature in the combustion cycle and flame speed (Sher, 1998). Near-stoichiometric mixtures have higher flame speed, which gives less time for NO_x to form. However, rich mixtures have a lower concentration of oxygen, which leads to particulate emissions (sometimes referred to as smoke emissions) due to fuel pyrolysis (Dec, 1997). The need to simultaneously reduce NO_x and particle emissions, by reducing fuel concentrations where NO_x and particulate emissions are produced, a better mixing of fuel with air is essential, thus providing a more homogeneous spatial distribution of the injected fuel.

With the introduction of the first generation solenoid controlled injectors, for accurate dispensation of fuel, short dwell periods between consecutive injections were not possible under a minimum threshold (injection duration), mainly due to the response time of the injector and the needle ascent characteristics, as explained in chapter 3. Consequently, multiple injection strategies were not possible, or limited to a very large dwell periods between the pre-, main and, possibly, post-injections. However, recent studies have shown the increased benefit of combining high injection pressures, with splitting the injection interval in several consecutive stages, thus improving the emission due to a better control of the combustion processes (Lee & Reitz, 2003; Tow et al., 1994; Nehmer & Reitz 1994; Pierpont et al., 1995; and Su et al., 1996).

For example, Nehmer & Reitz (1994) investigated the effect of split injection on emissions such as NO_X and particulates. The authors noted the quantity of fuel in the first injection has a significant effect on the rate of in-cylinder pressure rise. The percentage of fuel during the first injection event was also found to correlate with the engine emissions. The authors came to a conclusion that, as more fuel was injected during the first injection event, NO_X emissions increased while particulate emissions decreased. With no apparent correlation between injection timing and engine emissions, NO_X emission for ¼ - ¾ and ½ - ½ split injection fuelling was reduced with no increase in soot formation. Nehmer & Reitz (1994) also indicate from their findings that split injection allows combustion to continue into the expansion stroke without an increase in particulate emission contrary to what was expected. This phenomenon was thought to be the result of split injection affecting soot production, since the mechanism of particulate reduction could be due to increased particulate oxidation late in the cycle rather than a reduction in the amount of particulate formed initially.

An experiment by Tow et al. (1994) was conducted to evaluate the effectiveness of using double and triple injection, to simultaneously reduce NO_X and particulate.

The test results showed, at 1,600 *rpm* 75% load, the double injection with significantly long dwell period (10° crank angle equalling 1 *ms* at 1,600 *rpm*) reduced particulate by as much as a factor of three when compared with a single injection strategy at the same load condition with no apparent increase in NO_X. For short dwell periods at 75% load, no significant reduction in particulate and NO_X was found. At 25% load, due to the ignition delays being longer, shorter dwell periods for double injection were found to reduce the premix burn fraction and NO_X. Also, the triple injections were found to be effective, if the dwell period between the second and the third injection was long. At 25% load, triple injections were found to reduce particulate by as much as 50% and NO_X by 30%.

The authors conclude that the dwell period is a critical parameter, as did Nehmer & Reitz (1994). That is, the mechanism of particulate reduction could be due to increased particulate oxidation late in the cycle rather than a reduction in the amount of particulate formed initially. Also from the experimental results for the triple injection case, the authors indicate that the same magnitude of particulate reduction

was achieved either by 19% of the total fuel mass during the last injection or 49% of the total fuel mass during the last injection. Thus, only a short injection pulse is needed for the last stage of triple injection strategy to increase particulate oxidation rate late in the cycle.

An emission and performance study by Pierpont et al. (1995) was conducted to investigate the combined effect of exhaust gas recirculation (*EGR*) and multiple injection strategy for two different diesel injector nozzles, one with 125° separation angle and the other with 145° separation angle. For the 125° nozzle, EGR was found to reduce NO_X effectively, whilst a small increase in specific fuel consumption (*SFC*) was detected. As for the 145° nozzle, a substantial increase in SFC was observed. Pierpont concluded that, the optimum multiple injection strategy depends upon many factors including the spray inclination angle. Also, the authors indicate that with cooling the recirculation exhaust gases, improved emission and performance should be obtained.

In general, whilst substantial literature exists on experimental investigation of the effects of multiple injection strategy on the performance of the combustion process, little is known about the dynamic characteristics of diesel fuel spray in a realistic diesel engine environment. For example, Farrell et al. (1996) investigated the effect of multiple injection strategy on the rate of penetration. The authors utilised an injector with a nozzle hole diameter of 0.26 *mm*, injecting fuel at 90 *MPa* in to a pressurised chamber at 1.65 *MPa* room temperature. They concluded that the second or the third spray penetrated faster than the first split spray. Also, the shorter the dwell time between the two split sprays, the faster the following split spray was found to penetrate. In addition, the authors found that during an injection interval, the overall Sauter Mean Diameter (*SMD)* increased, and after or between injection intervals the overall *SMD* decreased. Hence, the longer the injection duration, the larger the *SMD* becomes, and the longer the dwell time the smaller the overall *SMD*.

Yoshizu & Nakasyama (1991) used *PDA* technique to measure the spray droplet size spatial distribution at some location. The fuel was injected at 25 *MPa* via 0.25 *mm* nozzle hole diameter. The authors found that the pilot injection spray had a more stratified size distribution, meaning that the drop sizes increased from the spray axis

to some radial location, and then from that location they decreased to the spray edge. The change in distribution of drops with pilot injection was thought to result from the interaction of main and pilot fuel spray volume.

Arai & Amagai (1997) studied the dynamic behaviour of a pilot injection using high speed camera recording. With a nozzle hole size of 0.27 *mm* in diameter, the maximum injection pressure was 25 *MPa*, injecting in to a vessel at 3 *MPa* at room temperature. The authors observed that the spray tip velocity of the second spray was higher than that of the first. Also, this tendency increased as the dwell time decreased. The results were explained due to the flow field formed by the first spray. Furthermore, the internal gas velocity from the velocity difference between the two spray tips was estimated by the author in the region of 10 *m/s*. This value was found to coincide with the tail velocity of the first spray, being considerably slower than the injection velocity.

As discussed, many of the experimental investigations regarding the characteristics of the split injection strategy have been undertaken at unrealistic injection pressures, in-cylinder pressures, ambient room temperatures and, by today's standards, large nozzle hole diameters, which are known to increase droplet size, reduce atomisation and, hence, lengthen evaporation time. Also, no attention has been given to the interaction between the split injected portions of fuel (liquid and vapour) in any of the aforementioned studies.

With reference to the effects of multiple injection strategy with regard to combustion processes, the information available on the dwell period is inconclusive. The dwell period is key to a successful injection strategy, as it governs the temporal and spatial fuel distribution/concentration responsible for engine knock and emissions.

The fuel injector considered in the current study for the split injection strategy is a solenoid actuator type injector (Delphi). It is thought that the Delphi system can deliver up to five injections per cycle allowing high flexibility for combustion optimisation, and providing a level of economy and performance that is usually available with the piezo type system (Birch, 2004). The Delphi injector is also

understood to support Euro IV and Euro V compliance without the expense of the piezo technology. Therefore, the aim of the current study is to assess the potential of this injector, with reference to split injection strategy, and to benchmark the characteristics of the spray for a variety of split injection strategies under realistic diesel engine environment.

In the current study, details of the experiments undertaken are given to quantify both the liquid spray and vapour phase propagation with regard to split injection strategy through a 7-hole *VCO* single guided Delphi injector, injecting into a realistic diesel engine environment at low and high air intake temperature.

The low air intake temperature was chosen for several reasons; to simulate cold starting; validation of spray penetration in the absence of significant evaporation; and for modelling.

The results obtained by simultaneous Planar Laser Induced Fluorescence (*PLIF*) and *Mie* scattering techniques are presented in this chapter for the split injection strategy. For comparative reasons and for ease of post-processing in section **6.2.5**, reference is also made to the single injection strategy.

The current chapter is separated into two main sections followed by analysis and conclusion. In section **6.2,** the configuration of the experimental equipment and the experimental set-up is given. The experimental results and their analysis are then presented in section **6.3.**

6.2   EXPERIMENTAL CONFIGURATION, SET-UP AND PROCEDURE

The laser used in the current experiment was made by Spectra-Physics, Quanta-Ray GCR 150 pulsed Nd:YAG Laser. The laser was capable of delivering pulses up to 300 *mJ* of energy, with a frequency of $10Hz$ capable of matching the frequency of the optical Proteus rig. With a beam diameter of 8.7 *mm* and pulse width of 4-5 *ns* at Full Width at Half Maximum (*FWHM*), the laser pulses were spatially and temporally Gaussian. With a quantum efficiency tuned for *UV* range, the Diesel fuel was exited at the 4th harmonic of the laser (266 *nm*) for the *LIF* images.

6.2.1 Laser Optics

To simplify the alignment and to avoid losses of laser energy, the beam of the laser was brought to the same height as the object under study with the use of two mirrors. The way and the number of mirrors to be used are fundamental as the optical properties of the mirrors at the edges of the mirror cannot be guaranteed. To maximise the reflection of the laser beam, one should ensure that the beam makes contact at the centre of the mirrors.

The sheet forming optics used within this study consists of two cylindrical lenses, one in the horizontal and the other in the vertical plane, as well as two collimating lenses (Fig 6-1). The laser beam enters the sheet forming optics through cylindrical lens $\underline{A}$. The beam is then expanded vertically before entering the spherical lens $\underline{B}$, which collimates the beam. The cylindrical lens $\underline{C}$ narrows the beam into a sheet, whilst the final spherical lens $\underline{D}$ collimates it in to the required width. The divergence and the focus of the sheet can be varied by the adjusters on the sheet forming optics (Fig 6-1). Once adjusted, the resultant sheet laser light thickness and sheet height at the point of measurement typically have dimensions in the order of 0.75 *mm* and 55 *mm* respectively.

Fig 6-1. A photograph of a four-lens sheet forming optics

To ensure maximum potential of the laser sheet, proper positioning of the mirrors and the sheet forming optics are essential. Furthermore, failure in correct positioning of the optics results in a Non-Gaussian beam profile. By careful alignment, the laser beam will follow the central axis of the cylindrical lens $\underline{A}$ in the sheet forming optics (Fig 6-1).

With the provisional adjustments in place, the laser sheet is positioned at a correct distance from the subject. This task is relatively straightforward, since the entire laser and corresponding mirrors/optics are mounted on a transportable rig. Once the measured area is relatively within the depth of field of the laser sheet optics, fine adjustments can be made with the focal length and the divergence of the laser sheet forming optics by rotating the thumb wheels on the sheet optic assembly (Fig 6-1).

6.2.2 Image Acquisition

6.2.2.1 Camera Configuration

During the course of study in the current experiment, a single La Vision Flow Master *CCD* camera with optical links was utilised. The camera featured with a resolution of 1,280 ⊂ 1,024 pixels, a frame rate 8 *Hz*, pixel size of 6.7 ⊂ 6.7 *μm*, a dynamic range of 12 bit (4096 levels of gray), and a sensitivity range from 290-1,100 *nm*. However, due to the use of an image intensifier, the overall spectral range of the final image will be affected.

The images were downloaded in real time to a *PCI* interface card controlled by La Vision software via the cameras optical links.

Standard lens fittings on the *CCD* camera allowed the use of conventional lenses, image intensifiers and other specialist lenses to be utilised.

6.2.2.2 Image Doubler

As explained in the introduction, the current study involves utilisation of simultaneous Planer Laser Induced Fluorescence (*LIF*) and *Mie* scattering methods. For this reason, an image-doubling unit was fitted to the *CCD* camera to facilitate the acquisition of two views of the same subject in a single image. With each view being individually filtered, different representation of the same event (*LIF* and *Mie*) will be provided. Since the integrated filter holders were inadequate in size, external filter holders were individually placed in front of the image double unit (Fig 6-2).
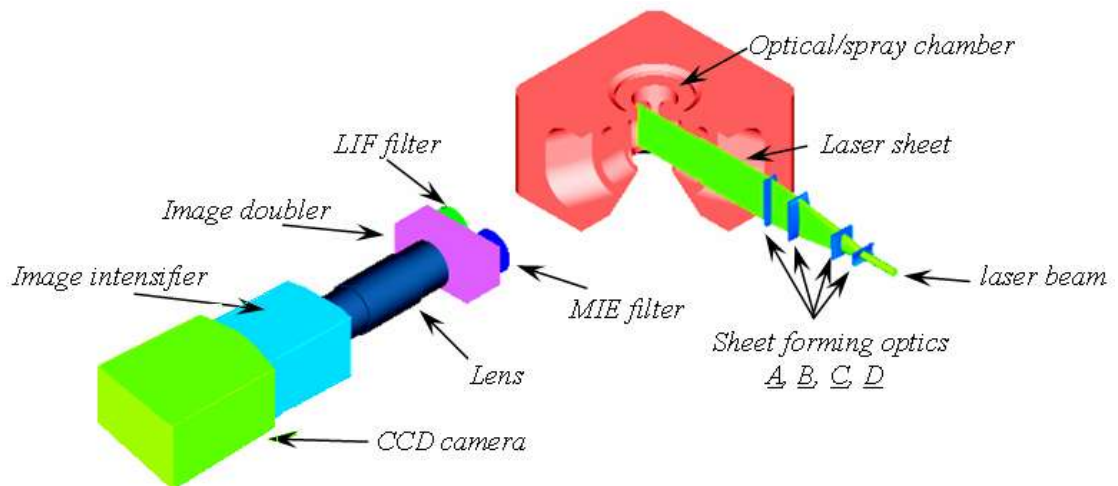
Fig 6-2. Schematic of the optical Proteus spray chamber, the optical systems, and setup

6.2.2.3 Filter and Lens Selection

The selected lens for the camera was a 105 *mm* focal length. To differentiate between the *LIF* and the *Mie* images, two different spectral filters were used; a band-pass filter centred at the laser wavelength (532 *nm*) for the *Mie* scatter, and a long-pass filter for the *LIF* signal (>266 *nm* laser cut-off).

For the *Mie* images, since the elastic scattering was intense, a neutral density filter (0.7) was used to avoid overloading the sensor chip on the image intensifier and the camera.

6.2.2.4 Image Intensifier

An image intensifier was used in the current experiments to compensate for any low levels of light/signal. This device is mounted between a *CCD* camera and the camera lens. The image intensifier or intensified relay optics allow image amplification gain from 0 to 1000 via a control box, shown in Fig 6-3. Throughout the acquisition of the images in the current experiment, the gain was set to 800. Additional adjustments on the image intensifier are the gate width and delay, allowing further control over the acquisition of the images. For example, the *CCD* camera has a minimum gating of 100 *ns*, whilst the image intensifier is capable of gating down to 5 *ns*.

Fig 6-3. La Vision image intensifier control front panel

To operate at minimum gating values, and since the camera shutter also needs to be triggered for acquisition of an image, the usual exposure of the camera must be increased to a value about 1 *ms* in order to allow the photocathode decay time, whatever the actual exposure (Crua, 2002).

With the delay and the width setting corresponding to a value in microseconds (*µs*), the delay function allows variation in the time between receiving a trigger and the actual opening of the intensifier shutter. The width input is the opening level of the intensifier shutter. Both the delay and width were adjustable from zero to 999.999 *µs* in steps of 1 *ns*. In the current experiment, the delay was set to 2,200 *µs* and the width to 500 *ns*.

6.2.3   Synchronisation and Acquisition

Most systems suffer from an inherited delay, and for a correct acquisition of the data timing becomes an important parameter. In the current experiment, synchronisation (of the laser, image intensifier, fuel injection equipment (*FIE*)), monitoring and acquisition of the data were performed as follows.

With the acquisition timing based on 3,600 pulses per revolution encoder fitted to the crankshaft of the Proteus rig (Chapter 4), the marked *BDC* signal provided both the laser system and the *FIE* a reference clock. The recording of the signals was performed by a LeCroy LT224 fast digital storage oscilloscope, offering a sampling frequency up to 200 *MHz*. The actual triggering of the oscilloscope was performed using the injection trigger signal as the reference signal. With the encoder signals received from the crankshaft of the Proteus rig, the N^o board on the La Vision laser

system outputs a trigger signal to the *YEX* module (board), based on a value set in the (dialog box of) DaVis software (Fig 6-4).

Fig 6-4. Trigger dialogue box in DaVis software

The *YEX* synchronisation module designed for in-cylinder diagnostics allows the deviation of the laser pulse repetition rate (from 9.30 *Hz* to 10.4 *Hz*) to be synchronised with the frequency of the engine cycle/speed. With Proteus operating at 8.33 *Hz* (500 *rpm*), it was necessary to skip eight cycles to avoid unnecessary window fouling, maximise in-cylinder purging and ensure proper laser synchronisation. Thus, with an injection rate at 1:8 cycles, this gave a frequency of 1.04 *Hz*. Taking into account the variation of the laser repetition rate from 9.30 *Hz* to 10.4 *Hz*, the synchronisation was given at 1.04 *Hz* ⊂ 10 equalling 10.4 *Hz*.

With the laser pulse duration of 5 *ns* and an elastic scattering of the same duration, the fluorescence time decay (defined as the time necessary for 86.5% of the fluorescence intensity to be emitted) for diesel fuel occurs within approximately 80 *ns* (Pastor et al., 2002). Thus, for all the tests in the current experiment, the image intensifier gate was fixed for a total duration of 500 *ns* (20 *ns* of which was open prior to laser pulse duration).

6.2.4   Fluorescence Absorption and Emission Spectra of Diesel Fuel

Generally, the fluorescence absorption and emission intensity spectrum of the reference fuel (diesel in the current study) is investigated prior to filter selection.

This task was achieved for the absorption of fuel, with a Cary 50 Scan *UV*-Visible Spectrophotometer, and for fluorescence emission intensity, a Cary Eclipse Varian

Fluorescence Spectrophotometer. The results are shown in Fig 6-5 for an excitation at 266 *nm* wavelength.
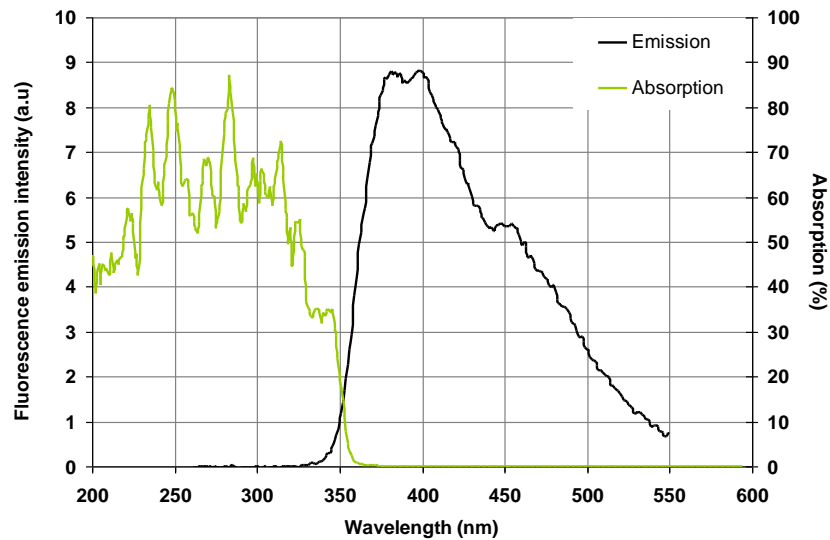

Fig 6-5. Absorption and fluorescence emission of Diesel fuel at excitation wavelength of 266 nm

6.2.5   Post Processing of the Data

Simultaneous *PLIF* and *Mie* images throughout the injection period for liquid and vapour diesel fuel propagation were recorded for the experimental test conditions shown in Tab 6.1.

Test conditions for split injection strategy								
Fuel injection pressure (*MPa*)	**In-cylinder air pressure at *TDC* (*MPa*)**	**Target dwell period (*ms*)**	**In-cylinder air temperature at *TDC* (*K*)**		**In-cylinder air density at *TDC* (*kg/m³*)**		**Injected volume (*mm³*)**	
			Cold	**Hot**	**Cold**	**Hot**	**1st split**	**2nd split**
100	2	0.325, 0.425, 0.625, 0.825	350	448	20	16	10	10
	6		448	667	47	31		
140	2	0.325, 0.425, 0.625, 0.825	345	448	20	16	10	10
	6		448	667	47	31		

Tab 6-1. Experimental test conditions for split injection strategy

Data were recorded for the entire liquid and vapour observation interval. In order to address possible cycle-to-cycle variation in the position of the liquid or vapour spray, 15 images per time-bin were recorded.

Prior to the acquisition of the simultaneous *PLIF* and *Mie* spray images, a background image was taken for subtraction from the main images during post-processing.

For the cold air intake, image acquisition was carried out for every 10 μs, and for the hot air intake, every 30 μs of the total injection duration. For dwell periods of 0.825 *ms*, image acquisition was also carried out for every 30 μs. This gave a total of more than 70,000 images. The images were inspected randomly to ensure quality and repeatability.

The images captured using DaVis software were saved in *IMX* format. This gave a monochromatic 12-bit greyscale the same as the camera's configuration in the current study. Hence, parameters such as pixel count resulting from background noise could be removed during post-processing. Also, the surround noise was eliminated by a template subtraction. The template was the same size and shape as that of the actual optical viewing window. Fig 6-6 shows an image with and without background and surround noise subtraction.
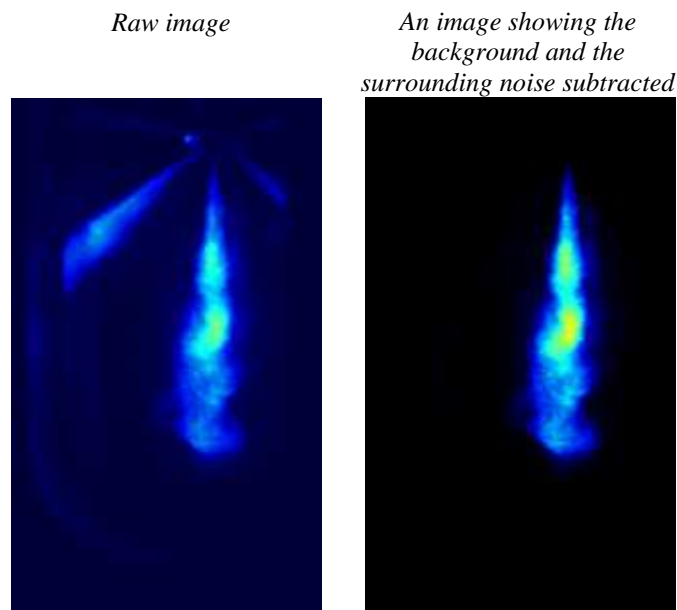
Fig 6-6. An image before and after background and noise subtraction

Post-processing of the images was performed by purpose-developed macro written for the DaVis software (by Dr De Sercey, at the University of Brighton).

Unlike the definition of the penetration length in the last chapter, the macros written for the post-processing of the penetration data (in the current section) use the

following definition. The penetration length is taken as the furthest length or fuel parcel downstream of the nozzle exit, as opposed to furthest unbroken portion of the spray from the nozzle exit.

The post-processing of the images was based on pixel thresholding and the conversion of the images to a binary format (Abu-Gharbieh, 2001). The tip of the spray or furthest cluster of droplets away from the nozzle exit was then tracked by the software. Furthermore, pixel thresholding allowed differentiation between the interacting spray of the first and the second of the split injection strategy. This will be explained in more detail later in the text. The threshold level was subjectively chosen by selecting a complete test run and varying the threshold level to obtain optimum results. Thus, the threshold level became suitable for all images in that batch, since the quality of the spray images and the intensity of the laser energy remained almost constant (Fig 6-7).
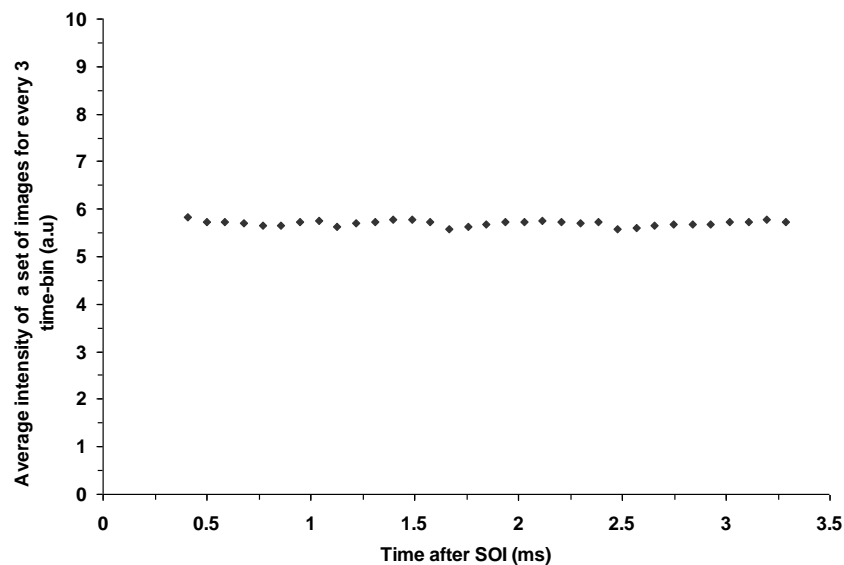
Fig 6-7. Variation of laser energy for every 3 time-bin (15 images per time-bin), from the start of injection trigger; 100 MPa injection pressure; 20 kg/m³ in-cylinder density; 2MPa in-cylinder pressure; cold air intake; 0.825 ms dwell period (split injection strategy)

Fig 6-8 shows the effect of threshold level on the average penetration length taken from 15 images per time-bin. With a change of *6%* threshold level, the maximum variation in the measured penetration length was within ± 2 % of 45 *mm*. This effect was more noticeable close to the limit of the window at 45 *mm* (Fig 6-9).

As can be seen from Fig 6-9 even with background removal prior to start of image acquisition, the bottom edge of the window shows low levels of reflection. For the processing software to avoid such reflections and locking onto ghost droplets as the furthest point of spray penetration, the threshold level was set to 8% of the total image intensity. This allowed elimination of undue light scattering, with little compromise on accuracy for measured penetration length.

The threshold method was also beneficial in the determination and elimination of the background scatter/reflection of the spray itself. This phenomenon can be best explained by the images shown in Fig 6-10. As can be seen, the spray reflection gives the impression of large clusters of droplets on one side of the spray image. Thus, without reasonable thresholding the spray would appear more dispersed.
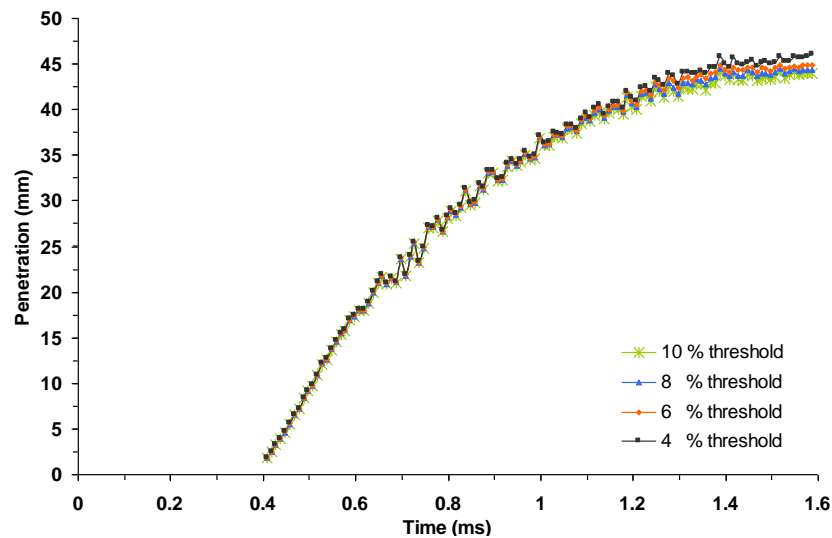
Fig 6-8. The effect of threshold level in steps of 2% on maximum penetration length; single injection strategy; 60 MPa injection pressure; 20 kg/m^3 in-cylinder density; 2 MPa in-cylinder pressure; cold air intake (350 K at TDC)

Laser sheet direction
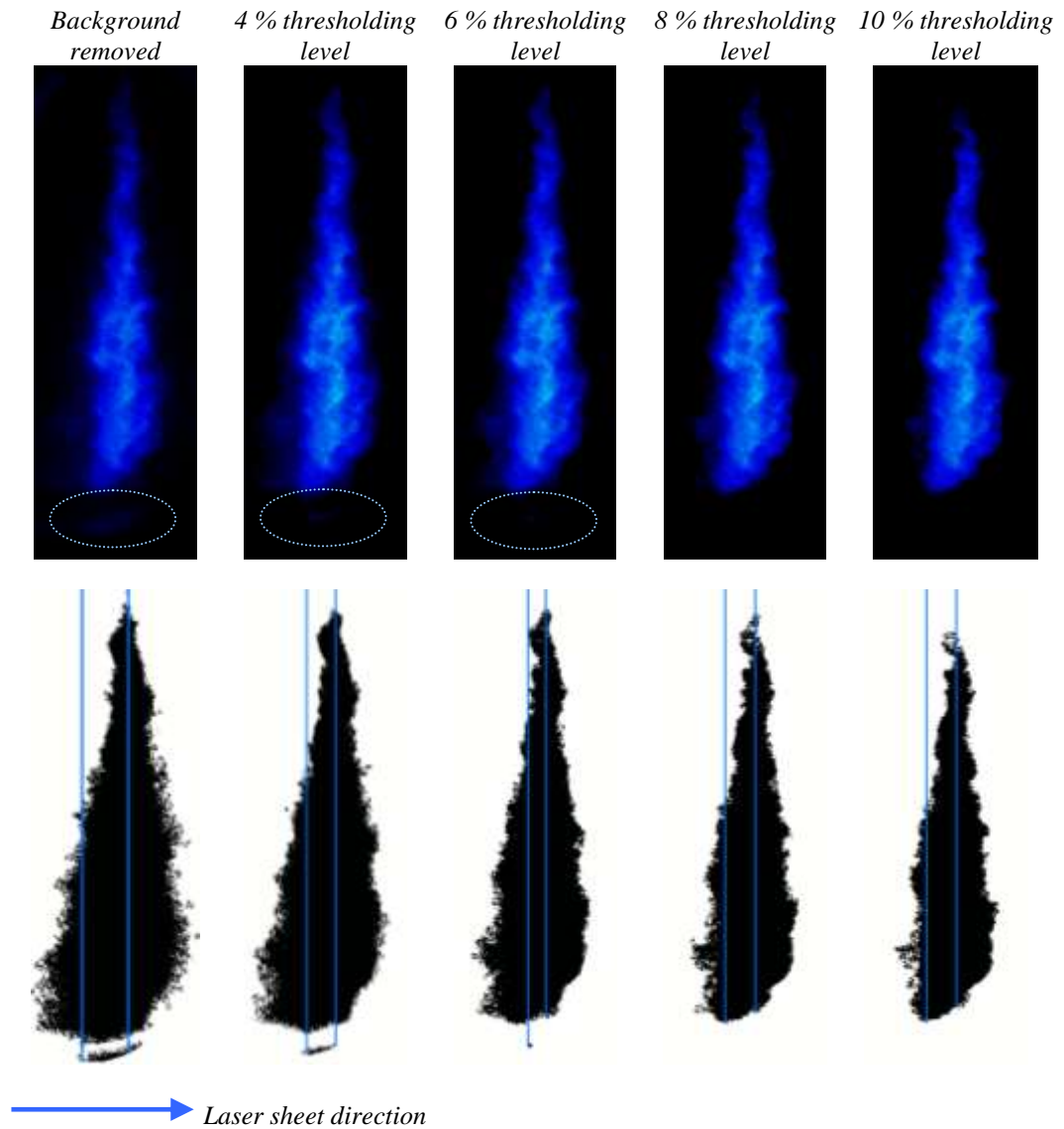
Fig 6-9. Images of liquid spray and the reflection of the window at the bottom of the images for various threshold levels; single injection strategy; 60 MPa injection pressure; 20 kg/m³ in-cylinder density; 2 MPa in-cylinder pressure; cold air intake (350 K at TDC); time after start of injection trigger 1.5875 ms; the line on the right hand side indicates the maximum penetration length on the central spray axis, whilst the left hand side line represents the maximum penetration length
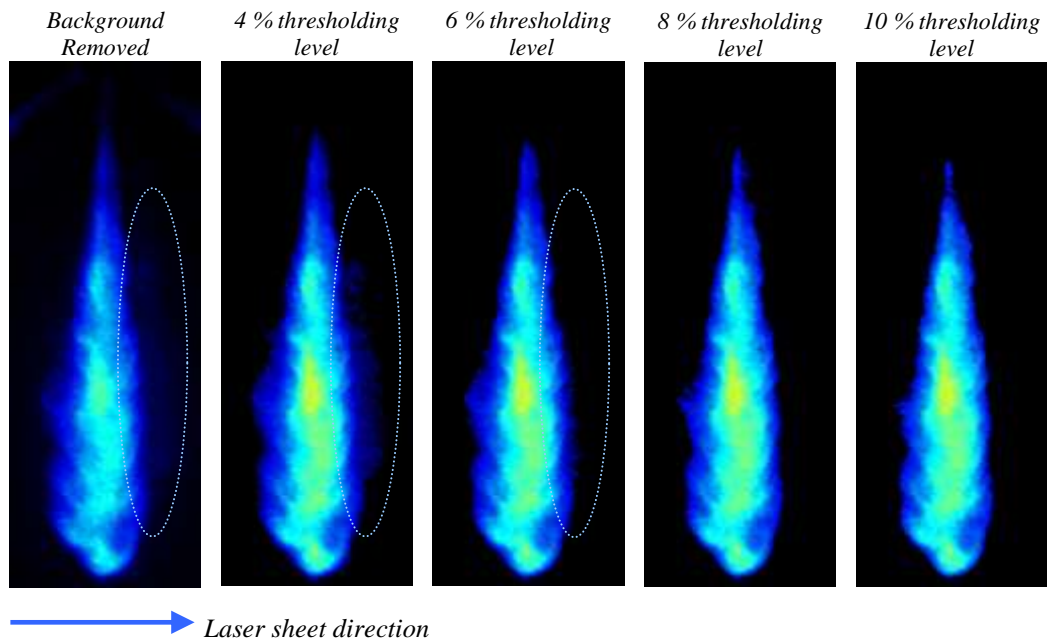
Fig 6-10. Images of liquid spray and background reflection for various threshold levels; the in-cylinder and injection pressure conditions are the same as Fig 6-9; time after start of trigger 0.8975 ms

The automated processing of the split injection data is based on prior knowledge of the second split spray. This knowledge is gained by examining several cases for varied parameters prior to automation of post-processing.

The spray analysis post-processing macro dialogue box written for DaVis's software by De Sercey requires an input for the first sight of fuel in milliseconds, and a rough estimation for the rate of penetration for the second split spray (Fig 6-11). Whilst tip penetration tracking for the first split is performed as normal by the software, on arrival of the second split spray the software initiated a variable mask in length.

The variable mask lengthens, covering the tail of the first split spray at a rate slightly ahead of the second split spray.

Since the intensity of the first split spray at the end of first split injection is lower than the second split spray (due to reduced droplet concentration and dispersion at the end of first injection), by setting an individual threshold for each split the software differentiates between the penetration length of the first and the second split spray (Fig 6-12).

At the end of processing with the raw data given in a txt format, the output files were converted in to Excel worksheets, where statistical analyses for the maximum

penetration length on and away from the spray axis were carried out. The data presented in the results section are therefore the mean values of 15 sets of images for a given time-bin (Yule & Filipovic, 1991) unless otherwise stated.
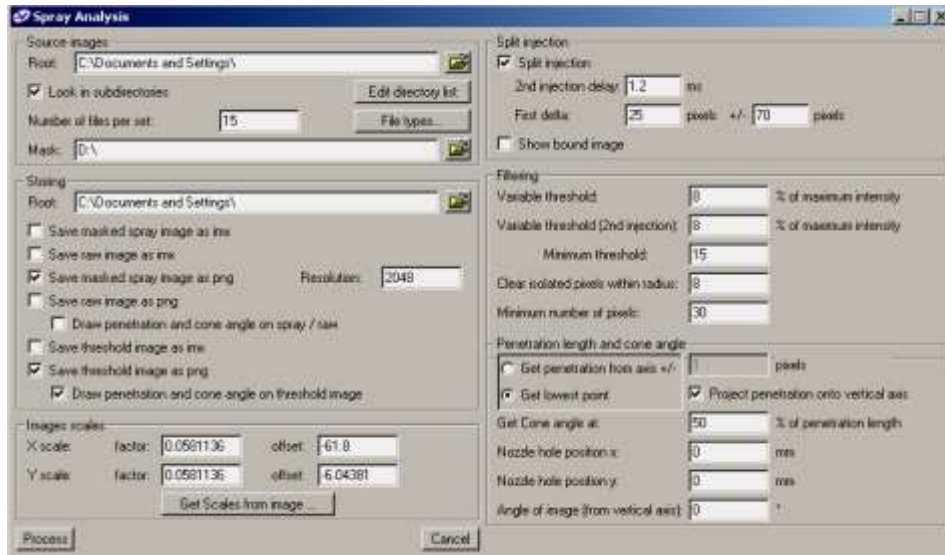

Fig 6-11. Spray analysis post-processing macro dialogue box written for DaVis's software (De Sercey)
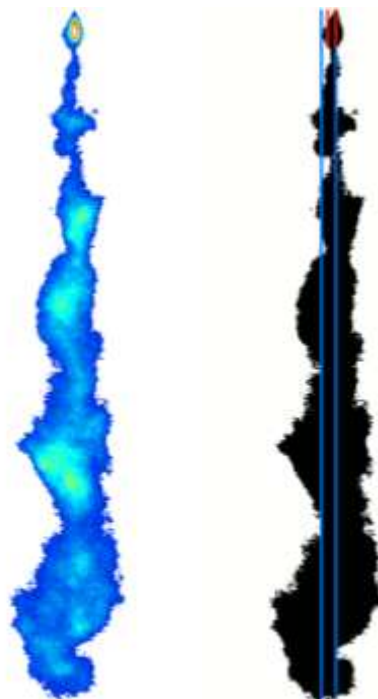
Threshold image   Threshold/Binary image

Fig 6-12. Tracking of tip penetration for the first and the second of the split injection strategy; the red line on the binary image indicates the length of the second split, whilst the blue line indicates the length of the first split automated by the software; both the red and the blue lines on the right hand side of the binary image indicate the maximum penetration length on the central spray axis, whilst the lines on the left hand side indicate maximum penetration length

6.2.6 Possible Sources of Error

The overall accuracy for quantitative data acquisition is a complex function of error introduced by every single element in the chain of events (Crua, 2002). For qualitative observation, they need not be all assessed as long as they are not all ignored.

For example, optical diagnostics require optical access which often means windows to enclosure where the process under investigation takes place. Subsequently, window contamination often occurs, resulting in attenuation of the laser intensity. The one source of error is the attenuation of the laser intensity between the energy monitor and through the optical windows (Fig 6-13). The windows were removed and cleaned for every 45 images in the current study. The energy monitor is one other source of error in interpretation of the laser pulse energy. The energy monitor used to associate laser pulse energy to every capture was tested against a reference calibrated energy meter. The output of the energy monitor was found to be accurate within 4% of the total energy. Laser pulse energy fluctuations are additional inherited laser diagnostics. The Nd:YAG laser systems may have shot-to-shot energy fluctuations due to the intensity fluctuations of the lamps used as excitation source. Additional sources of errors are image acquisition time jitter and camera jitter that could be due to vibrations caused by the Proteus rig. Consequently, if the camera is susceptible to small vibrations, the algorithm does not recognise the shift in datum. A summary of errors is presented in Tab 6-2.
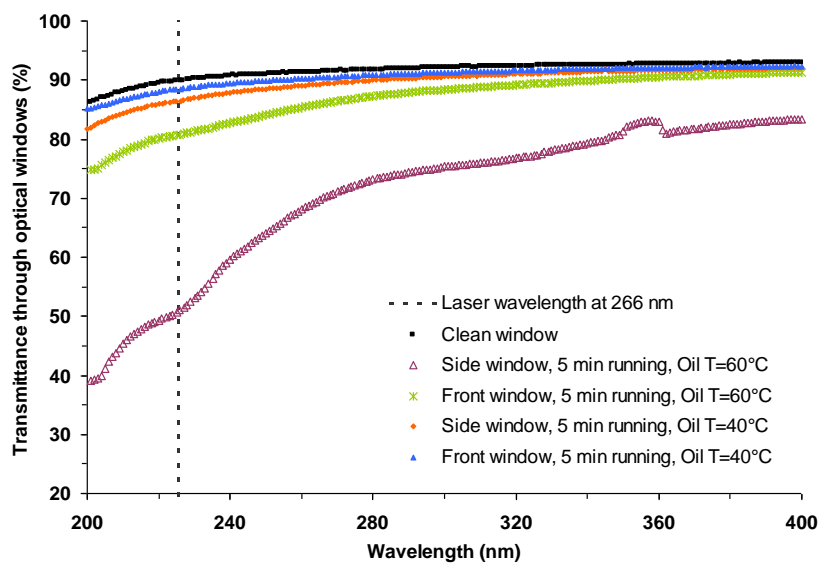
Fig 6-13. Transmittance through the optical windows with air as the only constituent in the spray chamber; side window, referring to the planar-laser sheet entry; front window, referring to the acquisition side by the camera

Possible cause of error	Error magnitude	Assessment method
Attenuation of laser intensity due to window contamination	*15 %*	*Measured*
Accuracy of energy monitor	*4 %*	*Measured*
Laser pulse energy fluctuations	*< 4 %*	*Measured*
Image acquisition time jitter	*Not detected*	*Measured*
Camera jitter and subsequent change of datum for algorithm	*> 1 mm*	*Measured*
Error in penetration length due to thresholding level	*±2 %, ≈2 mm*	*Measured*

Tab 6-2. Summary of errors for simultaneous LIF and Mie experimental technique

6.3   EXPERIMENTAL RESULTS

6.3.1   The Effect of Dwell Period at Low In-Cylinder Pressures on Liquid Fuel Penetration

In Chapter 5, the effects of injection pressure, number of nozzle holes, in-cylinder density and the ambient gas temperature on the rate of liquid fuel penetration were examined for single injection strategy. For split injection strategy, however, there are additional parameters influencing the characteristics of the subsequent fuel spray emerging from the nozzle. One such parameter is the time or the dwell period between the end of one injection, and the beginning of the next within a cycle.

Fig 6-14 shows the liquid spray tip penetration length for a single and split injection strategies for the 0.325 *ms*, 0.425 *ms*, 0.625 *ms*, and 0.825 *ms* dwell periods. The injection and the in-cylinder pressures as indicated in the caption of Fig 6-14 are 100 *MPa* at 2 *MPa* respectively. As can be seen from the same figure, during the first split interval all four sprays agree well to the single injection strategy, having an almost identical penetration profile.
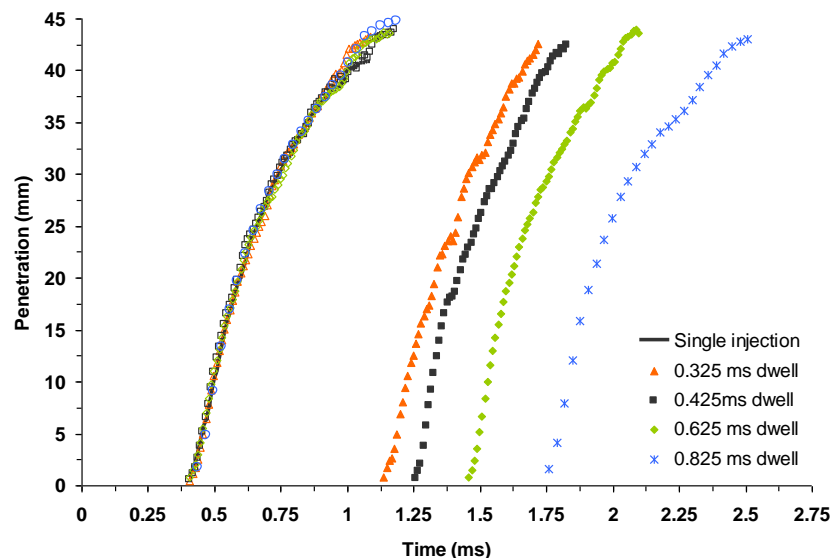
Fig 6-14. Comparison of the liquid spray tip penetration, for single and split injection strategies (processed from Mie images); injection pressure 100 MPa; in-cylinder pressure 2MPa; cold air intake (corresponding to 350 K at TDC); density 20 kg/m³; for consistency, the initial delay (0.4075 ms) described in chapter five has also been shown

Fig 6-15 shows the penetration length profile for 0.425 *ms* dwell period and a single injection strategy.
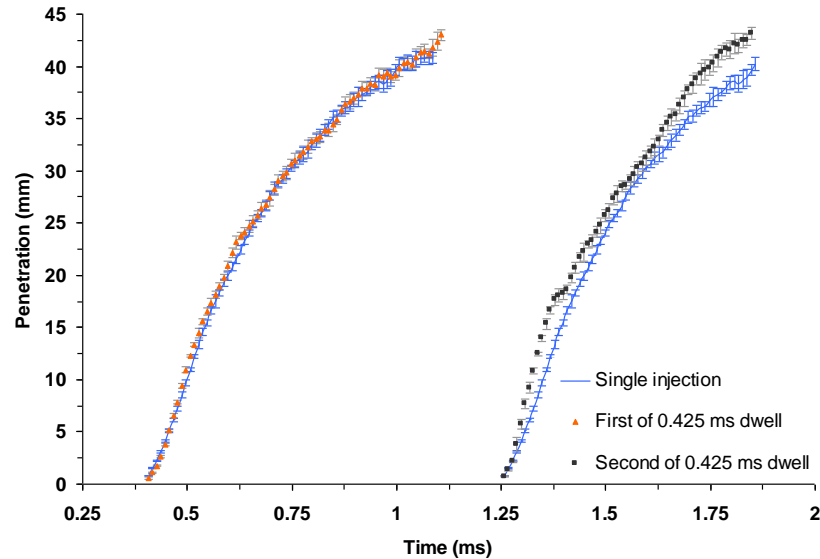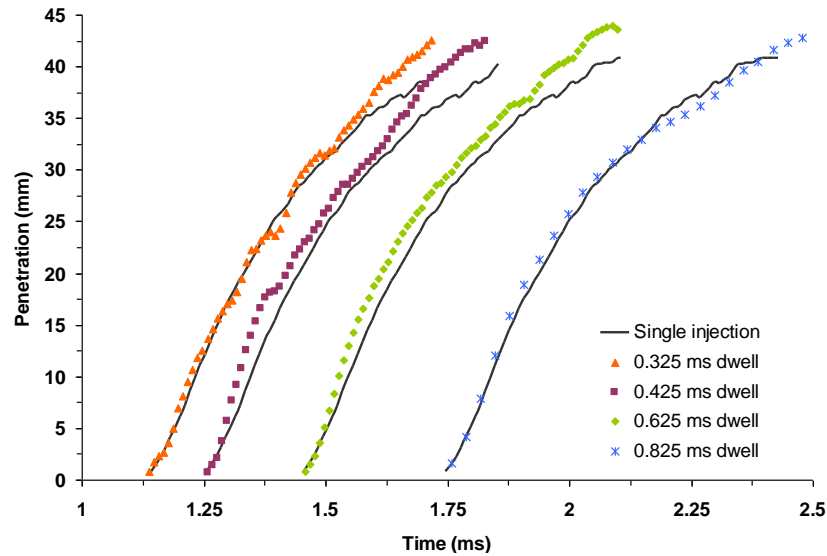

Fig 6-15. Comparison of the liquid tip penetration for the single injection and the 0.425 ms dwell period strategy (processed from Mie images); the bars represent the standard deviation; injection pressure 100 MPa; in-cylinder pressure 2MPa; cold air intake (corresponding to 350 K at TDC); 20 kg/m³in-cylinder density

As can be seen, whilst the first of the split injection and the single injection strategy agree well within the error band, the deviation between the single injection and the second of the split is much greater. In the current study, the penetration of the second split spray for dwell periods of 0.325, 0.425, and 0.625 *ms* is more rapid, particularly later in the injection period when compared with the first of the split or the single injection strategy as shown in Fig 6-16. The same figure also shows the second split spray for the 0.825 *ms* dwell period penetrating more slowly than those with the shorter dwell periods.

Fig 6-16. Comparison of the liquid spray tip penetration, for single and the second of the split injection strategies (processed from the Mie images); injection pressure 100 MPa; in-cylinder pressure 2MPa; cold air intake (corresponding to 350 K at TDC); density 20 kg/m^3 (the single injection strategy data has been superimposed on the same graph several times for comparative reasons)

As mentioned, the acquisition of the penetration data for cold air intake at 0.325, 0.425 and 0.625 *ms* dwell periods was conducted at 10 μs intervals. For convenience, Fig 6-17 shows the evolution of the penetration length for every 30 μs for both *LIF* and *Mie* images.

To appreciate the behaviour of the liquid spray penetration during the second phase of the split, reference is made to Fig 6-17 for the 0.425 *ms* dwell period study, at 100 *MPa* injection pressure, 2 *MPa* in-cylinder pressure and cold air intake corresponding to 350° *K* at *TDC*.

As expected, Fig 6-17 highlights the slow rate of evaporation at 350 *K* at *TDC*. At the end of an injection period, or the end of the first split, needle closure is not instant. As a result, the emerging spray out of the nozzle exit has considerably lower injection velocity, and, hence, penetration velocity. Therefore, the tail of the first split spray not only moves at a considerably lower velocity in comparison to the main body of the spray, but it could also contain large droplets.

In the current study, the average axial tail velocity of the first split was estimated at circa 5 *m/s* for the 100 *MPa* injection pressure condition from the *Mie* images.

With variable axial and radial droplet velocities along the spray axis, the air entrainment into the spray plume creates a highly heterogeneous spray structure. At the end of injection duration (when *t* = 0.8375 *ms* for 10 *mm^3* fuelling at 100 *MPa*

injection pressure), the spray structure expands further, more so where the spray droplet momentum is at its highest. However, with almost a negligible tail velocity and large droplets concentration close to the nozzle exit, the start of the second split for the relatively short dwell periods penetrates into the tail of the first, as shown in Fig 6-17 (at 1.2575 *ms* onwards). Collision and interaction between the tip of the second split and the tail of the first split could prevent a significant increase in the rate of penetration for the second split, due to slow movement of the tail of the first split spray. Thus, a reasonable agreement between the penetration of the first split (or the coinciding single injection strategy) and the second split for the earlier part of injection period is observed (Fig 6-16).

Further downstream of the nozzle exit (at a later stage of injection for the second split, as shown in Fig 6-16 and Fig 6-17), with the vanishing tail and directly into the wake created by the first split due to faster motion of the spray and enhanced air entrainment, an increased growth of the second split occurs, thus exceeding that of the previous split.

LIF,0.4175ms Mie,0.4175ms LIF,0.4475ms Mie,0.4475ms LIF,0.4775ms Mie,0.4775ms LIF,0.5075ms Mie,0.5075ms

LIF,0.5375ms Mie,0.5375ms LIF,0.5675ms Mie,0.5675ms LIF,0.5975ms Mie,0.5975ms LIF,0.6275ms Mie,0.6275ms
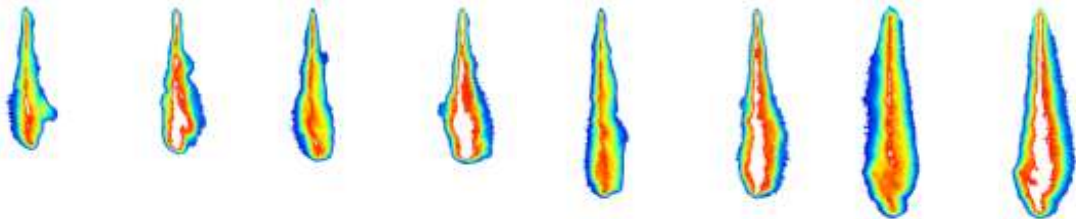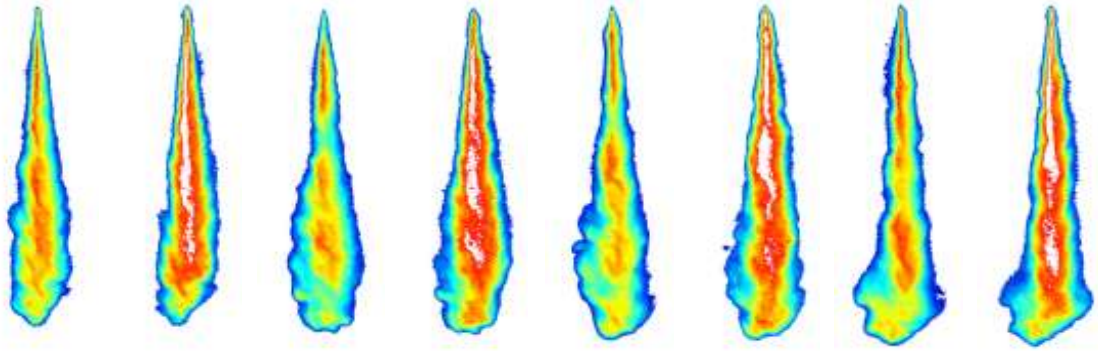
LIF,0.6575ms Mie,0.6575ms LIF,0.6875ms Mie,0.6875ms LIF,0.7175ms Mie,0.7175ms LIF,0.7475ms Mie,0.7475ms
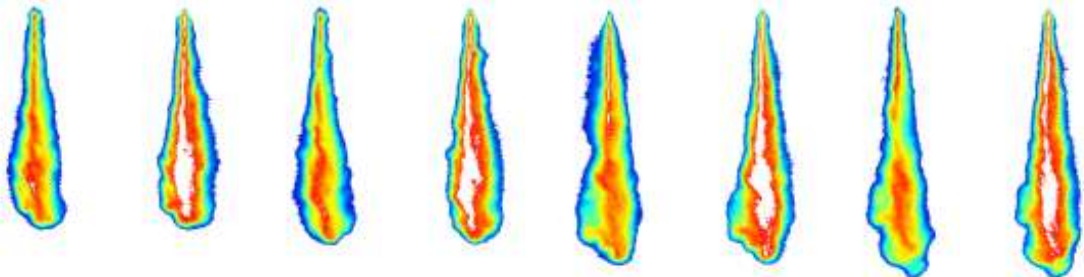
LIF,0.7775ms Mie,0.7775ms LIF,0.8075ms Mie,0.8075ms LIF,0.8375ms Mie,0.8375ms LIF,0.8675ms Mie,0.8675ms
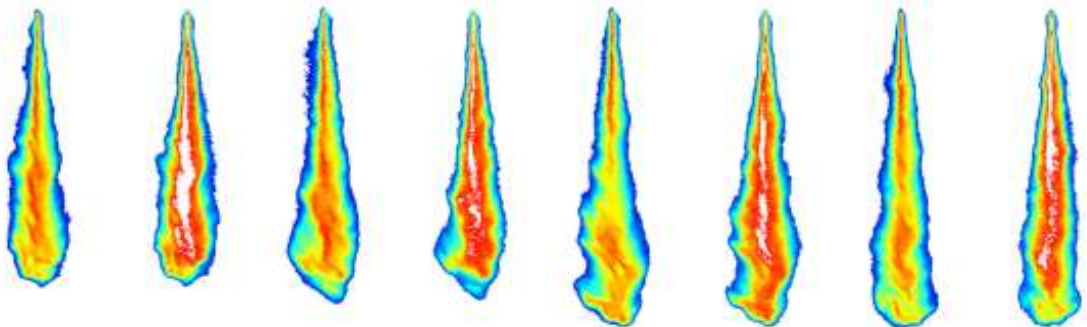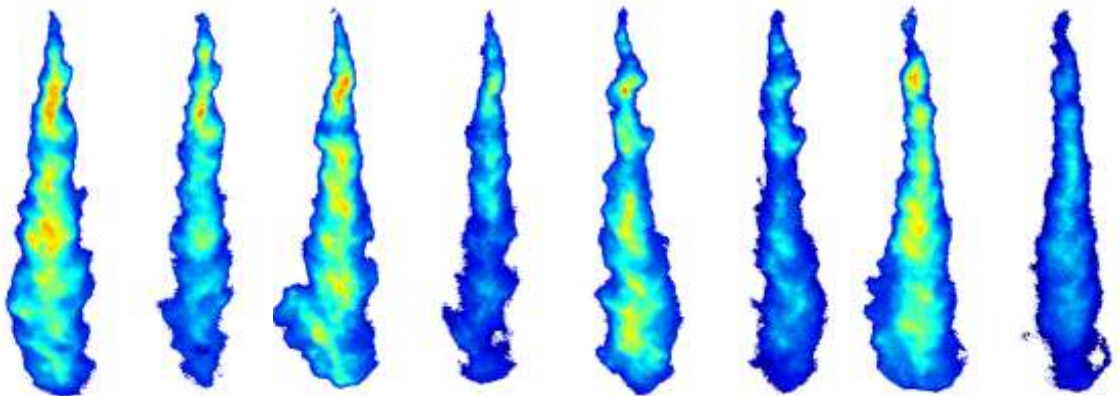
LIF,0.8975ms Mie,0.8975ms LIF,0.9275ms Mie,0.9275ms LIF,0.9575ms Mie,0.9575ms LIF,0.9875ms Mie,0.9875ms

LIF,1.0175ms Mie,1.075ms LIF,1.0475ms Mie,1.0475ms LIF,1.0775ms Mie,1.0775ms LIF,1.1075ms Mie,1.1075ms
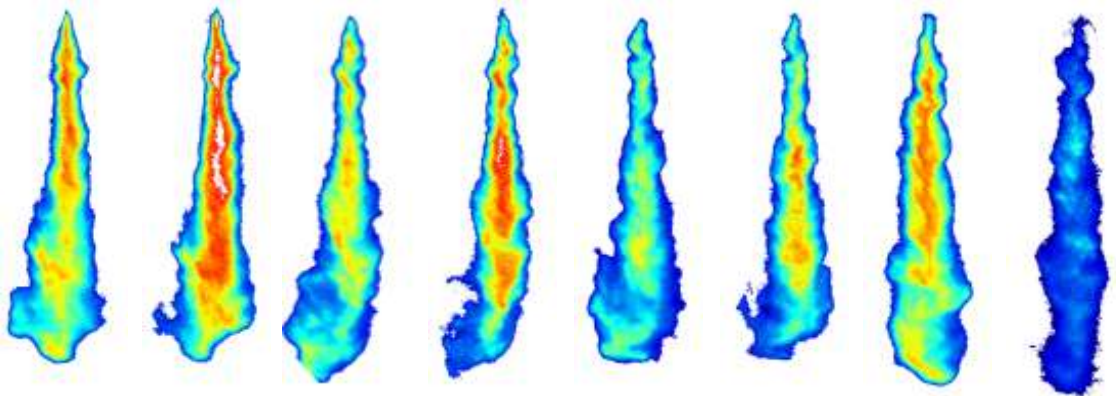
LIF,1.1375ms Mie,1.1375ms LIF,1.1675ms Mie,1.1675ms LIF,1.1975ms Mie,1.1975ms LIF,1.2275ms Mie,1.2275ms
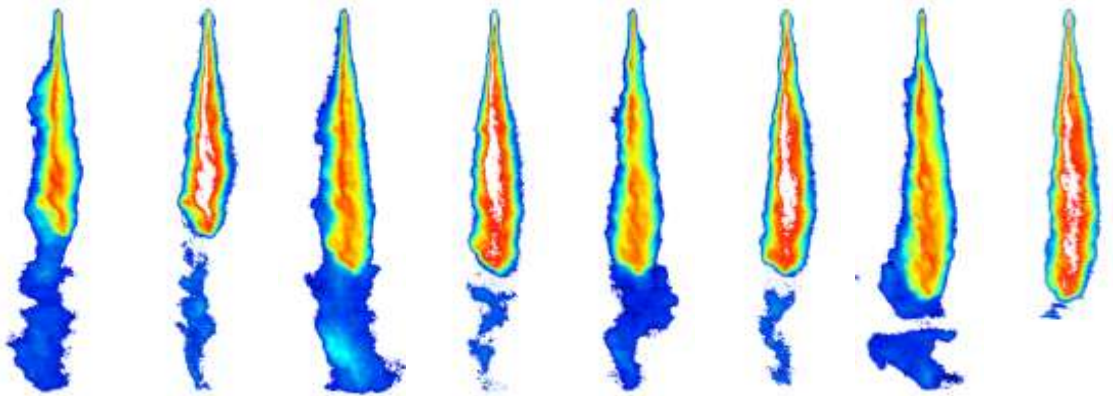
*LIF,1.2575ms Mie,1.2575ms LIF,1.2875ms Mie,1.2875ms LIF,1.3175ms Mie,1.3175ms LIF,1.3475ms Mie,1.3475ms*
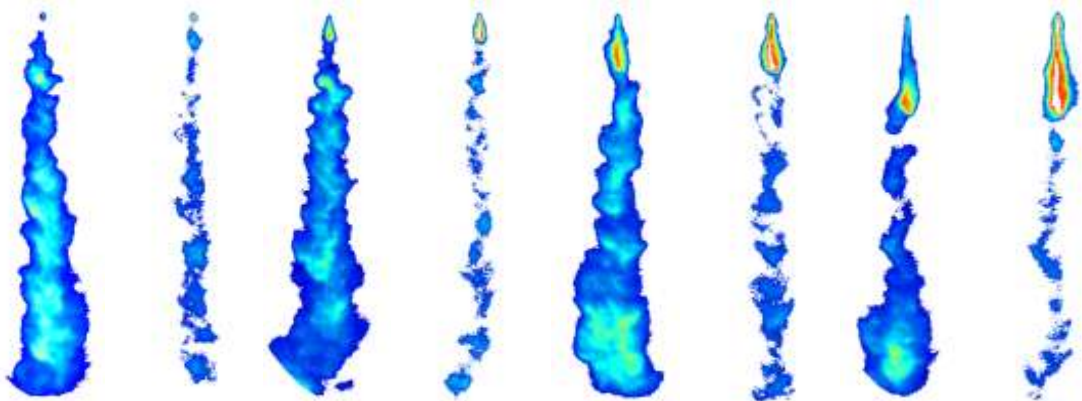
LIF,1.3775ms Mie,1.3775ms LIF,1.4075ms Mie,1.4075ms LIF,1.4375ms Mie,1.4375ms LIF,1.4675ms Mie,1.4675ms
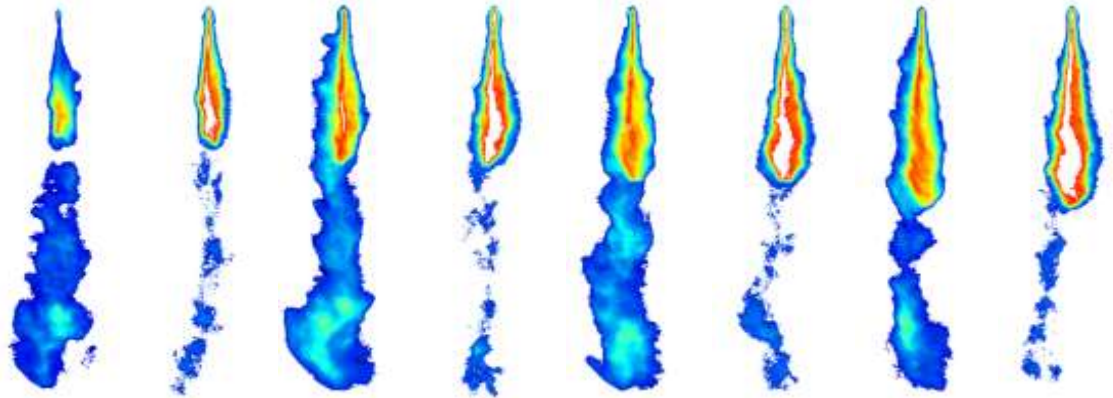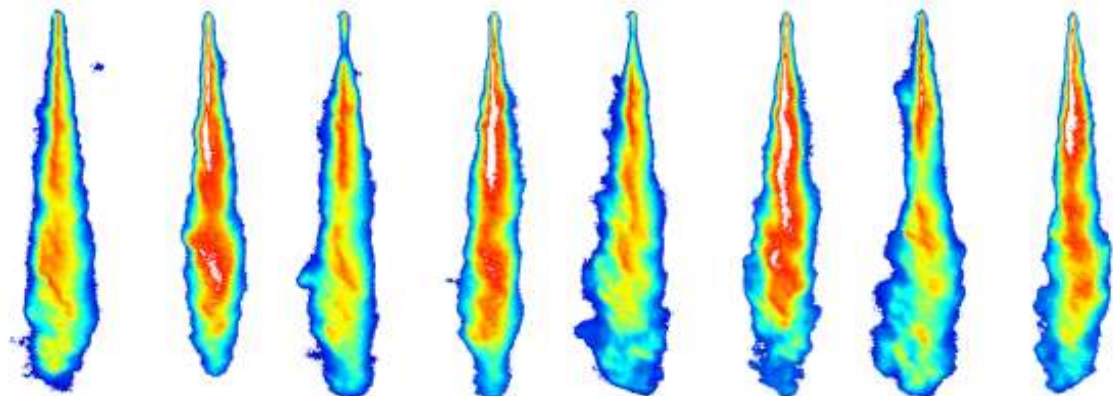
LIF,1.4975ms Mie,1.4975ms LIF,1.5275ms Mie,1.5275ms LIF,1.5575ms Mie,1.5575ms LIF,1.5875ms Mie,1.5875ms
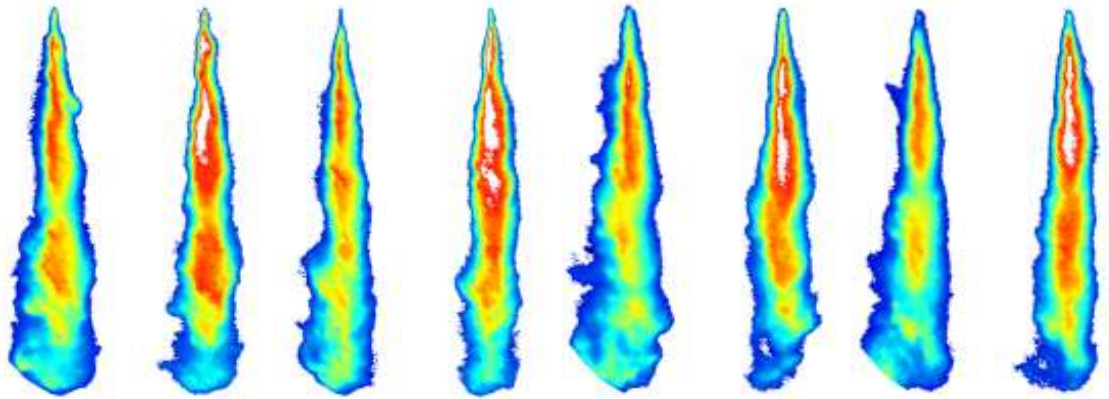
LIF,1.6175ms Mie,1.6175ms LIF,1.6475ms Mie,1.6475ms LIF,1.6775ms Mie,1.6775ms LIF,1.7075ms Mie,1.7075ms
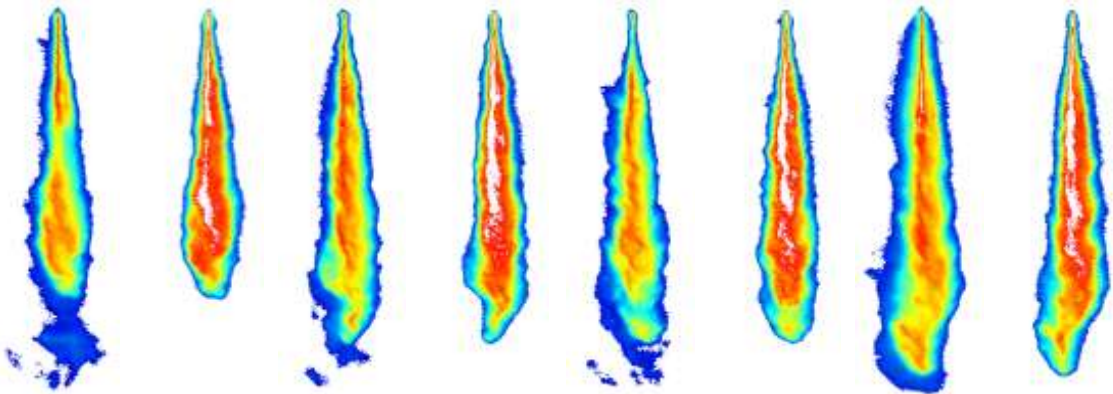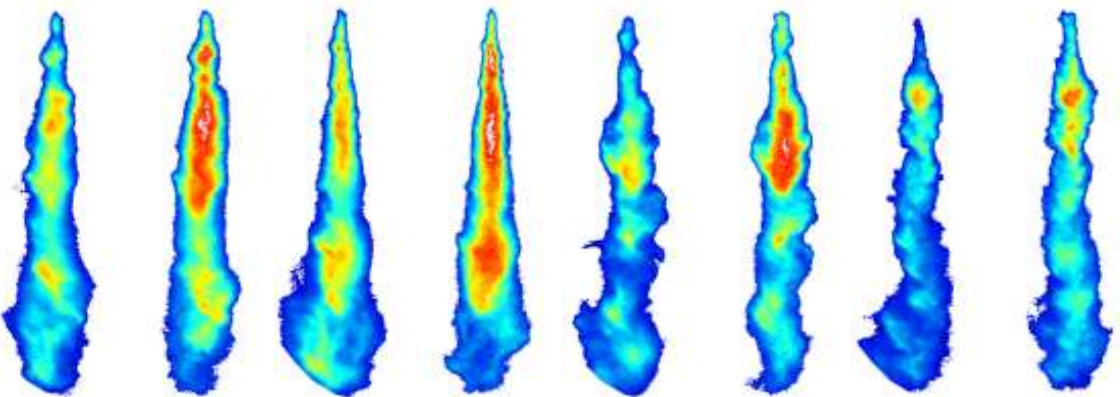
LIF,1.7375ms Mie,1.7375ms LIF,1.7675ms Mie,1.7675ms LIF,1.7975ms Mie,1.7975ms LIF,1.8275ms Mie,1.8275ms
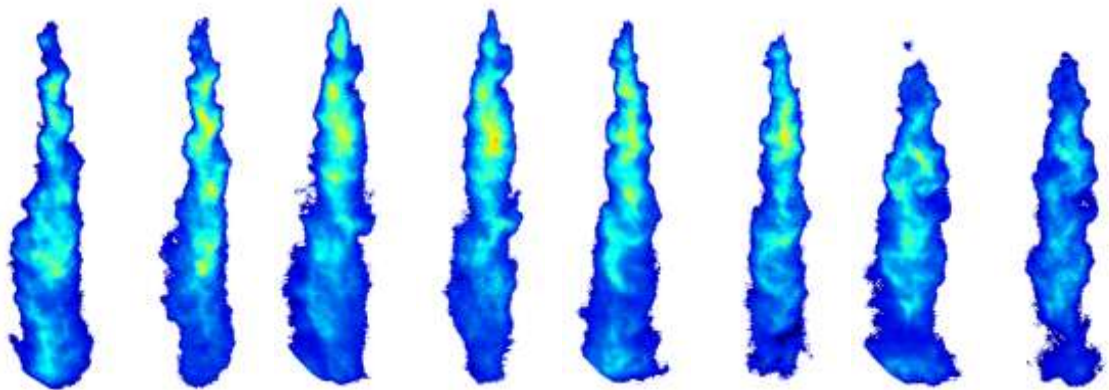
128

LIF,1.8575ms Mie,1.8575ms LIF,1.8875ms Mie,1.8875ms LIF,1.9175ms Mie,1.9175ms LIF,1.9475ms Mie,1.9475ms
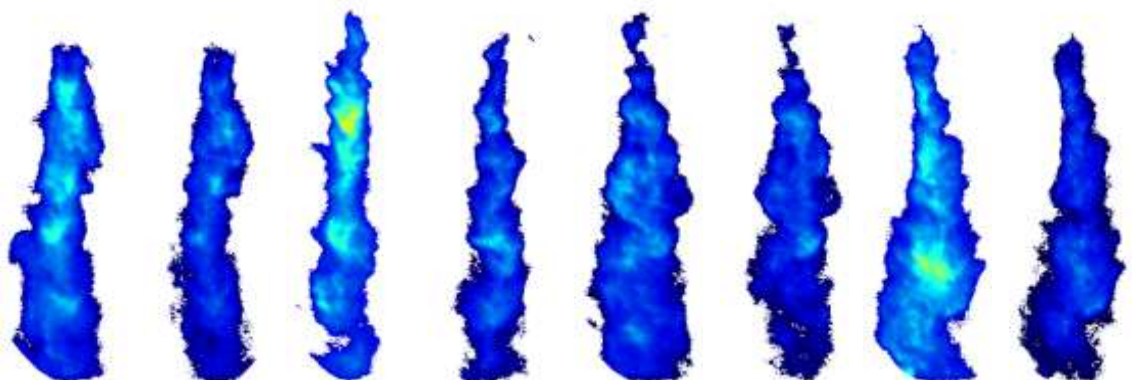

LIF,1.9775ms Mie,1.9775ms LIF,2.0075ms Mie,2.0075ms LIF,2.0375ms Mie,2.0375ms LIF,2.0675ms Mie,2.0675ms
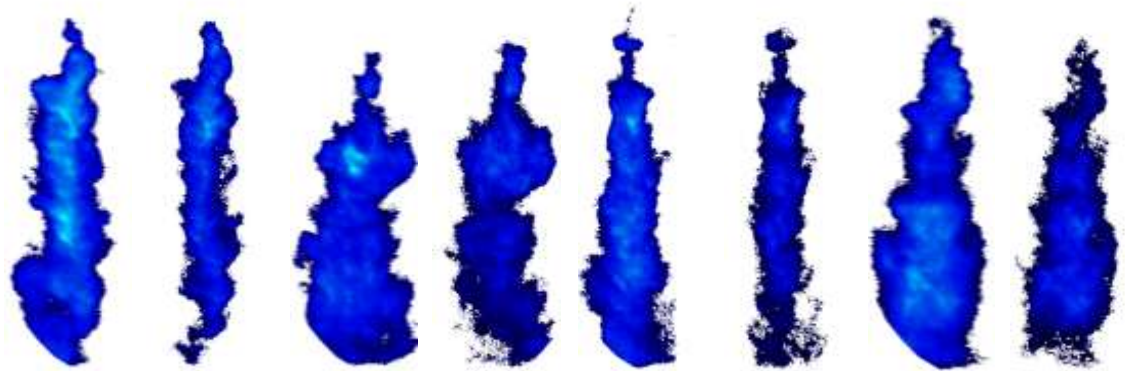

LIF,2.0975ms Mie,2.0975ms LIF,2.1275ms Mie,2.1275ms LIF,2.1575ms, Mie,2.1575ms LIF,2.1875ms Mie,2.1875ms

LIF,2.2175ms Mie,2.2175ms LIF,2.2475ms Mie,2.2475ms LIF,2.2775ms Mie,2.2775ms LIF,2.3075ms Mie,2.3075ms

LIF,2.3375ms Mie,2.3375ms LIF,2.3675ms Mie,2.3675ms LIF,2.3975ms Mie,2.3975ms LIF,2.4275ms Mie,2.4275ms

LIF,2.4575ms Mie,2.4575ms LIF,2.4875ms Mie,2.4875ms LIF,2.5175ms Mie,2.5175ms LIF,2.5475ms Mie,2.5475ms
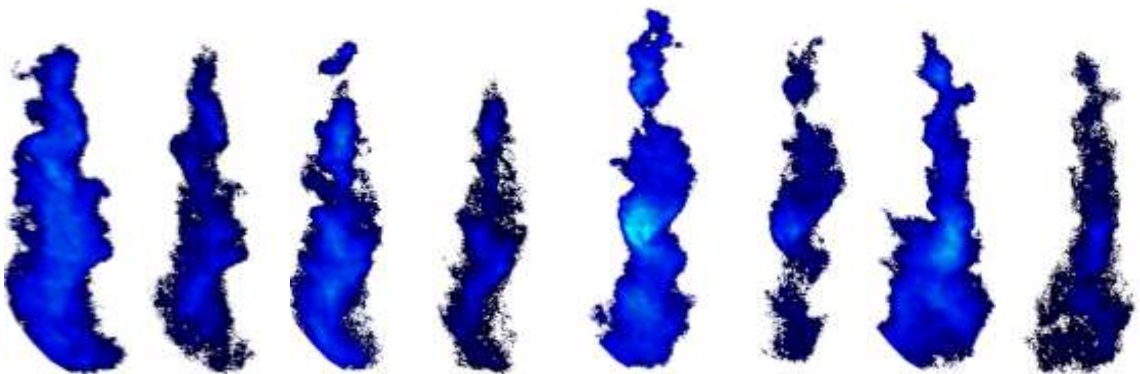
Fig 6-17. Evolution of the spray penetration (threshold images) at 0.425 ms dwell period; injection pressure 100 MPa; in-cylinder pressure 2 MPa; 20 kg/m³ in-cylinder density; cold air intake corresponding to 350°K at TDC; time increments 30μs intervals the blue markings indicate the start of injection; the actual end of injection are indicated in red; the colour chart below indicates the intensity and thus, the density concentration of the liquid/vapour spray
Very low ▐▬▬▬▬▬▬▌ *Very high*

With an increase in the dwell period, this tendency appeared to reduce. For the 0.825 *ms* dwell period case in particular, no liquid fuel interaction between the first and the second of the split sprays were observed, due to the dispersion and evaporation of the fuel droplets from the first split spray (Fig 6-18). Indeed, for the 0.825 *ms* dwell period at 20 *kg/m³* in-cylinder density, increased dispersion of vapour fuel eliminated the interaction between the liquid phase of the second split and the vapour phase from the first split. This suggests, once the wake or the gas flow induced by the first split vanishes completely, the tip velocity of the second split must equal that of the first split with no remaining mechanism to create the higher velocity for the second split to occur. It can be concluded that the 0.825 *ms* dwell period is too long for any droplet/spray interaction to take place (in the current experiment).

For the 0.325 *ms* dwell period (as can be seen from Fig 6-16), the penetration rate for the second split spray and the single injection strategy agrees well, particularly for the first 35 *mm* of the penetration length. This can be attributed to two splits penetrating in tandem for very short dwell periods (0.325 *ms*).

LIF,1.7575ms *Mie,1.7575ms* *LIF,1.8175ms Mie,1.8175ms LIF,1.8775ms Mie,1.8775ms LIF,1.9375ms Mie,1.9375ms*
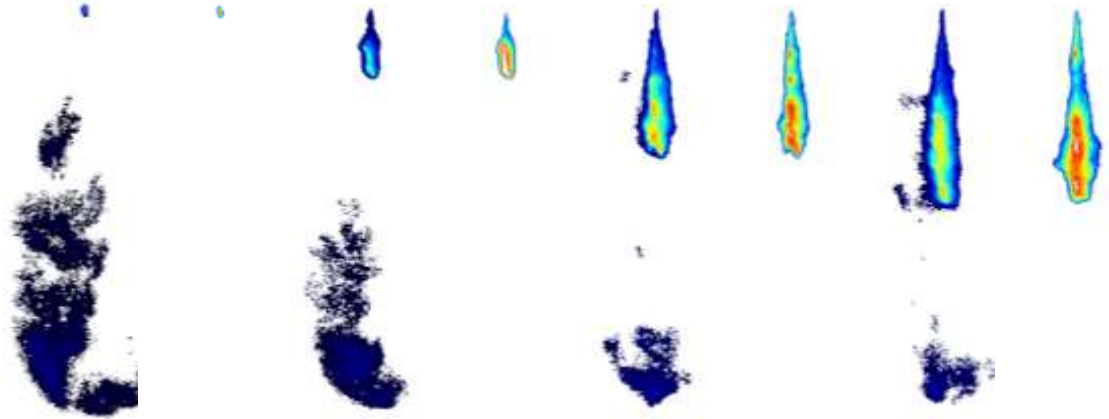

Fig 6-18. Evolution of the spray penetration at the start of the second injected split at 1.7575ms (blue marking) for the 0.825 ms dwell period; the injection pressure and the in-cylinder conditions are the same as Fig 6-16; time increments 60μs intervals; very low ▓▓▓▓ *very high*

For the 140 *MPa* injection pressure studies, the increased rate of penetration for the second of the splits in comparison to that of the first was also evident at the same in-cylinder conditions as for the 100 *MPa* injection pressure case (as shown in Fig 6-19). For the tail velocity at 140 *MPa* injection pressure, however, this was estimated at circa 6.5 *m/s* from the *Mie* images.
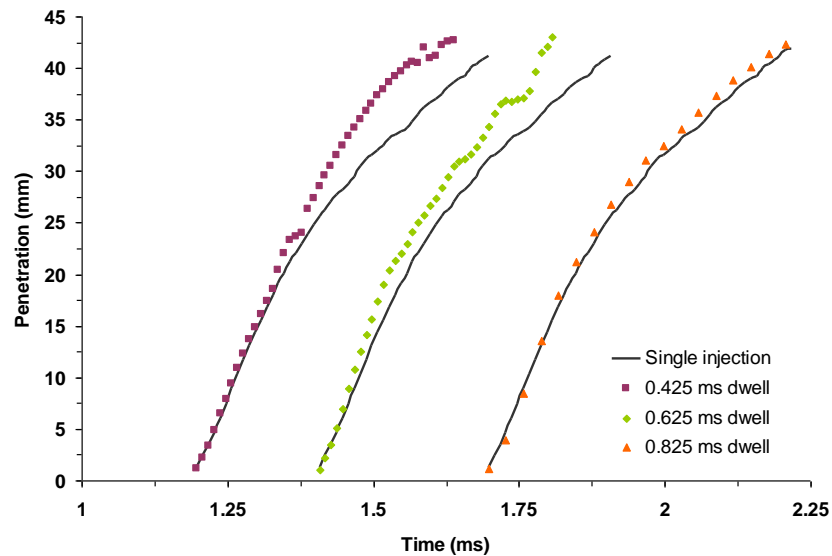

Fig 6-19. Comparison of the liquid spray tip penetration, for single and the second of the split injection strategies (processed from the Mie images); 140 MPa injection pressure; 20 kg/m³ in-cylinder density; 2MPa in-cylinder pressure; cold air intake (corresponding to 350 K at TDC); the single injection strategy data has been superimposed on the same graph several times for comparative reasons

131

6.3.2   Estimation of the Induced Gas Velocity

The comparison of the first split spray and the second split penetration can be used as a tool to analyse the heterogeneous structure of a single injection strategy. This is with reference to a relatively short dwell period if the penetration rate of the second split does not coincide with that of the first split spray. Since in the current study the penetration rate of the second split exceeds that of the first, the drag force opposing the second split must be lower than that for the first. In an initial quiescent environment and assuming that the air density is uniform, the spray motion of the first split results in an induced velocity profile along the spray axis for the gas in the wake. Thus, by comparison between tip velocity of the first split and the interacting tip velocity of the second split, the gas flow velocity induced by the first split can be estimated. Assuming the tip velocity of the spray is a function of the penetration position, the velocity differences are estimated by:

$$u_{tip,i} = \frac{dL_{p,i}}{dt}, \qquad\qquad\qquad (8.1)$$

$$\Delta u_{tip} = u_{tip,2} - u_{tip,1}. \qquad\qquad\qquad (8.2)$$

Where i represent the split number, u_{tip} is the tip velocity, and L_p is the spray tip position from the nozzle or the penetration distance, and Du_{tip} represents the difference in the tip velocity of the first (or the single injection strategy) and the second split. It is suggested that Du_{tip} is indicative of velocity of the gas at the position of the second split spray (Arai & Amagai 1997).

Fig 6-20 shows the tip velocity trends for the split injection strategies (0.425 ms and 0.625 ms dwell periods) at 100 MPa injection pressure. The velocity axis is shown to start with a negative value so that values close to zero are not obscured by the time axis.
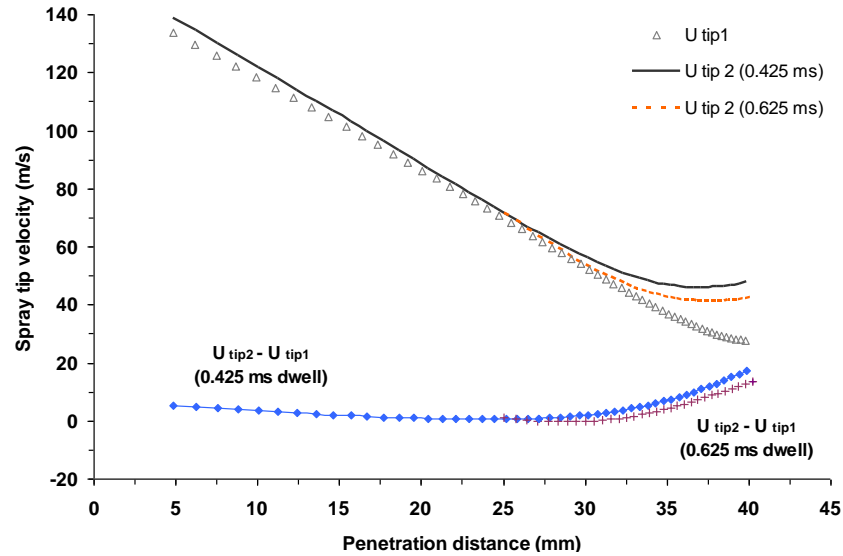
Fig 6-20. Tip velocity trend for first and the second of the split injection strategy; dwell periods of 0.425 and 0.625 ms; 100 MPa injection pressure; 20 kg m^{-3} in-cylinder density ; 2 MPa in-cylinder pressure; cold air intake (corresponding to 350 K at TDC)

As can be seen from Fig 6-20, during the initial stage of penetration, the magnitude of internal velocity of the gas phase is at circa 5 *m/s*, corresponding to the tail velocity of the first split. With the increase of the penetration distance downstream of the nozzle exit, the velocity of the second split (and Du_{tip}) first decreases (wake impingement, Prasad & Williamson (1997)) and then increases even further (cavity wake), indicating a reduction in the drag force. This is attributed to induced gas velocity growing in the direction of the penetrating spray. The maximum induced velocity measured for both dwell periods was at circa 40 *mm* downstream of the nozzle exit in the current study. The velocity differences for the 0.425 and 0.625 *ms* dwell periods were at circa 17 *m/s* and circa12 *m/s* respectively. This indicates a longer catch-up time (to reach the location of the first spray) for the 0.625 *ms* dwell due to a longer separation time involved. In the current study, the wake boundaries estimated by the induced gas velocity were at circa 23 and 32 *mm* downstream of the nozzle exit respectively.

It is clear from the above analysis that induced gas velocity in diesel sprays can exist in the wake of the first split.

6.3.3 The Effect of Dwell Period at High In-cylinder Pressures on Liquid Fuel Penetration

In the previous section it was concluded that the spray growth of the second split spray occurs within the gas flow induced by the first split, thus creating a mechanism for the tip velocity of the second split to exceed that of the first split spray velocity. This observation was made within and up to the first 45 *mm* of the penetration length due to the size limitation of the optical windows on the Proteus rig (as explained in Chapter 3). In the previous section at low in-cylinder pressure (2 *MPa*), it was assumed that the final tip position of the first split spray is caught up by the tip of the second split spray, in the absence of any significant evaporation during the later stage of spray growth. Arai & Amagai (1994) also observed the spray tip position of the first split spray being caught up by the tip of second split spray, with the exception that this phenomenon occurred at the same moment in time after start of first injected fuel portion. The authors named this behaviour the catch-up type.

They also recognised another type of spray pattern growth, namely the push-away type. The push-away type was described as the tip of the second split not catching up with the tip position of the first split spray due to the first split having a larger axial velocity.

In the current study, a third spray growth pattern is observed at high in-cylinder pressure (6 *MPa*) and expressed as the exceed type, where the tip penetration of the second split spray exceeds that of the final tip position of the first split spray (as was the case with Arai & Amagai (1994) catch-up type), but at a different time in space, as shown in Fig 6-21 and Fig 6-22.
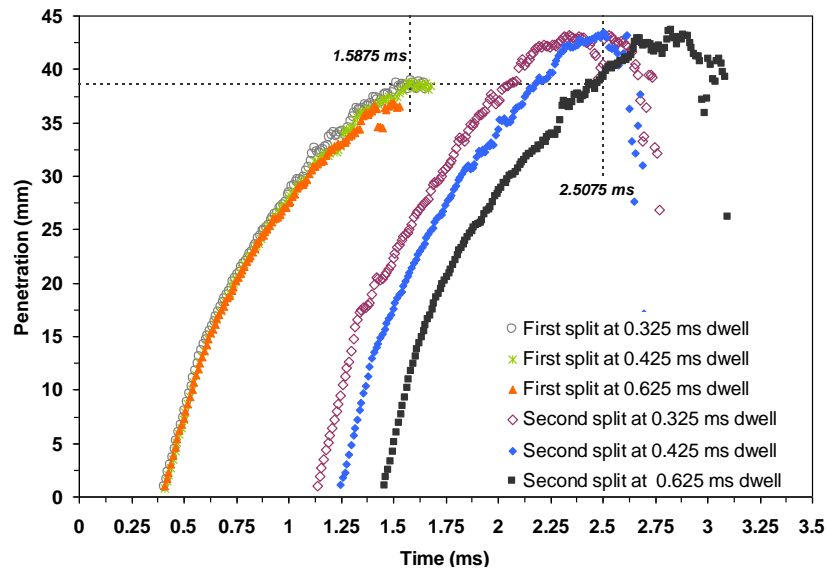
Fig 6-21. Comparison of the liquid fuel spray tip penetration for the split injection strategies showing the exceed type pattern (processed from the Mie images); 100 MPa injection pressure; 47 kg/m³ in-cylinder density; 6 MPa in-cylinder pressure; cold air intake (corresponding to 448 K at TDC)
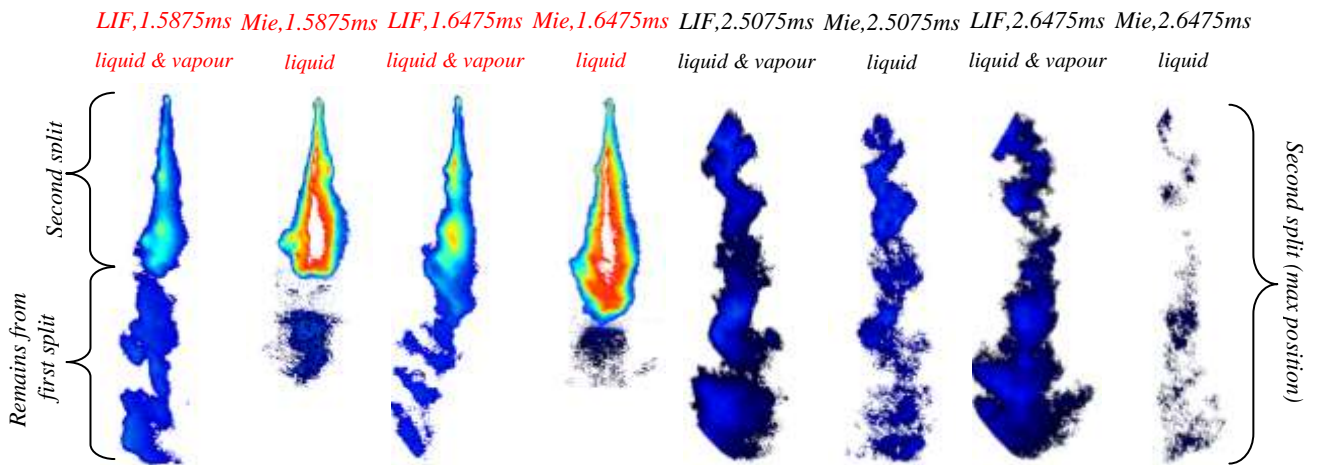

Fig 6-22. Typical images showing the liquid (Mie images) and the vapour/liquid (LIF images) spray tip penetration, for the split injection strategy at 0.425 ms dwell period; 100 MP injection pressure; 47 kg/m³ in-cylinder density; 6 MPa in-cylinder pressure (at TDC); cold air intake (corresponding to 448 K at TDC); the red marking indicates the first and second split spray; the black marking indicates the second split only; the colour chart below indicates the intensity and thus, the density concentration of the liquid/vapour spray; very low ▮▮▮▮▮▮ very high

As can be seen from Fig 6-22, the maximum penetration lengths for the 100 *MPa* injection pressure at 6 *MPa* in-cylinder pressure occur within the limits of the optical window.

Fig 6-23 also indicates the level of consistency between the first and the second of the split injection strategies with the injection rate pattern.
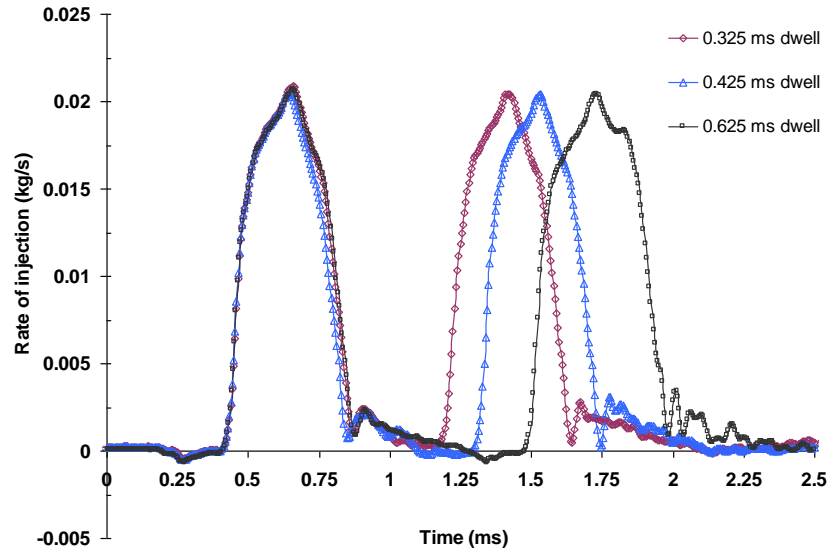
Fig 6-23. Comparison of the injection rate pattern for various split injection strategies at 100 MPa injection pressure; fuelling, 10 mm³ for each split

As in the low in-cylinder pressure case, for the 6 *MPa ICP*, the second of the splits is influenced by the gas flow induced by the first split, increasing the tip velocity of the second split spray. Moreover, in the current study, with the increase of in-cylinder gas pressure the in-cylinder gas temperature also increases (Tab 6-1). Hence, the introduction of the first injected spray in to the combustion chamber causes droplet heating and vapour fuel mass transfer to the surrounding gas (Abdelghaffar, 2005). Given sufficient time, the in-cylinder gas could become denser, due to liquid and vapour fuel mixture. This has two consequences on the injection of the second split spray; a reduction in the rate of evaporation (in the aftermath of the first split spray) due to fuel vapour pressure and cooling of the in-cylinder gas mostly due to the latent heat of evaporation, and an increase in the drag force due to increased density. However, in the current study, assumption is made that the local temperature is the dominant factor, and, thus, combined with higher spray tip velocity (due to induced gas by the first split spray), the resultant effect is longer penetration length for the second of the split sprays (Fig 6-21 and Fig 6-22).

The average increase in the final tip position of the second split spray in comparison with that of the first split (in the current study at 6 *MPa* in-cylinder pressure) was calculated at 12% for the 100 *MPa* injection pressure case. The downside to this effect is possible impingement of the piston crown and/or the cylinder wall chamber. This could lead to undesired unburned fuel and higher soot concentration (Crua 2002).

For the 140 *MPa* injection pressure as shown in Fig 6-24, similar results were observed to those expressed for the 100 *MPa* injection pressure case. However, due to higher injection velocity at 140 *MPa* injection pressure, the second split exceeded the view limitation of the optical window. Nevertheless, even with the aforementioned constraints, the resultant increase in penetration rate for the second split can be seen from Fig 6-25.
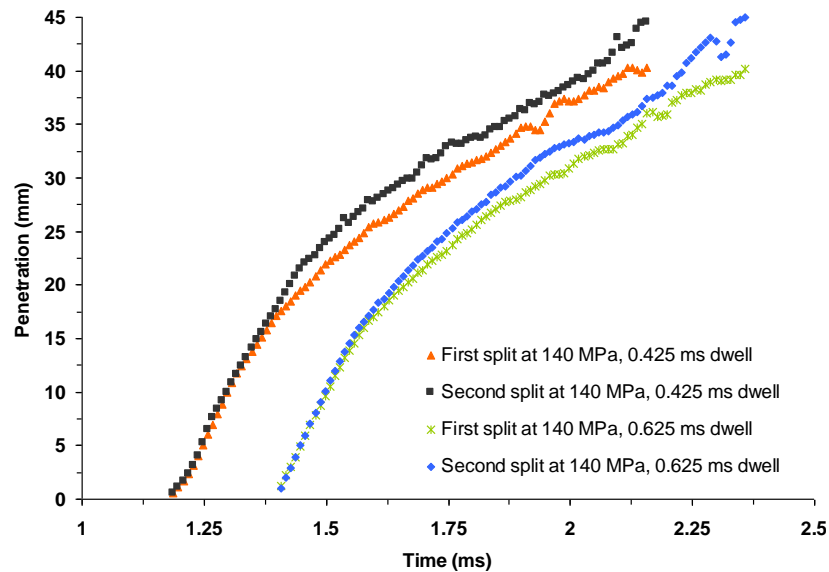

Fig 6-24. Comparison of the liquid spray tip penetration for the first and the second of the split injection strategy (processed from the Mie images); 140 MPa injection pressure; 47 kg/m³ in-cylinder density; 6 MPa in-cylinder pressure (at TDC); cold air intake (corresponding to 448 K at TDC); the data for the first split at 0.425 ms and 0.625 ms dwell periods has been offset for comparative reasons
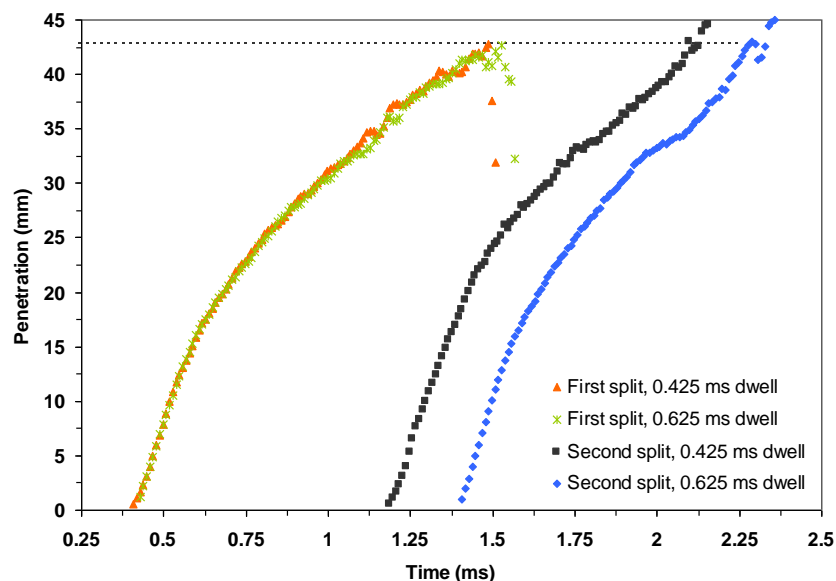

Fig 6-25. Comparison of the liquid spray tip penetration for the split injection strategies showing the exceed type pattern (processed from the Mie images); 140 MPa injection pressure; 47 kg/m³ in-cylinder density; 6 MPa in-cylinder pressure (at TDC); cold air intake (corresponding to 448 K at TDC)

6.3.4 The Effect of Hot Air Intake on Split Injection

For the hot air intake, the temperature of the charge was set to circa 375 *K* corresponding to a *TDC* temperature of 448 *K* at 2 *MPa* in-cylinder pressure, and 667 *K* at 6 *MPa* in-cylinder pressure respectively.

With the current experimental injector (Delphi), full needle lift occurs within approximately 0.15 *ms* from the rate of injection profiles (Chapter 3). During this period of time, the emerging liquid fuel out of the nozzle exits has a significantly lower discharge coefficient owing to reduced nozzle exit flow area. Within this period of time the liquid fuel core is assumed to be unbroken, and the penetration velocity during the transient break-up length is close to the injection velocity (Karimi et al., 2006; Arai et al., 1984; Dent, 1971). During this initial stage of injection, since the evaporation rate is very slow on the penetrating liquid core, the penetrating liquid jets of the first and the second of the splits coincide even for hot air intake (Fig 6-26). For the later stage of injection at 2 *MPa* in-cylinder pressure and hot air intake, no significant change to that emphasised with the cold air intake takes place (Fig 6-26 and 6-27); namely the gas flow induced by the first split spray increases the tip velocity of the second split spray.
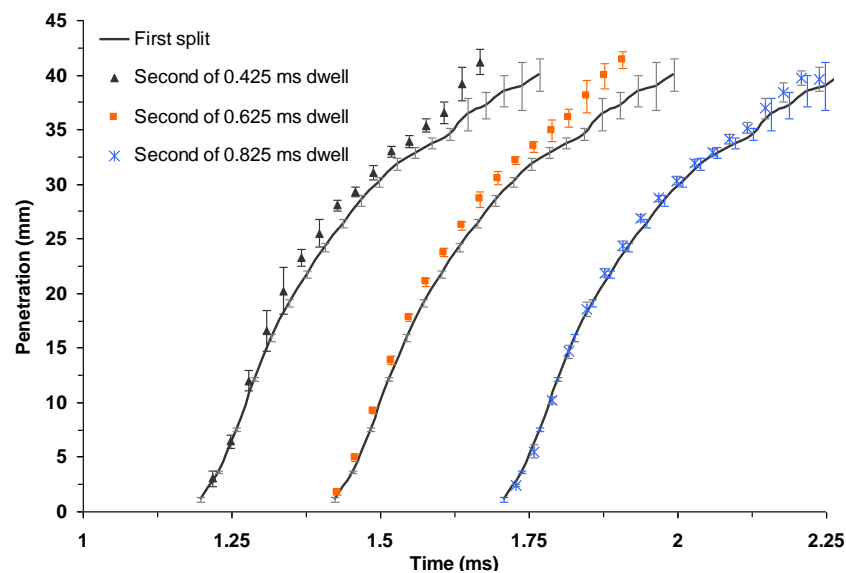

Fig 6-26. Comparison of the liquid spray tip penetration for the single and split injection strategy (processed from Mie images); the bars indicate the standard deviation; 140 MPa injection pressure; 16 kg/m³ in-cylinder density; 2 MPa in-cylinder pressure (at TDC); hot air intake (corresponding to 447 K at TDC); the data for the single injection strategy has been offset for comparative reasons
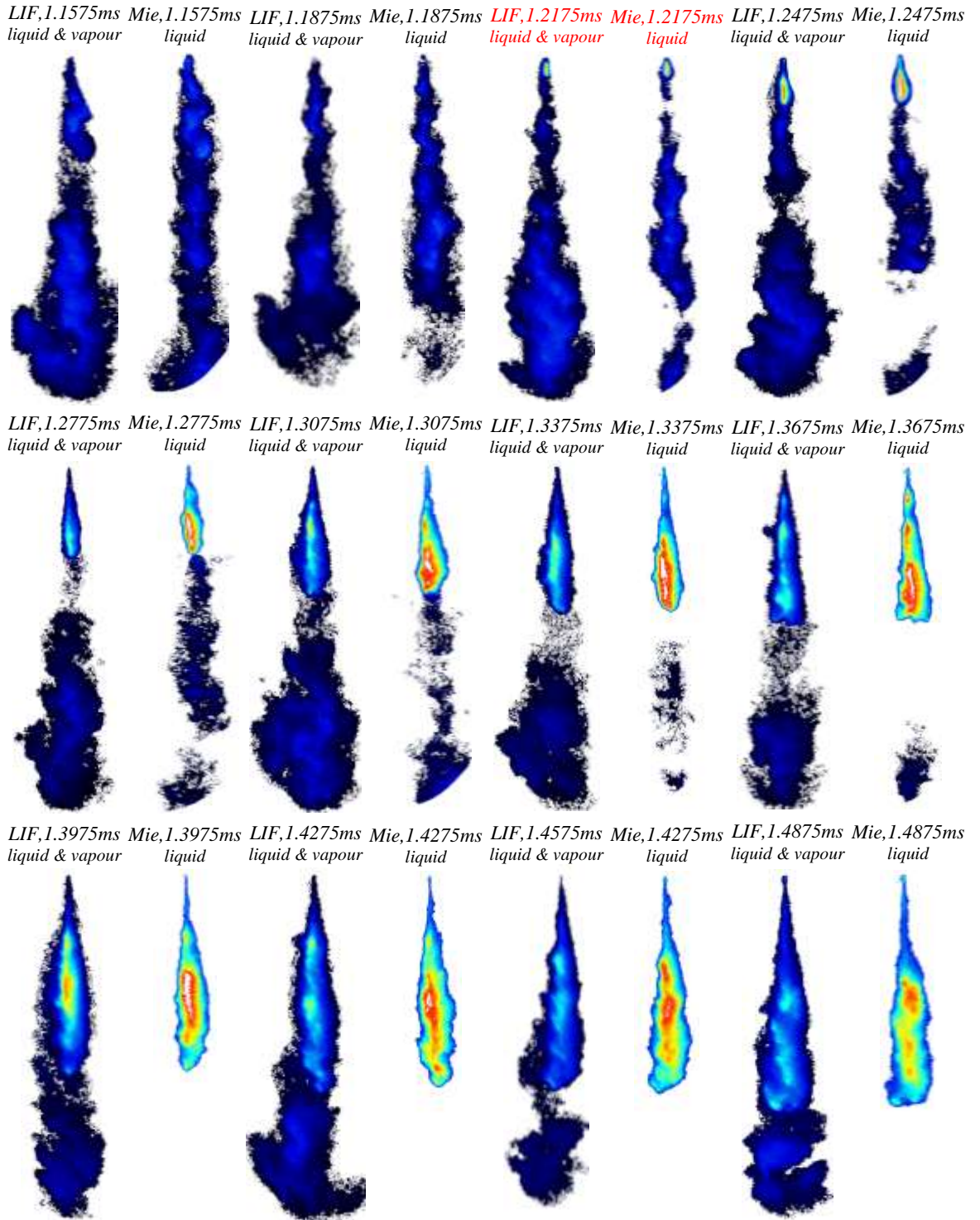
LIF,1.1575ms liquid & vapour   Mie,1.1575ms liquid   LIF,1.1875ms liquid & vapour   Mie,1.1875ms liquid   *LIF,1.2175ms liquid & vapour*   *Mie,1.2175ms liquid*   LIF,1.2475ms liquid & vapour   Mie,1.2475ms liquid

LIF,1.2775ms liquid & vapour   Mie,1.2775ms liquid   LIF,1.3075ms liquid & vapour   Mie,1.3075ms liquid   LIF,1.3375ms liquid & vapour   Mie,1.3375ms liquid   LIF,1.3675ms liquid & vapour   Mie,1.3675ms liquid

LIF,1.3975ms liquid & vapour   Mie,1.3975ms liquid   LIF,1.4275ms liquid & vapour   Mie,1.4275ms liquid   LIF,1.4575ms liquid & vapour   Mie,1.4275ms liquid   LIF,1.4875ms liquid & vapour   Mie,1.4875ms liquid

Fig 6-27. Typical images showing the liquid (Mie images) and the vapour/liquid (LIF images) spray tip penetration, for the split injection strategy at 0.425 ms dwell period;140 MPa injection pressure; 16 kg/m^3 in-cylinder density; 2 MPa in-cylinder pressure (at TDC); hot air intake (corresponding to 448 K at TDC); the red marking indicates the start of the second split spray; the colour chart below indicates the intensity and thus, the density concentration of the liquid/vapour spray
Very low   *Very high*

With the increase of exit flow area (due to needle lift), the discharge coefficient, the injection velocity and, hence, the penetration velocity increase. Therefore, the increase in the penetration velocity has the tendency to increase the atomisation process and the air entrainment within the spray.

With the increase of the intake gas temperature and high in-cylinder pressures (at 6 *MPa*), the evaporation of fuel droplets significantly increases. Therefore, a reduction in the exchange of momentum between evaporating droplets and the surrounding air could occur (additional images can be found in Appendix D). The resultant effect would be reduced air entrainment into the conventional diesel fuel spray as well as the first of a multiple injection strategy. Therefore, this would significantly lower the induced air entrainment by the first split into the second split. Fig 6-28 shows the level of agreement between the first and the second of the split injection strategies for 6 *MPa* in-cylinder pressure, with a *TDC* temperature of 667 *K*. The same figure also shows the standard deviation for 15 sets of spray penetration data. Fig 6-29 also highlights the increased rate of liquid evaporation when compared to the 2 *MPa* in-cylinder pressure case in Fig 6-27. It must be emphasised at this stage that the *LIF* signal for the *LIF* images shown (for the liquid and vapour penetration) at high in-cylinder pressure and temperature (namely Fig 6-29) are subjected to oxygen and temperature quenching (electron energy transfer) (Seitzman & Hanson, 1993). Hence, for the *LIF* images the signal intensities are captured at a reduced magnitude.
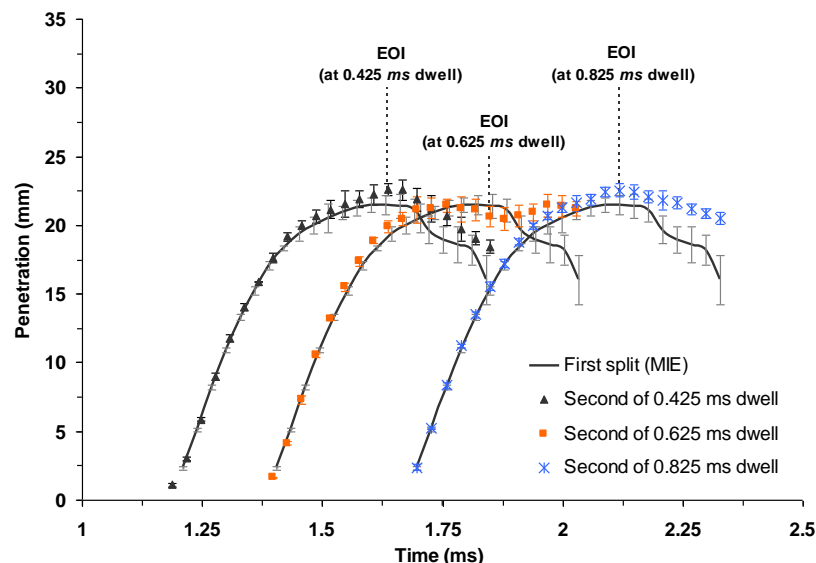

Fig 6-28. Comparison of the liquid spray tip penetration for the single and split injection strategy; the bars indicate the standard deviation; 140 MPa injection pressure; 31 kg/m³ in-cylinder density; 6 MPa in-cylinder pressure (at TDC); hot air intake (corresponding to 667 K at TDC); the data for the single injection strategy has been offset for comparative reasons
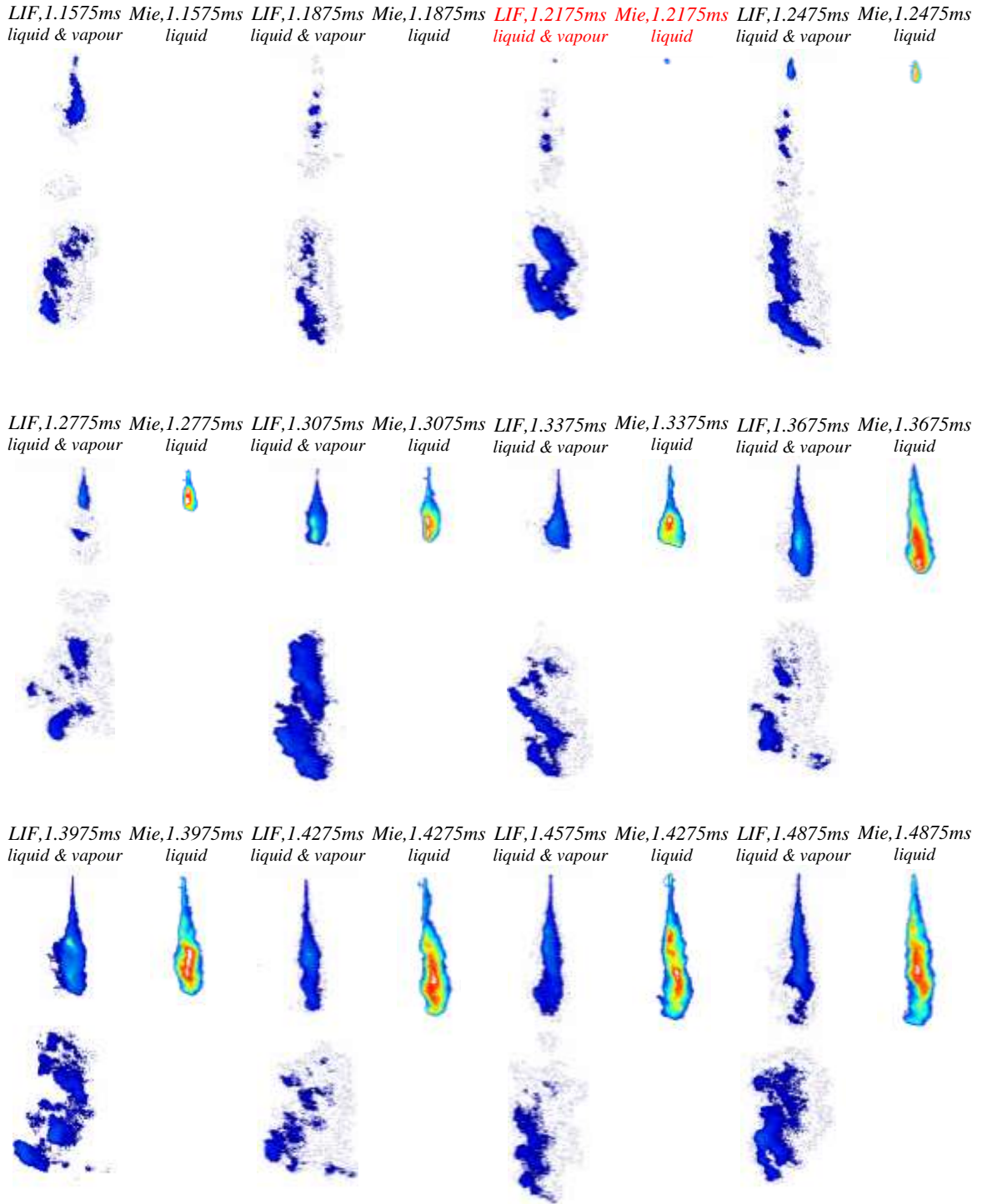
LIF,1.1575ms Mie,1.1575ms LIF,1.1875ms Mie,1.1875ms *LIF,1.2175ms Mie,1.2175ms* LIF,1.2475ms Mie,1.2475ms
liquid & vapour *liquid* *liquid & vapour* *liquid* *liquid & vapour* *liquid* *liquid & vapour* *liquid*

LIF,1.2775ms Mie,1.2775ms LIF,1.3075ms Mie,1.3075ms LIF,1.3375ms Mie,1.3375ms LIF,1.3675ms Mie,1.3675ms
liquid & vapour *liquid* *liquid & vapour* *liquid* *liquid & vapour* *liquid* *liquid & vapour* *liquid*

LIF,1.3975ms Mie,1.3975ms LIF,1.4275ms Mie,1.4275ms LIF,1.4575ms Mie,1.4275ms LIF,1.4875ms Mie,1.4875ms
liquid & vapour *liquid* *liquid & vapour* *liquid* *liquid & vapour* *liquid* *liquid & vapour* *liquid*

Fig 6-29. Typical images showing the liquid (Mie images) and the vapour/liquid (LIF images) spray tip penetration, for the split injection strategy at 0.425 ms dwell period; 140 MPa injection pressure;31 kg/m³ in-cylinder density; 6 MPa in-cylinder pressure (at TDC); hot air intake (corresponding to 667 K at TDC); the red marking indicates the start of the second split spray; the colour chart below indicates the intensity and thus, the density concentration of the liquid/vapour spray

Very low ▐██████████▌ *very high*

141

6.3.5 Vapour Dispersion

The results described in the previous sections have been mainly focused on liquid fuel penetration data gained by the *Mie* scattering technique. In the current section, the result of vapour penetration will be presented. However, since the current method of processing the *LIF* images is unable to differentiate between the vapour position of the first split and the vapour portion of the second split phase, reference will be made to the actual images where appropriate. Fig 6-30 shows the results for the liquid and vapour penetration data gained by simultaneous *LIF* and *Mie* experiments. The differentiation between the liquid and vapour penetration (in the current study) is assumed to take effect with the divergence of the data shown as different markers (Fig 6-30). It should also be remembered that the limit of the optical window is 45 *mm* downstream of the nozzle exit. As can be seen from Fig 6-30, for 20 *kg/m³* in-cylinder density (2 *MPa* in-cylinder pressure), vapour penetration closely follows the liquid path and can be considered negligible. At 47 *kg/m³* in-cylinder density (6 *MPa* in-cylinder pressure), however, due to an increase in the in-cylinder gas temperature, the separation between the liquid and the vapour phases is more apparent, starting at circa 35 *mm* downstream of the nozzle exit. This is in keeping with the previous results and hypothesis (in section 6.3.3), that due to enhanced evaporation of the first split spray, the second split penetrates into a cooler vapour/gas stream (Fig 6-31), reducing the tip evaporation of the second split spray, thus exceeding in length when combined with higher tip velocity.
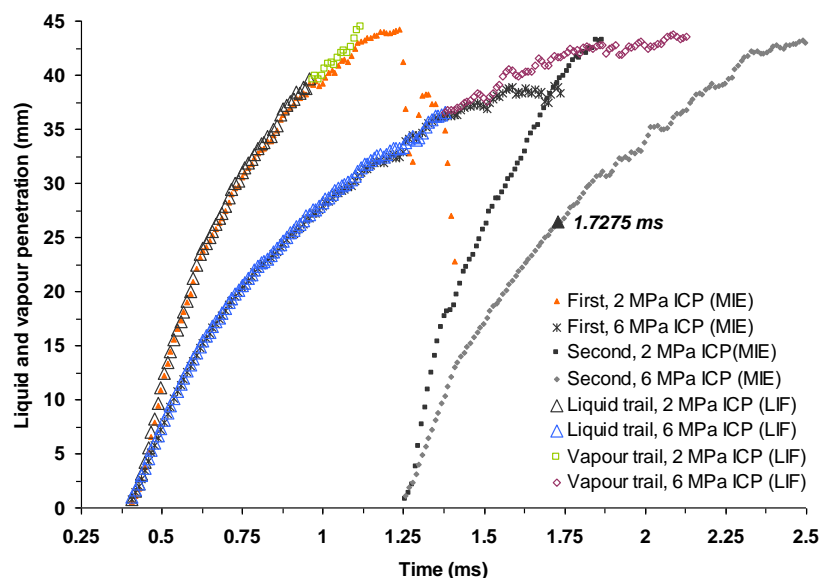

Fig 6-30. Liquid and vapour penetration at 2 and 6 MPa in-cylinder pressure; 100 MPa injection pressure; 0.425 ms dwell period; Cold air intake
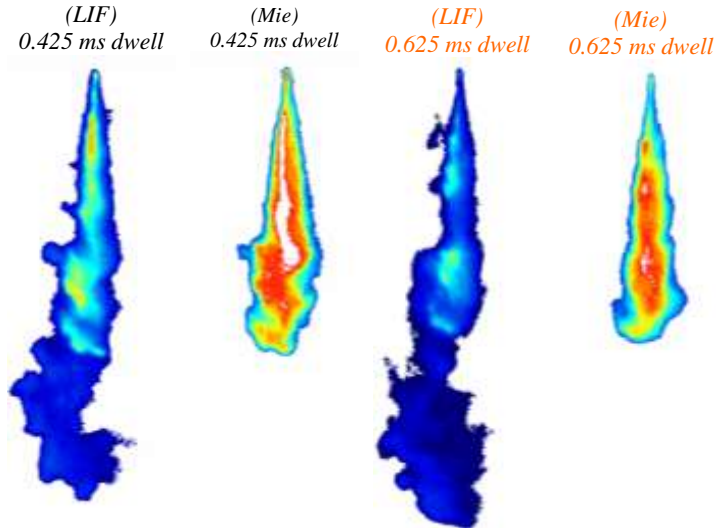
Fig 6-31. Image of liquid (Mie) and vapour (LIF) penetration for the 2 dwell periods; 0.47 ms after the start of the second split spray (at 1.7275 ms, the same as the above figure); 100 MPa injection pressure; 47 kg/m³ in-cylinder density; 6 MPa in-cylinder pressure; cold air intake (corresponding to 448 K at TDC); very low ▥ *very high*

Results for the hot air intake at 0.425 *ms* dwell period are presented in Fig 6-32, for 16 and 31 *kg/m³* in-cylinder gas density conditions, corresponding to 2 *MPa* and 6 *MPa* in-cylinder pressure respectively. As can be seen, for 2 *MPa* ICP with an equivalent in-cylinder gas temperature of 448 *K* (16 kg/m³ in-cylinder density), the start of evaporation occurs at circa 32 *mm* downstream of the nozzle exit. Interestingly, this is almost at the same position as for the cold air intake at 6 *MPa* in-cylinder pressure, and the same estimated *TDC* temperature (448 *K*). This phenomenon further suggests the dominance of local (jet stream) temperature as an additional means for the second split spray to propagate further (Fig 6-26 and 6-27).
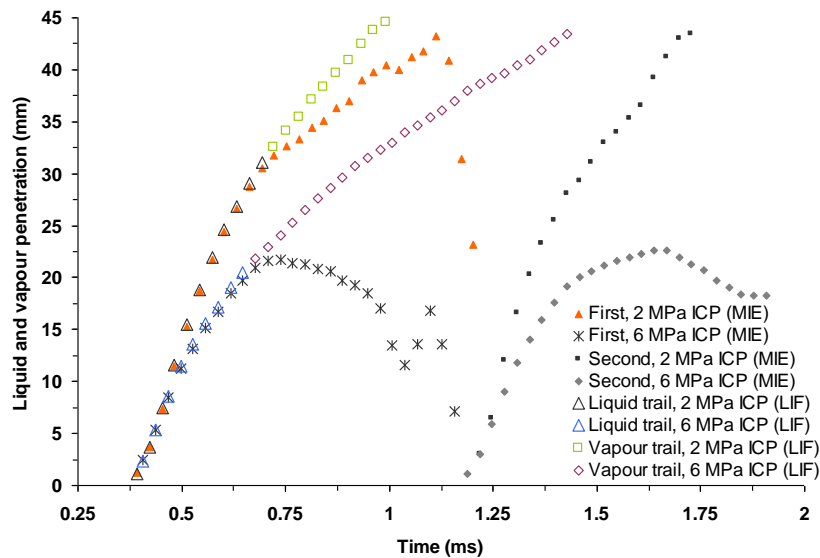
Fig 6-32. Liquid and vapour penetration for hot air intake; 140 MPa injection pressure; 0.425 ms dwell period

Up to now from the *LIF* images, the vapour fuel distribution in the leading region of the liquid fuel penetration has been covered. However, considering the images shown in the current chapter, and Fig 6-33, there is strong evidence of vapour fuel alongside the penetrating liquid spray (for the first split spray), starting with a thin or an almost non-existent layer and progressively increasing in thickness. With the liquid fuel spray reaching its stable length, the vapour phase continues to penetrate across the chamber (Fig 6-33).
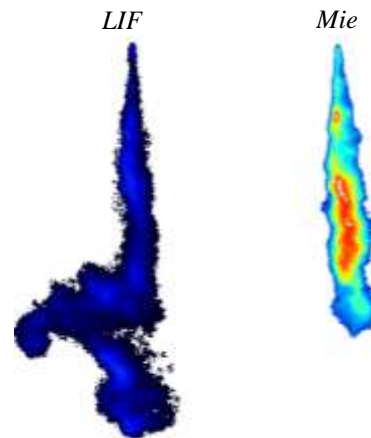
Fig 6-33. Liquid and vapour propagation for the first of the split injection strategy; 100 MPa injection pressure: 31 kg/m³ in-cylinder density; 6 MPa in-cylinder pressure; hot air intake (corresponding to 667 K at TDC); 0.425 ms dwell; the images shown are 0.9475 ms after start of injection trigger

Whilst the vapour fuel is penetrating downstream of nozzle exit, the width of the vapour spreads in an approximately linear manner. The resultant effect is a width considerably wider than that of the liquid spray widest point, by an axial distance just upstream of the maximum liquid penetration (Fig 6-33).

Dec (1997) and Naber & Siebers (1996) also report similar results, indicating vapour fuel distribution alongside the liquid spray. Furthermore, the coherent structure of the vapour phase appears to have a nearly constant cone shape for a given operational condition (Fig 6-17 and 6-27). This phenomenon appears to start a short distance downstream of the nozzle exit and spreads outwards continuously with increasing axial direction.

Fig 6-34 shows the effect of in-cylinder gas pressure/density and the injection pressure on the rate of vapour penetration. From the LIF images, the vapour penetration is found to be subjected to the same effect as the liquid fuel propagation; namely an increase in the rate of penetration results from a decrease in the in-cylinder

gas density and an increase in the injection pressure. Also, a decrease in the in-cylinder density helps to promote the vapour width dispersion but a lower vapour fuel concentration (Fig 6-27). Consequently, this has the tendency to reduced chances of auto-ignition. With an increase in the in-cylinder gas density/pressure, the dispersion and diffusion of vapour fuel will also reduce where there is a sharp well-defined boundary (Fig 6-27 and Fig 6-29/6-31) separating this relatively uniform mixture from the surrounding air. It is quoted that, "near stoichiometric mixtures occur only in a very narrow region at the edges, and therefore contains only a small fraction of the premixed fuel" (Dec, 1997). Therefore, although the likelihood of auto-ignition will increase for high in-cylinder pressure conditions, the premix burn will probably be fuel-rich. In the current experiment, the assumption for the concentration of the vapour fuel is taken based on the intensity of the *LIF* signal being proportional to the mass fraction of the fuel (Le Gal et al., 1999).
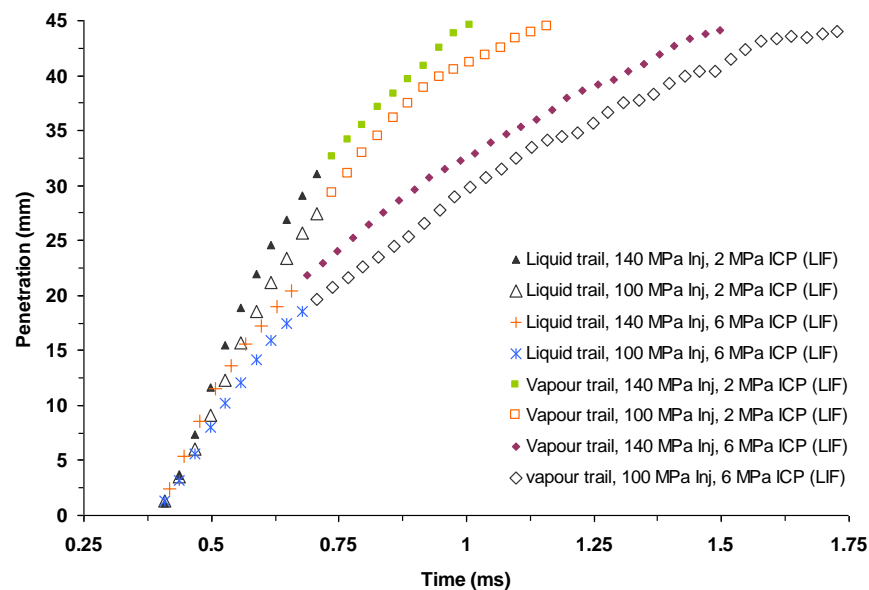
Fig 6-34. Evolution of liquid and vapour penetration for various injection and in-cylinder pressure; hot air intake (at 2 MPa ICP, 16 kg/m³ in-cylinder density, 448 K at TDC, and for 6 MPa ICP, 31kg/m³, 667 K at TDC); 0.425 ms dwell period

As explained, as the in-cylinder gas density increases due to increased in-cylinder gas pressure, the vapour phase expands slowly and consequently gathers into pockets where conditions for auto-ignition can be more favourable. Hence, from this reasoning, it is supposed that due to slow propagation of vapour fuel at high in-cylinder densities, the effect of cold fuel being added during the second split remains

significant for a longer time, resulting in an overall colder vapour that may require additional time to reach auto-ignition conditions. However, it is possible for the vapour fuel belonging to the first injected split to increase in dispersion and propagation, if the in-cylinder gas is further disturbed by the motion of the second split spray, resulting in a more homogeneous mixture.

The auto-ignition and ignition sites of the diesel vapour fuel were observed by Crua (2002) downstream of the liquid spray. The author reports occasional ignition sites on the periphery of the jet, particularly at high in-cylinder pressures where the concentration of the vapour fuel is high as opposed to low in-cylinder pressure conditions. These observed locations of auto-ignition sites by Crua (2002) are consistent with the computer simulations of Sazhina et al. (2000), and the observed vapour sites and concentrations for high in-cylinder densities in the current study.

With an increase of in-cylinder gas density due to increased in-cylinder gas pressure, the ignition delay increases due to a reduction in the equivalence ratio (Sazhina et al., 2000). This gives rise to the expected chemical delay (Crua 2002). However, most often, the chemical delays in diesel engines are much smaller than physical delays (Sazhin et al., 2001a) which are effectively the time taken for the sum of penetration, droplet break-up, evaporation and mixing with the surrounding air to occur.

6.3.6   Comparison of the High Speed Video (*HSV*) and the *Mie* Scattering Technique

The results described in this section relate to the differences in the definition of the penetration length and the techniques applied for the study of split injection strategy. For the high speed video (*HSV*), the experimental set-up is described in Chapter 5. However, the results shown in this section for *HSV* technique are the mean values of 10 different cycles.

Fig 6-35 and Fig 6-36 show the penetration lengths for two definitions with the following description.

- *HSV* - the furthest spray distance from the nozzle that is unbroken (Fig 5-2).

- *Mie* scattering - the distance of the parcel that precedes the farthest length downstream of the nozzle exit.

The rationale for the study of unbroken portion of the spray was to understand the behaviour and to some degree the onset of maximum air entrainment, and in what is considered as the critical length, where cluster shedding starts to occur. Nevertheless, as can be seen from Fig 6-35 and Fig 6-36, the agreement between two different techniques up to the point of cluster shedding is excellent. This agreement was uniform throughout the experiment (additional profiles can be found in Appendix D).
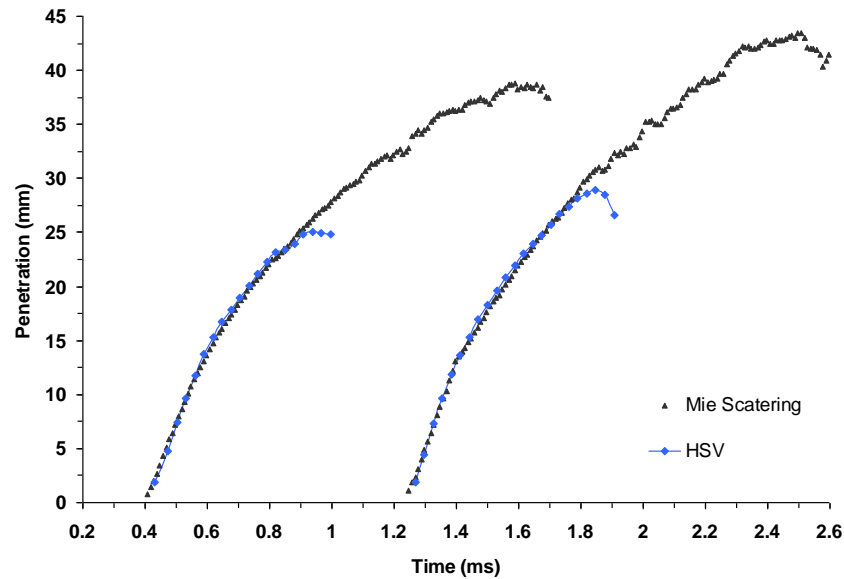

Fig 6-35. Comparison of the penetration length for split injection strategy with HSV and Mie scattering technique; 100 MPa injection pressure; 6 MPa in-cylinder pressure: 47 kg/m³ in-cylinder density; cold air intake (corresponding to 448 K at TDC); 0.425 ms dwell period
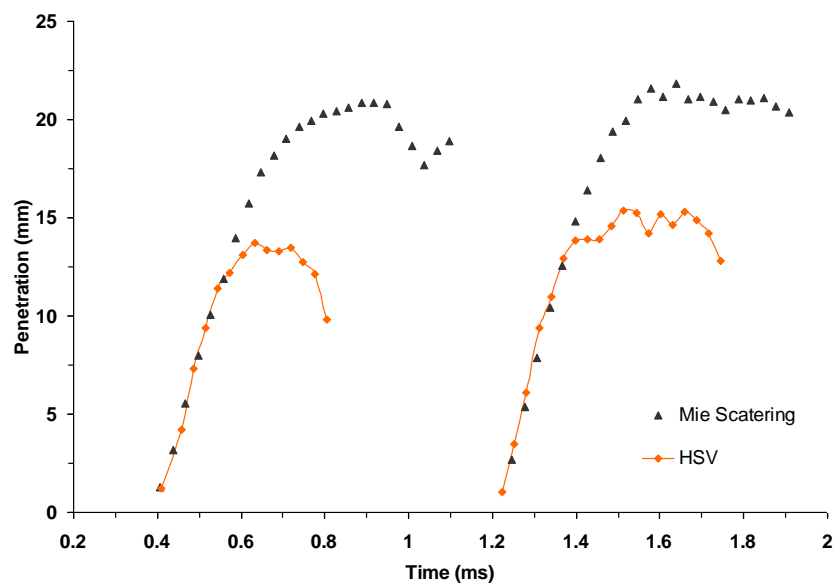
Fig 6-36. Same as Fig 6-37, with the exception of hot air intake (corresponding to 448 K at TDC); 31 kg/m³ in-cylinder density

147

6.4   CONCLUSIONS OF CHAPTER 6

The results obtained via simultaneous Planar Laser Induced Fluorescence (*PLIF*) and *Mie* scattering technique throughout the evolution of liquid and vapour phase for a range of injection and in-cylinder pressures conditions has been studied. The main conclusions drawn from the above analysis are as follows.

For multiple injection strategy, an additional parameter (to conventional diesel spray) is the injection dwell period influencing the characteristics of the subsequent fuel spray. For the first of the split, an excellent agreement between the single injection strategy and the first of the split sprays was found for all injection and in-cylinder pressure conditions. For the second of the split injection strategies, in particular the 0.425 *ms* and 0.625 *ms* dwell periods, the second split spray compared with that of the first had a higher tip velocity for in-cylinder pressures of 2 and 6 *MPa* during cold air intake. The velocity difference between the first and the second of the split was estimated at 17 *m/s* and 12 *m/s* for 0.425 *ms* and 0.625 *ms* dwell period respectively, at 2 *MPa* in-cylinder pressure. This was attributed to the wake or the gas flow induced by the first split, reducing the resistance force on the tip of the second split. With an increase in dwell period, namely 0.825 *ms*, the tip velocities of the first and the second of the split were comparable. This was attributed to the longer duration between the two splits, and, hence, the collapse of the wake or the induced gas flow created by the first split spray.

The internal gas phase velocity was estimated by the velocity differences between the two split sprays. The gas flow velocity was found to increase with a decrease in the dwell period, a decrease in the in-cylinder pressure and an increase in the injection pressure.

The tail velocity of the first split spray was also estimated. It was found that the tail of the first split moves at a reduced rate in comparison to the tip of the spray. It is assumed that, since the injection velocity is considerably lower at the end of injection, large droplets are more likely to be found. Furthermore, since the spray tail velocity is considerably lower that the tip velocity, an elongated effect on the coherent structure of the spray is likely to occur.

Since tip penetration during high in-cylinder pressures is reduced, the maximum penetration length was observed within the limit of the optical window. Hence, for an in-cylinder pressure of 6 *MPa*, it was found that the second split penetrates further than the first split spray. This phenomenon was expressed as the exceed type, and further attributed to the combined effect of cooler jet stream and induced gas flow created by the first split. The cooler jet stream is thought to reduce the second split spray tip evaporation. The tip of the second split was clearly visible within the fuel vapour of the first split (Fig 6-21 and 6-30).

For the hot air intake at 2 *MPa* in-cylinder pressure, the observed trend was similar in nature to the cold air intake experiments; namely the second split spray exceeded in tip velocity due to entrained gas flow induced by the first split spray.

With a *TDC* gas pressure of 6 *MPa* and a corresponding temperature of 667 *K*, the increased rate of evaporation was clearly evident from the images (Fig 6-28 and Fig 6-32). The resultant effect was reduced tip penetration and velocity of the first split spray, and subsequent reduction in the exchange of momentum between the evaporating droplets and the surrounding in-cylinder gas. Hence, little or no increase in the tip velocity of the second split spray was found.

From the images shown throughout, and for the first of the split sprays, the dispersion of the vapour fuel was evident alongside the penetrating liquid, starting with a thin or an almost non-existent layer, and progressively increasing in thickness with an increase in the axial distance.

With the liquid fuel spray reaching its stable length, the vapour phase continues to penetrate across the chamber, and also grows in width in an approximately linear manner. The resultant effect was a width considerably wider than that of the liquid spray widest point. Furthermore, the coherent structure of the vapour phase appeared to have a nearly constant cone shape for a given operational condition.

The vapour penetration and concentration was also found to be subjected to in-cylinder and injection pressure effects. An increase in the injection pressure and a decrease in the in-cylinder pressure promoted the rate of vapour penetration and the width dispersion.

Results obtained for the dynamic behaviour of split injection strategy with diesel sprays were investigated utilising several different experimental method. From the results obtained, the agreement between each method proved the validity of each technique relative to the applied definitions.

7.   INVESTIGATION OF SPRAY LIQUID CORE AND PENETRATION LENGTH BASED ON TRANSIENT MASS FLOW RATE

7.1   INTRODUCTION

The in-cylinder penetration of fuel is widely recognised as an important parameter for optimisation of the combustion processes in IC engines. This phenomenon has been extensively studied, both theoretically and experimentally (Levich, 1962; Dent, 1971; Reitz & Bracco, 1982; Andrews, 1993; Savic, 2000; Sazhin et al., 2001b; Crua, 2002; Yi & Reitz, 2004; Karimi et al., 2006).

Conventionally, the liquid spray is divided into two main regions - a dispersed region and a dense region (Sazhin et al., 2001b). In a dispersed spray region, the distance between the drops is larger than the drop diameter, and the interactions between these drops are small. In a dense spray region, the interactions between the droplets and ligaments are very strong (Yi & Reitz, 2004). A general term for the dense region of the spray close to the nozzle exit is the intact liquid core. In some cases, this region is referred to as the break-up zone with the associated break-up length. Many attempts have been made to study the break-up zone using different techniques. Unfortunately, due to the nature of the dense spray emerging from the nozzle, the outer part of the intact liquid core within the break-up zone is shrouded with very small droplets of high concentration. This makes insertion of physical or optical probes, or optical visualisation of the inner core, almost impossible (Arai et al., 1984; Chehroudi et al., 1985; Hiroyasu & Arai, 1990; Yule & Aval, 1989; Pitcher & Wigley, 1992; Pitcher et al., 1990). Serious experimental uncertainties, such as multiple elastic scattering of the incident beam, could hinder optical diagnostics. For these reasons, experimental determination of the length of the intact liquid core can prove difficult. The intact core length is also referred to as the break-up length. Experimental analysis of the break-up length by an electrical resistance method has been performed by Arai et al. (1984), Chehroudi et al. (1985) and others. It should be emphasised that they effectively ignored the contribution of the transient region in the spray development with time. Although this approach is valid as the initial stage of the analysis, a model taking into

account the transient injection behaviour would be relevant. This is particularly important for highly transient sprays, where the injection duration is very small when multi-hole nozzles and multiple injection strategies are utilised.

The work presented in the current chapter focuses on the analysis of the time evolution of the break-up length, both within the complete and incomplete atomised spray regions. This task was carried out using an indirect technique based on a spray penetration correlation, and experimental results on the transient evolution of the mass flow rate as described in Chapter 3.

For spray penetration, a fully multi-dimensional coupled modelling of the spray break-up length, size distribution of ligaments, and droplets, droplet break-up and evaporation and air entrainment would be too complex (Faeth, 1990; Faeth et al., 1995). A self-contained model of all the above-mentioned phenomena for dense sprays is still a major challenge. In many cases, simplified models are more suited to practical applications. Hence, a modelling approach for the study of the penetration length is suggested in the current chapter. This model is based on the conservation of mass and momentum of the injected fuel. The motion of the spray is slowed down by the drag force acting on the spray from the in-cylinder quiescent gas.

The current chapter is separated into two main sections, followed by conclusions. In section **7.2** of this chapter, the approach for the Centre-of-Mass (*CoM*) model is discussed. This is followed by the validation of the results against experimental spray penetration data. In section **7.3**, the evolution of the break-up length based on an empirical correlation and transient mass flow rate data is explored.

7.2 MODELLING OF PENETRATION LENGTH

7.2.1 Prediction of Penetration Length Based on Centre of Mass (*CoM*)

The velocity of liquid spray injected from a diesel injector nozzle is much greater than the velocity of in-cylinder gas in an initially quiescent environment. Furthermore, whilst the liquid spray is slowed down due to the drag force, the in-cylinder gas could start to accelerate due to the motion of the spray.

In general, the equation of motion of a droplet with a mass m_d in the direction of the spray axis is given as:

$$\frac{d\,(m_d u_d)}{dt} = -\frac{1}{2}\,C_{Drop}\;\rho_g\;A_d\;(u_d - u_g)^2\,, \tag{7.1}$$

where u_d is the droplet velocity, u_g is the in-cylinder gas velocity, A_d is the projected droplet area, ρ_g is the in-cylinder gas density, and C_{Drop} is the drag coefficient for an isolated droplet as a function of Reynolds number (Sazhin et al., 2003).

Generally, the droplet motion via Eq. (7.1) is solved in all three dimensions, taking into account droplet heating and evaporation. In the current study, it is assumed that there is no significant heat and mass transfer between droplets for in-cylinder gas under cold air intake conditions (Sazhin et al., 2003). Furthermore, the radial and circumferential components of the injection velocity are assumed to be zero. This is a realistic assumption since the injector used in the current experiment is not a swirl injector, and the in-cylinder gas is quiescent.

A modelling approach from first principles for the spray penetration in a dense diesel environment is presented in this section. This approach is based on the conservation of mass and momentum applied to the whole spray as opposed to individual droplets (Eq. (7.1)). The new model incorporates instantaneous experimental injection velocity data as an input into the calculations. The experimental injection velocity data are obtained from the rate of injection data described in Chapter 3. Hence, the equation of mass and momentum conservation for the whole spray can be written as:

$$\frac{d\,(m\,u_P)}{dt} = \rho_l\,A_n\,u_{inj}^2\;-\frac{1}{2}\,C_D\;\rho_g\;A\,u_P^2\,. \tag{7.2}$$

Where u_p is the penetration velocity, u_{inj} is the injection velocity, A_n is the nozzle hole area, C_D is the drag coefficient for the whole spray (as opposed to a droplet), and A is the projected area of the spray. In Eq. (7.2), m is the instantaneous injected mass of the liquid fuel, i.e. when:

$$m = \int_0^t \dot{m}_f \, dt \,,$$

where the mass flow rate is measured experimentally (Chapter 3), and t is the time from the start of injection.

Given the overall shape of the spray as a first approximation, the tip velocity u_p is assumed to be close to the velocity of its centre-of-mass (*CoM*) u_{cm} for a continuous spray in the absence of major spray instability such as cluster shedding described in Chapter 5. Therefore, the drag force acting on the injected fuel mass as a physical body on the right side of the Eq. (7.2) can be written as:

$$\frac{d(m\, u_{cm})}{dt} = \rho_l \, A_n \, u_{inj}^2 \; - \frac{1}{2} \, C_D \, \rho_g \, A \, u_{cm}^2 \,. \tag{7.3}$$

The drag coefficient C_D for the spray as a bluff deformable body in the presence of air entrainment and droplet stripping is quite difficult to evaluate. Mulholland et al. (1988) explored the drag coefficient in an ensemble of droplets as a function of droplet spacing. For dense diesel sprays (when droplet spacing tends to zero), the expression for drag on a rod is applied following Mulholland et al. (1988). It gives $C_D = 0.755/Re_{initial}$, where the Reynolds number, $Re_{initial}$ is based on the value of the rod diameter and its velocity.

In the current study, the same approach is adopted immediately after first sighting of fuel out of the nozzle exit. Also, the value of Reynolds number at the early stage of injection $Re_{initial}$ will be defined by the nozzle diameter and some initial value of the injection velocity. The latter can be considered as a tuneable parameter of the model since a degree of uncertainty regarding the initial injection velocity value exists.

For the upper limit of the drag coefficient, C_D is taken at 1.54. This is the value presented for a deformable droplet by Liu & Reitz (1993).

From the experimental penetration results presented in the previous chapters, the penetration length was found to reach a critical value associated with the onset of

cluster shedding. This length is referred to as the critical length (L_{crit}) as shown in Fig 7-1.

In the current study, a linear variation between the upper and the lower limits is assumed for the drag coefficient as a function of penetration length. Hence, the expression for C_D can be written as:

$L_{cm} \leq L_{crit}$

$$C_D = \frac{0.755}{\text{Re}_{initial}} + \left(1.54 - \frac{0.755}{\text{Re}_{initial}} \right) \left(\frac{L_{cm}}{L_{crit}} \right),$$ (7.4)

where L_{cm} is the distance from the nozzle exit to the *CoM* of the spray.

$$L_{cm} = \int_0^t u_{cm} \, dt \ .$$
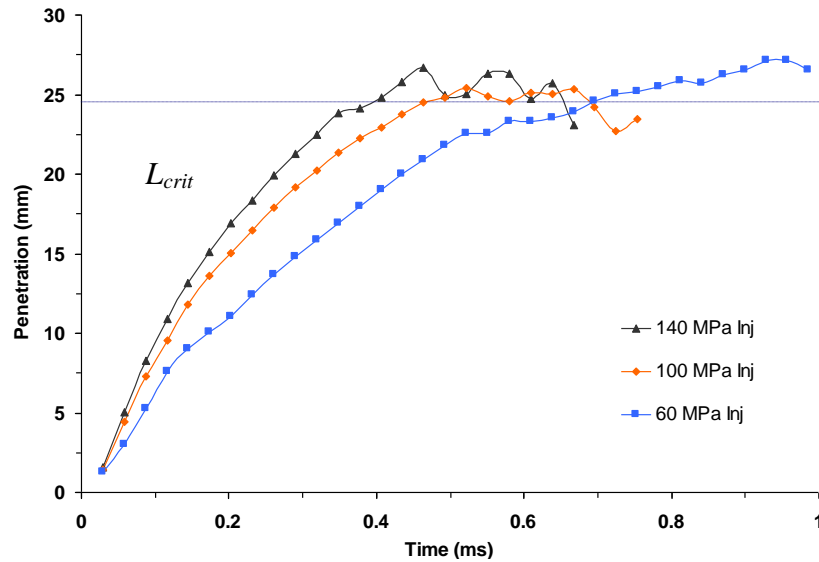
Fig 7-1. Definition of critical length L_{crit} for 6 MPa in-cylinder pressure; cold air intake (corresponding to 448 K at TDC); 7-hole nozzle (Tab 5-1)

Assuming the drag force is amplified by the air entrainment, the projected spray area *A* in Eq. (7.3) should accordingly account both for the liquid part of the spray and the surrounding boundary layer. The former contribution comes from the radius equal to the sum of nozzle radius, and the product of L_{cm} and the tangent of half of the spray cone angle. The latter is taken in the Blasius form (Douglas et al., 1995) as boundary layer thickness over a plate. Hence, the expression for the spray frontal area becomes:

$$A = \pi \left(0.5 D_n + L_{cm} \tan \frac{\theta}{2} + C_{blasius} \frac{L_{cm}}{\sqrt{\text{Re}}} \right)^2,$$ (7.5)

where $C_{blasius}$ is the Blasius scaling constant, θ is the spray cone angle, and the Reynolds number is defined as $Re = (\rho_g L_{cm} u_{cm}) / \mu$.

Since integration and solving Eq. (7.3) gives the position of the centre-of-mass L_{cm} of the injected liquid fuel, the calculated values of L_{cm} should not exceed the experimental values of spray tip penetration L_p. The calculated results are shown against the experimental data for two values of in-cylinder pressure in Fig 7-2 and Fig 7-3.
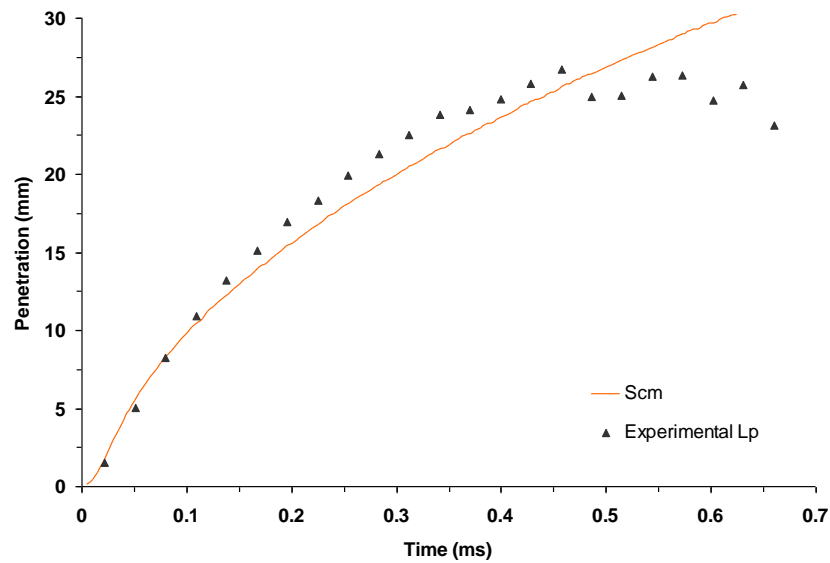
Fig 7-2. Calculated position of L_{cm} against experimental tip penetration length; 140 MPa injection pressure; 47 kg/m³ in-cylinder density; 6 MPa in-cylinder pressure; cold air intake (corresponding to 448 K at TDC); 20 mm³ fuelling; 7-hole nozzle; the model parameters are $Re_{initial} = 0.831$, $C_{blasius} = 50$, $L_{crit} = 24.5mm$
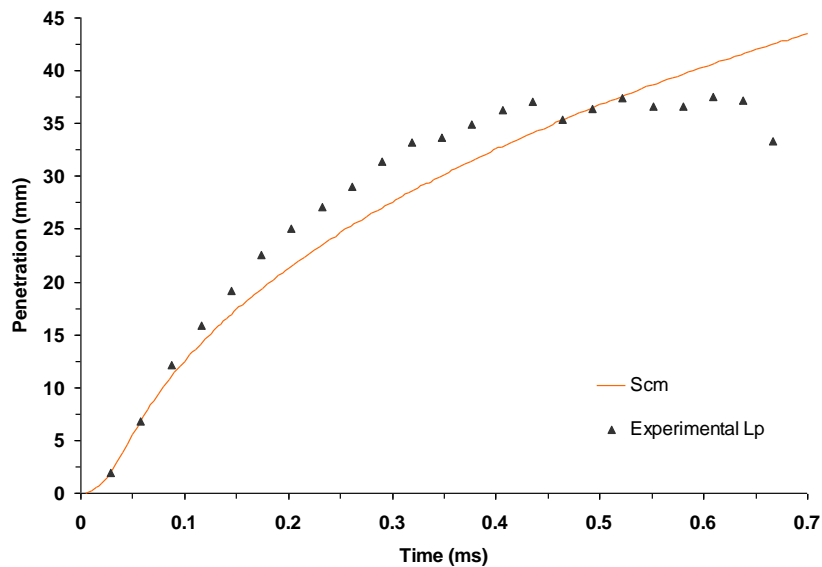
Fig 7-3. Calculated position of L_{cm} against experimental tip penetration length; 140 MPa injection pressure; 20 kg/m³ in-cylinder density; 2 MPa in-cylinder pressure; cold air intake (corresponding to 350 K at TDC); 20 mm³ fuelling; 7-hole nozzle; the model parameters are $Re_{initial} = 0.831$, $C_{blasius} = 1$, $L_{crit} = 37.5mm$

156

As can be seen from Fig 7-2 and Fig 7-3, the agreement between the calculated and experimental data is reasonable. However, whilst the value of $Re_{initial}$ is identical for the above cases, $C_{blasius}$ is assigned a much larger value for the 6 *MPa* in-cylinder pressure for a better agreement between the calculated and the experimental results. This is attributed to increased rate of stripping (as described in sections 5.3.3 and 5.3.6) associated with high in-cylinder densities (47 *kg/m³*), and thus resulting in a larger boundary layer thickness.

The variation of the Blasius scaling constant between the cases under consideration, $C_{blasius} = 1$ for *ICP = 2 MPa,* and $C_{blasius} = 50$ for *ICP = 6 MPa* is rather large. Hence a new approach for the modelling of the projected area *A* is sought. Furthermore, since the critical length (L_{crit}) is not a priori known, it is replaced by a modelling parameter with a constant value of $L_{def} = 15mm$ for all cases under consideration. Therefore, Eq. (7.4) can be rewritten as:

$$C_D = \frac{0.755}{Re_{initial}} + \left(1.54 - \frac{0.755}{Re_{initial}}\right)\left(\frac{L_{cm}}{L_{def}}\right).$$

(7.6)

The drag force is augmented by air entrainment and, hence, the projected frontal spray area *A* in Eq. (7.3) should account for this change. It is assumed that liquid volume fraction in the spray, ε, decreases exponentially with time as:

$$\varepsilon = \varepsilon_0 \, e^{-t/\tau},$$

(7.7)

where $\varepsilon_0 = 1$, represents the initial liquid fraction in the spray, and τ is the characteristic decay time.

As described in Chapter 5, an initial injection delay period from the start of injection trigger to the first sight of fuel is identified. For the injector in the current experiment, this time delay (t_{OD}) is constant (0.4075 *ms*). Therefore, the liquid fraction as a function of time can be written as:

$$\varepsilon(t) = \varepsilon_0 \, e^{-\left(\frac{t - t_{OD}}{\tau}\right)},$$

(7.8)

where ε is liquid volume fraction in the spray. Since the volume occupied by the spray consists of injected fuel and entrained air, the volume of the spray as a function of time can be written as:

$$V(t) = \frac{m(t)}{\rho_l \, \varepsilon(t)} \tag{7.9}$$

Conventionally, it is accepted that the spray from a standard common rail fuel injector nozzle has a conical shape (Delacourt et al., 2005; Heimgartner & Leipertz, 2000) prior to onset of cluster shedding. Following this assumption, the height of the cone is assumed to be equal to the calculated spray tip penetration length L_p. This gives the expression for the volume of the spray cone as:

$$V = \frac{1}{3} A \, L_p \, . \tag{7.10}$$

Based on the experimental Laser Induced Fluorescence (*LIF*) images obtained for cold air intake conditions in Chapter 6, the data was processed for the position of the centre-of-mass (*CoM*) of the spray. It was assumed that pixel intensities of the *LIF* images are proportional to the volume fraction of the fuel (Eq. (2.23), following Le Gal et al., (1999). Fig 7-4 shows the experimentally assessed *CoM* position, $L_{cm\,(exp)}$, and the tip penetration length $L_{p\,(exp)}$.
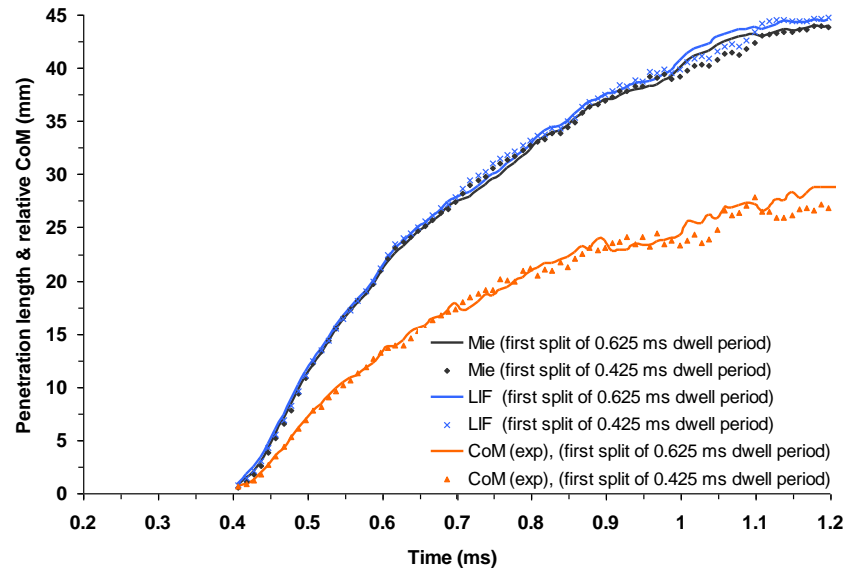
Fig 7-4. The experimental spray penetration length obtained from LIF and Mie technique, compared to the experimental CoM position obtained from the LIF data; 100 MPa injection pressure; 20 kg/m³ in-cylinder density; 2 MPa in-cylinder pressure; cold air intake (corresponding to 350 K at TDC)

Previously it was assumed that the tip velocity u_p is close to the *CoM* velocity u_{cm} for a continuous spray in the absence of major spray instability. However, from Fig 7-4 it

can be observed that the positions of *CoM* and penetration length are not close. Therefore the following empirical parameter is introduced.

$$\beta = \frac{L_{p\,(exp)}}{L_{cm\,(exp)}}.$$ (7.11)

The derivative of Eq. (7.11) for a constant value of β gives:

$$u_p = \beta\,u_{cm}.$$ (7.12)

Substituting $\beta\,u_{cm}$ for u_p in Eq. (7.2) gives:

$$\frac{d(m\,u_{cm})}{dt} = \rho_l\,A_n\,u_{inj}^2 - \frac{1}{2}\,C_D\,\rho_g\,A\,\beta^2\,u_{cm}^2.$$ (7.13)

Also, L_p can be replaced by $\beta\,L_{cm}$ in Eq. (7.10), and the expression for frontal area as a function of time can be written as:

$$A(t) = \frac{3V(t)}{\beta\,L_{cm}(t)}.$$ (7.14)

Numerical integration of Eq. (7.13) is performed by the Euler method. Further numerical integration of u_{cm} with respect to time gives L_{cm}, the calculated position of *CoM* for the spray.

Although the instantaneous values for β can be obtained from the experimental results, in the absence of systematic dependency on operating conditions such as *ICP*, an average value of 1.45 is taken for the case presented in Fig 7-5. The standard deviation is 0.3 and it allows estimation of an uncertainty margin for the model relative to the experiment results. The results are shown in Fig 7-5. As can be seen, the calculated *CoM* is within the experimental *CoM* uncertainty limits before the onset of cluster shedding.
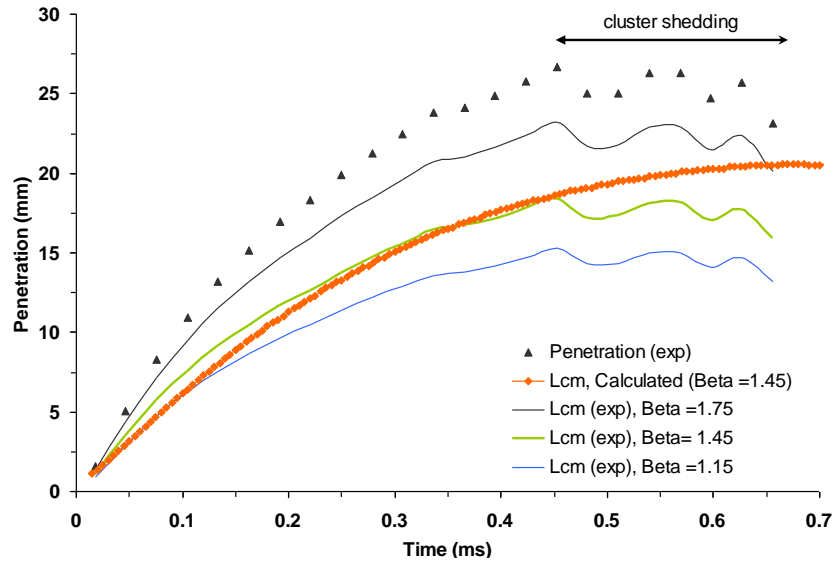
Fig 7-5. Comparison between calculated position CoM L_{cm}, and experimental CoM $L_{cm\,(exp)}$; 140 MPa injection pressure; 47 kg/m^3 in-cylinder density; 6 MPa in-cylinder pressure; cold air intake; 20 mm^3 fuelling; 7-hole nozzle; the model parameters are $Re_{initial}$ =1, L_{def} =15 mm, τ = 0.15 ms

7.2.2 Application of Centre of Mass (*CoM*) Model to Multiple Injection Strategy

The model described in section 7.2.1 is validated against the experimental data for the multiple injection strategy. The same values of modelling parameter $Re_{initial}$ = 1, L_{def} = 15 *mm*, and τ = 0.15 *ms* are taken for the cases under consideration.

The value of empirical parameter β is estimated as 1.85 ± 0.3 from the LIF experiment for the multiple injection cases. This is the ratio of $L_{p\,(exp)}$ to $L_{cm\,(exp)}$ for an injection pressure of 100 *MPa*.

For model validation against the experimental tip penetration length, the calculated values of L_{cm} are multiplied by β thus giving the calculated penetration length L_p.

Figs 7-6 to 7-9 show the results obtained for two values of in-cylinder pressure and two dwell periods. As can be seen, the agreement between the experimental data and the model is reasonable for the first of the split injections. For the second injection (within a cycle), the agreement is slightly worse, since the model does not take into account the effect of interaction between the first spray injection and the second (Chapter 6). This is believed to result in a subsequent increase in the rate of penetration. It should be remembered that the in-cylinder gas is no longer quiescent at the start of the second injected split. However, bearing in mind the uncertainty

involved in the experimental estimation of β, particularly for the second split spray, the overall agreement between the model and the experimental data is reasonably good for constant values of $Re_{initial}$, L_{def} and τ for all cases.
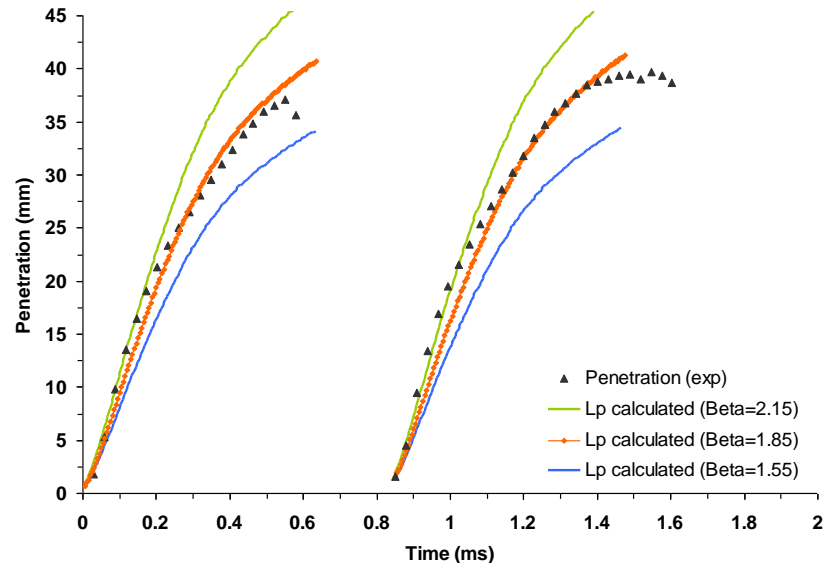
Fig 7-6. Comparison between experimental and calculated penetration length L_p ; 100 MPa injection pressure; 20 kg/m³ in-cylinder density; 2 MPa in-cylinder pressure; cold air intake; 7-hole nozzle; the model parameters are $Re_{initial} =1$, $L_{def} =15$ mm, $\tau = 0.15$ ms; 0.425 ms dwell period
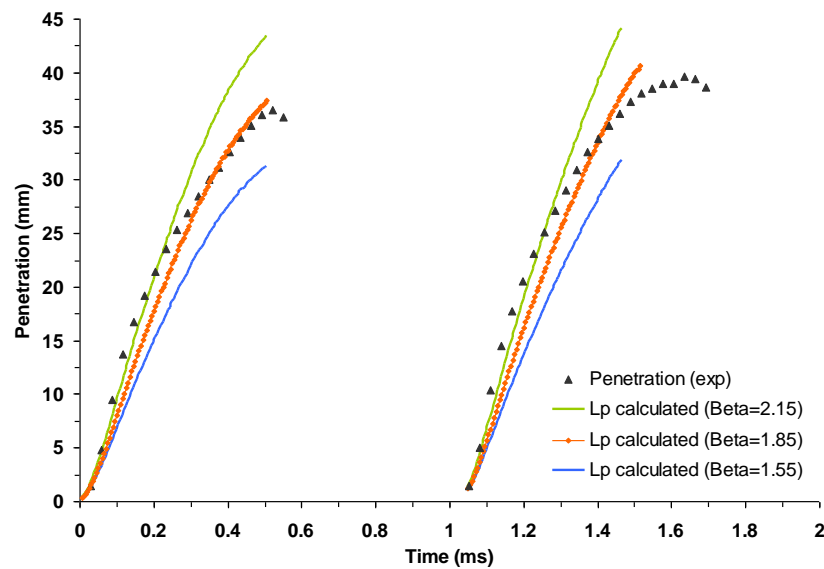
Fig 7-7. Same as Fig 7-6, with the exception of 0.625 ms dwell period

161
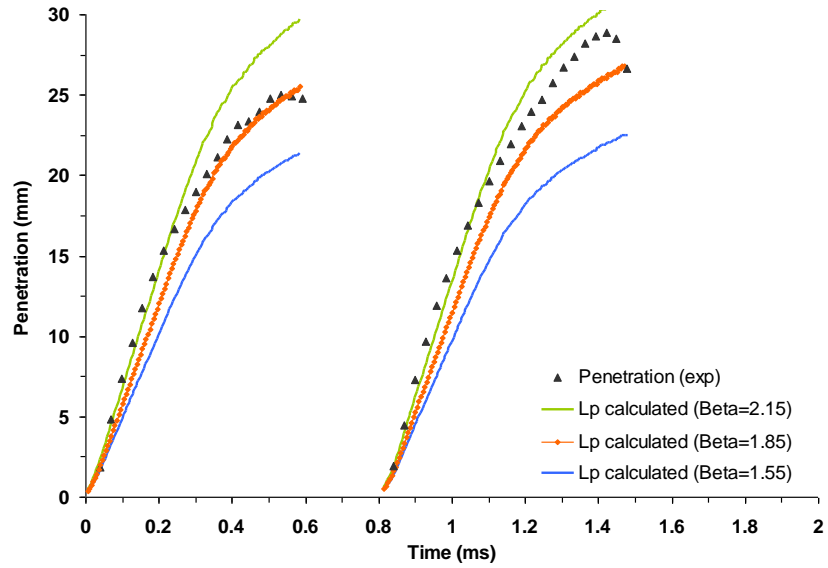
Fig 7-8. Comparison between experimental and calculated penetration length; 100 MPa injection pressure; 47 kg/m³ in-cylinder density; 6 MPa in-cylinder pressure; cold air intake; 7-hole nozzle; the model parameters are $Re_{initial} = 1$, $L_{def} = 15$ mm, $\tau = 0.15$ ms; 0.425 ms dwell period
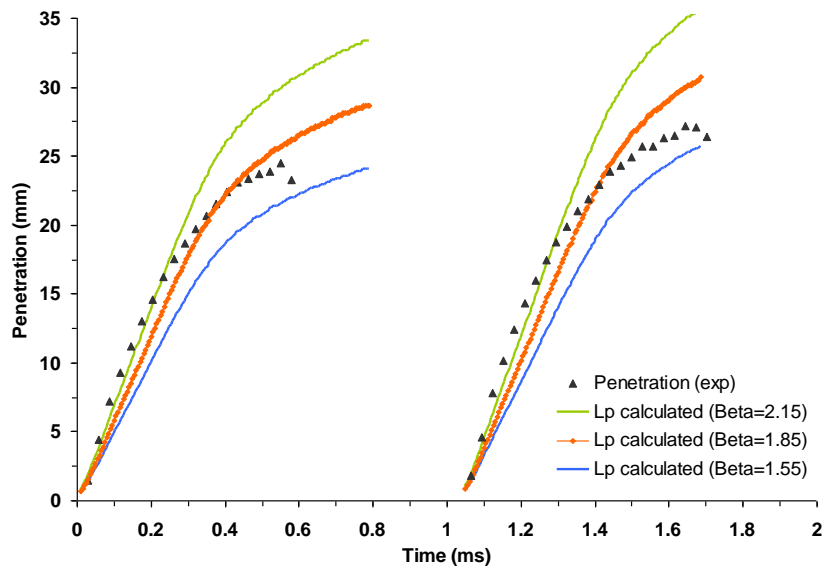
Fig 7-9. Same as Fig 7-8, with the exception of 0.625 ms dwell period

7.3   INTACT LIQUID CORE AND BREAK-UP LENGTH

7.3.1   Empirical Modelling of Break-up Length based On Penetration Correlation

Extensive experimental study into momentum and mass transfer in the mixing of coaxial gas jets has been conducted by Forstall & Shapiro (1950). The results from their experiments have been applied to the formulation of spray penetration length correlations by a number of authors (e.g. Dent, 1971; Hiroyasu & Arai, 1990; Yule & Filipovic, 1991). For the velocity field downstream of the break-up length L_b, Forstall & Shapiro (1950) found the following empirical formulation to hold when the penetration length L_p is greater than L_b.

$$L_p \left(u_p - u_g\right) = L_b \left(u_{inj} - u_g\right), \tag{7.15}$$

where u_p is the spray penetration velocity, u_g is the gas velocity, and u_{inj} is the injection velocity as shown in Fig 7-10.
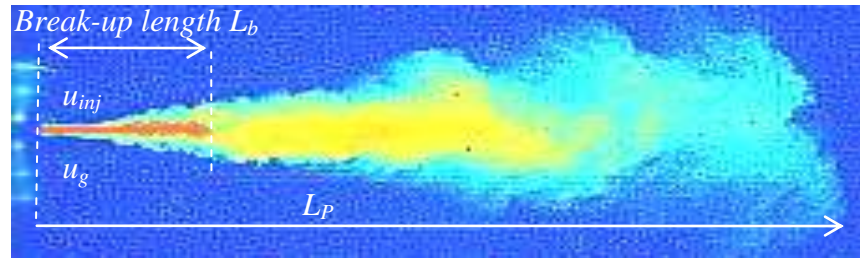
Fig 7-10. Illustration of the breakup length (L_b) and spray tip penetration length (L_p)

Assuming a quiescent environment when u_g is small when compared with u_{inj} and u_p, the contribution of u_g can be ignored in Eq. (7.15). In this case Eq. (7.15) can be written as:

$$u_p = u_{inj} \frac{L_b}{L_p}. \tag{7.16}$$

When $L_p > L_b$ the axial spray tip velocity by definition equals:

$$u_p = \frac{dL_p}{dt}. \tag{7.17}$$

Substituting Eq. (7.17) in to Eq. (7.16) and integrating with the initial condition that $L_p = 0$ at $t = 0$ gives:

$$\int_0^{L_p} L_p \; dL_p \; = \; u_{inj} \; . \; L_b \int_0^t \; dt \; , \tag{7.18}$$

$$L_p \; = \; \sqrt{2 \; u_{inj} \; L_b \; t} \; . \tag{7.19}$$

This expression predicts the conventional dependence of the penetration length on time as being proportional to $t^{1/2}$.

Assuming the working fluid is incompressible, isothermal, steady-state and the flow through the nozzle is in one direction only (direction of flow), i.e. with a velocity component normal to the cross-sectional area, from the continuity equation the mass flow rate through the injector can be expressed as:

$$\dot{m} \; = \; \rho_l \; A_t \; u_t \; = \; \rho_l \; A_n \; u_{inj} \; , \tag{7.20}$$

where ρ_l is the density of the injected fuel, A_t is the area at which the pressure transducer is placed, u_t is the velocity of the fuel at the pressure transducer, and A_n is the area of the nozzle hole outlet as shown in Fig 7-11. Rearranging Eq. (7.20) in terms of u_t gives:

$$u_t \; = \; \frac{A_n}{A_t} \; u_{inj} \; . \tag{7.21}$$
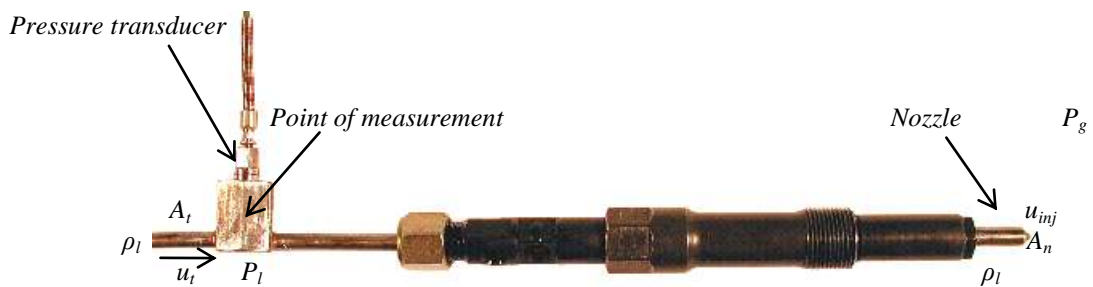
Fig 7-11. An injector showing points of measurement

From the energy equation the following can be written.

$$P_l + \frac{\rho_l}{2} u_t^2 = P_g + \frac{\rho_l}{2} u_{inj}^2 \, , \tag{7.22}$$

where P_l is the fuel pressure at the transducer (point of measurement), and P_g is the in-cylinder gas pressure. Substituting Eq. (7.21) in to Eq. (7.22), and rearranging for u_{inj} gives:

$$u_{inj} = \sqrt{\frac{1}{1 - (A_n / A_t)^2}} \sqrt{\frac{2 \, \Delta P}{\rho_l}} \, , \tag{7.23}$$

where ΔP is the differential pressure between the upstream and downstream of the nozzle exit ($P_l - P_g$). Putting:

$$C_\beta = \frac{1}{\left(1 - (A_n / A_t)^2\right)} , \tag{7.24}$$

Eq. (7.23) can be rewritten as:

$$u_{inj} = C_\beta^{1/2} \sqrt{\frac{2 \, \Delta P}{\rho_l}} . \tag{7.25}$$

Since in reality the actual flow rate is less than the theoretical flow rate due to losses such as friction, a discharge coefficient (C_d) is introduced. Hence:

$$C_d = \frac{\dot{m}_{actual}}{\dot{m}_{theoretical}} . \tag{7.26}$$

By rearranging Eq. (7.26) in terms of actual mass flow rate, and substituting Eq. (7.25) in to Eq. (7.20) the expression becomes:

$$\dot{m}_{actual} = \rho_l \; A_n \; C_d \; C_\beta^{1/2} \; \sqrt{\frac{2 \; \Delta P}{\rho_l}} \; . \tag{7.27}$$

In the current experimental set-up, A_t is 100 times greater than A_n. Hence, the term $C_\beta^{1/2}$, as can be seen from Eq. (7.24), has a value close to unity and can be ignored. Therefore, the standard expression for the injection velocity is obtained:

$$u_{inj} = C_d \; \sqrt{2 \Delta P / \rho_l}$$

Substituting the standard velocity expression into Eq. (7.19) gives:

$$L_p = \left(\sqrt{2\sqrt{2}} \right) \; C_d^{1/2} \left(\frac{\Delta P}{\rho_l} \right)^{1/4} \; L_b^{1/2} \quad t^{1/2} \; . \tag{7.28}$$

Close to the vicinity of the injector nozzle, the intact core length, or the break-up length (L_b), is found to be proportional to the nozzle exit diameter by Arai et al. (1984) and Chehroudi et al. (1985). Hence, the break-up length is expressed as:

$$L_b = \omega \; D_n \; \sqrt{\frac{\rho_l}{\rho_g}} \; . \tag{7.29}$$

Where ω is a dimensionless proportionality constant.

For a direct assessment of constant ω, Chehroudi et al. (1985) measured the break-up length using conductivity probes and assigned a value of 7.0 for the constant ω.
Arai et al. (1984) utilised the same technique and assigned a value of $\omega = 15.8$, thus giving a break-up length twice that of Chehroudi. This discrepancy can be attributed to the different experimental location in the spray, and by the way that the signal was analysed. Chehroudi et al. (1985) judged that the technique is not suitable for direct quantitative information about the break-up length.

Given the uncertainty in determination of ω, and hence the break-up length for a range of experimental conditions and injector types, the following procedure is proposed. Substitution of Eq. (7.29) into Eq. (7.28) gives:

$$L_p = \left(\sqrt{2\sqrt{2}} \right) (\omega \cdot C_d)^{1/2} \left(\frac{\Delta P}{\rho_g} \right)^{1/4} (D_n \cdot t)^{1/2} , \tag{7.30}$$

and

$$C_{L_p} = \left(\sqrt{2\sqrt{2}} \right) (\omega \cdot C_d)^{1/2} . \tag{7.31}$$

Therefore,

$$L_p = C_{L_p} \left(\frac{\Delta P}{\rho_g} \right)^{1/4} (D_n \cdot t)^{1/2} . \tag{7.32}$$

The penetration correlation of the form given in Eq. (7.32) has been presented by many authors, for C_{Lp} defined by an average value of C_d and ω.

In general, Eq. (7.32) is found to overestimate the penetration rate during the early stage of injection when compared with experimental data. This is because Eq. (7.32) is applicable for the completely atomised region (Hiroyasu & Arai, 1990).

With this in mind, Yule & Filipovic (1991) presented a single equation (Eq. (7.33)) applicable to both incomplete and completely atomised regions (from t to $t^{1/2}$).

$$L_p = C_{L_p} \left(\frac{\Delta P}{\rho_g} \right)^{\frac{1}{4}} (D_n t)^{\frac{1}{2}} \tanh \left[\left(\frac{t}{C_t} \right)^{\frac{3}{5}} \right] . \tag{7.33}$$

C_t is a time constant corresponding to the break-up time (Yule & Filipovic, 1991) for a given experimental condition such as the injection pressure. The expression *tanh* $[(t/C_t)^{3/5}]$ is a fitting factor for the initial stage of penetration (incompletely atomised region). The time constant C_t will be examined in more detail later in the text.

Historically, C_{Lp} is assigned a value by various authors, depending on an average value for the discharge coefficient C_d, and either an experimentally determined average value for ω (Arai et al., 1984; Chehroudi et al., 1985) or an average model value (Dent, 1971).

With the current experiments, the value of ω is not known. In order to determine the value of $C_{Lp,}$ therefore, Eq. (7.33) was fitted to the experimental data by the Least

Squares Fit method. This is the mathematical procedure for finding the best-fitting curve for a given set of experimental data points by minimising the sum of the squares of the (vertical) offsets of the points from the curve.

Fig 7-12 shows the average output value for C_{Lp}= 2.37 for a range of injection pressures (60 to 160 MPa) and in-cylinder pressure conditions between 2 to 6 MPa.
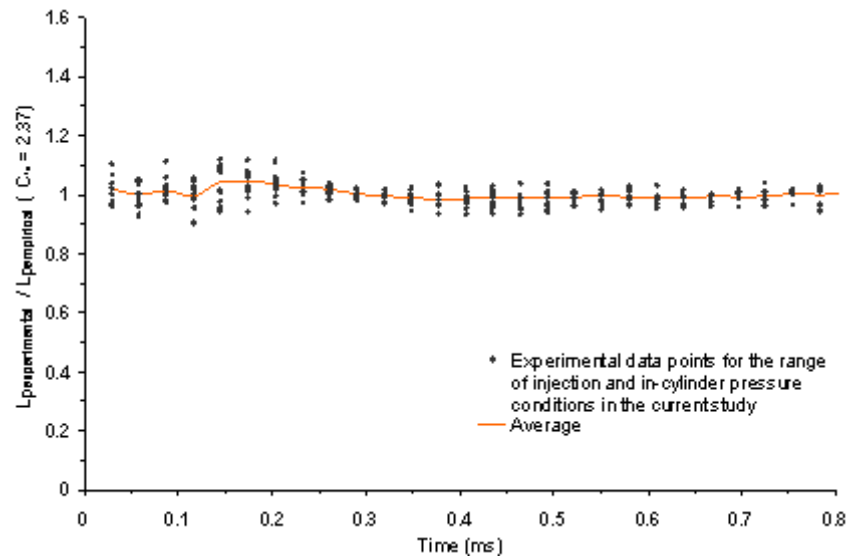
Fig 7-12. Determination of the empirical constant C_{Lp} for the range of injection and in-cylinder pressures in the current experiment; each marker in the above graph corresponds to the ratio of the experimental data point and the empirical data point (Eq. 7.33); the average of the data points are also shown for each time step; the average for the total duration corresponds to $C_{Lp} = 2.37$

Fig 7-13 shows the agreement between an experimentally determined penetration length and Eq. (7.33), with $C_{Lp} = 2.37$.

This agreement was consistent throughout the experiments for all operating conditions (additional profiles can be found in Appendix E).
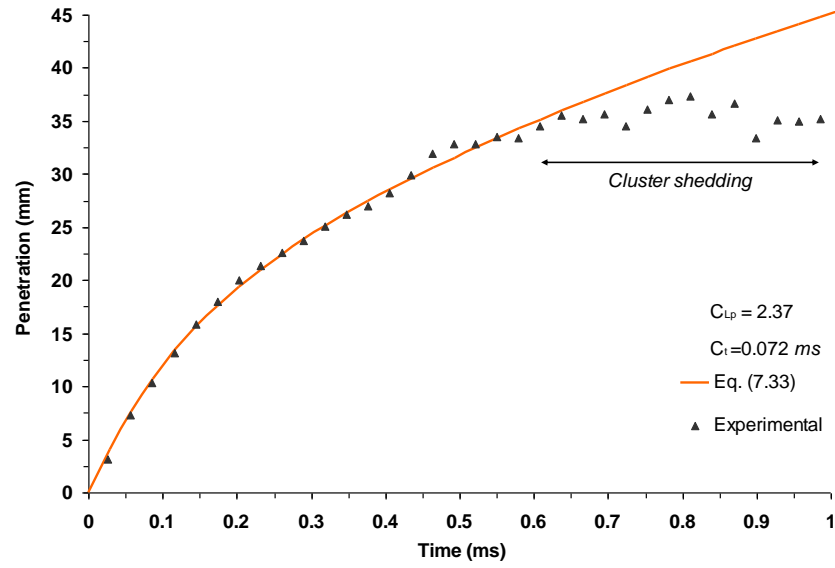
Fig 7-13. Comparison between Eq. (7.33) and experimental data; the experimental results are for cold air intake (corresponding to 448 K at TDC); 160 MPa injection pressure; 47 kg/m³ in-cylinder density; 6 MPa in-cylinder pressure

By substituting the value of the empirical constant (C_{Lp} = 2.37) into Eq. (7.31), and substituting for ω in Eq. (7.29) gives:

$$L_b(t) = \frac{\left[2.37 \Big/ \left(\sqrt{2\sqrt{2}} \right) \right]^2}{C_d(t)} \quad D_n \cdot \sqrt{\frac{\rho_l}{\rho_g}} \,. \tag{7.34}$$

With the experimental set-up described in Chapter 3, and the collected data from the instantaneous rate of injection tests ($\dot{m}_{actual}$), the evolution of the discharge coefficient (C_d) and the instantaneous injection velocity (u_{inj}) was deduced via Eq. (7.27). Fig 7-14 shows the evolution of the discharge coefficient as a function of time for a 3-hole Bosch injector nozzle. The nozzle parameters are given in Tab 3-1 and Tab 5-1.

169
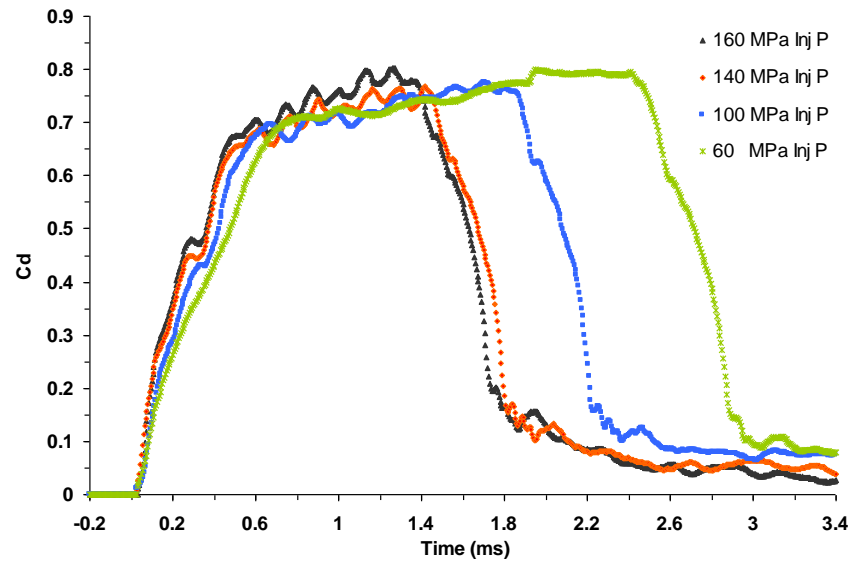
Fig 7-14. C_d as a function of time, for a 0.2 mm single guided 3 hole VCO nozzle at 4 MPa back pressure; 50 mm^3 fuelling; the data has been offset on the time axis for presentation reasons

The results presented in Fig 7-14 demonstrate the evolution of C_d as the injector needle lifts. The increase from zero to a relatively steady value occurs within circa 0.6 *ms* after commencement of injection depending on the injection pressure and the injector type (section 3.2.3). This period is consistent with the recorded needle lift traces. Other researchers had previously assumed that the transient evolution of C_d occurred over a period less than 0.1 *ms* (Yule & Filipovic, 1991). With the introduction of shorter injection durations, particularly with multiple injection strategies, it is increasingly important to take into account the transient value of C_d.

During the initial stage of injection, before the onset of break-up, the intact core length and the penetration length are bound to coincide (Hiroyasu & Arai, 1990; Yule & Filipovic, 1991). At some time, the penetration length and the liquid core length start to diverge due to break-up processes. Therefore, with utilisation of Eq. (7.34) and the transient values of C_d as a function of time, it is possible to derive the subsequent evolution of the break-up length for the remainder of the injection phase. However, since the value of C_d rises rapidly from zero at the start time, the effective break-up length from Eq. (7.34) would initially be predicted as infinitely large. Obviously, this part of the curve has no physical meaning as the break-up length coincides with the penetration length at the start of the injection. To identify the onset of break-up, this is

recognised as the point at which the predicted break-up curve crosses the penetration curve (Fig 7-15).

It is important to point out that the value of C_{Lp} can also be obtained via Eq. (7.32) from which it was found to give the same value for C_{Lp}. However, care must be taken since Eq. (7.32) is applicable to the completely atomised region and the identification of the initial break-up point fails with Eq. (7.32) (Fig 7-15).
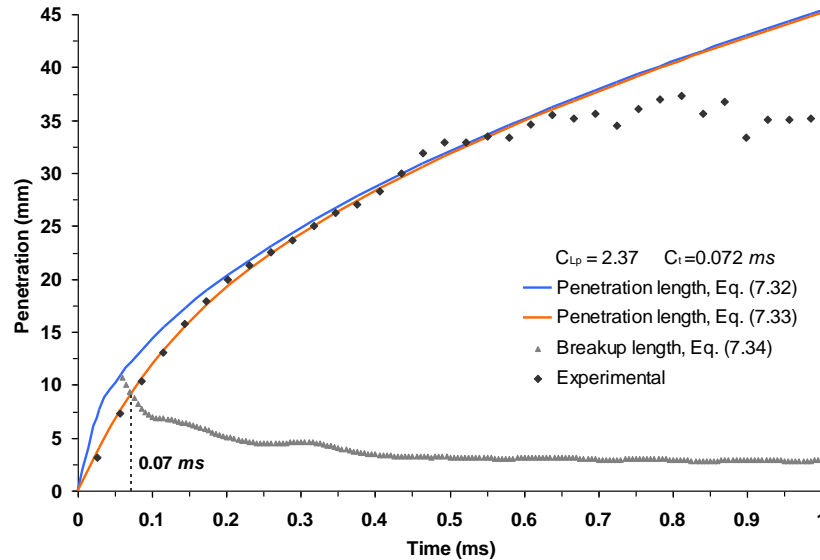
Fig 7-15. Experimentally determined penetration length against Eq. (7.18 and 7.19), and the breakup length; the intersection of breakup length and the experimental data/Eq. (7.19) indicates the real initial breakup point and the breakup time; 160 MPa injection pressure; 6 MPa in-cylinder pressure; cold air intake; 3-hole VCO Bosch injector nozzle

Fig 7-16 illustrates the break-up length as a function of time for the range of in-cylinder pressures. As mentioned above, the initial start of the break-up length has been determined by the crossing of the break-up length and the penetration length curves. As can be seen, the break-up length increases as the in-cylinder pressure decreases. The increase is evident during the complete and incomplete atomised region. This phenomenon is consistent with the trend reported by Hiroyasu (1998).
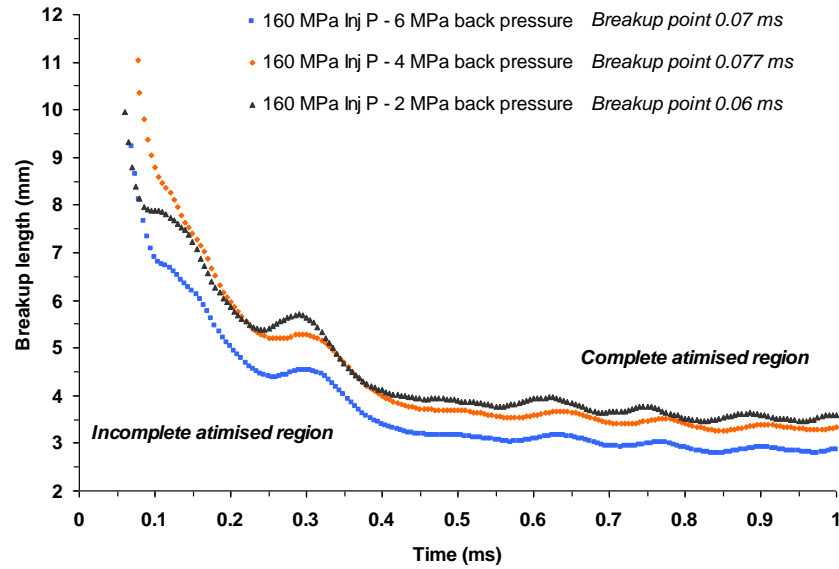
Fig 7-16. Breakup length (L_b) as a function of time for various in-cylinder pressure conditions; 3-hole VCO Bosch injector nozzle; 50 mm³ fuelling

Fig 7-17 shows the results of break-up length for the range of injection pressures in the current study. The reduction in the break-up length during the early stages of injection (in the incomplete region) is more rapid as the injection pressure increases. The increase in injection pressure contributes to the needle opening velocity. This increases the rate at which the nozzle holes are uncovered. Once the needle has reached its maximum lift position, the discharge coefficient (C_d) becomes steady assuming the needle upper bounce is neglected. Any further increase in injection pressure at this point results in no substantial decrease in the break-up length for the range of injection pressures in the current study (Fig 7-17). However, as can be seen from Fig 7-17, an increase in the injection pressure results in a decrease in the break-up length. This phenomenon is in agreement with the observation of Hiroyasu (1998).

Fig 7-18 shows the time constant C_t in Eq. (7.33), and the times when the predicted break-up length curves cross the penetration curves. By definition, the point at which the break-up length and the penetration length start to diverge is associated with the liquid core break-up, and thus the break-up time can be assessed (Hiroyasu et al., 1989).

Yule & Filipovic (1991) suggest that C_t could also correspond to the break-up time from Eq. (7.33). There is good agreement between the trends displayed for the two characteristic times in Fig 7-18. Although this phenomenon can not be further

explored because of the lack of experimental data on transient behaviour of break-up length L_b, the qualitative agreement between the estimates of break-up time is promising.

Furthermore, it is interesting to observe that the value of $\tau = 0.15$ *ms* in Section 7.2, approximately corresponds to the break-up time for the same injection pressures.
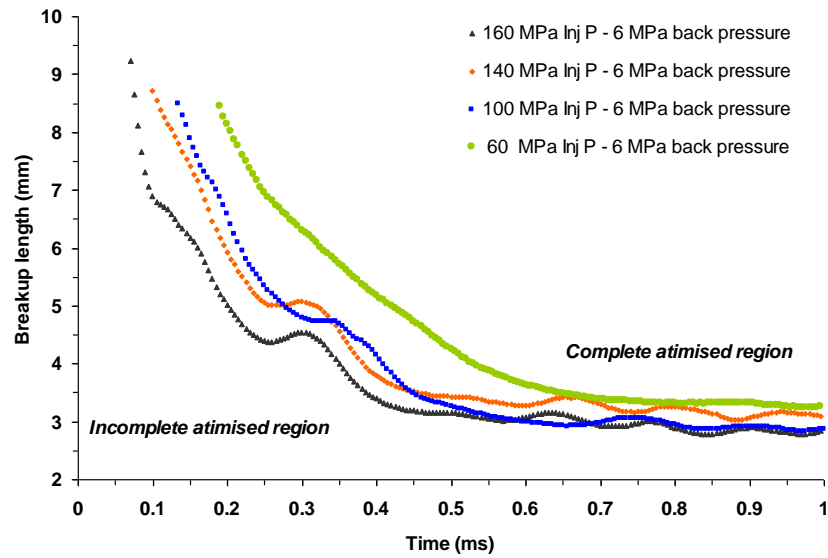
Fig 7-17. Breakup length (L_b) as a function of time from start of injection for various injection pressures; 3-hole VCO Bosch injector nozzle; 50 mm³ fuelling
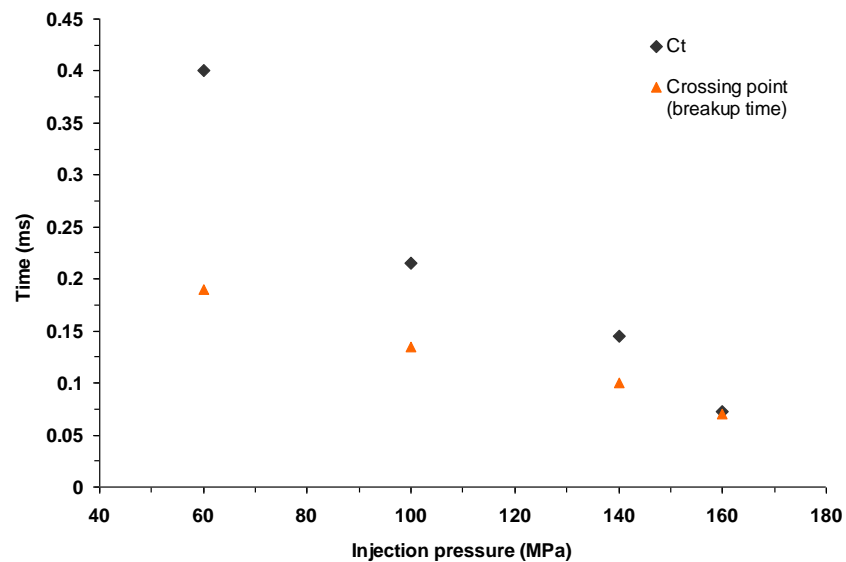
Fig 7-18. Breakup time and C_t as a function of injection pressure; 6 MPa in-cylinder pressure; 3-hole VCO Bosch injector nozzle

7.3   CONCLUSIONS OF CHAPTER 7

Two methods have been presented for spray characterisation. These are the determination of the transient liquid break-up length based on empirical correlations, and a penetration length model based on the conservation of mass and momentum for the whole spray as a physical body. The effects of injection pressure, in-cylinder conditions and dwell period on the break-up and the penetration lengths have been modelled and validated against available experiments. The main conclusions of this investigation are outlined below.

The model based on the conservation of mass and momentum for the whole spray as a physical body is shown to produce reasonable agreement between the numerical and the experimental results for both single and split injection strategy. For split injection strategy, the results showed good agreement between the experimental and numerical calculations for the first split. For the second split injection, the agreement between numerical and experimental results was not as satisfactory. This was attributed to the effect of air entrainment from the first split spray into the second injected portion, or second split spray. The uncertainty in the value of β for the second split requires further work for more accurate quantitative modelling. The results of modelling with the same values of modelling parameters are performed in the wide range of operating conditions. They showed good agreement within the confidence interval determined by the accuracy of the available experimental data.

The penetration correlation by Yule & Filipovic (1991) with a new empirical constant determined in the current experiment, gave a good fit to the experimental data. This also allowed an indirect determination of the developing break-up lengths, applicable for the complete and incomplete atomisation regions of a transient spray. This technique can be applied to any fuel injector.

The decrease in break-up length with time for the complete and incomplete regions is the result of increased in-cylinder gas density and injection pressure. The analysis assumes a constant effective nozzle diameter. No significant change in length due to an increase in the injection pressure in the complete atomised region was observed for the range of injection pressures in the current study.

8.   *CONCLUSIONS*

An experimental investigation into the behaviour of common rail fuel injection equipment and subsequent characteristics of diesel fuel spray was carried out. For the characteristics of the *FIE*, a long-tube rate of injection experimental programme was performed. This provided information on the evolution of the rate of injection and cycle-to-cycle variations. Prior to the study of diesel fuel spray formation, the rapid compression machine Proteus was characterised with respect to evolution of in-cylinder temperature and the effective polytropic coefficient. The study of conventional liquid fuel spray formation (single injection strategy) was performed utilising a high speed video technique. The results included hole-to-hole variation of the fuel spray, injection delay and its dependence on injection pressure, hesitation and fuel dribble, as well as the spray characteristics such as penetration and dispersion angle for a range of injection pressure and in-cylinder conditions.

For simultaneous study of the liquid diesel fuel spray and vapour propagation, Planar-Laser Induced Fluorescence and Mie scattering techniques were employed. A series of experimental measurements were performed both for single and split injection strategy. The results were applied as a benchmarking tool for spray modelling.

The *HSV* technique was also utilised for validation of the results against the *LIF* and *Mie* scattering technique for liquid spray characterisation. For split injection strategies, the influence of dwell period, injection pressure, in-cylinder density and temperature on the effect of spray penetration and evaporation, break-up and air entrainment were studied for their effects on liquid and vapour dispersion using the aforementioned techniques.

8.1   FUEL INJECTION SYSTEM

The results obtained via a long-tube rate of injection meter showed the dependence of the minimum quantity of fuel that could be injected on the injection pressure. This was attributed to the minimum time required for the injector needle to ascend and descend. For the split injection strategy, the minimum required time for the needle to descend and ascend was linked to the minimum time required for an effective dwell period. Furthermore, it was found that the rate of injection is 19% lower for the first split spray in comparison to the second split. The second of the split spray was

approximately 4% less in total mass than the single injection strategy. Although this tendency improved with an increase in the dwell period and a decrease in the injection pressure, this was in part attributed to the reduced magnitude of the upper needle bounce. The dependence of needle ascent and descent velocity on injection pressure was analysed. It was concluded that the rate at which the pressure rises between the needle opening pressure and the maximum injection pressure determines the needle ascent velocity.

Good agreement between the frequency of the upper needle lift trace signal and the corresponding rate of injection signal was observed at 7.2 *kHz* and 7.4 *kHz* respectively, with a standard deviation of 0.1 *kHz*.

8.2   CHARACTERISTICS OF CONVENTIONAL DIESEL FUEL SPRAY STRATEGY

From the *HSV* images, hole-to-hole variations were observed as a result of unbalanced fuel pressure distribution around the injector needle, causing transverse movement of the needle against the valve seat. The emerging spray had wide variations of the dispersion cone angle from hole-to-hole, as well as variation in penetration lengths. This phenomenon occurred regardless of the injection pressure or the in-cylinder pressure. For the 7-hole nozzle injector, a significant reduction in hole-to-hole variation was observed. This was attributed to improved fuel pressure distribution around the needle, and possibly more refined nozzle holes. The injection delays for the single-hole and the multi-hole nozzles were investigated. It was found that the Bosch injector exhibits a delay dependency on the injection pressure. This delay decreased with an increase in the injection pressure. The total reduction in injection delay from 60 *MPa* to 160 *MPa* was approximately 0.2 *ms*. The results were also confirmed with the rate of injection meter. For the Delphi injector, no dependency on the injection pressure was evident.

The hesitation of the emerging liquid fuel during the initial stage of injection was observed from the single-hole nozzle only. This was attributed to the transverse movement of the needle. After the initial hesitation of approximately 0.1 *ms*, the subsequent spray penetration appeared unaffected, even though, the corresponding upper injection rate fluctuations are shown to be irregular.

Increased detachment of large clusters of droplets from around the periphery of the leading edge, as well as stripping back of smaller clusters of droplets on the edge of the spray cone, were attributed to air entrainment. The detachment and stripping of the droplets were found to be directly dependent on the injection and in-cylinder pressures.

The spray penetration profiles for all the nozzles under study were dependent on the injection pressure and the in-cylinder conditions. The spray cone angle was found to be independent of the injection pressure. It has shown a dependence on the in-cylinder gas density and in-cylinder gas temperature. The reduction in full spray cone angle was found to reduce from circa 20° to 16° for an in-cylinder density of 47 kg/m^3 and 20 kg/m^3 respectively. At hot air intake, the mean spray full cone angle was estimated at 18° for an in-cylinder gas density of 31 kg/m^3 and 15° at 16 kg/m^3 in-cylinder gas density. This is attributed to increased rate of cluster shedding on the spray cone periphery and evaporation.

8.3   CHARACTERISTICS OF SPLIT INJECTION STRATEGY

Simultaneous acquisition of Planar Laser Induced Fluorescence and *Mie* scattering data on liquid and vapour fuel propagation was effectively performed for ranges of injection pressures and in-cylinder conditions.

For the first of the split injection strategy, excellent agreement based on the obtained data was observed between the single (conventional) strategy and the first of the injected split sprays. This was consistent for all injection pressures and in-cylinder conditions in the current study. For the second of the split injection strategies, namely the 0.425 *ms* and 0.625 *ms* dwell periods, the second split spray in comparison to that of the first had a higher tip velocity for 2 and 6 *MPa* in-cylinder pressures at cold air intake. The velocity difference between the first and the second of the split was estimated at 17 *m/s* and 12 *m/s* for 0.425 *ms* and 0.625 *ms* dwell period respectively, at 2 *MPa* in-cylinder pressure. This phenomenon was attributed to the wake or the gas flow induced by the first split, reducing the resistance to the tip of the second split. With an increase in dwell period (0.825 *ms*), the tip velocities of the first and the second of the splits were comparable. This was attributed to the long duration between the first and the second split spray. The induced gas velocity was estimated

by the velocity differences between the two split sprays. The induced gas flow velocity was found to increase with a decrease in the dwell period, a decrease in the in-cylinder pressure and an increase in the injection pressure. The tail velocity of the first split spray was estimated at circa 5 *m/s* when the injection pressure was at 100 *MPa*, and circa 6 *m/s* at 140 *MPa* injection pressure. It was found that the tail of the first split (at the end of injection) moves at a reduced rate in comparison to the tip of the spray.

With an increase in the in-cylinder gas density (6 *MPa* in-cylinder pressure), the tip penetration was found to be reduced. However, it was found that the second split penetrated further than the first split spray. This phenomenon was attributed to the combined effect of cooler jet stream and induced gas flow created by the first split spray. The cooler jet stream is thought to reduce the second split spray tip evaporation. The tip of the second split was clearly visible within the fuel vapour of the first split (Fig 6-31). During the hot air intake at 2 *MPa* in-cylinder pressure, the observed trend was similar in nature to the cold air intake experiments, namely the second split spray increased in tip velocity due to entrained gas flow induced by the first split spray. For an in-cylinder gas pressure of 6 *MPa* at *TDC* and corresponding temperature of 667 *K*, the increased rate of evaporation was clearly evident from the images. The resultant effect was reduced tip penetration and velocity of the first split spray and subsequent reduction in the exchange of momentum between the evaporating droplets and the surrounding in-cylinder gas. Therefore, since the mechanism for air entrainment into the first split spray had nearly vanished, the second split spray tip velocity could not exceed that of the first.

In general, the coherent structure of the spray dispersion for the first of the split strategies appeared to remain almost unchanged until the second split spray had caught-up with the tail of the first split. From the *LIF* images obtained, the dispersion of the vapour fuel was evident alongside the penetrating liquid, starting with a thin or almost non-existent layer, and progressively increasing in thickness with an increase in the axial distance. With the liquid fuel spray reaching a stable length, the vapour phase continued to penetrate across the chamber, and also grew in width with an approximately linear trend. The resultant effect was a width considerably greater than that of the liquid spray widest point. Furthermore, the coherent structure of the vapour phase appeared to have a nearly constant cone shape for a given operational condition. The vapour penetration and concentration was also found to be subjected to in-

cylinder and injection pressure effects. An increase in the injection pressure and a decrease in the in-cylinder pressure promoted the rate of vapour penetration and width dispersion.

The dynamic behaviour of split injection strategies with diesel sprays was investigated utilising several different experimental methods. From the results obtained, the agreement between each method proved the validity of each technique relative to the applied definition for the penetration length.

8.4   MODELLING

Two complementary methods have been presented for determination of the liquid break-up length and the penetration length. Both methods were based on determination of the transient rate of injection as an input to the models.

For the analysis of the liquid break-up length, empirical correlations were modified and utilised, and the effects of injection and in-cylinder pressures were studied. As follows from the results, the increase in the injection pressure and a decrease in the in-cylinder pressure yielded a decrease in the break-up length. The reduction in the break-up length from incomplete atomised region to complete atomised region was estimated between 6 *mm* and 8 *mm.*

20% reduction in break-up length in the complete atomised region, from 160 *MPa* injection pressure to 60 *MPa* injection pressure at 6 *MPa* in-cylinder pressure, and about 25% reduction from 6 *MPa* in-cylinder pressure to 2 *MPa* in-cylinder pressure at 160 *MPa* injection pressure was calculated.

The evolution of penetration length was studied and modelled, based on conservation of mass and momentum of the injected fuel mass of the complete spray, as opposed to spray droplets, for a range of injection pressures and in-cylinder conditions. The input to the numerical model was the experimentally determined transient rate of injection measurements, described in Chapter 3, at a sampling rate of 5 *µs*. The model traced the centre-of-mass of the spray as a physical body. The model was compared and validated against experimentally obtained Planar-Laser Induced Fluorescence (*PLIF*) data for centre-of-mass, based on the assumption that the LIF signal is proportional to the volume fraction distribution. Comparison of the centre-of-mass position and the penetration length allowed the introduction of an empirical parameter *β*, with an uncertainty margin ± 16%. Overall, there was good agreement for the same value of

modelling parameters, with reference to single and split-injection strategy for a number of dwell periods. However, the model agreement was more comparable for the first of the split injection strategy, in comparison to the second of the split. This was attributed to the uncertainty with regards to the value of empirical parameter β (for the second of the split), since the effect of air entrainment from the first split spray into the second split spray was not implemented into the model.

8.5   RECOMMENDATION FOR FURTHER WORK

The injectors used in this study are designed for pre-, main and post-injection with relatively long dwell period between each stage. These injectors were nevertheless explored for minimum permissible dwell period and fuel quantity at elevated injection pressures and in-cylinder conditions. As a way forward for reducing overall emissions, a number of car manufacturers have adopted up to six injections per cycle, allowing high flexibility for combustion optimisation as well as providing levels of economy and performance. Ultimately this would mean a very small quantity of fuel could be dispensed at each stage of injection, and this requires an accurate and fast response fuel injector. Piezoelectric injectors are known for their accuracy and tolerance. Such injectors are better suited for the analysis of multi-stage spray interaction, since possible cycle-to-cycle inconsistencies are reduced. Furthermore, with each injector having its own characteristics, a more robust control system is required. This will allow the engine management system to match injection pulse durations to the characteristics of each individual injector, which will provide consistency by greatly reducing fuel volume tolerance.

The current research programme has been focused on the qualitative spray characteristics of split stage injection strategy. There are uncertainties regarding the temporal and spatial distribution of fuel quantity in liquid and vapour form with multiple injection strategies. The next logical step should be the enhancement of the same experimental programme in terms of quantitative analysis of fuel dispersion with piezoelectric injectors, in liquid and vapour form, and subsequent combustion and emission diagnostics. Additional recommendations for detailed study are increased number of injections within a cycle, as well as reduced fuel mass (less than 10 mm^3) per injection.

REFERENCES

ABDELGHAFFAR, W., 2005. Modelling of fuel droplet heating in diesel engines. Thesis (PhD), University of Brighton, United Kingdom

ABDELGHAFFAR, W., KARIMI, K., HEIKAL, M.R., 2006. Fuel spray penetration in high pressure diesel engines. SAE Paper 07SFL-15

ABU-GHARBIEH, R., 2001. Laser sheet imaging and image analysis for combustion research. Thesis (PhD), Chalmers University of Technology S-412 96 Goteborg, Sweden

AFZAL, H., ARCOUMANIS, C., GAVAISER, M., KAMPANIS, N., 1999. Internal flow in diesel injector nozzles-modelling and experiments. I.Mech.E, S492/S2/99

ANEZAKI, Y., SHIRABE, N., KANEHARA, K., SATO, T., 2002. 3D Spray measurement system for high density field using laser holography. SAE Paper 2002-01-0739

ANDREWS, M.J., 1993.The large-scale fragmentation of the intact liquid core of a spray jet. Atomization and Spray, Vol.3, pp.29-54

ARAI, M., AMAGAI, K., 1994. Experimental study on a diesel spray of multi-stage injection. International Symposium COMODIA 94

ARAI, M., AMAGAI, K., 1997. Dynamic behaviour of multi-stage injection diesel spray. SAE Paper 97004

ARAI, M., TABATA, M., HIROYASU, H., SHIMIZU, M., 1984. Disintegration processes and spray characterization of fuel Jet injected by a diesel Nozzle. SAE Paper 840275

ARCOUMANIS, C., BANIASAD, M.S., GIBBINS, J.R., 1992. Measurement and analysis of injection rate variations in diesel engines. I.Mech.E seminar, Diesel fuel injection system

ARCOUMANIS, C., BANIASAD, M.S., 1993. Analysis of consecutive fuel injection rate signals obtained by the Zeuch and Bosch methods. SAE Paper 930921

ARCOUMANIS, C., FLORA, H., GAVAISES, M., BADAMI, M., 2000. Cavitation in real-size multi-hole diesel injector nozzles. SAE Paper 2000-01-1249

ARCOUMANIS, C., GAVAISES, M., FLORA, H., ROTH, H., 2001. Visualization of cavitation in diesel injectors. Mec.ind. 2, page 375-381

ARCOUMANIS, C., GAVAISES, M., FRENCH, B., 1997. Effect of fuel injection processes on the structure of diesel sprays. SAE Paper 970799

BADOCK, C., WRITH, R., FATH, A., LEIPERTZ, A., 1999. *Investigation of cavitation in real size diesel injection nozzles. Elsevier, International Journal of Heat and Fluid Flow, Vol. 20, PP 538-544*

BANIASAD, M.S., 1994. *Analysis of fuel injection rate in diesel injection systems. Thesis (PhD), University of London, united Kingdom*

BAE, C.H., KANG, J., 2000. *Diesel spray characterisation of common-rail VCO nozzle injector. THIESEL 2000. Thermofluidynamic Processes in Diesel Engine*

BAE, C.H., YU, J., KANG, J., KONG, J., LEE, K.O., 2002. *Effect of nozzle geometry on the common-rail diesel sprays. SAE Paper 2002-01-162*

BEGG, S.M., 2003. *In-cylinder airflow and fuel spray characterisation for a top entry direct injection gasoline engines. Thesis (PhD), University of Brighton, United Kingdom*

BERGSTRAND, P., DENBRATT, I., 2001. *Diesel combustion with reduced Nozzle orifice diameter. SAE Paper 2001-01-2010*

BIRCH, S., 2004. *New fuel injector technology from Delphi. Automotive Engineering International Magazine, Vol. 112, No. 2, Page 36 and 111*

BOSCH, W., 1966. *The Fuel Rate Indicator: A new Measuring Instrument for Display of the Characteristics of Individual Injection. SAE Paper 660749*

BOWER, R.G., FOSTER, D., 1991. *A Comparison of the Bosch and Zuech rate of injection meters. SAE Paper 910724*

BROWNE, K.R., PARTRIDGE, I.M., GREEVES, G., 1986. *Fuel property effect on fuel\air mixing in an experimental diesel engine. SAE Paper 860223*

BRUNT, M.F.J., PLATTS, K.C., 1999. *Calculation of heat release in direct injection diesel engines. SAE Paper 1999-01-0187*

CHAVES, H., KNAPP, M., KUBITZEK, A., 1995. *Experimental study of cavitation in the nozzle hole of diesel injectors using transparent nozzles. SAE Paper 950290*

CHAVES, H., OBERMEIER, F., SEIDEL, T., WEISE, V., 2000. *Fundamental investigation of the disintegration of a sinusoidally forced liquid let. Eighth International Conference on Liquid Atomisation and Spray Systems, Pasadena, CA, USA*

CHEHROUDI, B., CHEN, A.H., BRACCO, F.V., ONUMA, Y., 1985. *On the intact core of full-cone spray. SAE Paper 850126*

CHOU, W., FAETH, G.M., 1998. *Temporal properties of secondary drop breakup in the bag breakup regime. International Journal of multiphase Flow, Vol. 24, PP 889-912*

CRUA, C., 2002. *Combustion processes in a diesel engine. Thesis PhD, University of Brighton, United Kingdom*

DANTEC INSTRUCTION AND USER GUID., 2000. *Publication no: 9040U1101, date: 15 April 1999. Copyright 1999 by Dantec measurement technology A/S, P.O. Box 121, Tonsbakken 18, DK 2740 Skovlunde, Denmark*

DAI, Z., FAETH, G.M., 2000. *Temporal properties of secondary breakup multimode breakup regime. International Journal of multiphase Flow, Vol. 27, PP 217-236*

DEC, E.J., 1997. *A Conceptual Model of DI Diesel Combustion Based on Laser-Sheet Imaging. SAE Paper 970873*

DELACOURT, E., DESMET, B., BESSON, B., 2005. *Characterisation of very high pressure diesel sprays using digital imaging techniques. Fuel 84, (2005)859-867*

DENT, J.C., 1971. *A basis for the comparison of various experimental methods for studying spray penetration. SAE Paper 710571*

DE SERCEY. G., 2007. *University of Brighton, Cockcroft Building, Faculty of Engineering, Room 215*

DOLENC, A., 1990. *The injection equipment of future high speed DI diesel engine with respect to power and pollution requirements. I.Mech.E lecture, London, United Kingdom*

DOUGLAS, J.F., GASIOREK, J.M., SWAFFIELD, J.A., 1995. *Fluid Mechanics Text Book, 3rdEdition. Longman Group Limited*

DREXEL UNIVERSITY INFORMATION., 2004. *Laplacian edge detection. Available from: http://www.pages.drexel.edu/~weg22/edge.html*

FAETH, G.M., 1990. *Structure and atomization properties of dense turbulent sprays. Twenty-Third Symposium (International) on Combustion. The Combustion Institute. pp. 1345-1352*

FAETH, G.M., HSIANG, L.P., WU, P.K., 1995. *Structure and breakup properties of sprays. International journal on Multiphase Flow. Vol. 21, Suppl. pp. 99-127*

FARRELL, P.V., CHANG, C.T., SU, T.F., 1996. *High pressure multiple injection spray characteristics. SAE Paper 960860*

FORSTALL, W.JR., SHAPIRO, A.H., 1950. *Momentum and mass transfer in coaxial gas jets. Journal of Applied Mechanics, Vol. 17, p 399*

FOX, T.A., STARK, J., 1998. *Discharge coefficients for miniature fuel injectors. G 01188, I.Mech.E*

HATTORI, H., NARUMIYA, K., TSUE, M., KODOTA, T., 2002. Photographical analysis of initial breakup processes of diesel spray. Thiesel 2002, Conference on Thermal- and fluid Dynamic Process in Diesel Engines

HAWAS, M.M., MUNEER, T., 1981. Mathematical model for calculating the blowby rate. Energy Conservation & Mgmt, Vol. 21. pp 213-218

HEIMGARTNER, C., LEIPERTZ, A., 2000. Investigation on the primary spray breakup close to the nozzle of a common-rail high pressure diesel injection system. SAE Paper 2000-01-1799

HIROYASU, H., ARAI, M., TABATA, M., 1989. Empirical equation for the Sauter Mean Diameter of a diesel spray. SAE Paper 890646

HIROYASU, H., ARAI, M., 1990. Structure of fuel spray in diesel engines. SAE Paper 900475

HIROYASU, H., 2000. Spray breakup mechanism from the nozzle and its applications. Atomisation and Sprays, Vol 10, pp 511-527

HIROYASU, H., 1998. The structure of fuel sprays and the combustion processes in diesel engines. ASME 1998, ICE-Vol. 31-1, 1998 Fall Technical Conference, Paper No 98-ICE-117

HUH, K.Y., LEE, E., KOO, J., 1998. Diesel spray atomisation model considering nozzle exit turbulence conditions. Atomization and Sprays, Vol. 8, pp 453-469

HUH, K.Y., LEE, E., YANG, O.Y., 1991. An experimental study on initial behaviour of diesel fuel spray characteristics. ICLASS-91 Gaithersburg, MD, USA

KARIMI, E.R., 1989. High-speed photography of fuel spray and combustion event in a production diesel engine and combustion bomb. I.Mech.E, pp 269-281

KARIMI, K., SAZHINA, E.M., ABDELGHAFFAR, W.A., CRUA, C., COWELL, T., HEIKAL, M.R., GOLD, M.R., 2006. Development in diesel spray characterisation and modelling. Thiesel 2006 Conference on Thermo-and Fluid Dynamic Processes in Diesel Engines

KENNAIRD, D.A., CRUA, C., LACOSTE, J., HEIKAL, M.R., GOLD, M.R., JACKSON, N.S., 2002. In-cylinder penetration and breakup of diesel sprays using a common rail injection system. SAE Paper 2002-01-1626

KOO, J., MARTIN, J. 1990. Droplet size and velocities in a transient diesel fuel spray. SAE Paper 900397

LACOSTE, J., 2004. Characteristics of diesel sprays at high temperature and pressure. Thesis (PhD), University of Brighton, United Kingdom

LAOONUAL, Y., YULE, A.J., WALMSLEY, S.J., 2001. Internal fluid flow and spray visualisation for a large scale valve covered orifice (VCO) Injector. ILASS-Europe 2001, Zurich 2-6

LAPUERTA, M., ARMAS, O., BERMUDEZ, V., 2000. Sensitivity of diesel engine thermodynamic cycle calculation to measurement error and estimated parameters. Applied thermal Engineering, 843-861

LAPUERTA, M., ARMAS, O., MOLINA, S., 2003. Study of the compression cycle of a reciprocating engine through the polytropic coefficient. Applied thermal Engineering, 313-323

LE GAL, P., FARRUGIA, N., GREENHALGH, D.A., 1999. Laser sheet dropsizing of dense sprays. Optics and Laser Technology, Vol. 31, PP 75-83

LEE, C.S., PARK, S.W., 2002. An experimental and numerical study on fuel atomization characteristics of high-pressure diesel injection sprays. Elsevier, Fuel, pp 2417-2423

LEE, T., REITZ, R.D., 2003. The effect of split injection and swirl on a HSDI diesel engine equipped with a common rail injection system. SAE Paper 2003-01-0349

LEE, S.W., TANAKA, D., KUSAKA, J., DAISHO, Y., 2002. Effects of diesel fuel characteristics on spray and combustion in a diesel engines. Elsevier, JSAE Review 23, Page 407-414

LEFEBVRE, A.H., 1989. Atomisation and spray. Combustion: An International Series, Taylor and Francis Publishers

LEVICH, G.M., 1962. Physicochemical hydrodynamics. Prentice-Hall, Inc. Englewood Cliffs, N.J

LIU, A.B., REITZ, R.D., 1993. Mechanisms of air-assisted liquid atomisation. Atomization and Sprays, Vol. 3, pp. 55-75

LUCAS., 1995. Rate of injection manual; High Temperature and Pressure rate Gauge Manual; Issued 11/9/95.

MOHAMMADI, A., MIWA, K., ISHIYAMA, T., ABE, M., 1998. Investigation of droplets and ambient gas interaction in a diesel spray using a nano-spark photography method. SAE Paper 981073

MONTGOMERY, D.T., REITZ, R.D., 1996. Six-mode cycle evaluation of the effect of EGR and multiple injections on particulate and NOx emissions from a D.I. diesel engine. SAE paper 960316

MULHOLLAND, J.A., SRIVASTAVA, R.K., WENDT, J.O.L., 1988. Influence of droplet spacing on drag coefficient in nonevaporating, monodisperse streams. AIAA Journal, Vol. 26, NO. 10

NABER, D., SIEBERS, D.L., 1996. Effects of gas density and vaporization on penetration and dispensation of diesel spray. SAE Paper 960034

NEHMER, D.A., REITZ, R.D., 1994. Measurement of the effect of injection rate and split injections on diesel engine soot and NOx emissions. SAE Paper 940668

NURICK, W.H., 1976. Orifice cavitation and its effects on spray mixing. Journal of Fluids, Engineering

PASTOR, J.V., LOPEZ, J.J., ENRIQUE, J.J., BENAJES, V.J., 2002. Planar laser-induced fluorescence Fuel concentration measurements in isothermal diesel sprays. OPTICS EXPRESS 309, Vol. 10, No. 7

PIERPONT, D.A., MONTGOMERY, D.T., REITZ, R.D., 1995. Reducing particle and NOx using multiple injection and EGR in a D.I. diesel. SAE Paper 950217

PITCHER, G., WIGLEY, G., 1992. Application of phase doppler anemometry to combustion of diesel fuel spray measurements technique, Precision and Data Interpretation. 6th workshop on two-phase flow prediction, March 30 April 2, 1992 at Lehrstuhl fur Stromungsmechanik Cauerstr. 4, 8520 Erlangen FGR

PITCHER, G., WIGLEY, G., SAFFMAN, M., 1990. Velocity and drop size measurements in fuel sprays in a direct injection diesel engine. Particle and Particle Systems Characterisation, Vol. 7, pp. 160-168

PRASAD, A., WILLIAMSON, C.H.K., 1997. A method for the reduction of bluff body drag. Journal of Wind Engineering and Industrial Aerodynamics 69-71, pp 155-176

REITZ, R.D., BRACCO, F.V., 1982. Mechanism of atomization of a liquid jet. American Institute of Physics, Phys. Fluids 25 (10)

REITZ, R.D., DIWAKAR, R., 1987. Structure of high-pressure fuel sprays. SAE Paper 870598

SAVIC, S., 2000. Liquid fuel spray characteristics. Thesis (PhD), University of Brighton, United Kingdom

SAZHINA, E.M., SAZHIN, S.S., HEIKAL, M.R., BABUSHOK, V.I., JOHNS, R., 2000. A detailed modelling of the spray ignition process in diesel engines. combustion science and technology, 160, pp 317-344

SAZHIN, S.S., FENG, G., GOLDFARB, I., GOLDSHTEIN, V., KUZMENKO, G. (2001(a)). Thermal ignition analysis of a monodisperse spray with radiation. Combustion and Flame 124(4), 684-701

SAZHIN, S.S., FENG, G., HEIKAL, M.R, (2001(b)). A model for fuel spray penetration. Fuel 80(15), pp 2171-2180

SAZHIN, S.S., CRUA, C., KENNAIRD, D., HEIKAL, M.R., 2003. *The initial stage of fuel spray penetration. Fuel 82, pp 875-885*

SCHMIDT, D.P., CORRADINI, M.L., 2001. *The internal flow of diesel fuel injector nozzles: A Review. INT. J. Of Engine Res, 2001 2 (1), I0034104BN*

SCHMIDT, D.P., RUTLAND, C.J., CORRADINI, M.L., 1999. *Cavitation in two-dimensional asymmetric nozzles. SAE Paper 1999-01-0518*

SCHUGGER, C., RENZ, U., 2003. *Experimental investigation of the primary breakup zone of high pressure diesel sprays from multi-orifice nozzles. 9th International conference on liquid atomization and spray system, ICLASS-2003*

SHER, E., 1998. *Handbook of air pollution from internal combustion engines, Pollutant formation and Control. ACADEMIC PRESS*

SHIMIZU, M., ARAI, M., HIROYASU, H., 1984. *Measurements of breakup length in high speed jet. Bulletin of JSME, Vol. 27, No 230*

SHUNDOH, S., KOMORI, M., TSUJIMURA, K., 1992. *NOx reduction from diesel combustion using pilot injection with high pressure fuel injection. SAE Paper 920461*

SEITZMAN, J.M., HANSON, R.K., 1993. *Planar fluorescence imaging in gases. Instrumentation for Flows with Combustion, edited by A.M.K.P. Taylor, Academic press 405-466*

SOTERIOU, C., ANDREWS, R., SMITH, M., 1995. *Direct injection sprays and the effect of cavitation and hydraulic flip on atomization. SAE Paper 950080*

SOVANI, S.D., CHOU, E., SOJKA, P.E., GORE, J.P., ECKERLE, W.A., CROFTS, J.D., 2000. *High pressure effervescent atomisation: Effect of Ambient Pressure on Spray Cone Angle. Elsevier, Fuel, pp 427-435*

STRAKEY, P.A., TALLEY, D.G., 1998. *Phase doppler measurements in dense sprays. Also In ILASS (AMER)98 Proc. Carnegie Mellon Uni. Short Course On Spray Technology. Vol. 2*

SU, T.F., PATTERSON, A., REITZ, R.D., FARRELL, P.V., 1996. *Experimental and numerical studies of high pressure multiple injection sprays. SAE Paper 960861*

SUZUKI, K., HONDA, A., SUMI, S., KIBUNE, M., 1982. *Study of abnormal fuel delivery characteristics in high pressure injection systems. SAE Paper 821073*

TAKEDA, Y., NIIMURA, K., 1995. *Characteristics of diesel combustion and emissions with a multiple-injection system. SAE Paper 952511*

TOW, T.C., PIERPONT, D.A., REITZ, R.D., 1994. *Reducing particulate and NOx emissions by using multiple injection in a heavy duty D.I. diesel engine. SAE Paper 940897*

TSUE, M., HATTORI, H., SAITO, A., KADOTA, T., 1992. *Planer fluorescence technique for visualization of a diesel spray. SAE Paper 922205*

YI, Y., REITZ, R.D., 2004. *Modelling the primary breakup of high-speed jets. Atomization and Sprays, Vol. 14, pp. 53-80*

YOSHIZU, F., NAKASYAMA, M., 1991. *Spray characteristics of a pilot injection system operating in an idling D.I. diesel engine. Proceedings of the Fifth International conference on Liquid Atomization and Spray Systems, ICLASS-91; Gaithersburg, M.D., USA*

YULE, A.J., AKHTAR, P., SHRIMPTON, J.S., WAHNER, T., 1998. *PDA measurements of fuel effects on atomisation and spray structure from a diesel engine injector. SAE Paper 982544*

YULE, A.J., AVAL, S.M., 1989. *A technique for velocity measurement in diesel sprays. combustion and flame, Vol. 77, pp 385-394*

YULE, A.J., FILIPOVIC, I., 1991. *On the breakup times and length of diesel spray. International journal of Heat and Fluid Flow, Vol. 13, No 2*

YULE, A.J., SALTERS, D.G., 1995. *On the distance required to atomise diesel spray injected from orifice-type nozzle. I.Mech.E, Vol. 209*

PUBLICATIONS BY THE AUTHOR

KARIMI, K., CRUA, C., HEIKAL, M.R., SAZHINA, E.M., 2007. Split injection strategy for diesel sprays: experimental and modelling. The Development of Combustion Engines, PTNSS Congress-2007 B07-C165. Polish Scientific Society of Combustion Engines

MARTYNOV, S., SAZHIN, S., GOROKHOVSKI, M., CHATAB, A., KARIMI, K., CRUA, C., HEIKAL, M.R., 2007. A modified WAVE model for transient Liquid Sprays. Submitted to the International Journal of Heat and Fluid Flow

KARIMI, K., SAZHINA, E.M., ABDELGHAFFAR, W.A., CRUA, C., COWELL, T., HEIKAL, M.R., GOLD, M.R., 2006. Development in diesel spray characterisation and modelling. Thiesel 2006 Conference on Thermo-and Fluid Dynamic Processes in Diesel Engines

ABDELGHAFFAR, W., KARIMI, K., HEIKAL, M.R., 2006. Fuel spray penetration in high pressure diesel engines. SAE Paper 07SFL-15

SAZHIN, S., MARTYNOV, S., SHISHKOVA, I., CRUA, C., KARIMI, K., GOROKHOVSKI, M., SAZHINA, E.M., HEIKAL, M.R., 2006. Modelling of droplet heating, evaporation and breakup: recent Developments. 13th International Heat Transfer Conference (IHTC-13), Sydney, Australia

APPENDICES

APPENDIX A: FUEL INJECTION CHARACTERISATION AND ANALYSIS

APPENDIX B: CONSIDERATION OF THE OPTICAL TEST RIG AND ANALYSIS

APPENDIX C: DIESEL SPRAY CHARACTERISATION, CONVENTIONAL STRATEGY

APPENDIX D: EXPERIMENTAL STUDIES OF MULTIPLE INJECTION DIESEL SPRAY CHARACTERISATION

APPENDIX E: EXPERIMENTAL PENETRATION LENGTH AGAINST PENETRATION CORRELATION

APPENDIX A: FUEL INJECTION SYSTEM CHARACTERISATION AND ANALYSIS

Rate of Injection for 0.425 *ms* and 0.625 *ms* Dwell Periods
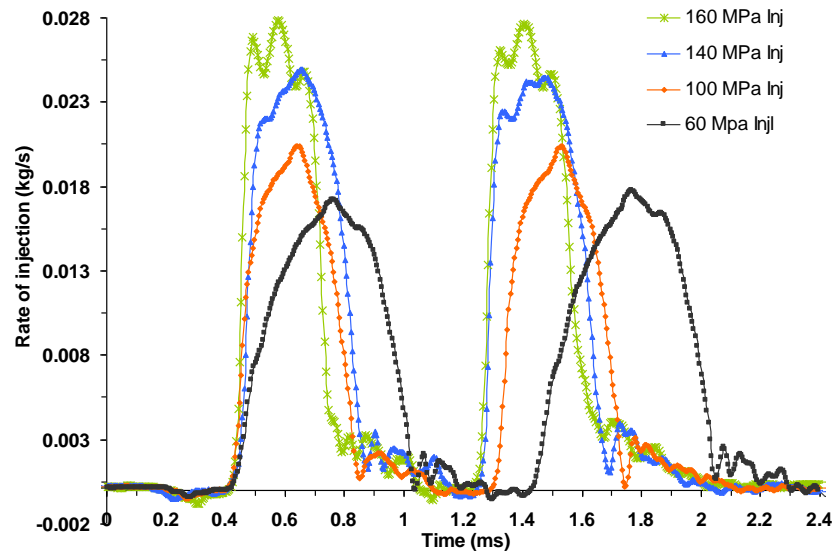
Fig AA-1. Comparison of rate of injection for 0.425 ms dwell period; 20 mm³ fuelling in total (2⊂10 mm³); Delphi injector
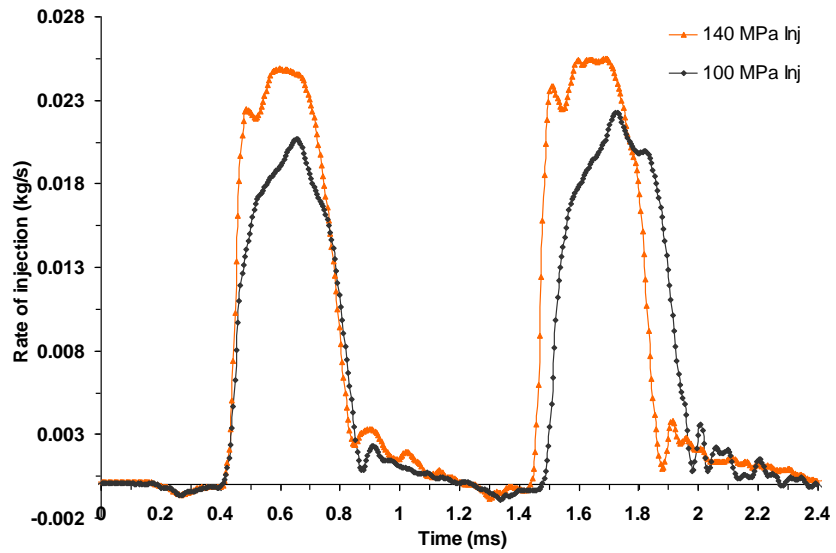
Fig AA-2. Comparison of rate of injection for 0.625 ms dwell period; 20 mm³ fuelling in total (2⊂10 mm³); Delphi injector

A1

APPENDIX B: CONSIDERATION OF THE OPTICAL TEST RIG AND ANALYSIS

Experimental Conditions for Determination of Compression Ratio and Polytropic Coefficient

Case Number	Plenum Air Temp (*K*)	Water Jacket Temp (*K*)	Heated Boost	In-Cylinder Pressure at TDC (*MPa*)
1	371.15	373.25	Yes	2
2	370.25	373.15	Yes	3.2
3	371.15	373.2	Yes	4
4	372.15	373.15	Yes	5.5
5	371.15	373.15	Yes	6
6	366.15	373	Yes	7
7	375.15	373.25	Yes	7.9
8	375.15	373.15	Yes	8.5
9	375.15	373	Yes	10
10	375.15	373.25	Yes	10.5
11	295.85	373.35	No	2
12	296.15	373.05	No	3
13	296.85	373.15	No	4
14	297.45	373.25	No	5
15	297.65	373.15	No	6
16	295.85	373	No	7
17	298.25	373.35	No	8

Tab AB-1. Test conditions for the assessment of compression ratio and Polytropic coefficient.

In-Cylinder and Intake Boost Pressure Traces
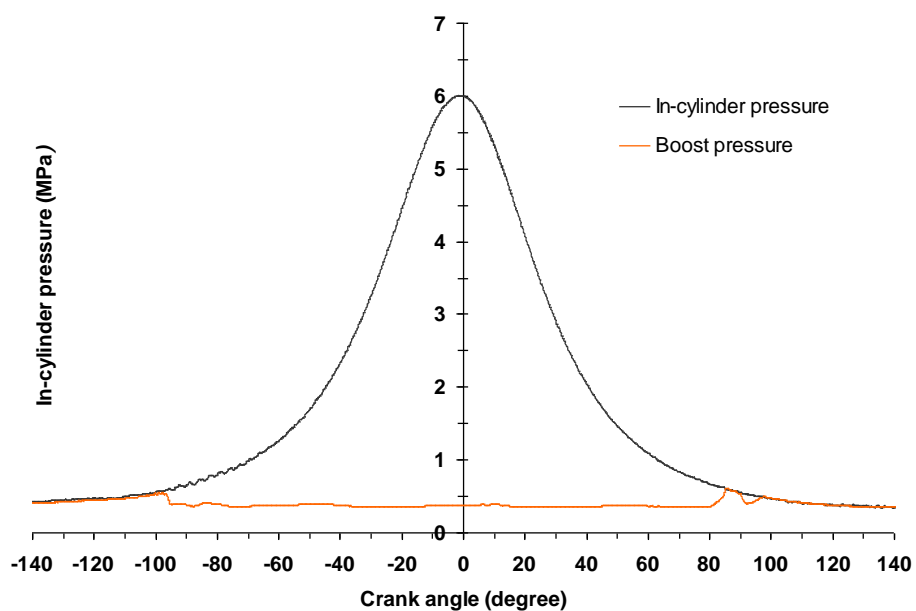
Fig AB-1. Evolution of the in-cylinder and intake boost pressures; 6 MPa at TDC
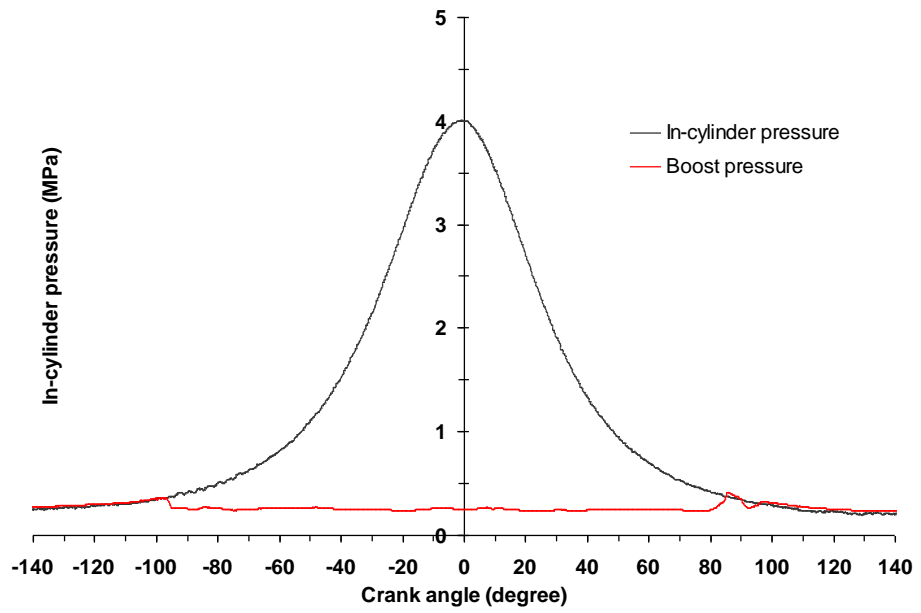
Fig AB-2. Evolution of the in-cylinder and intake boost pressures; 4 MPa at TDC
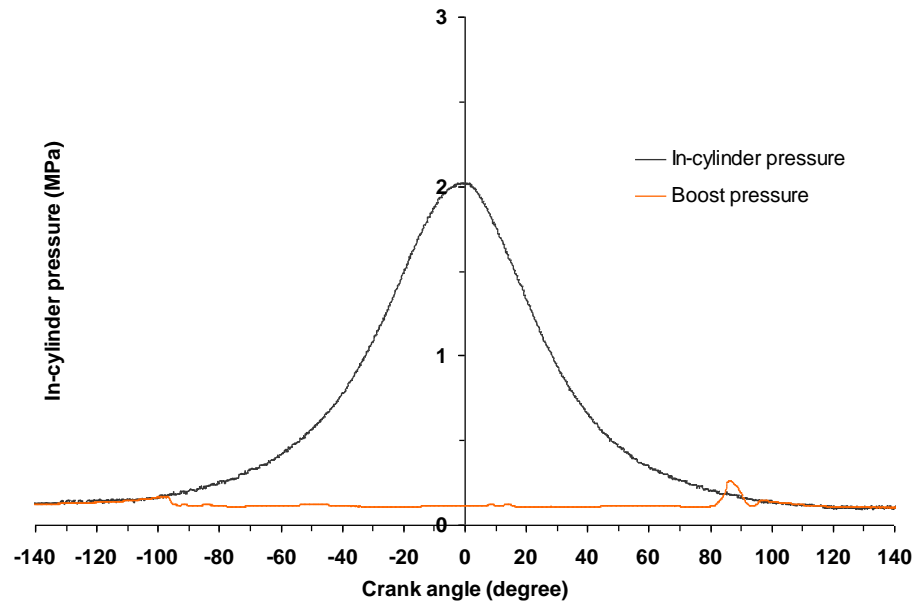
Fig AB-2. Evolution of the in-cylinder and intake boost pressures; 2 MPa at TDC

APPENDIX C: DIESEL SPRAY CHARACTERISATION, CONVENTIONAL STRATEGY

The Effect of Multi-Hole Nozzle on Common Rail Pressure

Bosch Injector
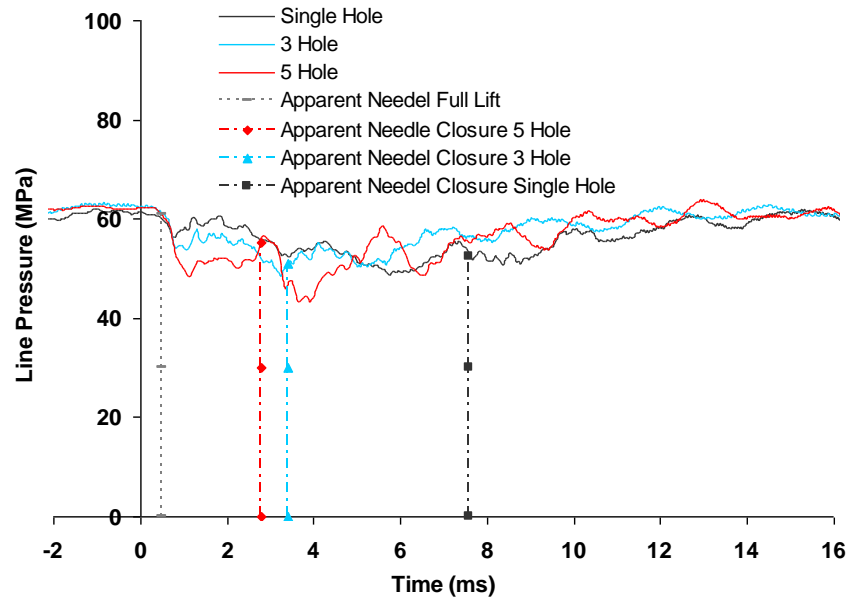
Fig AC-1. Rail pressure traces recorded by an AVL Indiset high speed data acquisition system at 60 MPa injection pressure, 6 MPa ICP, and 50 mm^3 fuelling. The broken lines indicate apparent needle full lift and closures. The nozzles tested were all 0.2 mm single guided VCO
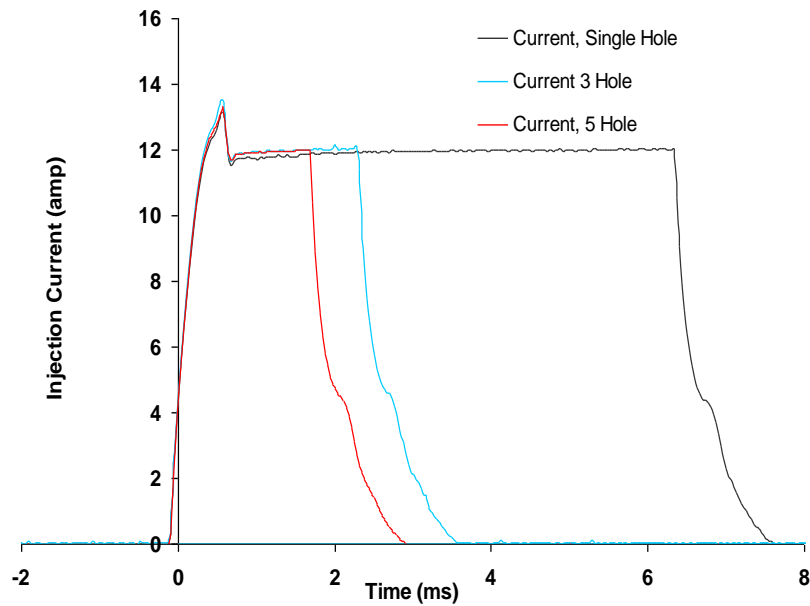
Fig AC-2. Injection current traces recorded by an AVL Indiset high speed data acquisition system at 60 MPa injection pressure, 50 mm^3 fuelling
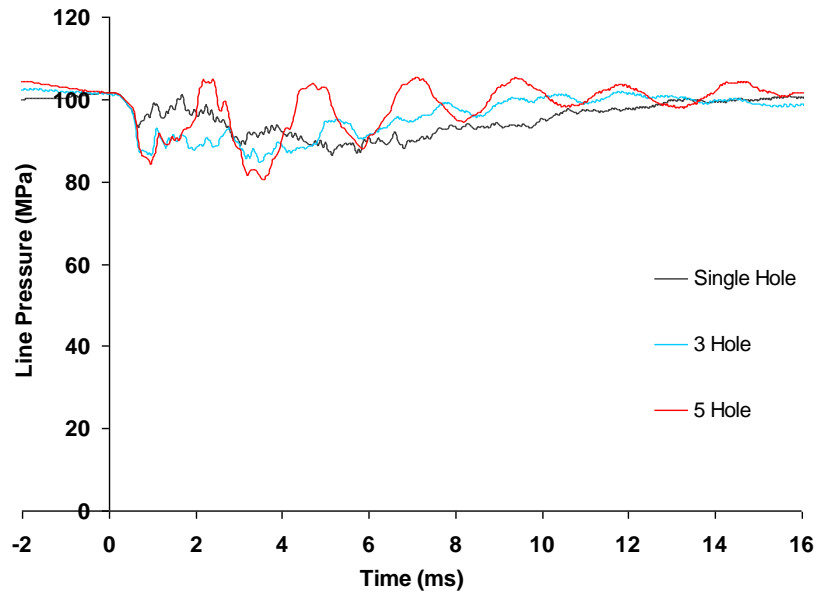
Fig AC-3. Rail pressure traces recorded by an AVL Indiset high speed data acquisition system at 100 MPa injection pressure, 6 MPa ICP, and 50 mm³ fuelling. The nozzles tested were all 0.2 mm single guided VCO
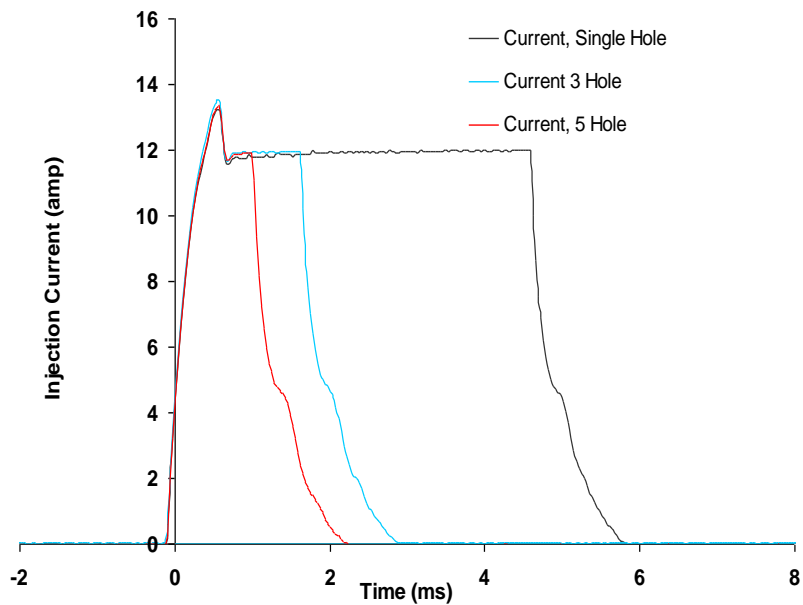
Fig AC-4. Injection current traces recorded by an AVL Indiset high speed data acquisition system at 100 MPa injection pressure, 50 mm³ fuelling
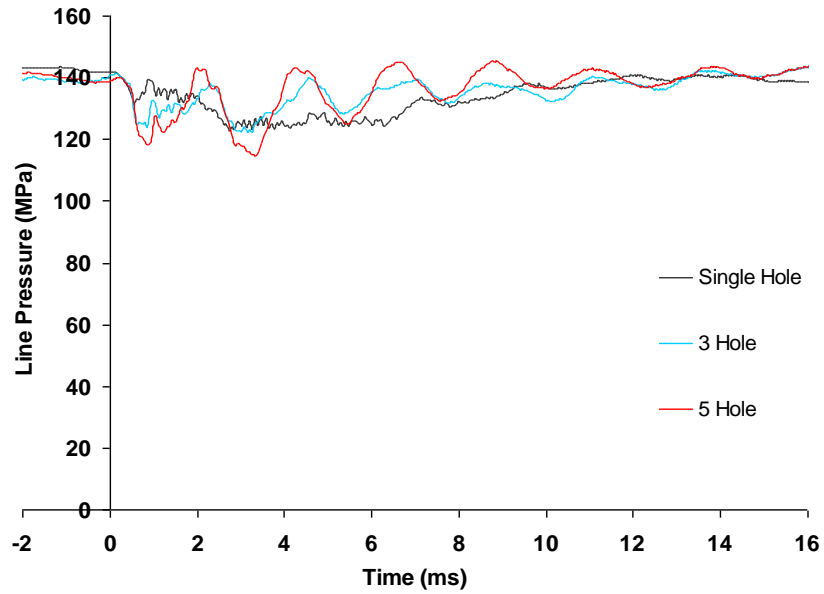
Fig AC-5. Rail pressure traces recorded by an AVL Indiset high speed data acquisition system at 140 MPa injection pressure, 6 MPa ICP, and 50 mm^3 fuelling. The nozzles tested were all 0.2 mm single guided VCO.
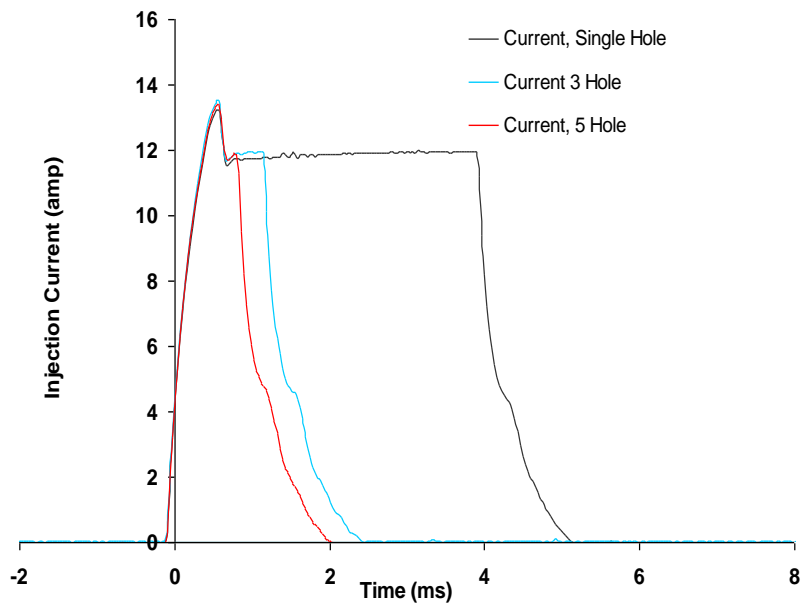
Fig AC-6. Injection current traces recorded by an AVL Indiset high speed data acquisition system at 140 MPa injection pressure, 50 mm^3 fuelling

C 6
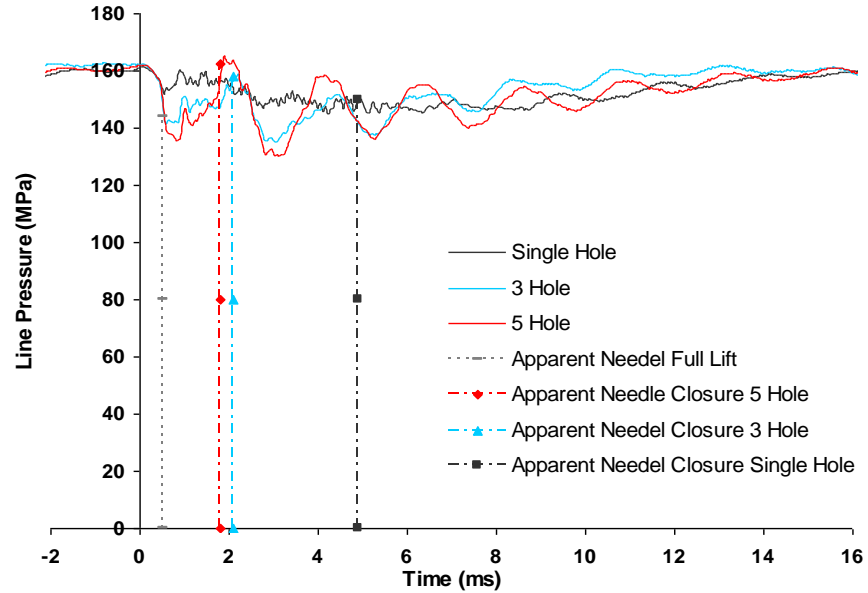
Fig AC-7. Rail pressure traces recorded by an AVL Indiset high speed data acquisition system at 160 MPa injection pressure, 6 MPa ICP, and 50 mm³ fuelling. The broken lines indicate apparent needle full lift and closures. The nozzles tested were all 0.2 mm single guided VCO
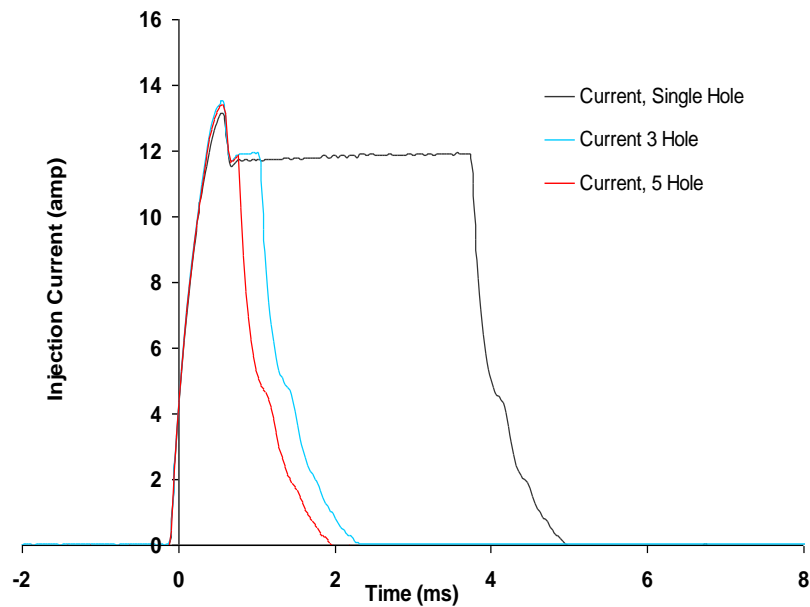
Fig AC-8. Injection current traces recorded by an AVL Indiset high speed data acquisition system at 160 MPa injection pressure, 50 mm³ fuelling

C 7

Delphi Injector
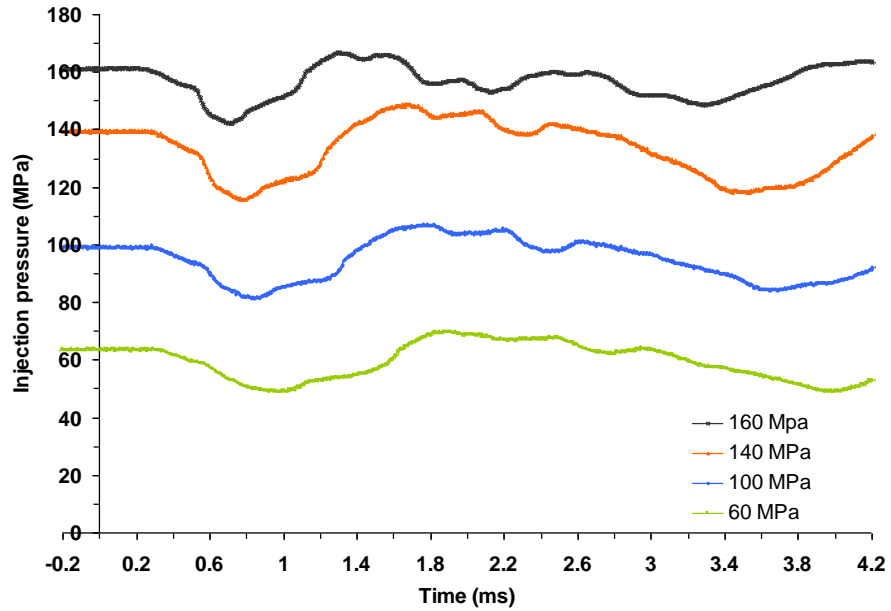
Fig AC-9. Rail pressure traces recorded by a LeCroy LT224 storage oscilloscope; 20 mm³ fuelling; 0.135 mm diameter nozzle, single guided VCO Delphi
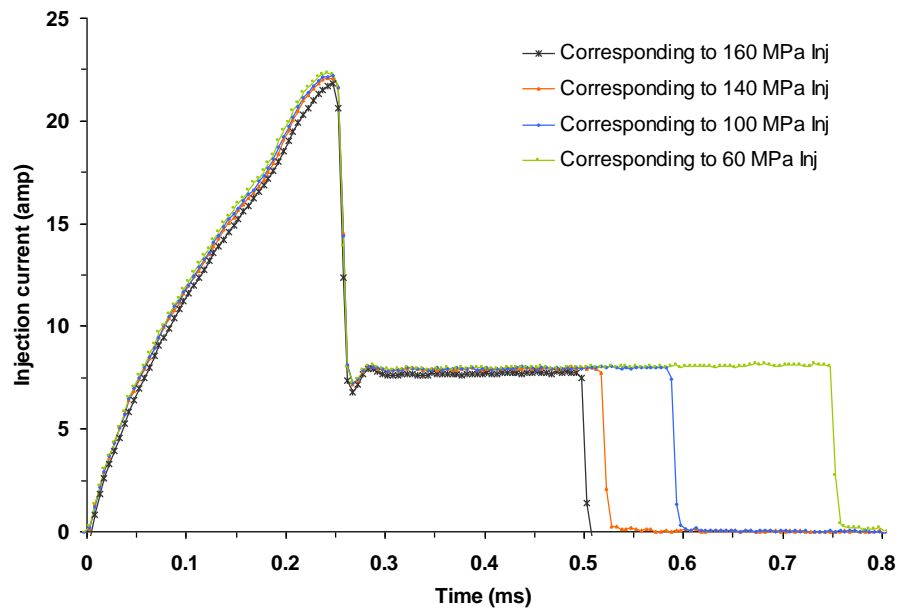
Fig AC-10. Injection current traces recorded by a LeCroy LT224 storage oscilloscope; 20 mm³ fuelling; 0.135 mm diameter nozzle, single guided VCO Delphi

The Effect of Injection Pressure on Spray Tip Penetration
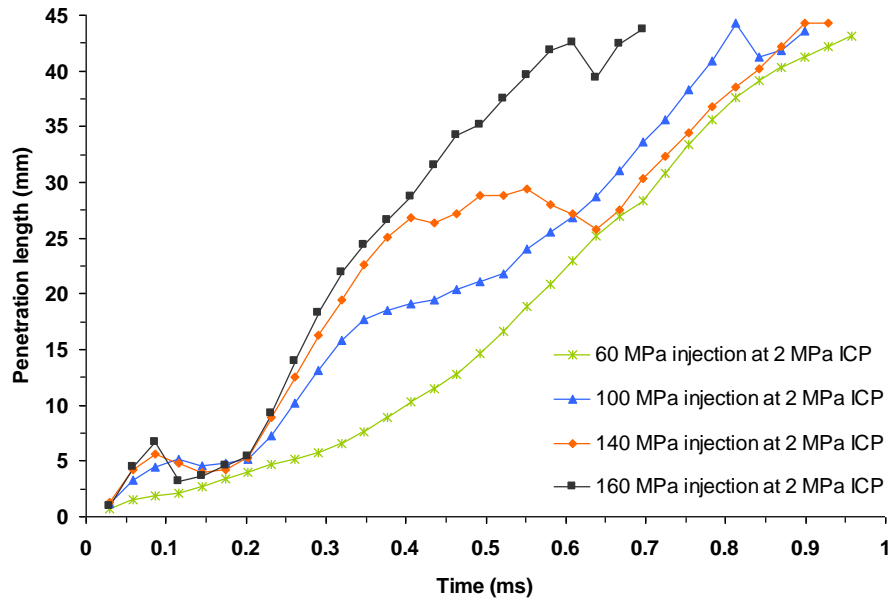
Single-Hole Nozzle

Fig AC-11. The effect of injection pressure on spray penetration for a 0.2 mm single-hole single guided VCO nozzle; 2 MPa in-cylinder pressure; 20 kg/m^3 in-cylinder gas density; cold air intake (corresponding to 350 K at TDC)
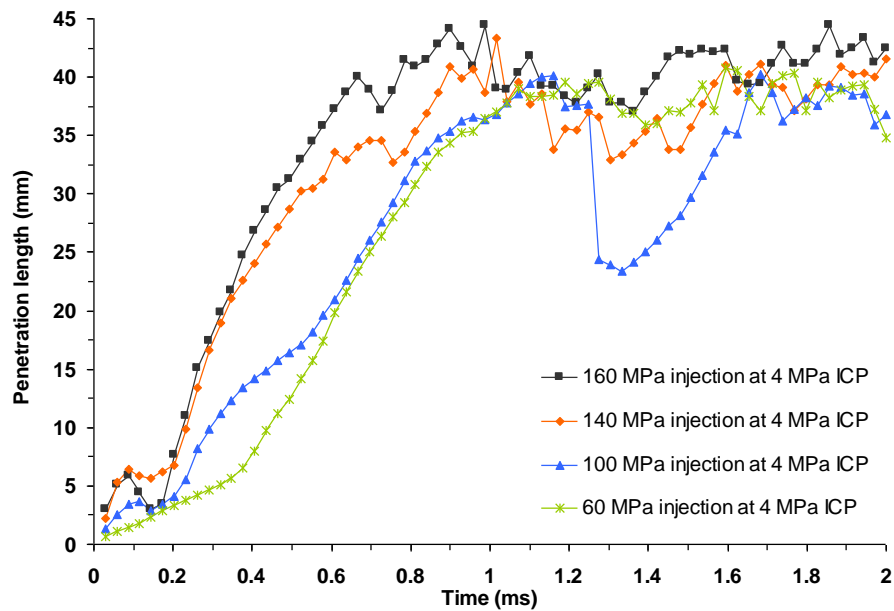
Fig AC-12. Same as Fig AC-11, with the exception of 4 MPa in-cylinder pressure; 34 kg/m^3 in-cylinder gas density; cold air intake (corresponding to 410 K at TDC)

C 9
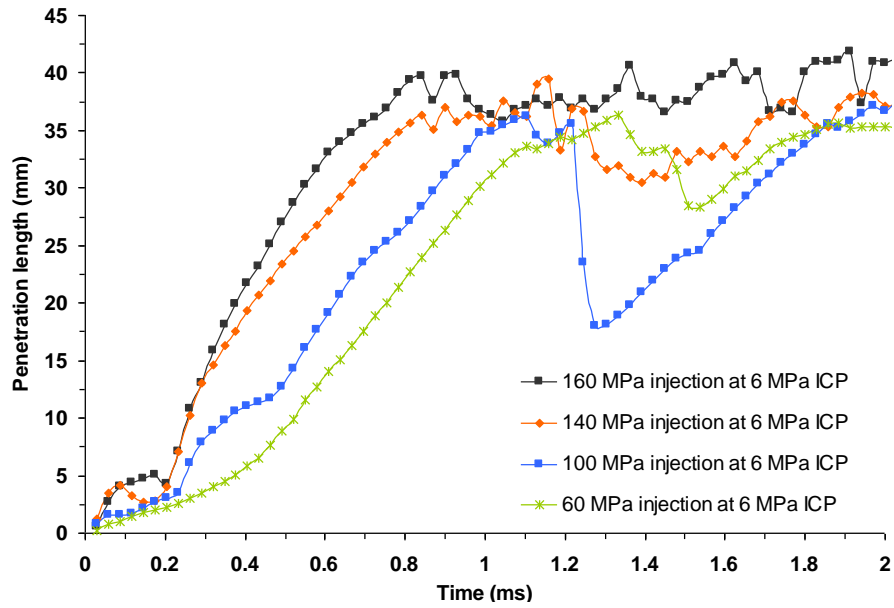
Fig AC-13. Same as the Fig AC-11, with the exception of 6 MPa in-cylinder pressure; 47 kg/m³ in-cylinder gas density; cold air intake (corresponding to 448 K at TDC)

3-Hole Nozzle
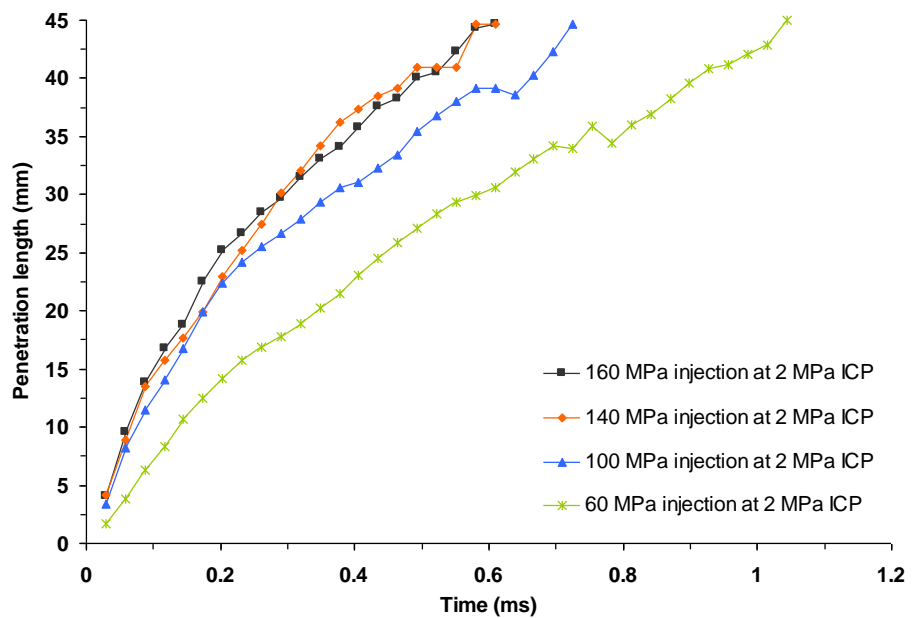
Fig AC-14. The effect of injection pressure on spray penetration for a 0.2 mm 3-hole single guided VCO nozzle; 2 MPa in-cylinder pressure; 20 kg/m³ in-cylinder gas density; cold air intake (corresponding to 350 K at TDC)

C10
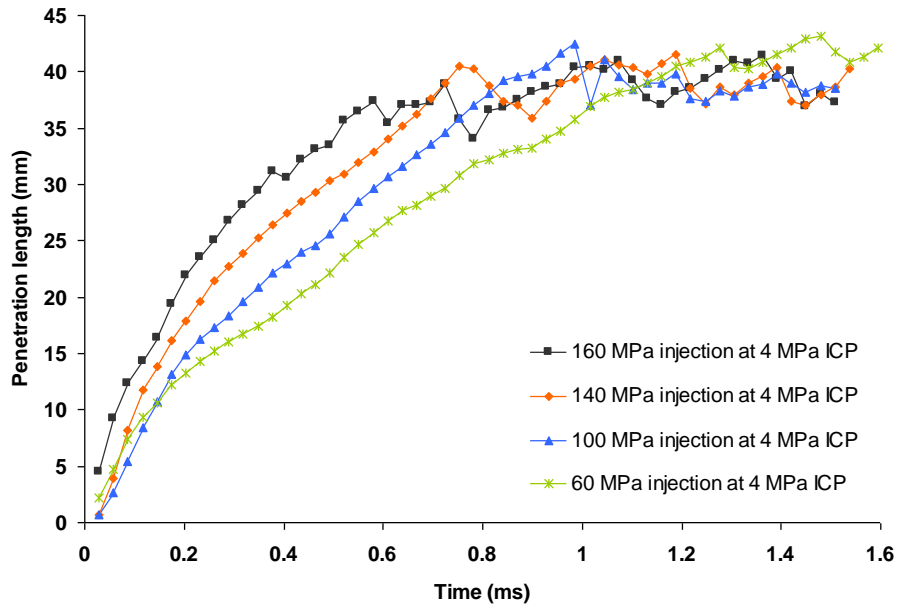
Fig AC-15. Same as Fig AC-14, with the exception of 4 MPa in-cylinder pressure; 34 kg/m³ in-cylinder gas density; cold air intake (corresponding to 410 K at TDC)
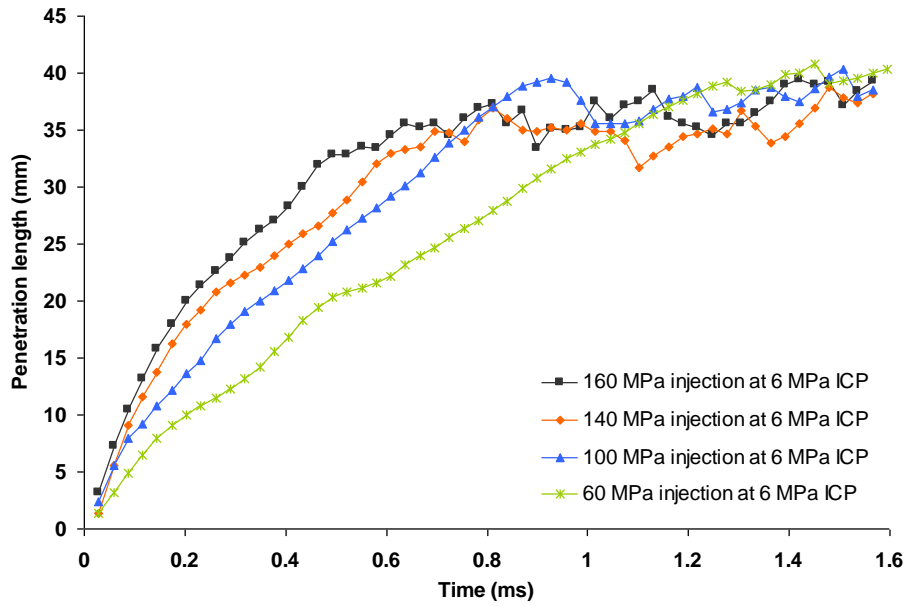
Fig AC-16. Same as Fig AC-14, with the exception of 6 MPa in-cylinder pressure; 47 kg/m³ in-cylinder gas density; cold air intake (corresponding to 448 K at TDC)

5-Hole Nozzle
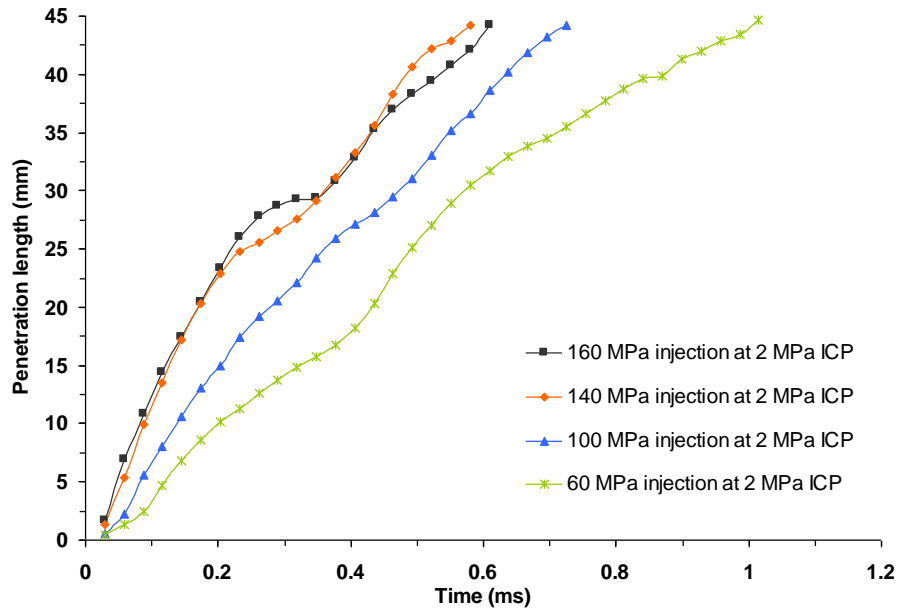
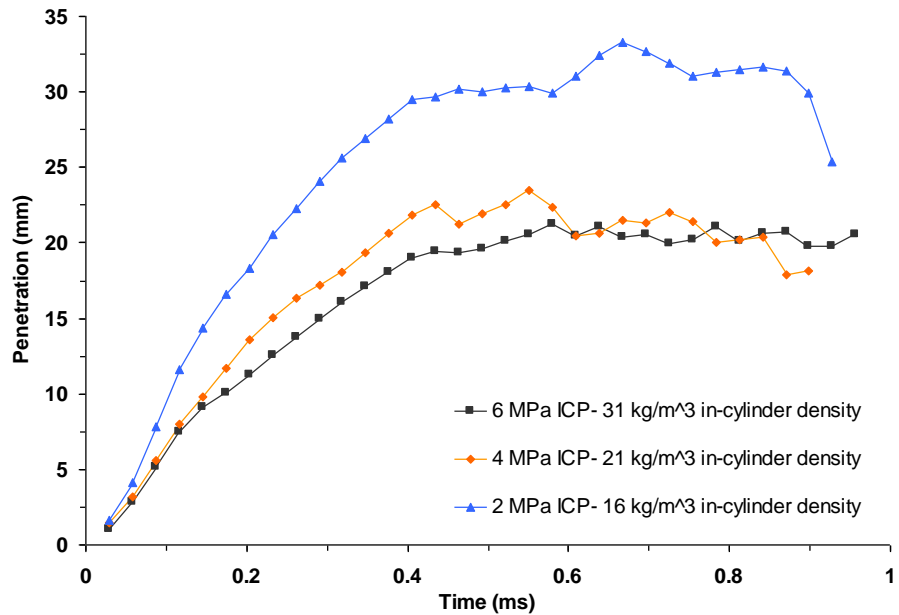*Fig AC-17. The effect of injection pressure on spray penetration for a 0.2 mm 5-hole single guided VCO nozzle; 2 MPa in-cylinder pressure; 20 kg/m³ in-cylinder gas density; cold air intake (corresponding to 350 K at TDC)*
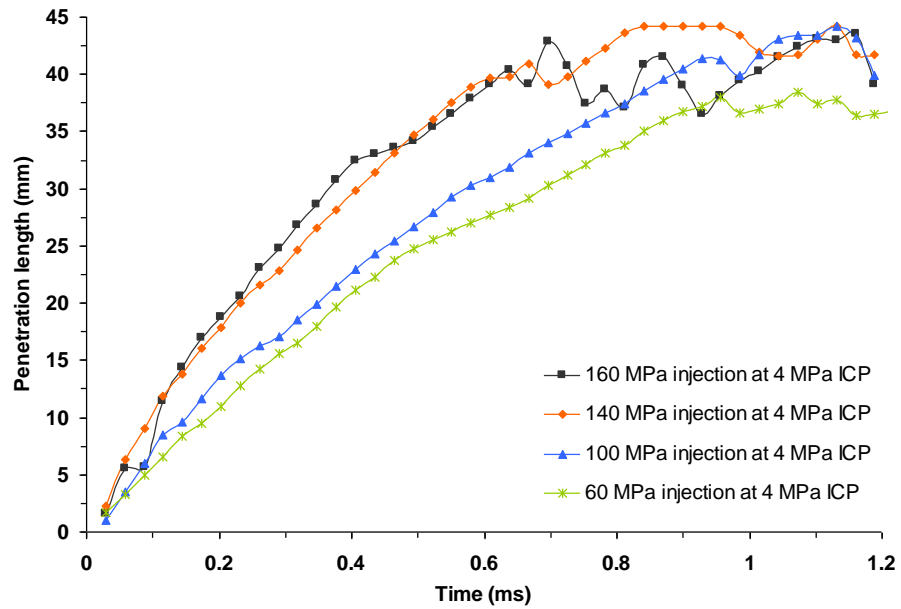
Fig AC-18. Same as Fig AC-17, with the exception of 4 MPa in-cylinder pressure; 34 kg/m³ in-cylinder gas density; cold air intake (corresponding to 410 K at TDC)
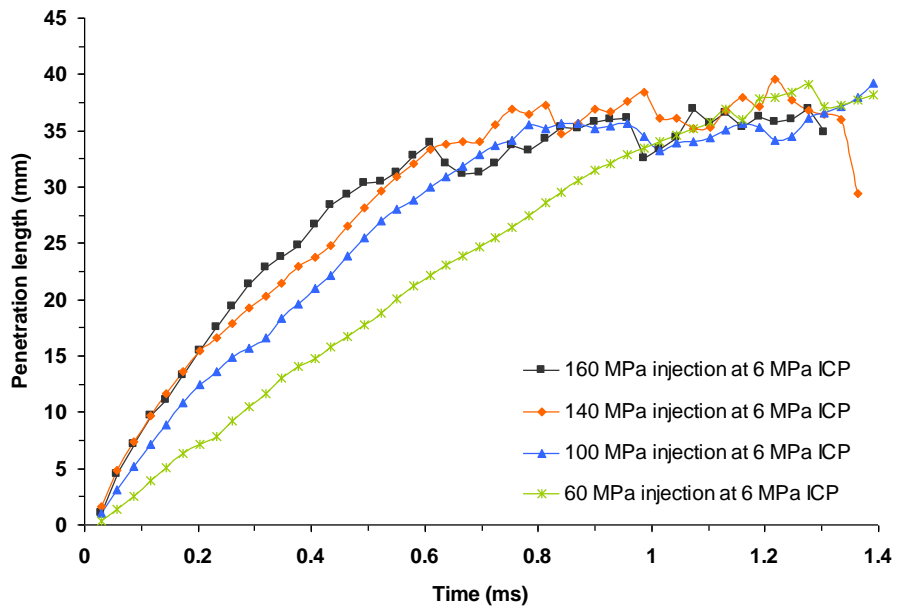
Fig AC-19. Same as Fig AC-17, with the exception of 6 MPa in-cylinder pressure; 47 kg/m³ in-cylinder gas density; cold air intake (corresponding to 448 K at TDC)

Delphi injector
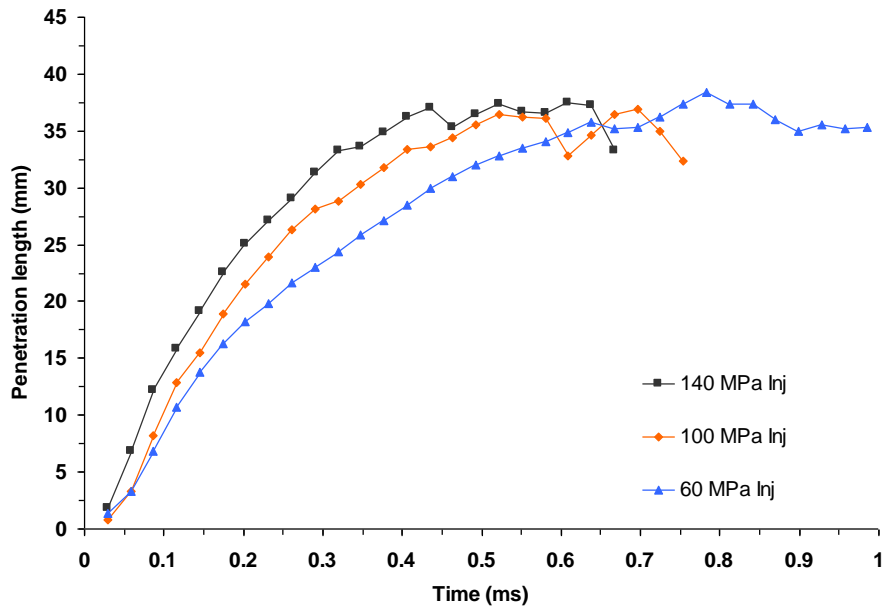
*Fig AC-20. The effect of injection pressure on spray penetration for a 0.135 mm 7-hole single guided VCO nozzle; 2 MPa in-cylinder pressure; 20 kg/m³ in-cylinder gas density; cold air intake (corresponding to 350 K at TDC)*
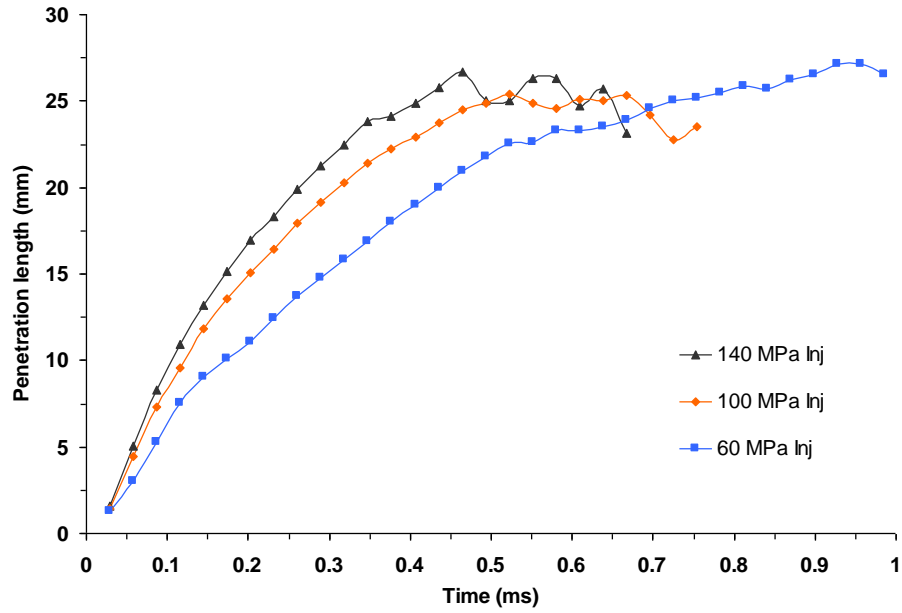
Fig AC-21. Same as Fig AC-20, with the exception of 6 MPa in-cylinder pressure; 47 kg/m³ in-cylinder gas density; cold air intake (corresponding to 448 K at TDC)

The Effect of In-Cylinder Gas Pressure at Cold Air Intake on Spray Tip Penetration
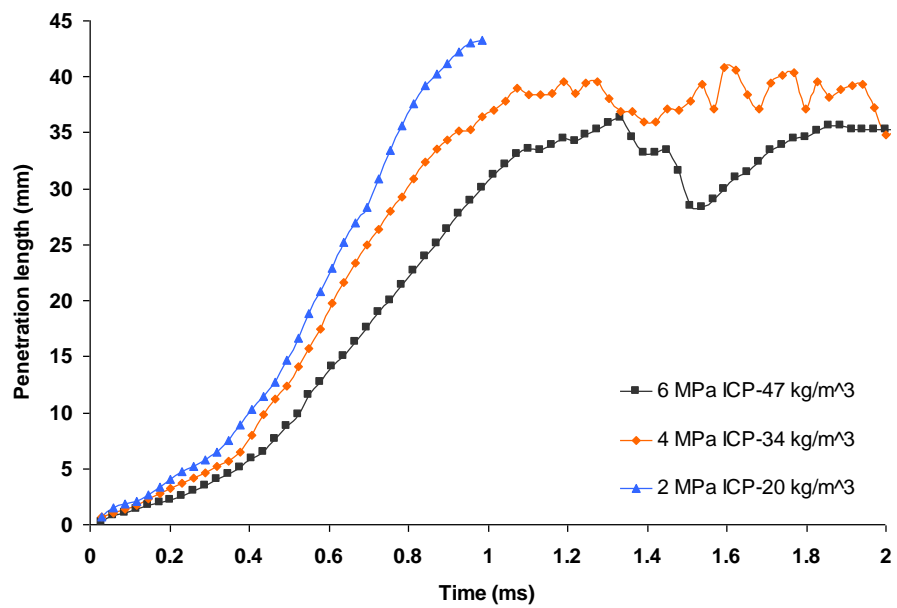
Single-Hole Nozzle

Fig AC-22. The effect of in-cylinder gas pressure on spray penetration for a 0.2 mm single-hole single guided VCO nozzle; 60 MPa injection pressure; cold air intake

C14
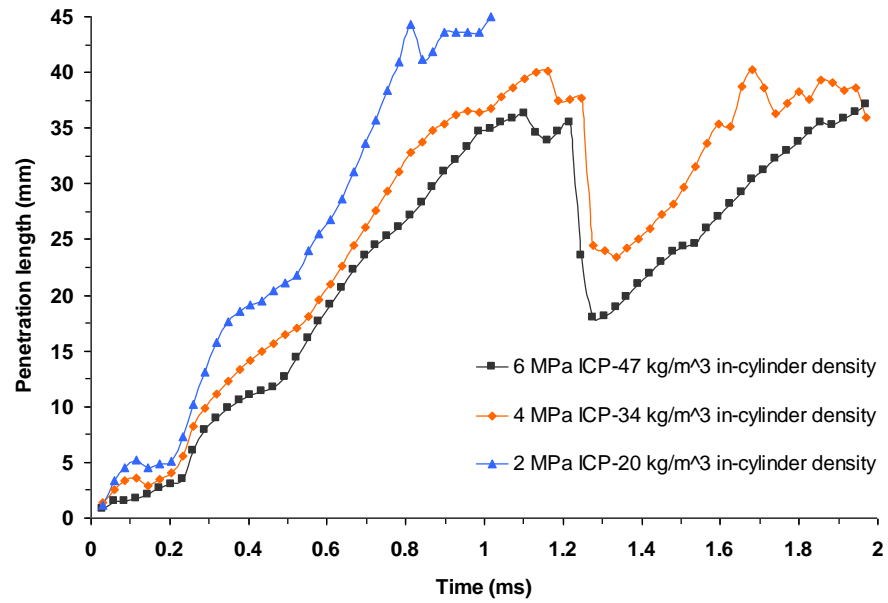
Fig AC-23. Same as Fig AC-22, with the exception of 100 MPa injection pressure
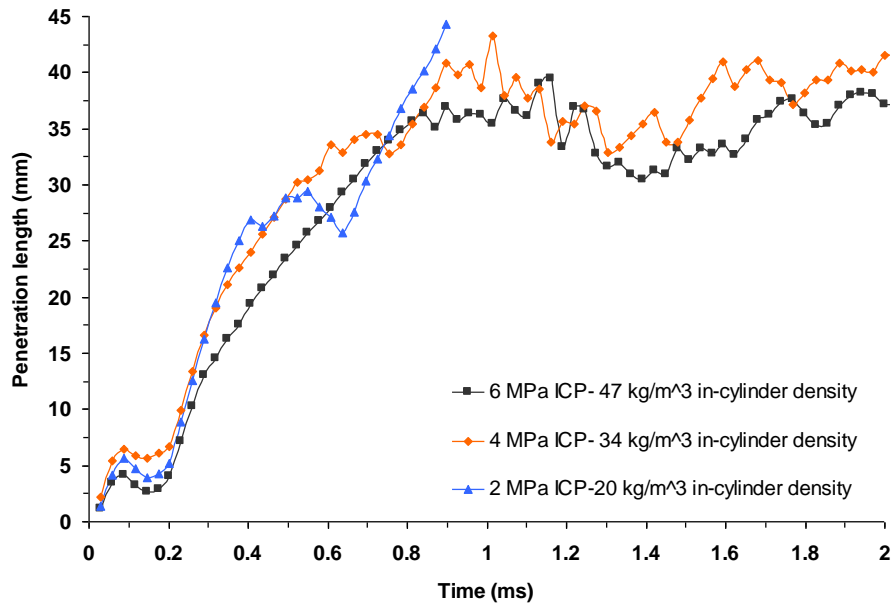
*Fig AC-24. Same as Fig AC-22, with the exception of 140 MPa injection pressure*
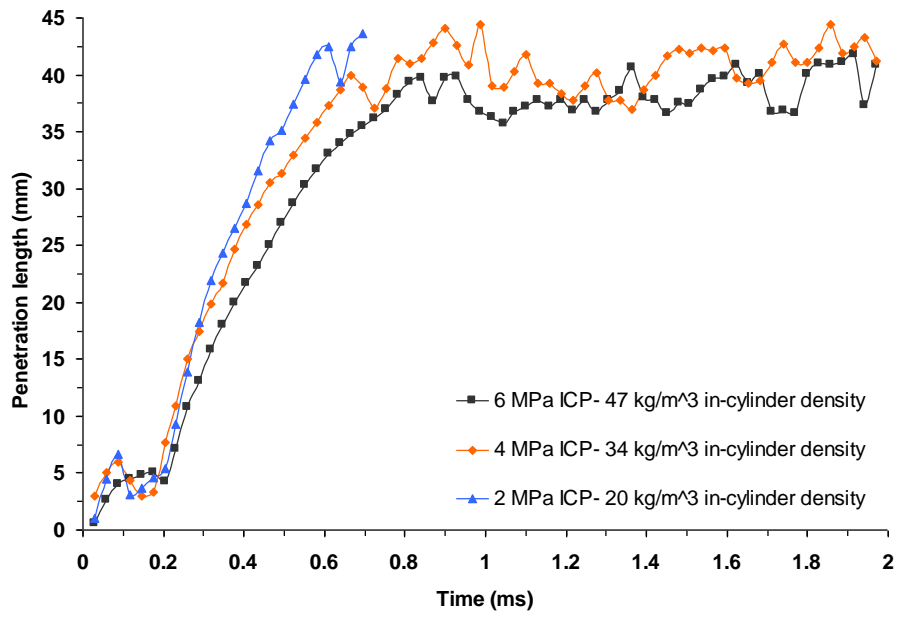
Fig AC-25. Same as Fig AC-22, with the exception of 160 MPa injection pressure
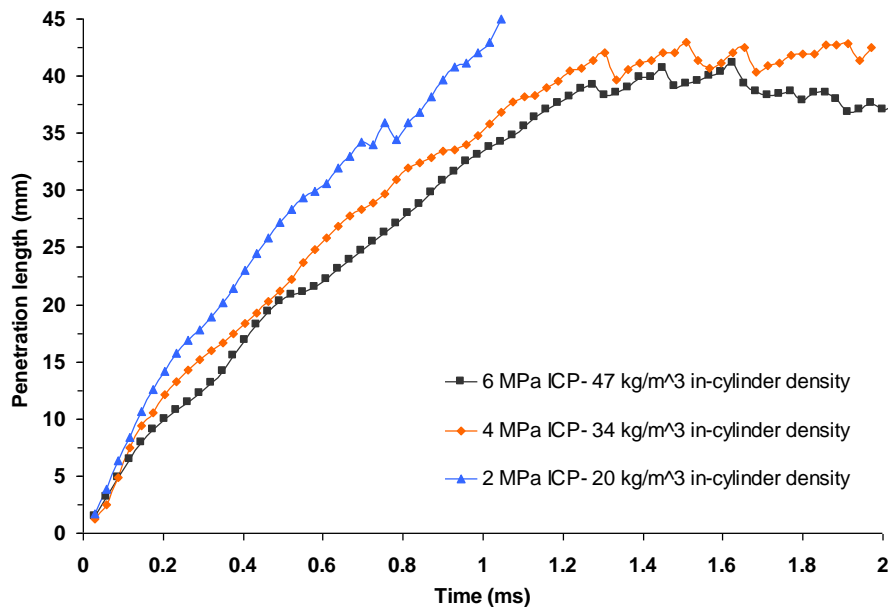
3-Hole Nozzle

Fig AC-26. The effect of in-cylinder gas pressure on spray penetration for a 0.2 mm 3-hole single guided VCO nozzle; 60 MPa injection pressure; cold air intake
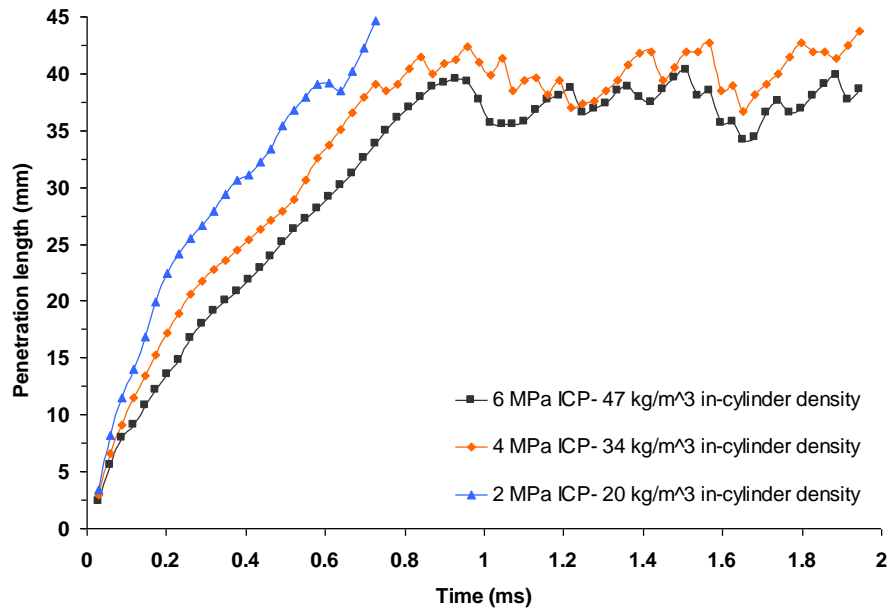
Fig AC-27. Same as Fig AC-26, with the exception of 100 MPa injection pressure
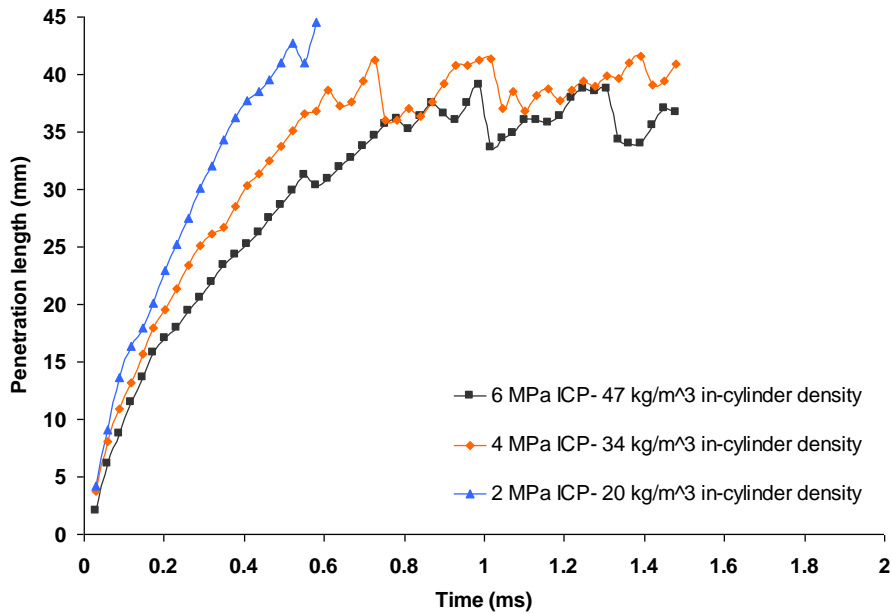
Fig AC-28. Same as Fig AC-26, with the exception of 140 MPa injection pressure

C17
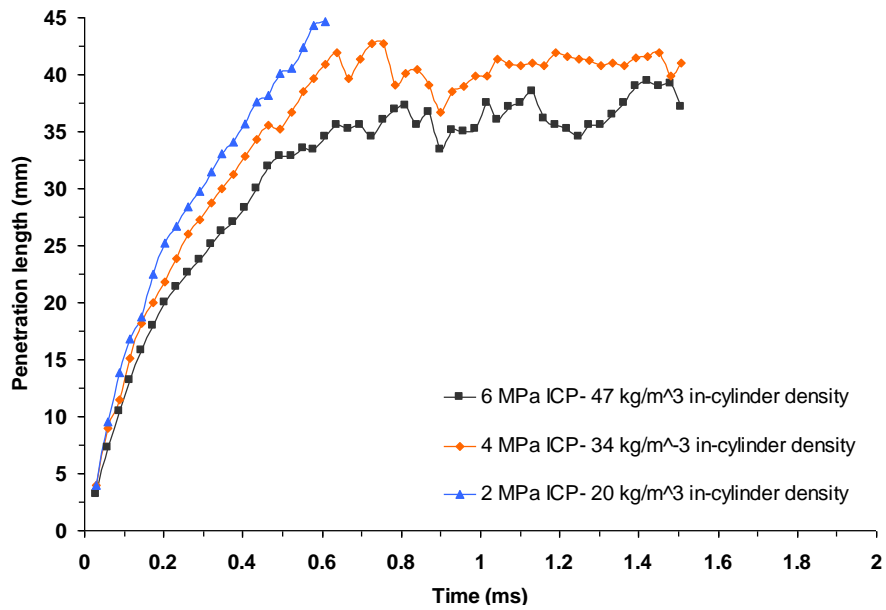
Fig AC-29. Same as Fig AC-26, with the exception of 160 MPa injection pressure
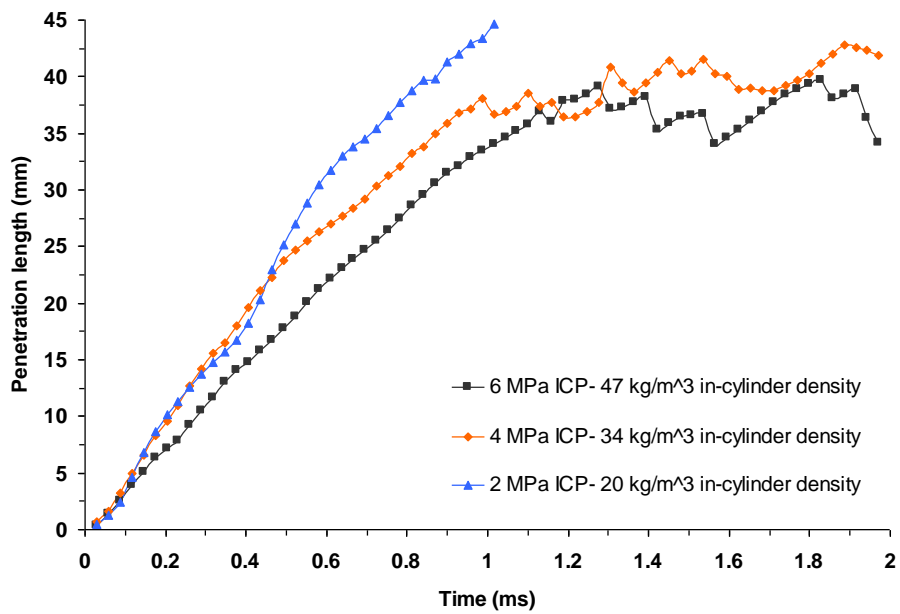
5-Hole Nozzle

Fig AC-30. The effect of in-cylinder gas pressure on spray penetration for a 0.2 mm 5-hole single guided VCO nozzle; 60 MPa injection pressure; cold air intake
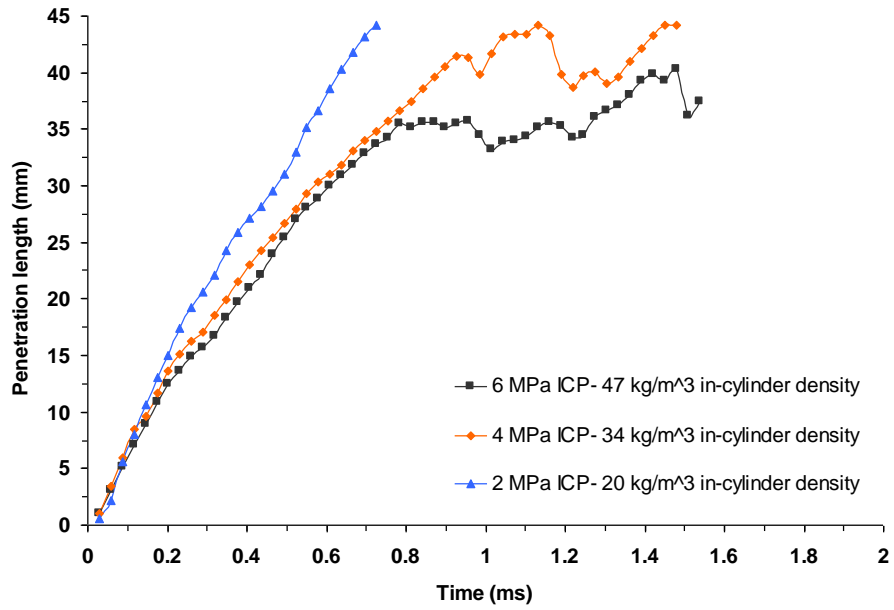
Fig AC-31. Same as Fig AC-30, with the exception of 100 MPa injection pressure
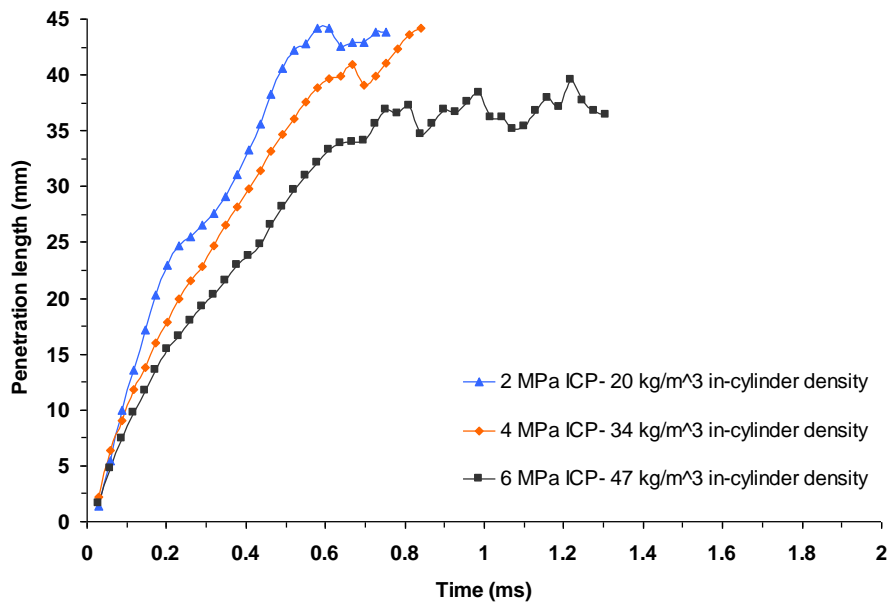
Fig AC-32. Same as Fig AC-30, with the exception of 140 MPa injection pressure
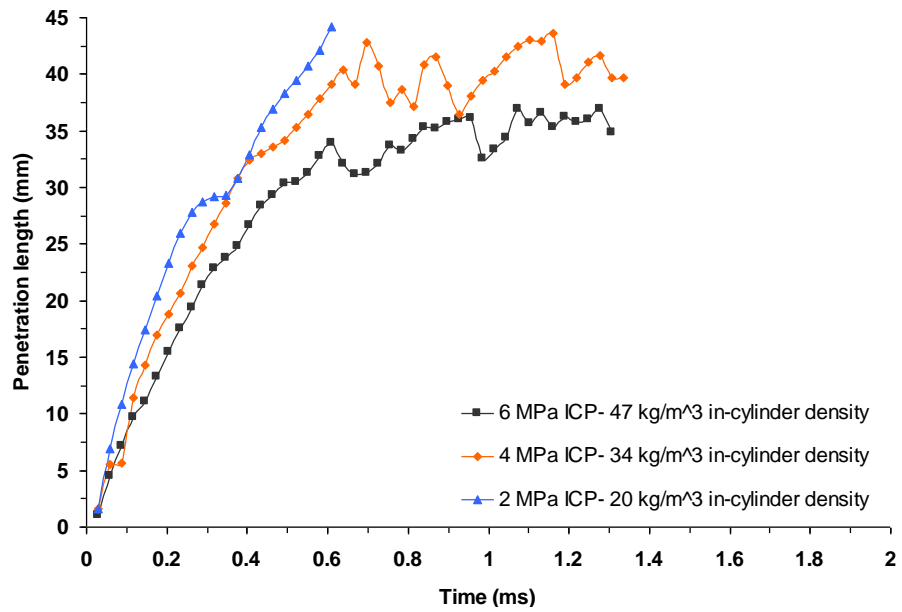
Fig AC-33. Same as Fig AC-30, with the exception of 160 MPa injection pressure

Delphi injector
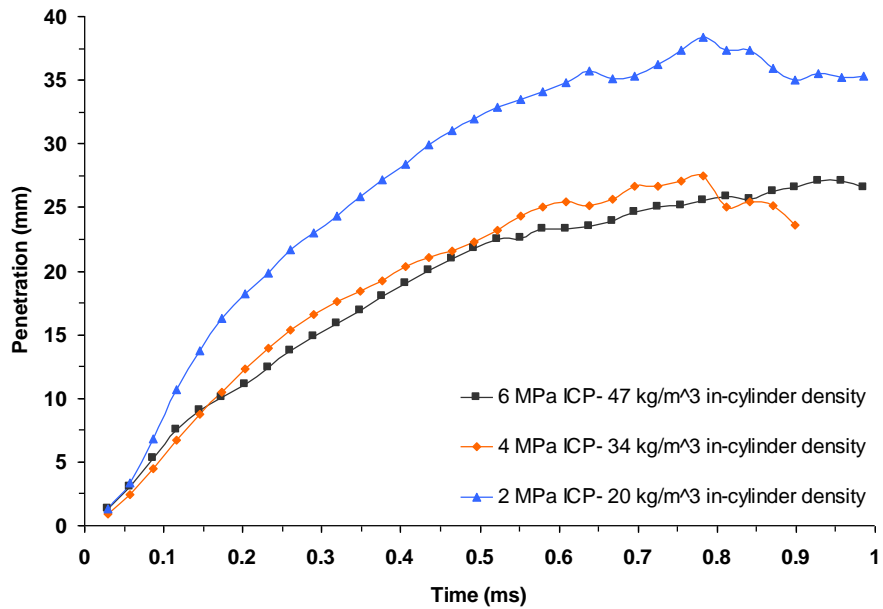
Fig AC-34. The effect of in-cylinder gas pressure on spray penetration for a 0.135 mm 7-hole single guided VCO nozzle; 60 MPa injection pressure; cold air intake
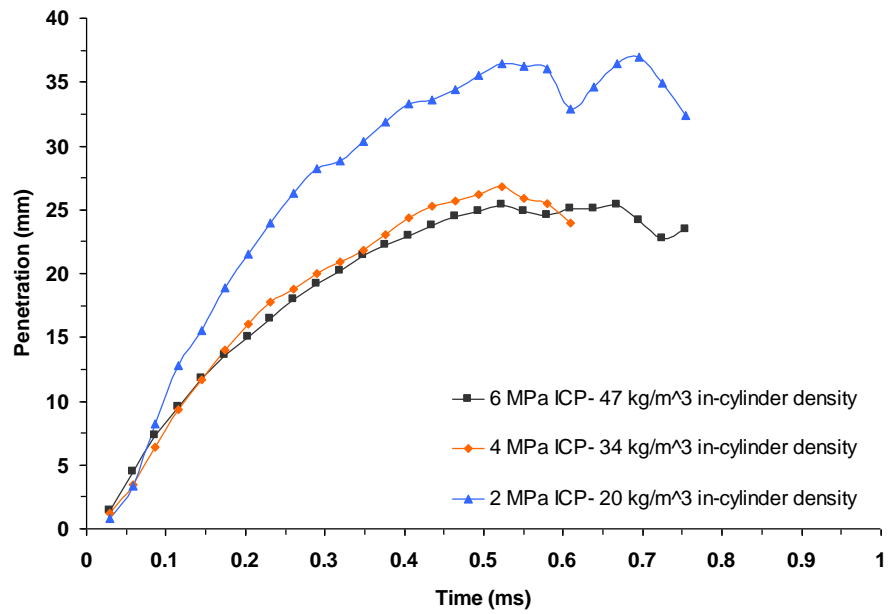
Fig AC-35. Same as the Fig AC-34, with the exception of 100 MPa injection pressure
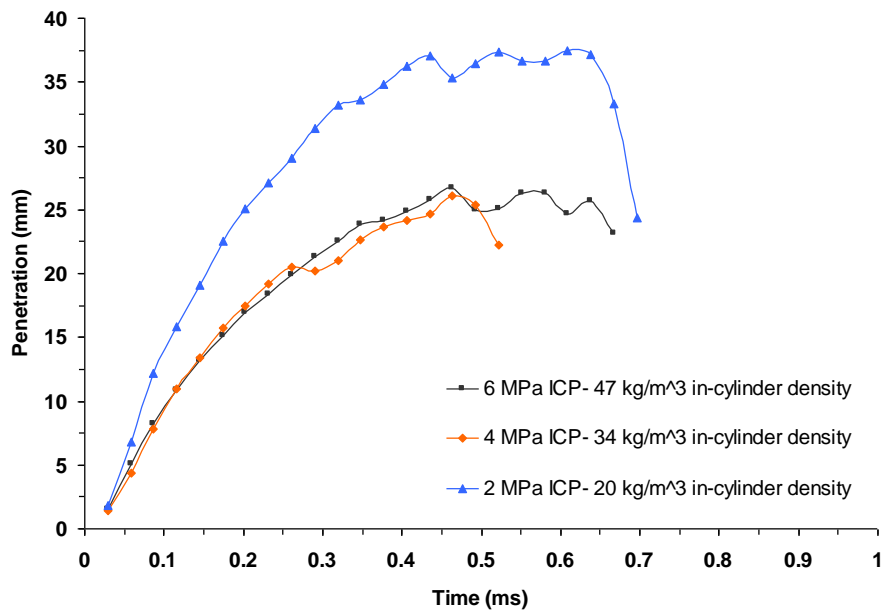
Fig AC-36. Same as Fig AC-34, with the exception of 140 MPa injection pressure
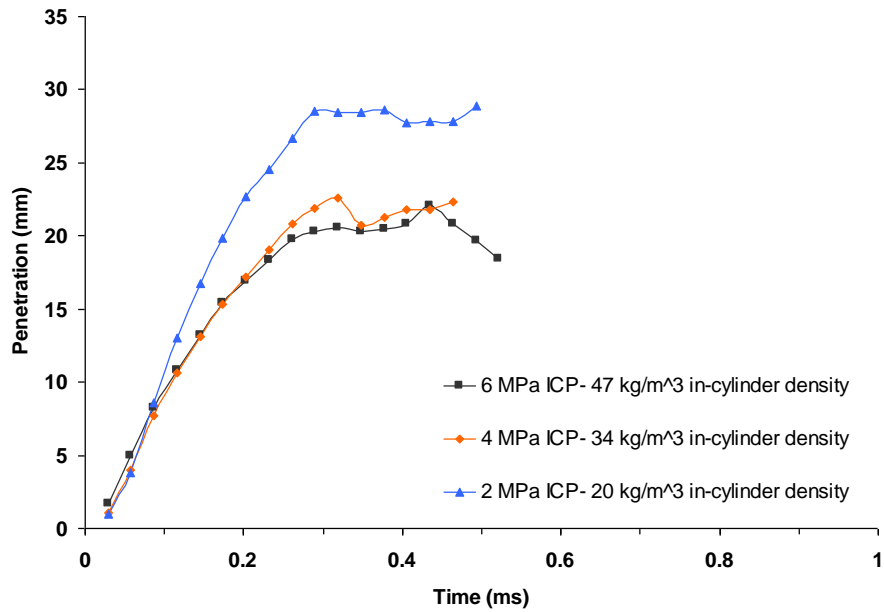
Fig AC-37. Same as Fig AC-34, with the exception of 160 MPa injection pressure

The Effect of In-Cylinder Gas Pressure at Hot Air Intake on Spray Tip Penetration
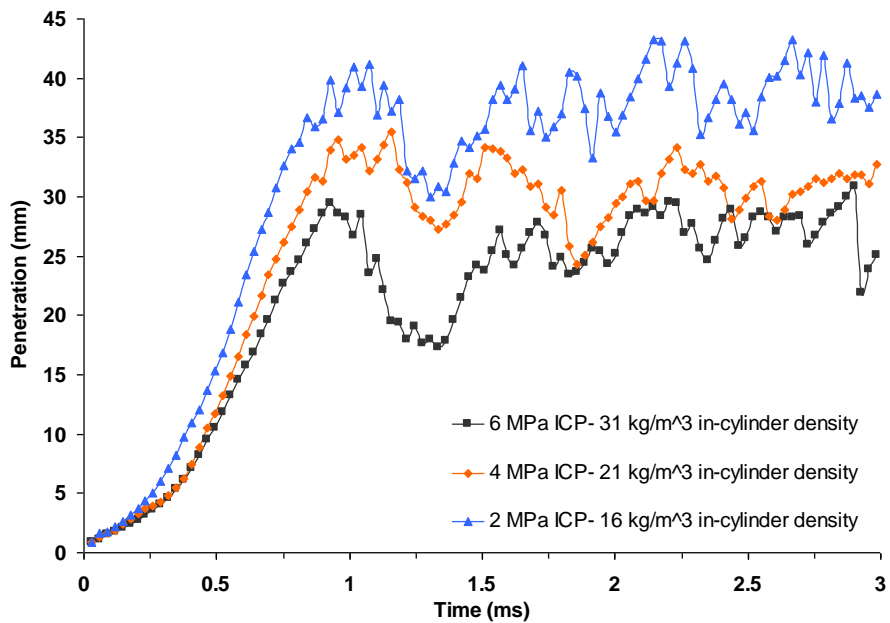
Single-Hole Nozzle

Fig AC-38. The effect in-cylinder gas pressure on spray penetration; 60 MPa injection pressure; 0.2 mm single-hole single guided VCO nozzle; hot air intake

C 22
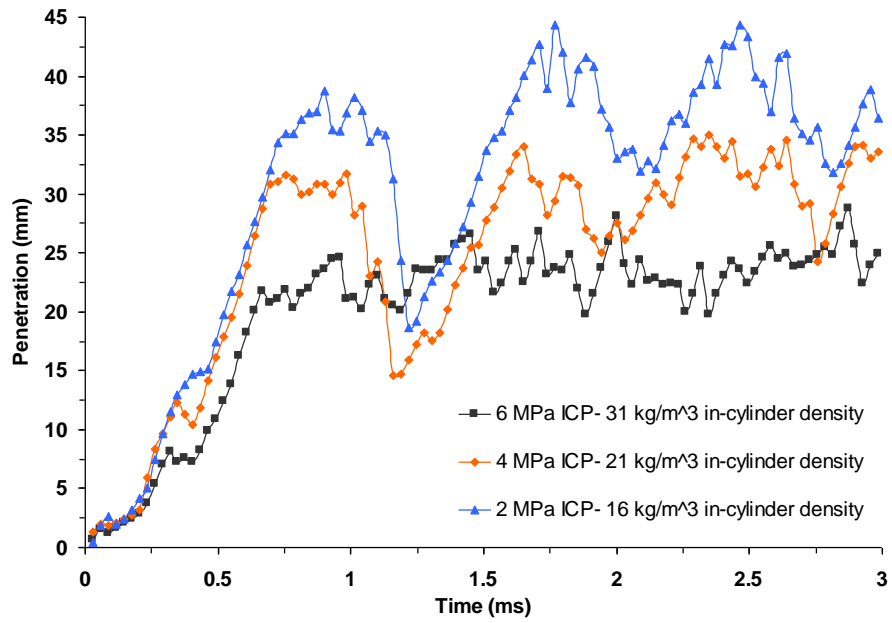
Fig AC-39. Same as Fig AC-38, with the exception of 100 MPa injection pressure
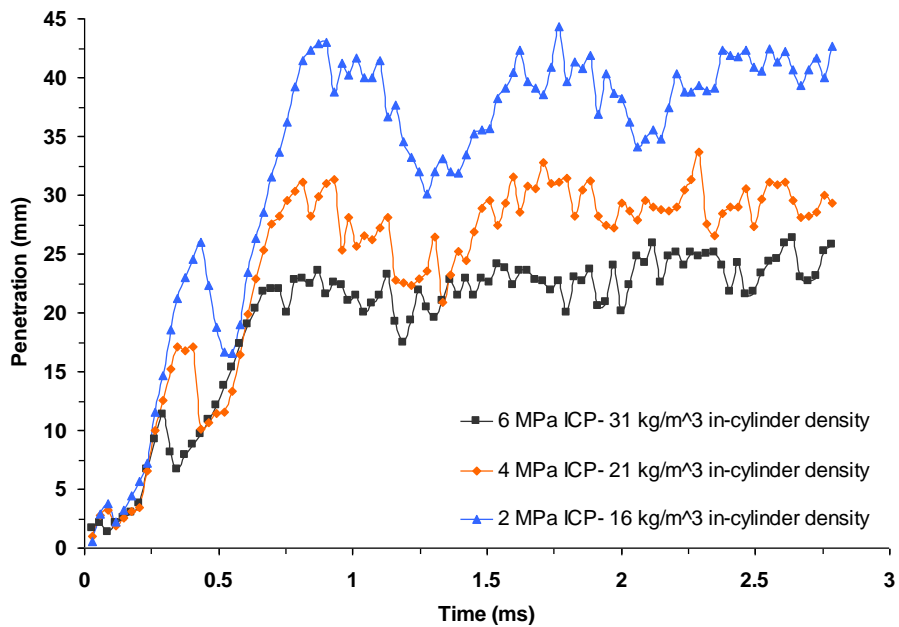
Fig AC-40. Same as Fig AC-38, with the exception of 140 MPa injection pressure
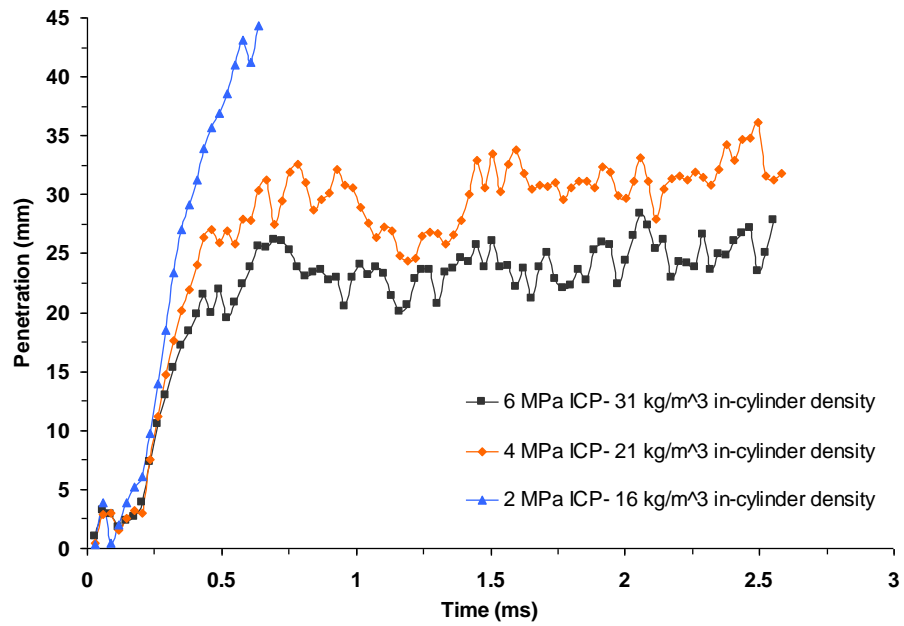
Fig AC-41. Same as Fig AC-38, with the exception of 160 MPa injection pressure
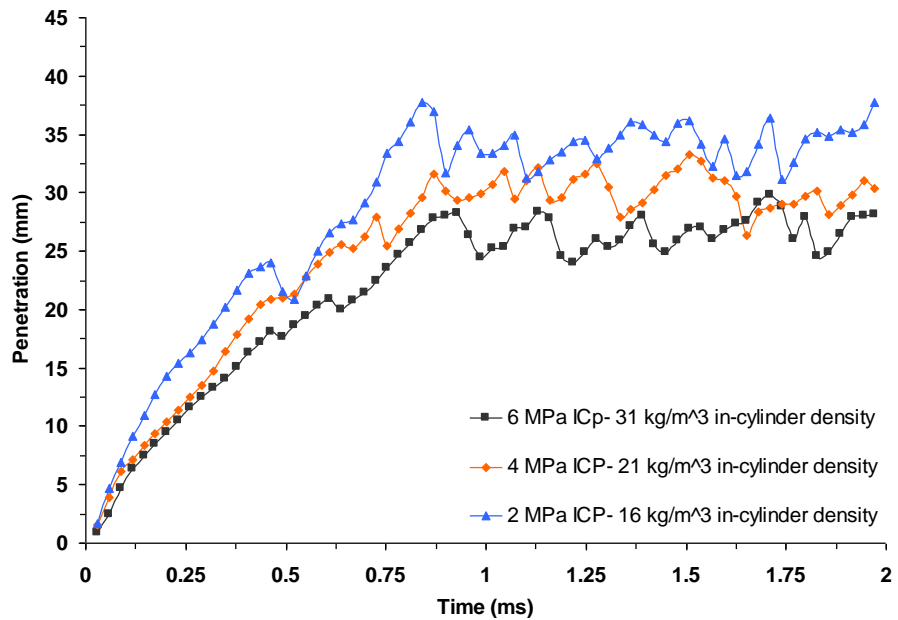
3-Hole Nozzle

Fig AC-42. The effect in-cylinder gas pressure on spray penetration; 60 MPa injection pressure; 0.2 mm 3-hole single guided VCO nozzle; hot air intake
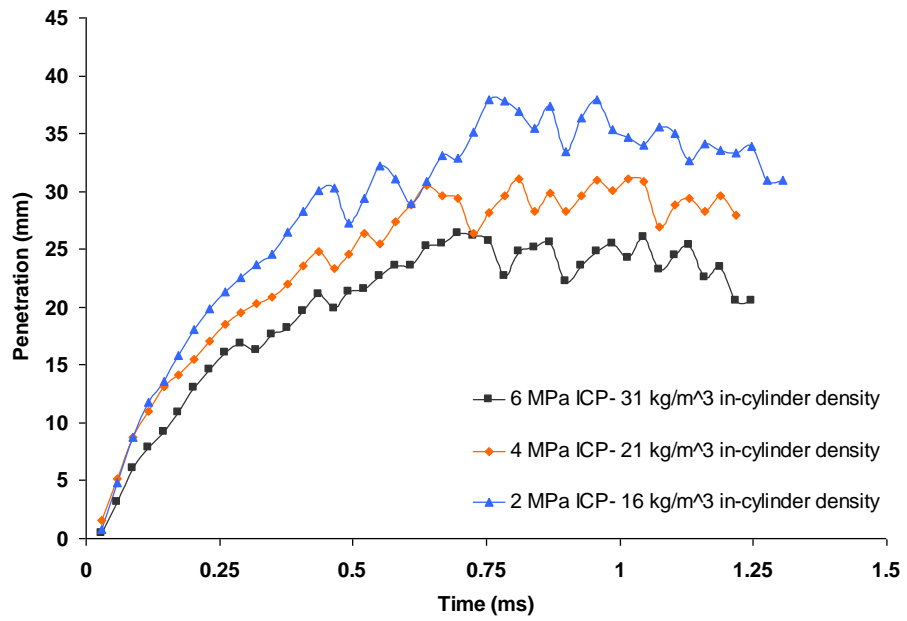
Fig AC-43. Same as Fig AC-42, with the exception of 100 MPa injection pressure
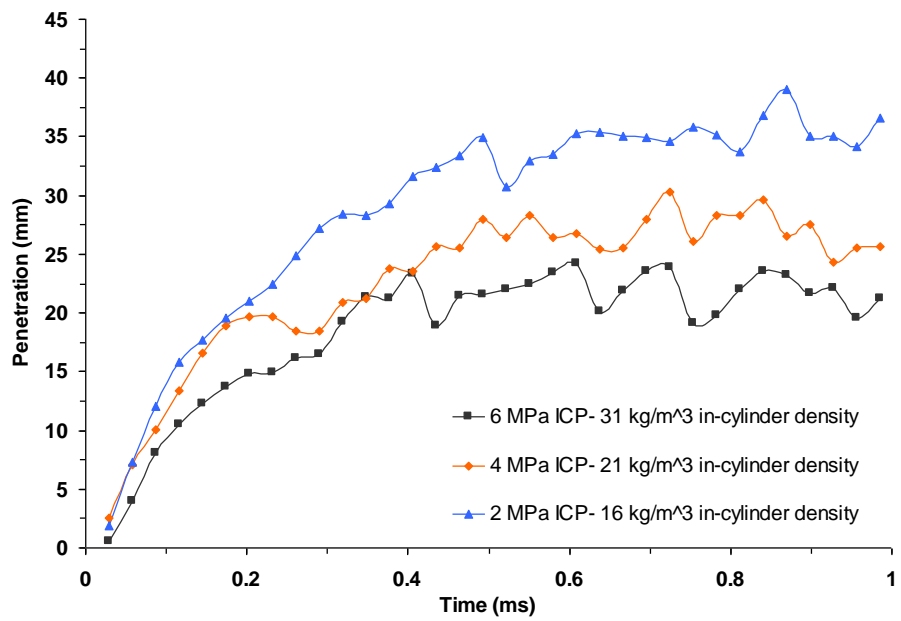
Fig AC-44. Same as Fig AC-42, with the exception of 140 MPa injection pressure

C 25
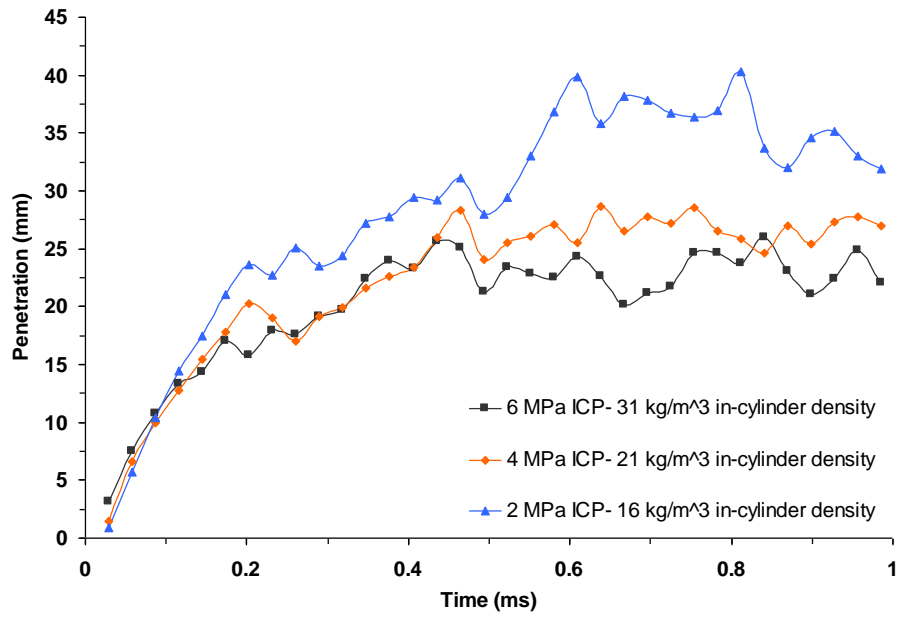
Fig AC-45. Same as Fig AC-42, with the exception of 160 MPa injection pressure
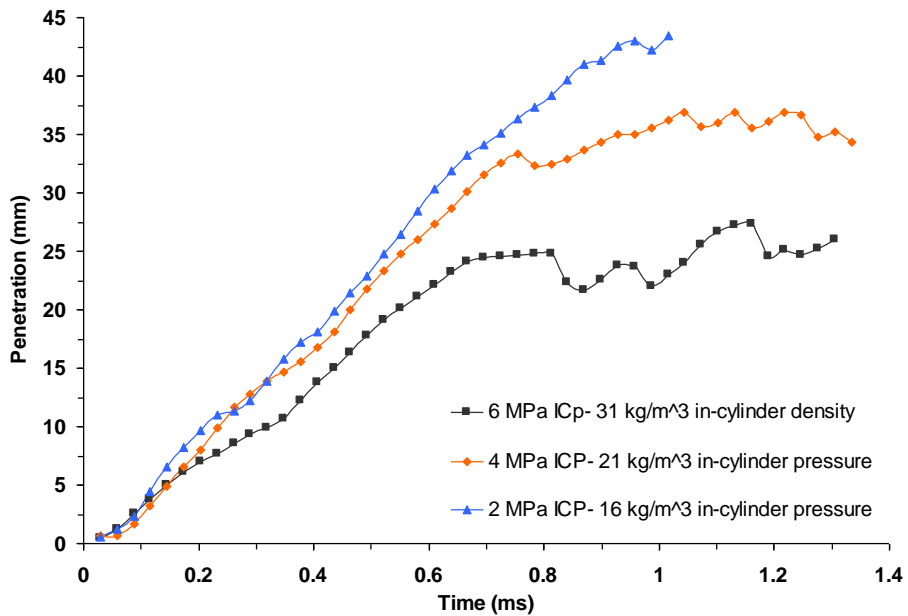
5-Hole Nozzle

Fig AC-46. The effect in-cylinder gas pressure on spray penetration; 60 MPa injection pressure; 0.2 mm 5-hole single guided VCO nozzle; hot air intake
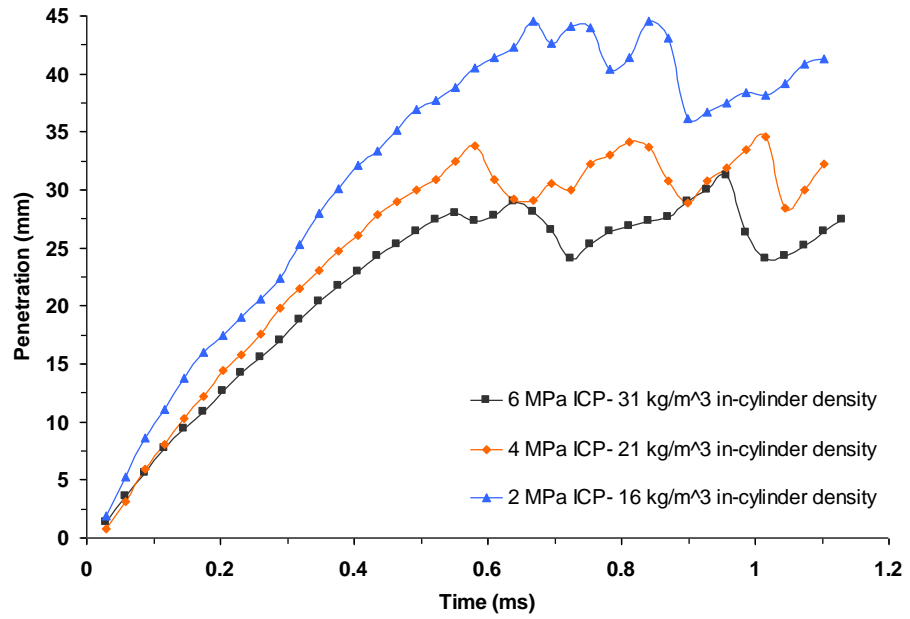
Fig AC-47. Same as Fig AC-46, with the exception of 100 MPa injection pressure
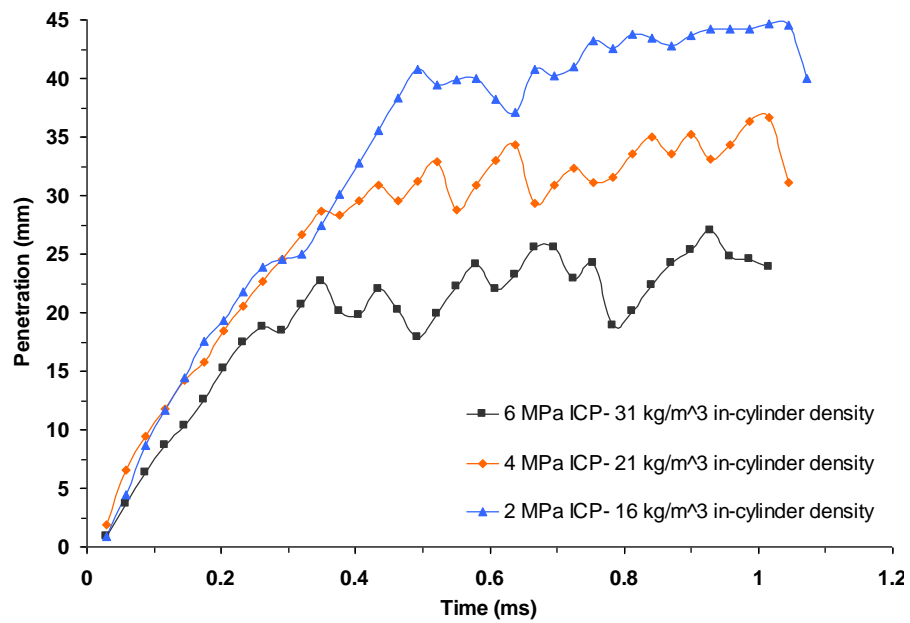
Fig AC-48. Same as Fig AC-46, with the exception of 140 MPa injection pressure
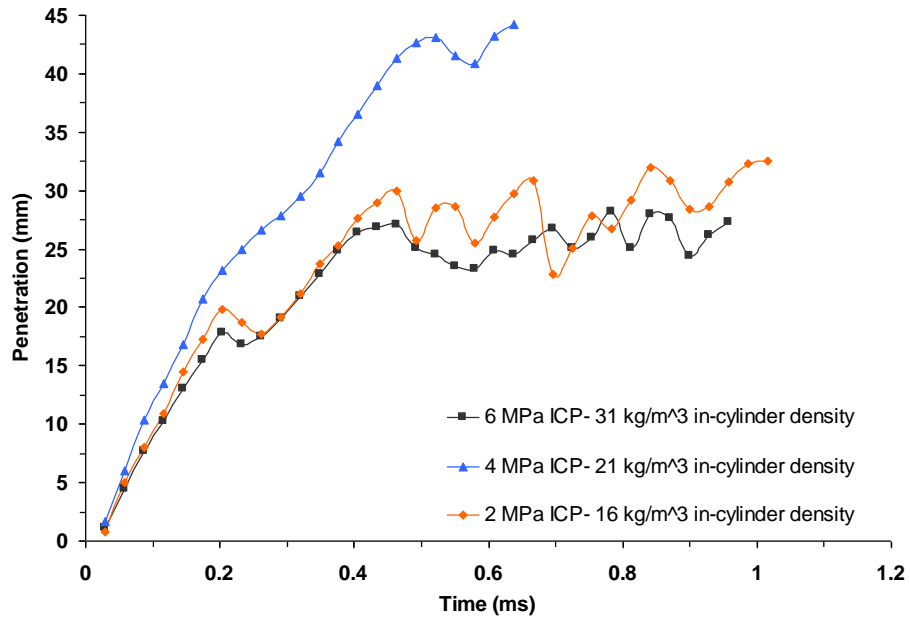
Fig AC-49. Same as Fig AC-46, with the exception of 160 MPa injection pressure

Delphi Injector

Fig AC-50. The effect of in-cylinder gas pressure on spray penetration for a 0.135 mm 7-hole single guided VCO nozzle; 60 MPa injection pressure; hot air intake

C 28
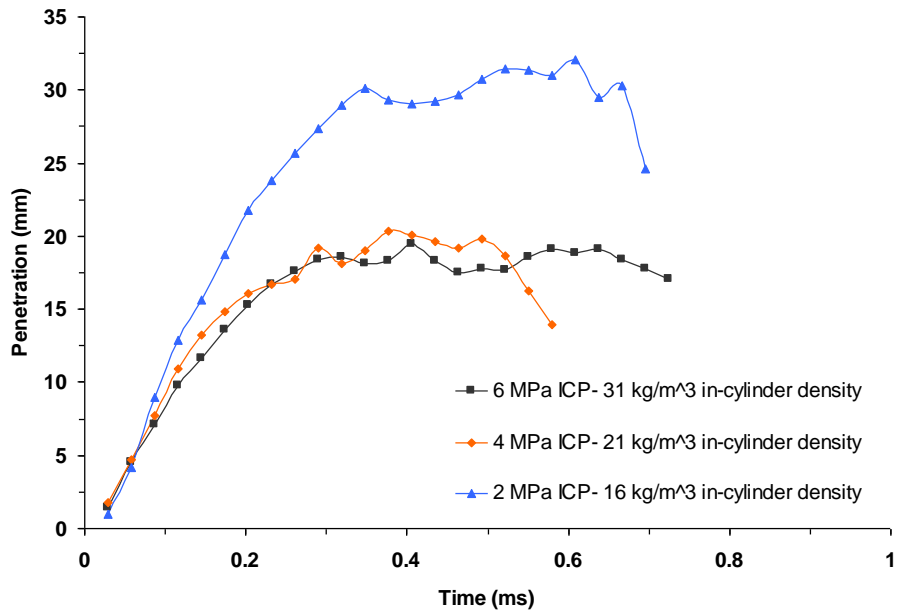
Fig AC-51. Same as Fig AC-50, with the exception of 100 MPa injection pressure
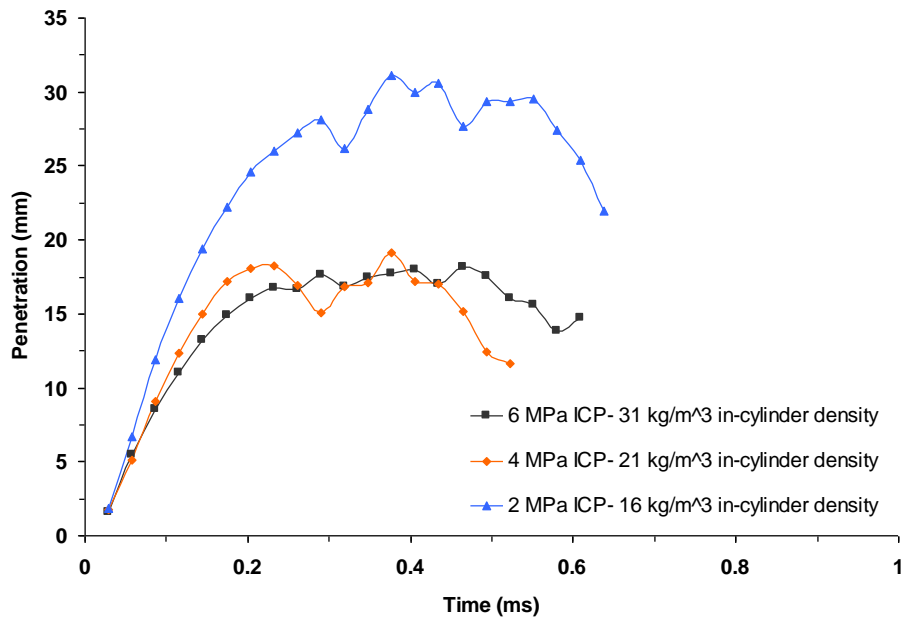
Fig AC-52. Same as Fig AC-50, with the exception of 140 MPa injection pressure
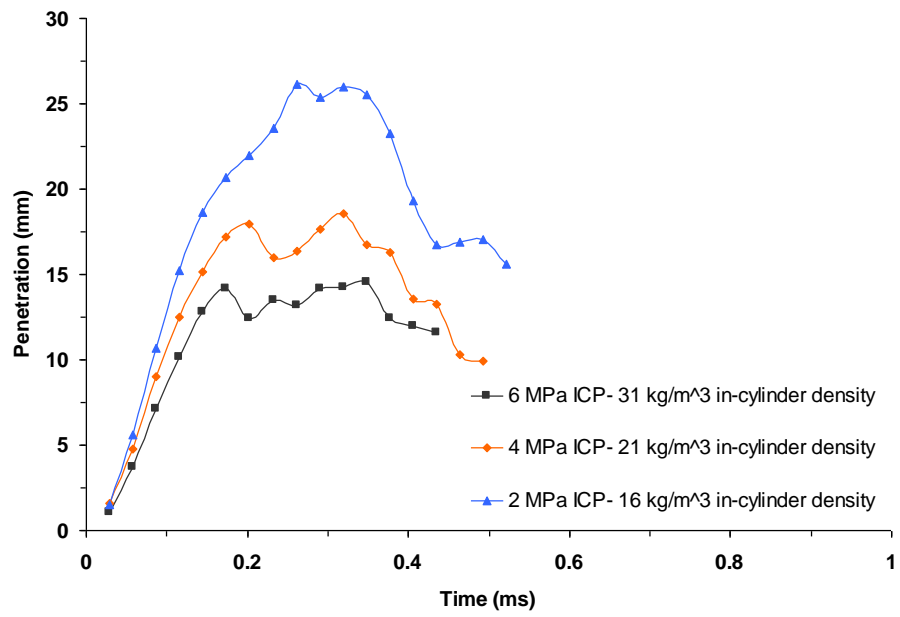
Fig AC-53. Same as Fig AC-50, with the exception of 160 MPa injection pressure

APPENDIX D: MULTIPLE INJECTION DIESEL SPRAY CHARACTERISATION

Comparison of the *Mie* Scattering Images for Hot and Cold Air Intake

The case shown below is for 140 *MPa* injection pressure, 6 *MPa* in-cylinder pressure, and 0.425 *ms* dwell period.

Cold,0.4075ms *Hot,0.4075ms* *Cold,0.4375ms* *Hot,0.4375ms* *Cold,0.4675ms* *Hot,0.4675ms* *Cold,0.4975ms* *Hot,0.4975ms*
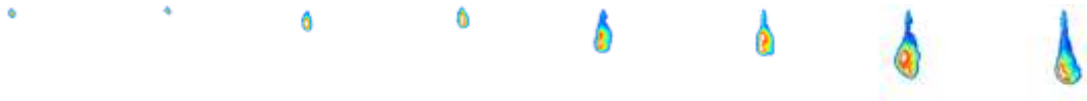
Cold,0.5275ms *Hot,0.5275ms* *Cold,0.5575ms* *Hot,0.5575ms* *Cold,0.5875ms* *Hot,0.5875ms* *Cold,0.6175ms* *Hot,0.6175ms*
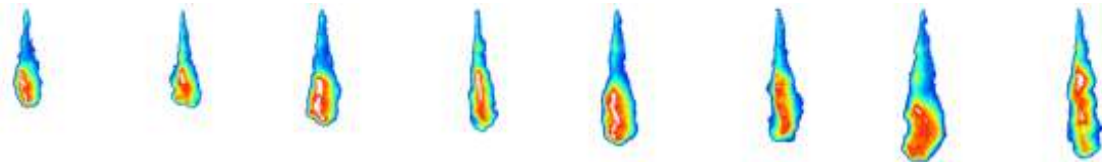
Cold,0.6475ms *Hot,0.6475ms* *Cold,0.6775ms* *Hot,0.6775ms* *Cold,0.7075ms* *Hot,0.7075ms* *Cold,0.7375ms* *Hot,0.7375ms*
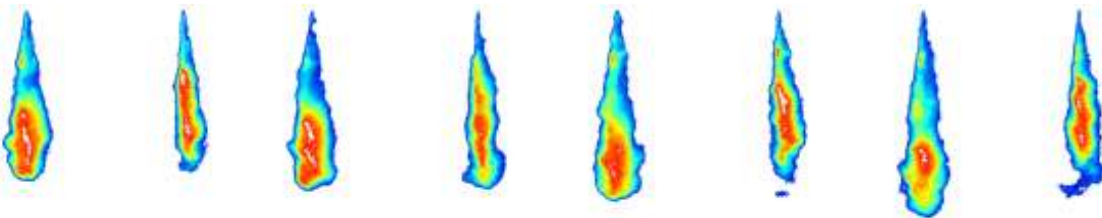
Cold,0.7675ms *Hot,0.7675ms* *Cold,0.7975ms* *Hot,0.7975ms* *Cold,0.8275ms* *Hot,0.8275ms* *Cold,0.8575ms* *Hot,0.8575ms*
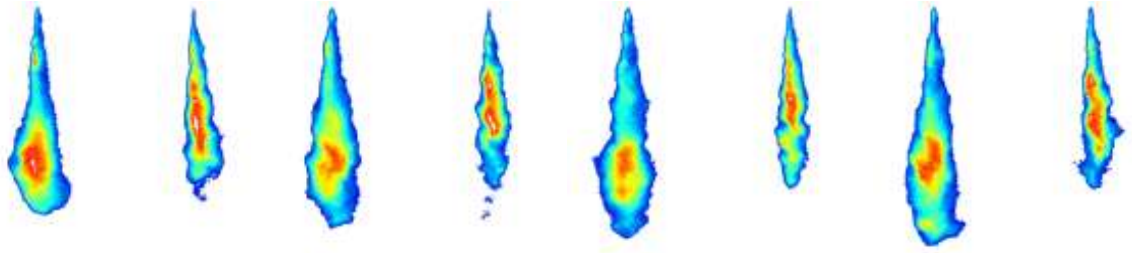
Cold,0.8875ms *Hot,0.8875ms* *Cold,0.9175ms* *Hot,0.9175ms* *Cold,0.9475ms* *Cold,0.9475ms* *Cold,0.9775ms* *Hot,0.9775ms*
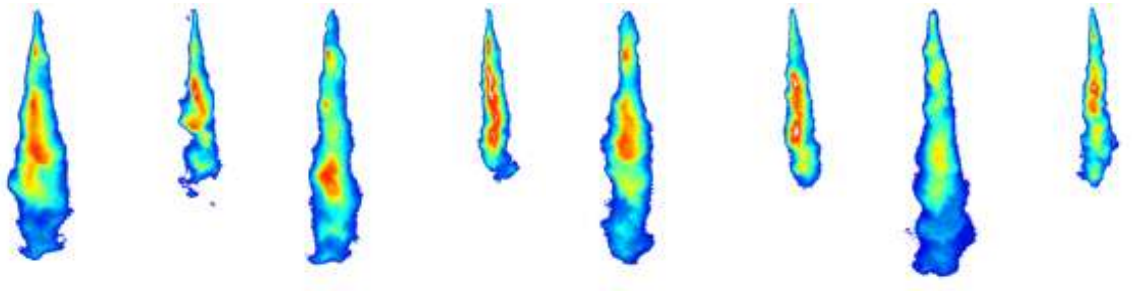
Cold,1.0075ms *Hot,1.0075ms* *Cold,1.0375ms* *Hot,1.0375ms* *Cold,1.0675ms* *Hot,1.0675ms* *Cold,1.0975ms* *Hot,1.0975ms*
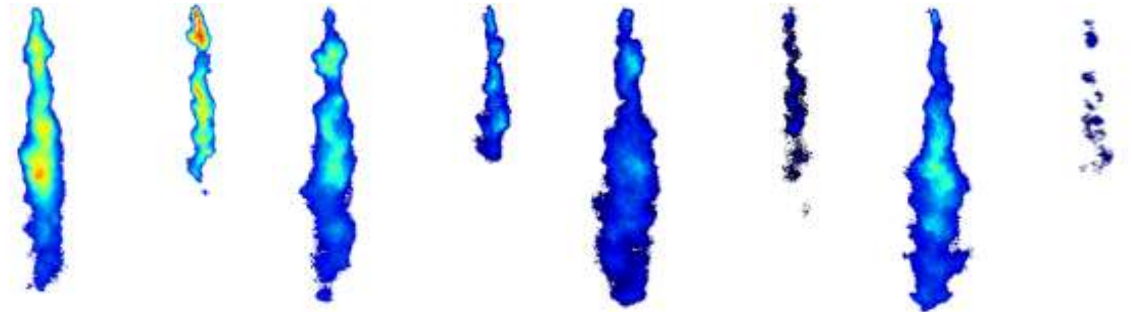
Cold,1.1275ms *Hot,1.1275ms* *Cold,1.1575ms* *Hot,1.1575ms* *Cold,1.1875ms* *Hot,1.1875 ms* *Cold,1.2175ms* *Hot,1.2175ms*

D 32
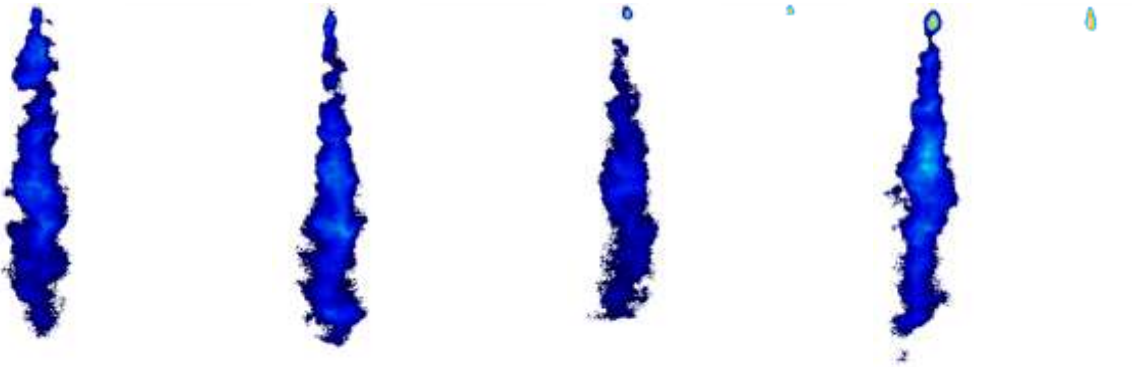
Cold,1.2475ms Hot,1.2475ms Cold,1.2775ms Hot,1.2775ms Cold,1.3075ms Hot,1.3075ms Cold,1.3375ms Hot,1.3375ms
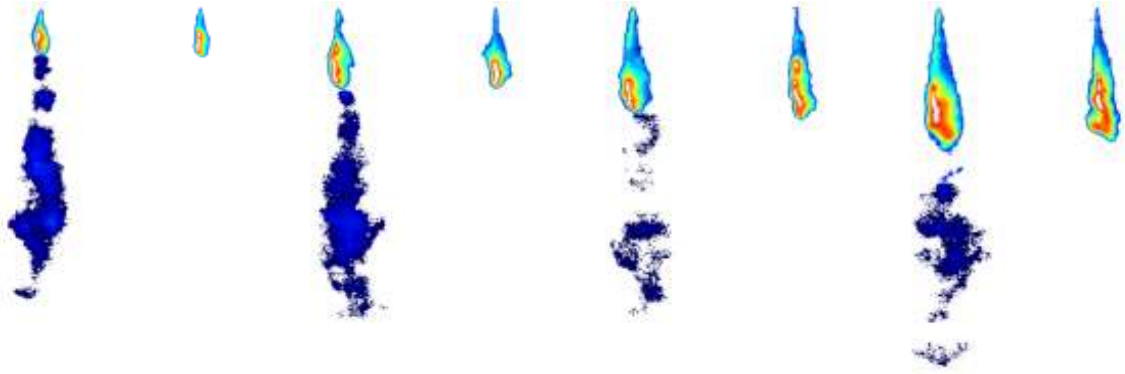
Cold,1.3675ms Hot,1.3675ms Cold,1.3975ms Hot,1.3975ms Cold,1.4275ms Hot,1.4275ms Cold,1.4575ms Hot,1.4575ms
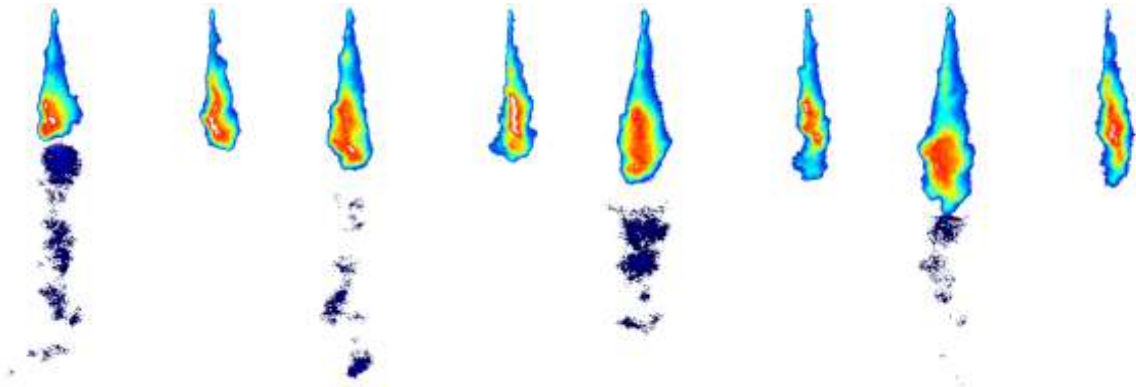
Cold,1.45ms Hot,1.4975ms Cold,1.48ms Hot,1.5275ms Cold,1.51ms Hot,1.5575ms Cold,1.54ms Hot,1.5875ms
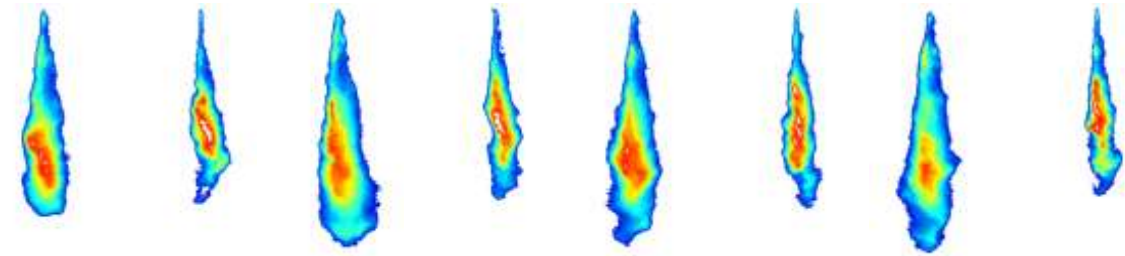
Cold,1.4875ms Hot,1.4875ms Cold,1.5175ms Hot,1.5175ms Cold,1.5475ms Hot,1.5475ms Cold,1.5775ms Hot,1.5775ms
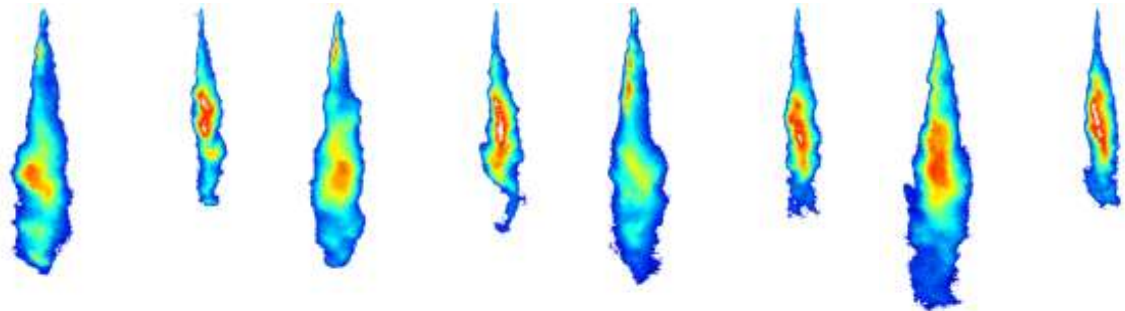
Cold,1.6075ms *Hot,1.6075ms* *Cold,1.6375ms* *Hot,1.6375ms* *Cold,1.6675ms* *Hot,1.6675ms* *Cold,1.6975ms* *Hot,1.6975ms*
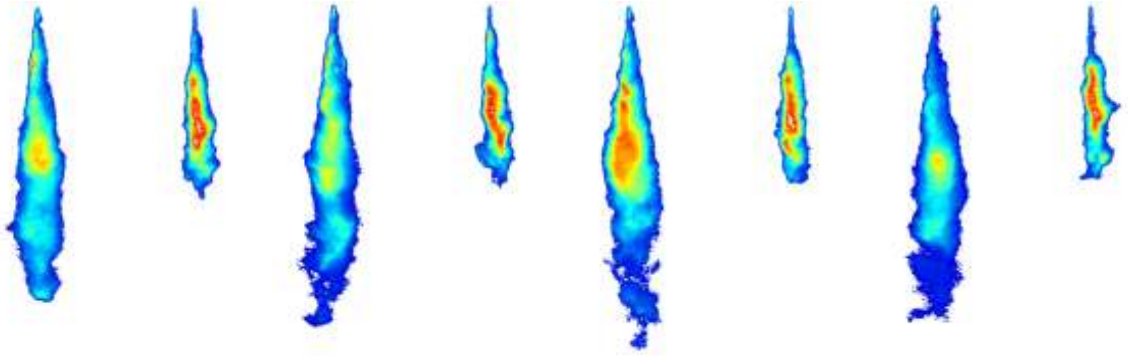
Cold,1.7275ms *Hot,1.7275ms* *LIF,1.7575ms* *Hot,1.7575ms* *Cold,1.7875ms* *Hot,1.7875ms* *Cold,1.8175ms* *Hot,1.8175ms*
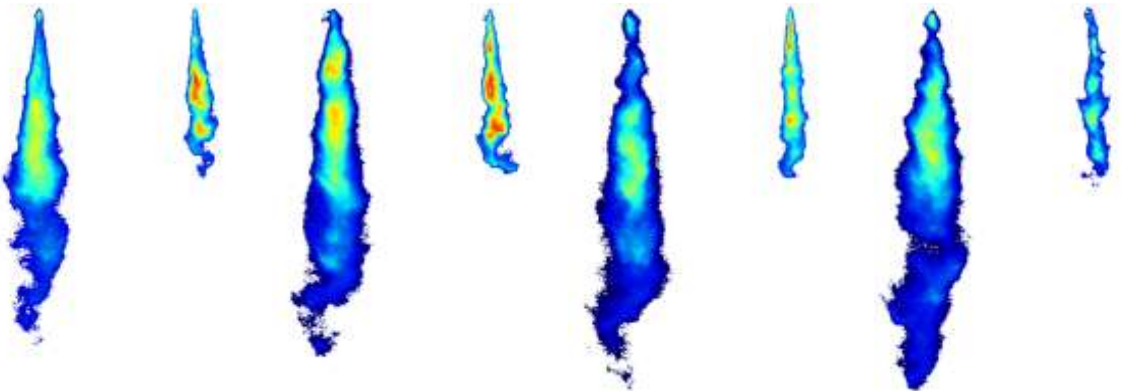
Cold,1.8475ms *Hot,1.8475ms* *Cold,1.8775ms* *Hot,1.8775ms* *Cold,1.9075ms* *Hot,1.9075ms* *Cold,1.9375ms* *Hot,1.9375ms*
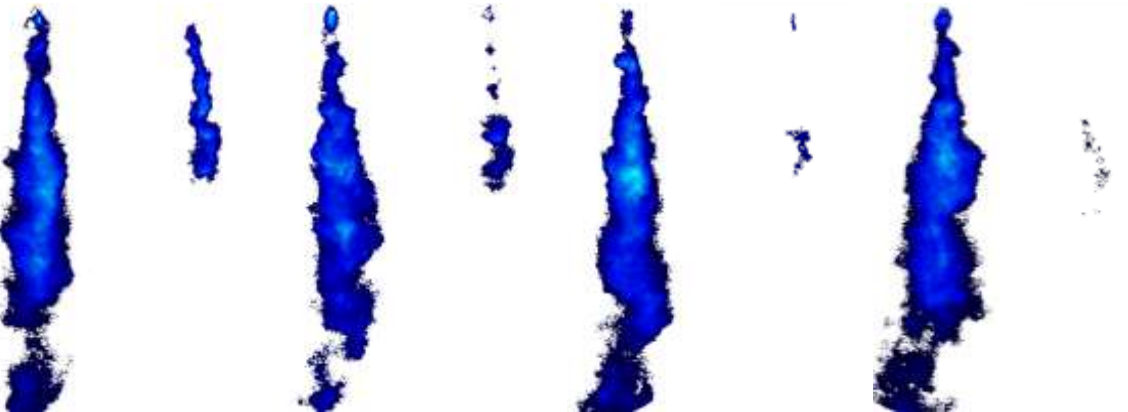
Fig AD-1. The Mie scattering images at 140 MPa injection pressure; 6 MPa in-cylinder pressure; 47 kg/m^3 in-cylinder density (cold air intake, corresponding to 448 K at TDC) ; 31 kg/m^3 in-cylinder density (hot air intake, corresponding to 667K at TDC); 0.425 ms dwell period

Comparison of the Spray Penetration Data Obtained via *HSV* and *Mie* Scattering Technique

Cold Air Intake
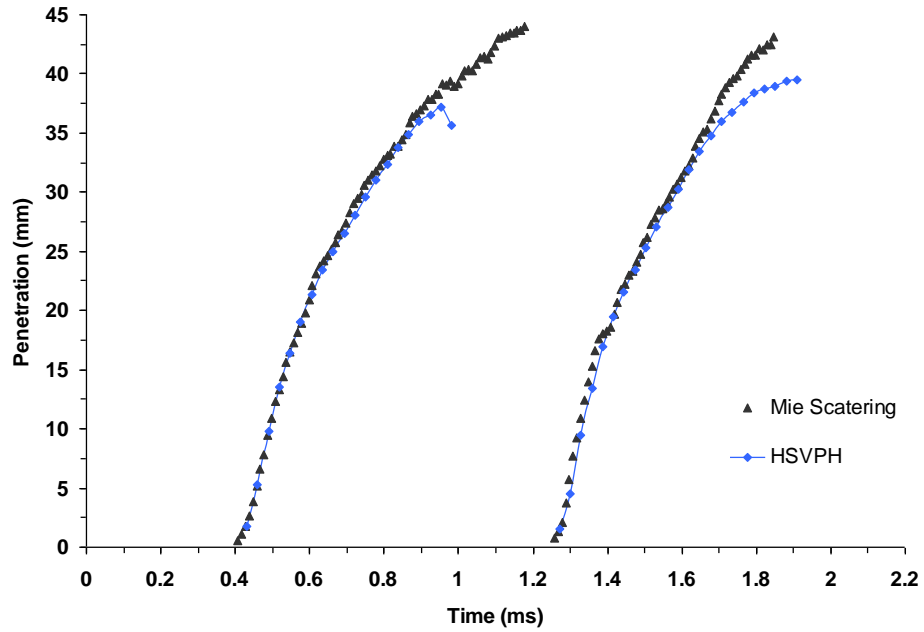
Fig AD-2. Comparison of spray penetration length for split injection strategy obtained via HSV and Mie scattering technique; 100 MPa injection pressure; 2 MPa in-cylinder pressure: 20 kg/m³ in-cylinder density; cold air intake (corresponding to 350 K at TDC); 0.425 ms dwell period
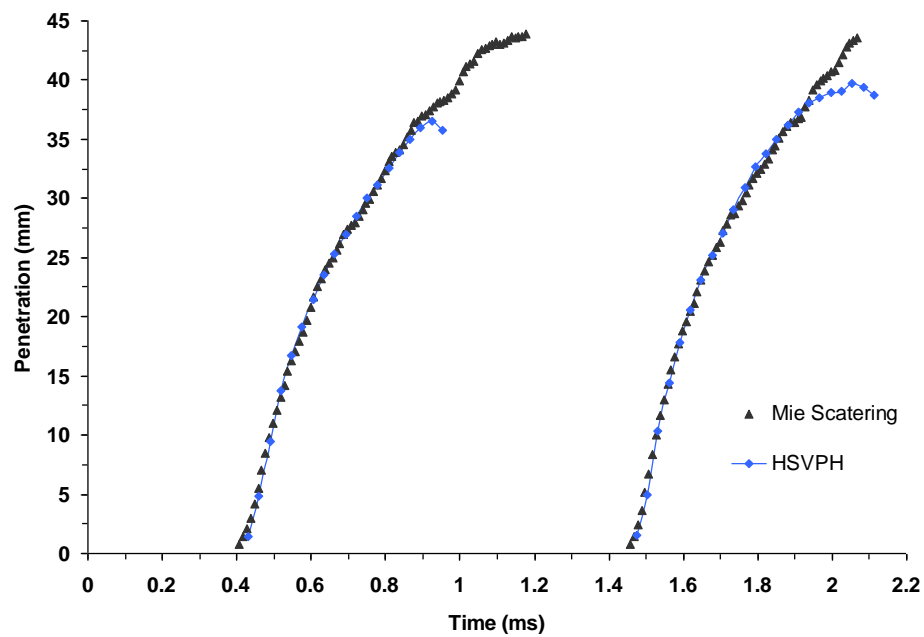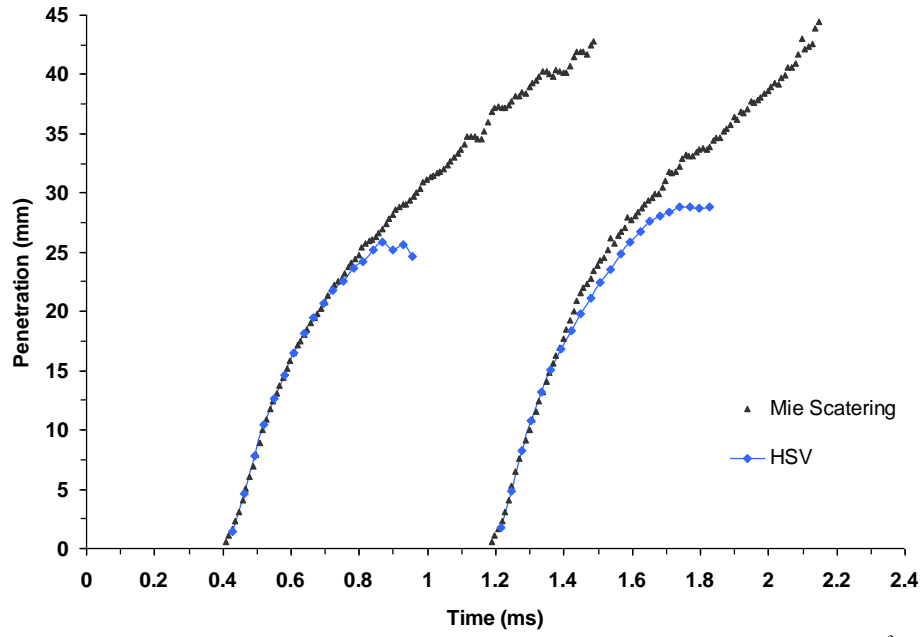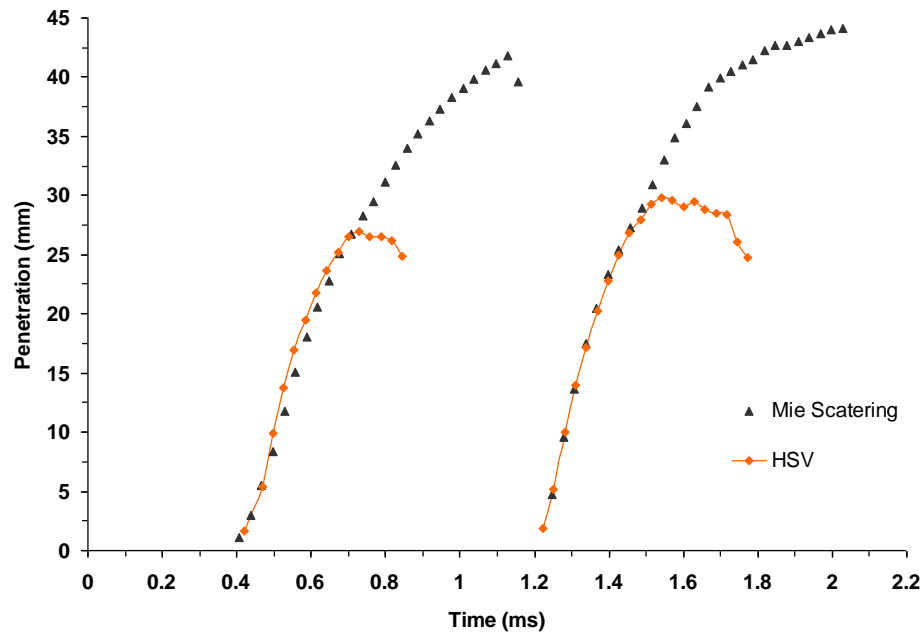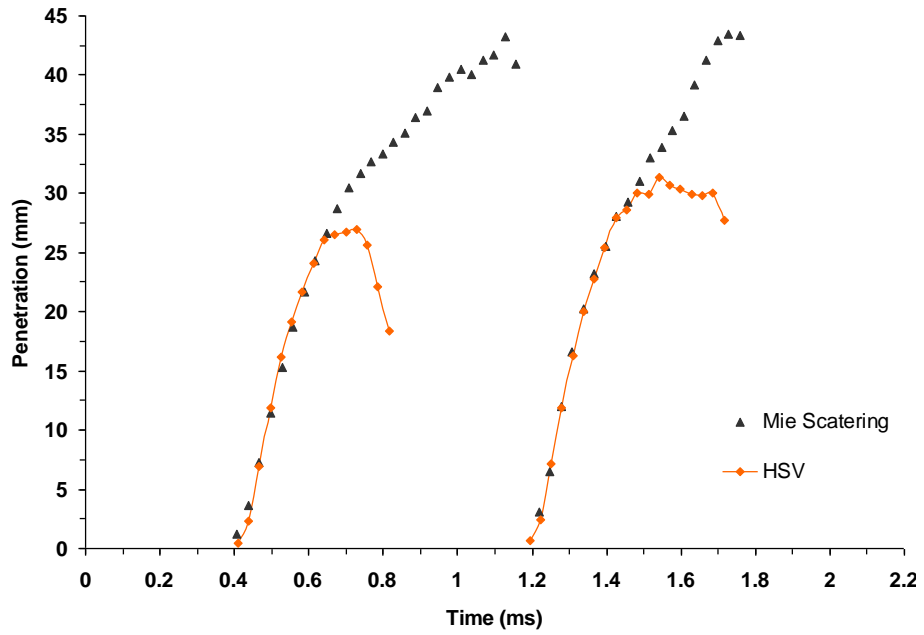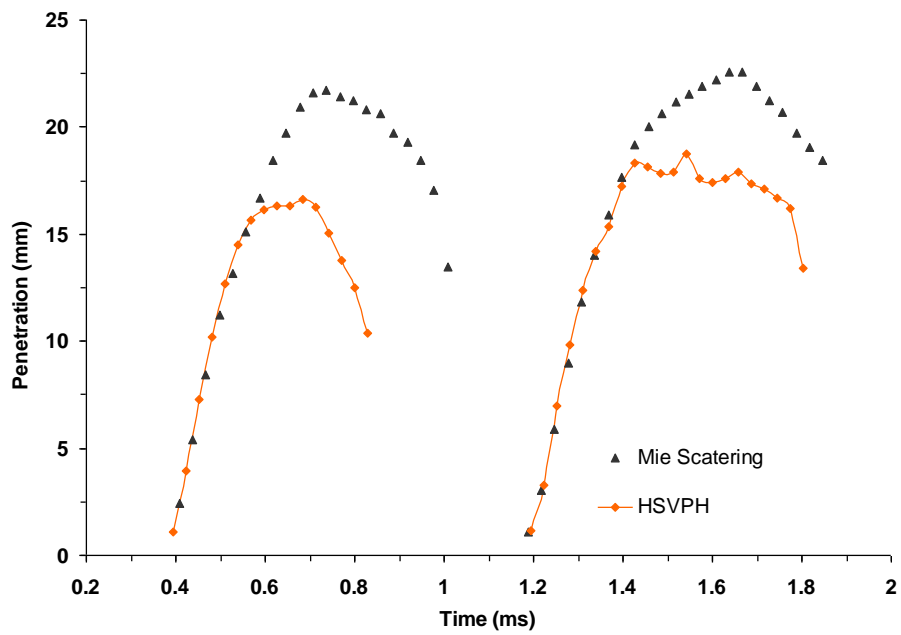

Fig AD-3. Same as Fig AD-2, with the exception of 0.625 ms dwell period
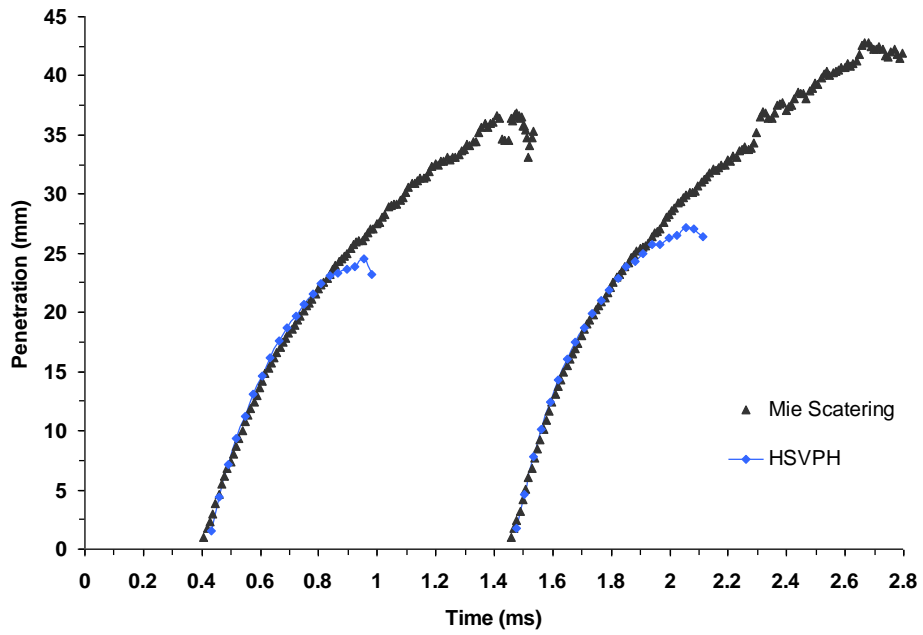
Fig AD-4. Comparison of spray penetration length for split injection strategy obtained via HSV and Mie scattering technique; 100 MPa injection pressure; 6 MPa in-cylinder pressure: 47 kg/m³ in-cylinder density; cold air intake (corresponding to 448 K at TDC); 0.625 ms dwell period
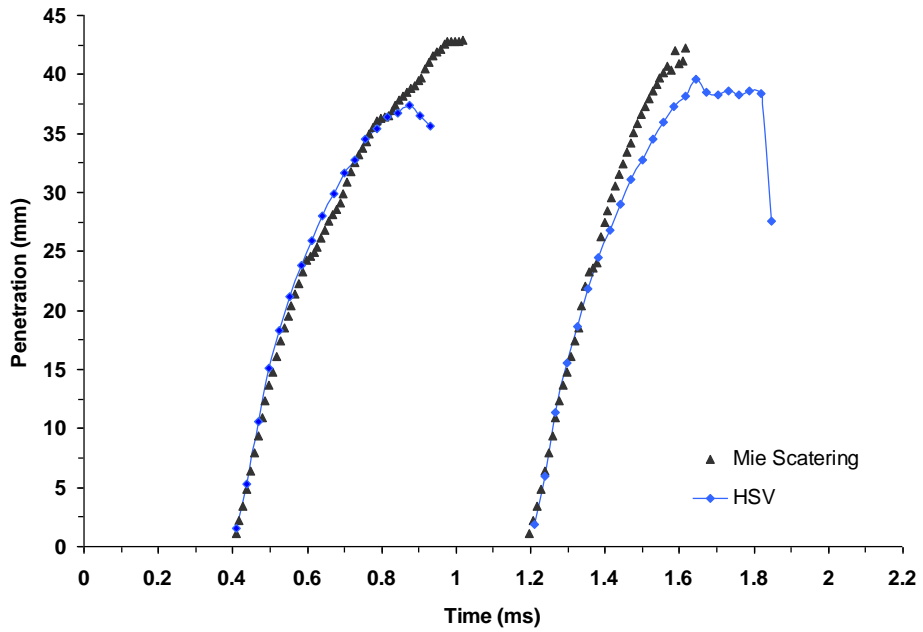
Fig AD-5. Comparison of spray penetration length for split injection strategy obtained via HSV and Mie scattering technique; 140 MPa injection pressure; 2 MPa in-cylinder pressure: 20 kg/m³ in-cylinder density; cold air intake (corresponding to 350 K at TDC); 0.425 ms dwell period

Fig AD-6. Same as Fig AD-5, with the exception of 6 MPa in-cylinder pressure; 47 kg/m^3 in-cylinder density; cold air intake (corresponding to 447 K at TDC)

Hot Air Intake

Fig AD-7 Comparison of spray penetration length for split injection strategy obtained via HSV and Mie scattering technique; 100 MPa injection pressure; 2 MPa in-cylinder pressure: 16 kg/m^3 in-cylinder density; hot air intake (corresponding to 448 K at TDC); 0.425 ms dwell period

Fig AD-8. Same as Fig AD-7, with the exception of 140 MPa injection pressure

Fig AD-9. Comparison of spray penetration length for split injection strategy obtained via HSV and Mie scattering technique; 140 MPa injection pressure; 6 MPa in-cylinder pressure: 31 kg/m³ in-cylinder density; hot air intake (corresponding to 667 K at TDC); 0.425 ms dwell period

APPENDIX E: EXPERIMENTAL PENETRATION LENGTH AGAINST PENETRATION CORRELATION

Comparison of the Experimental Penetration Length and the Penetration Correlation (C_{Lp} =2.37)
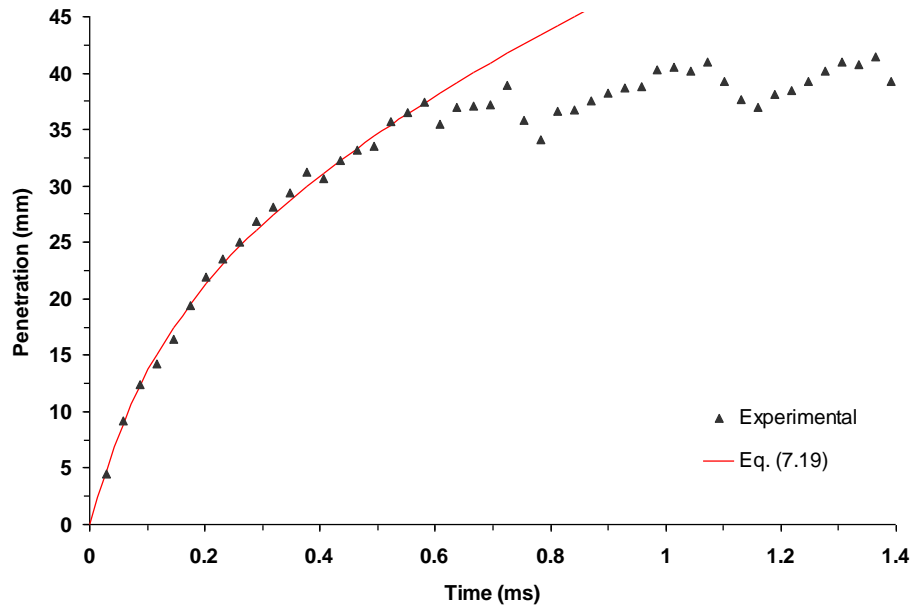
Fig AE-1. Comparison between Eq. (7.19) and experimental data; the experimental results are for cold air intake (corresponding to 410 K at TDC); 160 MPa injection pressure; 34 kg/m^3 in-cylinder density; 4 MPa in-cylinder pressure
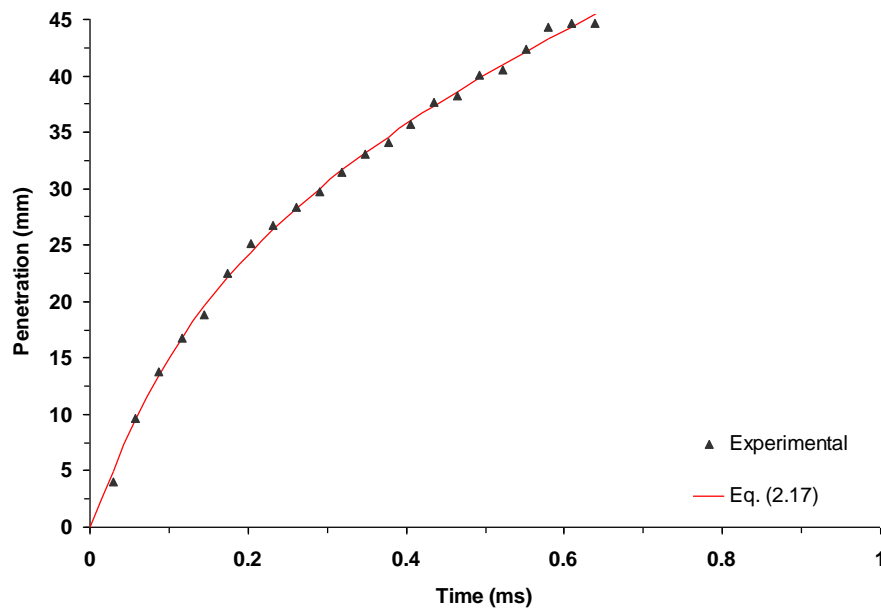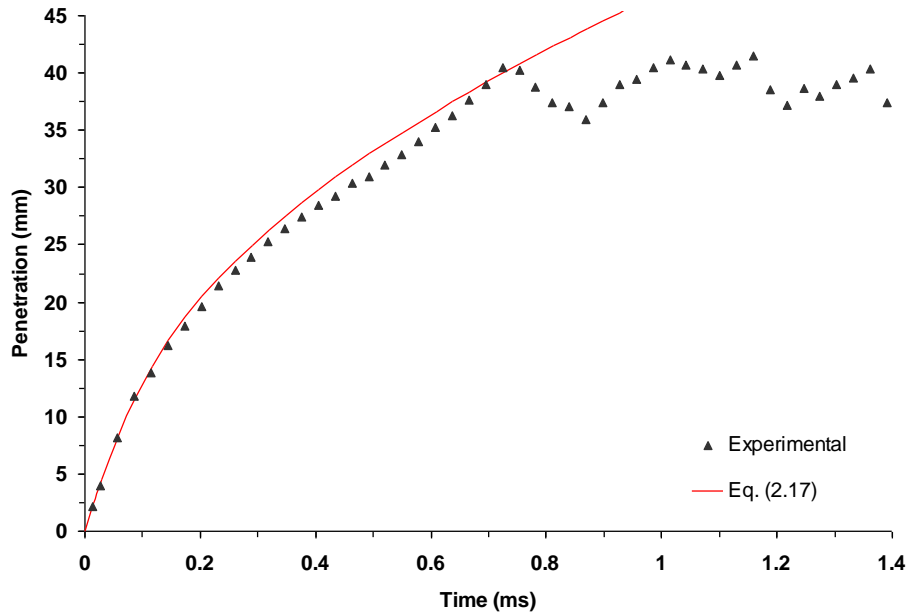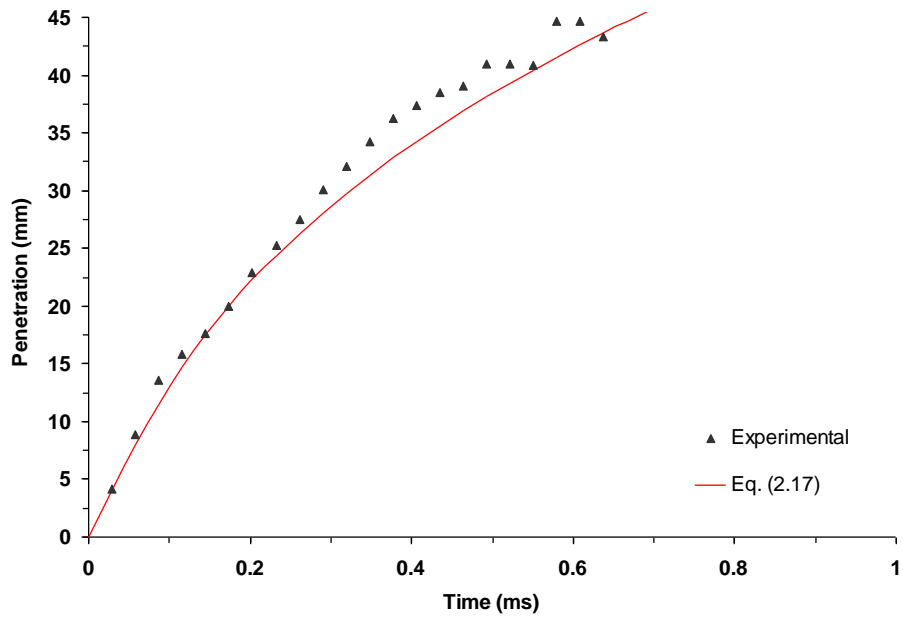

Fig AE-2. Same as Fig AE-1; the experimental results are for cold air intake (corresponding to 350 K at TDC); 160 MPa injection pressure; 20 kg/m^3 in-cylinder density; 2 MPa in-cylinder pressure
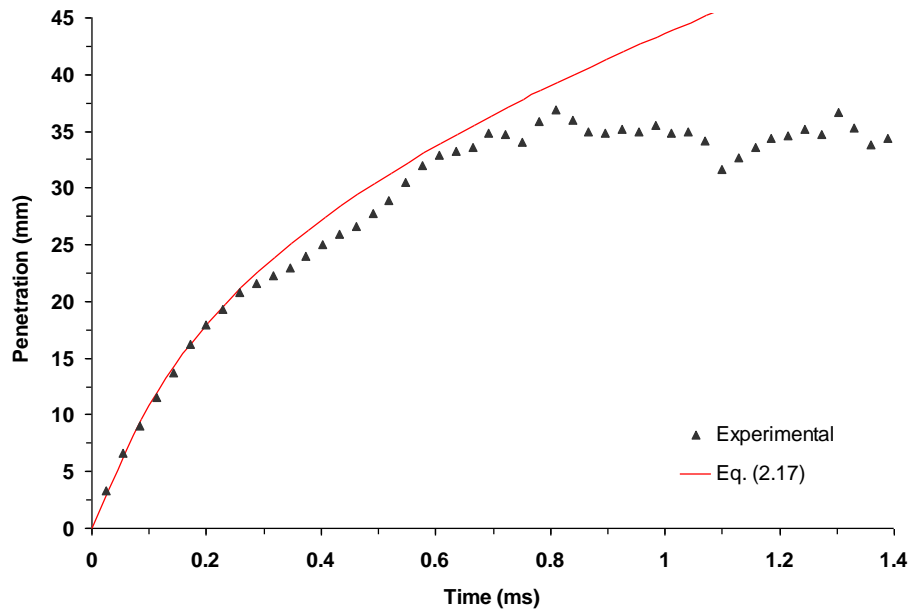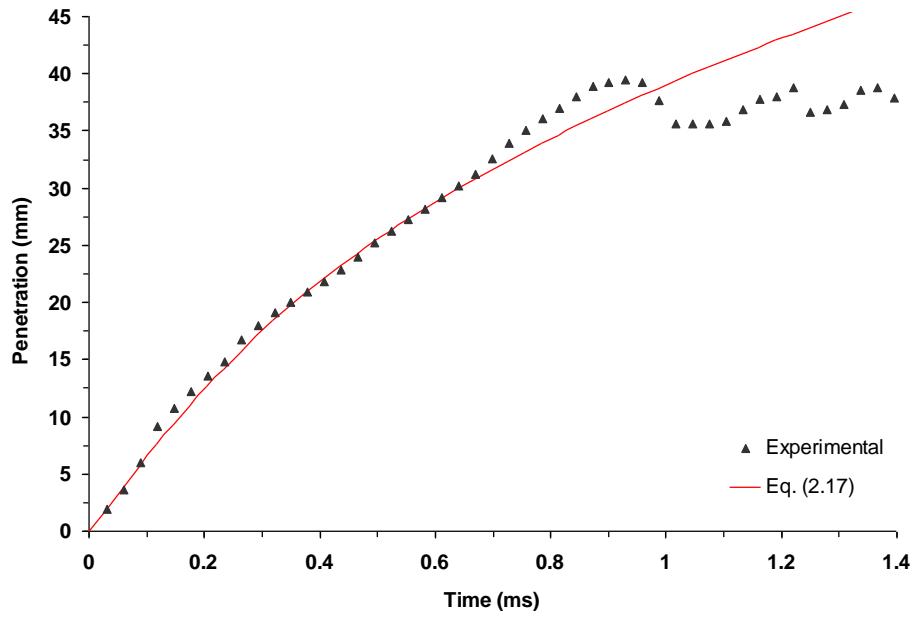
Fig AE-3. Same as Fig AE-1; the experimental results are for cold air intake (corresponding to 448 K at TDC); 140 MPa injection pressure; 47 kg/m^3 in-cylinder density; 6 MPa in-cylinder pressure
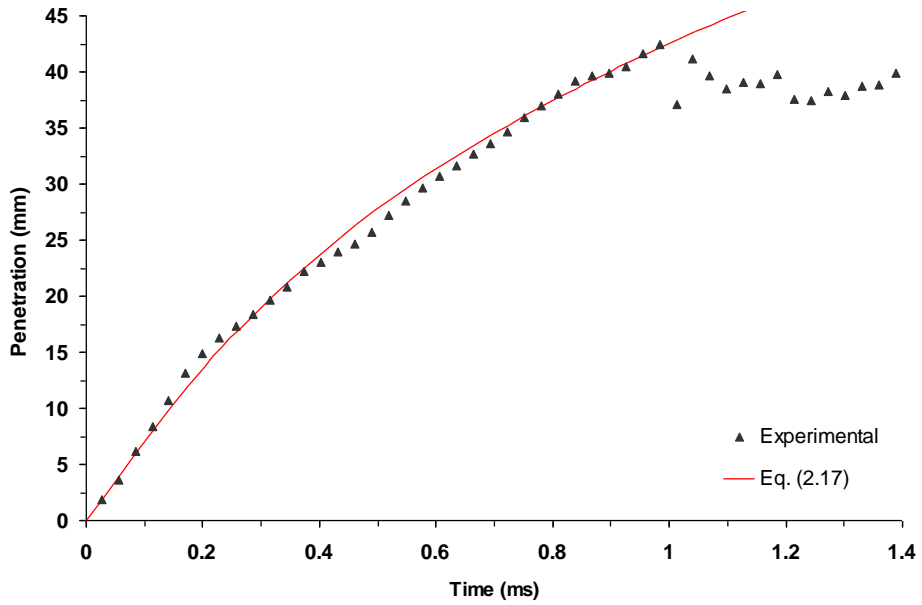

Fig AE-4. Same as Fig AE-1; the experimental results are for cold air intake (corresponding to 410 K at TDC); 140 MPa injection pressure; 34 kg/m^3 in-cylinder density; 4 MPa in-cylinder pressure

Fig AE-5. Same as Fig AE-1; the experimental results are for cold air intake (corresponding to 350 K at TDC); 140 MPa injection pressure; 20 kg/m³ in-cylinder density; 2 MPa in-cylinder pressure

Fig AE-6. Same as Fig AE-1; the experimental results are for cold air intake (corresponding to 448 K at TDC); 100 MPa injection pressure; 47 kg/m³ in-cylinder density; 6 MPa in-cylinder pressure

Fig AE-7. Same as Fig AE-1; the experimental results are for cold air intake (corresponding to 410 K at TDC); 100 MPa injection pressure; 34 kg/m³ in-cylinder density; 4 MPa in-cylinder pressure
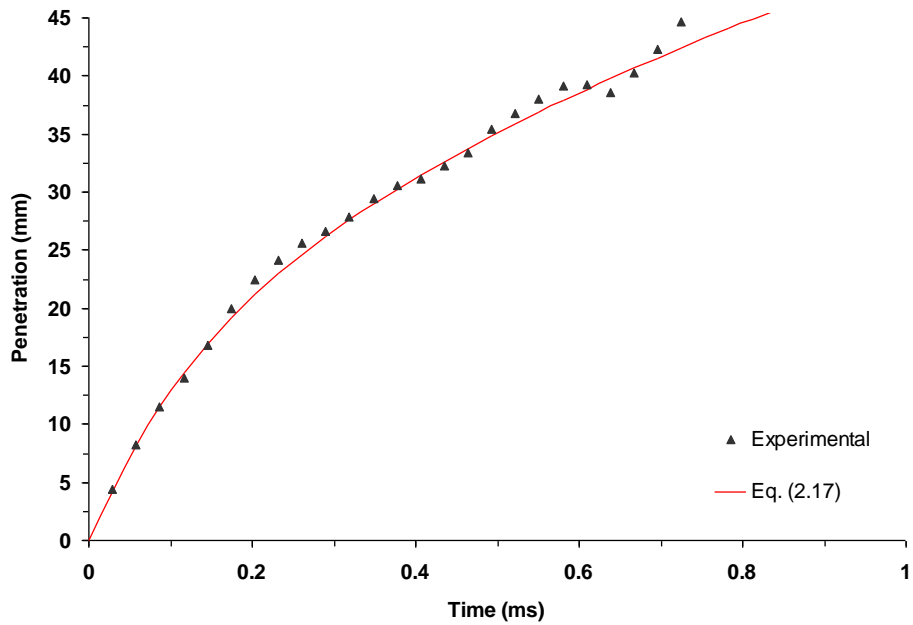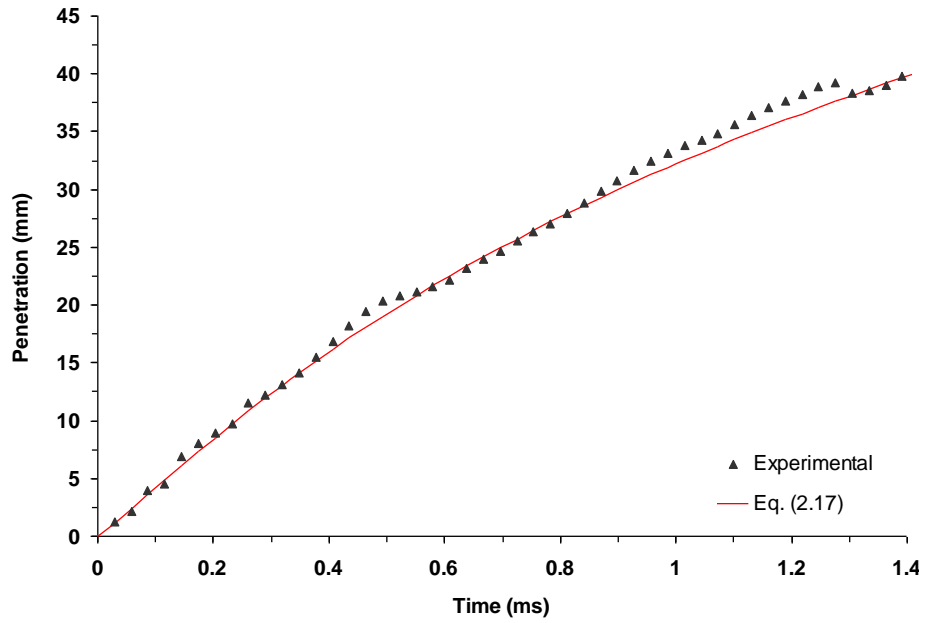

Fig AE-8. Same as Fig AE-1; the experimental results are for cold air intake (corresponding to 350 K at TDC); 100 MPa injection pressure; 20 kg/m³ in-cylinder density; 2 MPa in-cylinder pressure

Fig AE-9. Same as Fig AE-1; the experimental results are for cold air intake (corresponding to 448 K at TDC); 60 MPa injection pressure; 47 kg/m^3 in-cylinder density; 6 MPa in-cylinder pressure
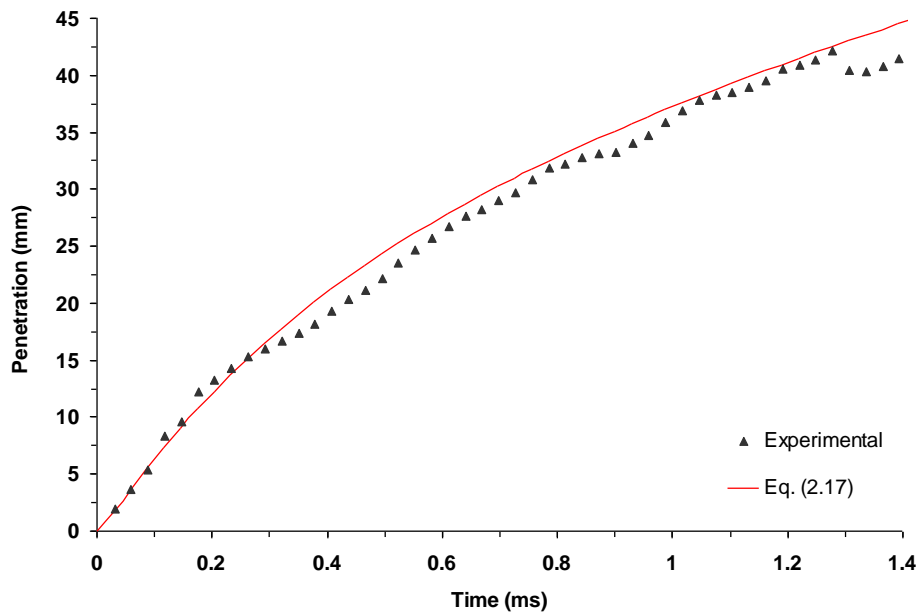

Fig AE-10. Same as Fig AE-1; the experimental results are for cold air intake (corresponding to 410 K at TDC); 60 MPa injection pressure; 34 kg/m^3 in-cylinder density; 4 MPa in-cylinder pressure
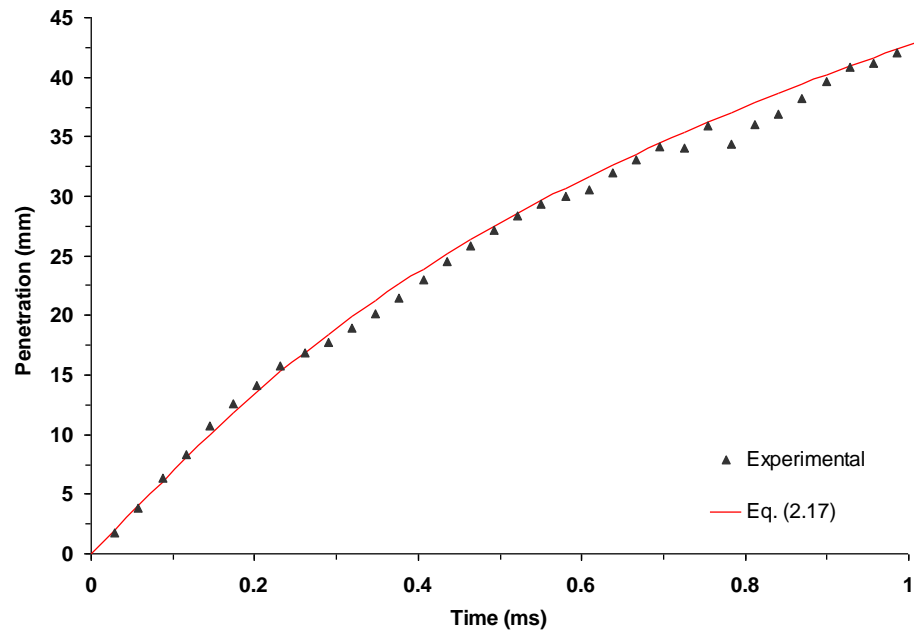
Fig AE-11. Same as Fig AE-1; the experimental results are for cold air intake (corresponding to 350 K at TDC); 60 MPa injection pressure; 20 kg/m^3 in-cylinder density; 2 MPa in-cylinder pressure